Contents

CHAPTER 1

Introduction

1.1 BACKGROUND AND MOTIVATION

During recent years, there has been an enormous growth in the wireless communications industry. The deployment of systems such as cellular telephone networks, wireless local loop networks and wireless local area networks, is rapidly evolving worldwide. As more and more people use these services, network operators are constantly forced to optimise their networks so that the maximum amount of capacity, together with quality coverage, can be squeezed out of these networks. The field of antenna engineering is of course central to all wireless technologies and plays a significant role in the successful deployment and optimisation of such systems. As such, the growing demand for wireless communications, has stimulated extensive research in order to find new solutions to problems in antenna engineering.

With the advances in wireless communications technologies and the associated proliferation of base stations throughout major cities and much of the countryside, a number of requirements are imposed on the antennas that are used. From a technological point of view, wireless communications antennas should be relatively cheap and easy to manufacture, they should be lightweight and they should be robust. From an environmental point of view, the antennas should have a minimum impact. As such, these antennas should have a low profile and should be as compact as possible. This of course also goes for handset antennas, where the size of such devices is constantly shrinking.

One type of antenna that fulfills these requirements very well, is the microstrip antenna. These antennas operate in the microwave frequency range and are widely used on base stations as well as handsets. They come in a variety of configurations and have been the topic of what is currently

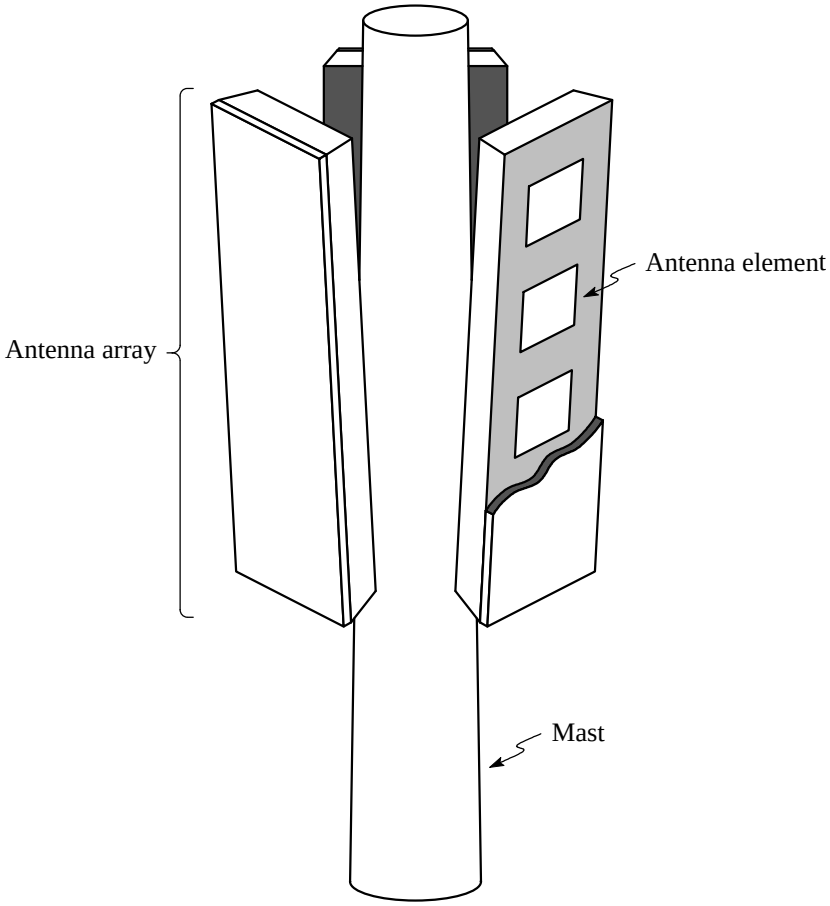

Figure 1.1 Cellular base-station antennas. Each antenna array comprises of a number of antenna elements.

probably the most active field in antenna research and development. In one of its most basic forms, a microstrip antenna is comprised of a metal patch that is supported above a larger ground plane. It is usually manufactured by printing the patch on a thin microwave substrate. This configuration is commonly known as the microstrip patch antenna. Microstrip patches are often used as single-element antennas, but are also very suitable for use within antenna arrays. Figure 1.1 shows a typical example of how they can be used in directional base-station antennas.

Rectangular and circular patches are most common, but any shape that possesses a reasonably well-defined resonant mode can be used [1]. These include, for example, annular rings, ellipses and triangles. The patch is a resonant element and therefore one of its dimensions must be approximately one half of the guided wavelength in the presence of the dielectric substrate. There are four fundamental techniques to feed or excite the patch [2–4]. These are shown in Figure1.2 and include the probe feed, the microstrip-line feed, the aperture-coupled feed and the proximity-coupled feed.

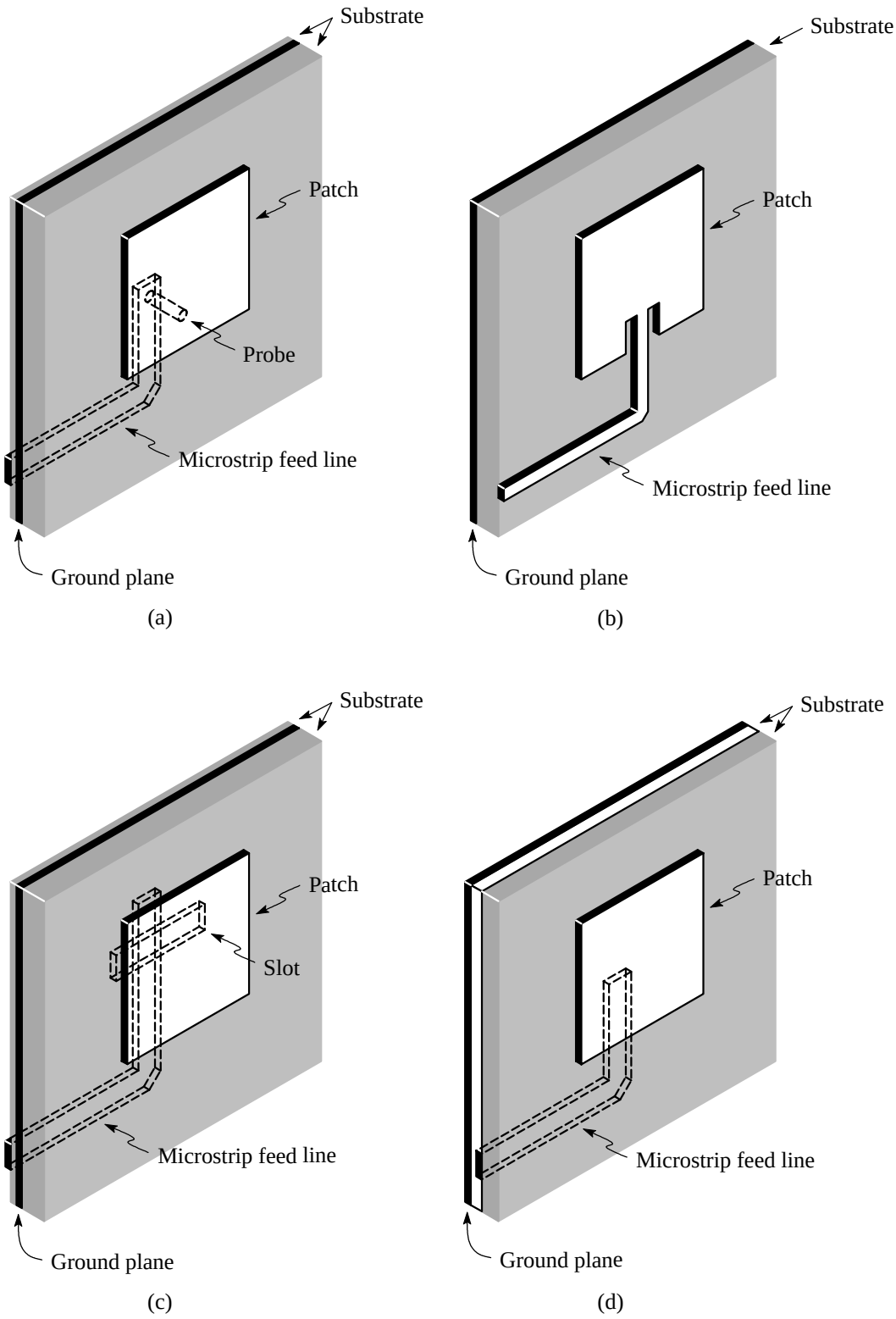

Figure 1.2 Typical feeding techniques for microstrip patch antennas. (a) Probe feed. (b) Microstrip-line feed. (c) Aperture-coupled feed. (d) Proximity-coupled feed.

The probe feed, as shown in Figure 1.2(a), is constructed by extending a probe through the ground plane and connecting it to the patch, typically by soldering it. If the patch is part of an antenna array, the feed network can be printed on a substrate behind the ground plane. In such a case, the other end of the probe will typically be soldered to a microstrip line that forms part of the feed network. In the case of single-element antennas, the probe is usually the inner conductor of a coaxial cable of which the outer conductor is soldered to the ground plane. The input impedance is controlled by the position of the probe-to-patch connection point. The microstrip-line feed, as shown in Figure 1.2(b), consists of a microstrip line that is connected to one of the edges of the patch. The position of the connection point is also used to control the input impedance. As shown in Figure 1.2(b), this can be achieved by insetting the microstrip line into the surface of the patch. With the aperture-coupled feed, as shown in Figure 1.2(c), the microstrip feed line and the patch are separated by a ground plane. Coupling between the feed line and the patch is then achieved via a small slot in the ground plane. Unlike the aperture-coupled feed, the proximity-coupled feed, as shown in Figure 1.2(d), has a microstrip feed line that is printed on a substrate layer between the ground plane and the patch. In this case, power from the feed line is electromagnetically coupled to the patch.

Each one of the feeding techniques has its own advantages and disadvantages. However, the probe feed has a number of characteristics that make it very suitable for applications in the wireless communications field. Due to the fact that the probe is connected directly to the patch, the antenna structure is quite robust. The probe feed is also less prone to alignment errors, which can significantly affect the performance of aperture-coupled and proximity-coupled feeds. Due to the fact that the feed network is separated from the patch, there is less spurious radiation from the feed network as compared to that of the microstrip-line feed and the proximity-coupled feed. A somewhat related disadvantage of the aperture-coupled patch, is that it can exhibit unwanted backward radiation through the slot in the ground plane. The probe feed also has the advantage that it can be driven directly via a coaxial cable, thereby avoiding the use of an additional substrate layer to support the feed line.

The main drawback associated with microstrip patch antennas in general, be they probe-fed or not, is that they inherently have a very narrow impedance bandwidth[1] (due to their multilayered configuration, aperture-coupled feeds and proximity-coupled feeds do tend to have a slightly wider bandwidth than probe feeds and microstrip-line feeds). In most cases, the impedance bandwidth is not wide enough to handle the requirements of modern wireless communications systems. The narrow impedance bandwidth of microstrip patch antennas can be ascribed to the thin substrates that are normally used to separate the patch and the ground plane. The general performance trends of a microstrip patch antenna are illustrated in Figure 1.3 [2–4]. Here, Figure 1.3(a) shows the typical trend for impedance bandwidth versus substrate thickness, as a function of the substrate's

[1] Impedance bandwidth refers to the frequency range over which the antenna can be matched to its feed line. It is usually specified in terms of the acceptable return loss or voltage standing-wave ratio at the antenna port.

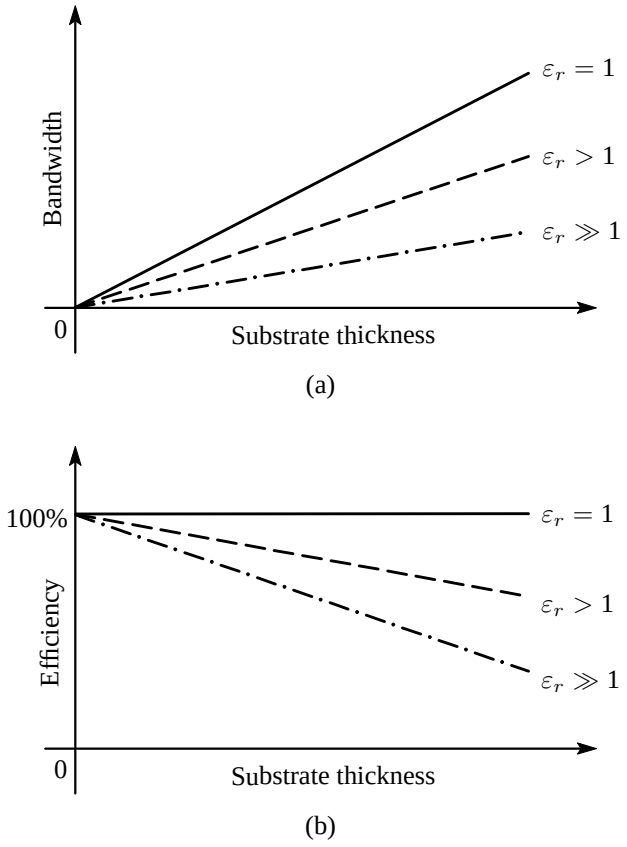

Figure 1.3 Illustrative performance trends of a microstrip patch antenna. (a) Impedance bandwidth. (b) Surface-wave efficiency.

dielectric constant, while Figure 1.3(b) shows the typical trend for surface-wave efficiency versus substrate thickness, also as a function of the substrate's dielectric constant. From these it can be seen that, in order to increase the bandwidth, the substrate thickness has to be increased, while the dielectric constant has to be kept as low as possible. A low dielectric constant is also required to keep surface-wave losses as low as possible. Therefore, in order to obtain a wideband microstrip patch antenna with good surface-wave efficiency, the performance trends of Figure 1.3 point to a thick substrate with a very low dielectric constant.

While a thick substrate does increase the impedance bandwidth of microstrip patch antennas, it also introduces a further complication for microstrip patch antennas with probe feeds. For thin substrates, the input impedance at the resonant frequency is basically purely resistive, but as the substrate thickness is increased, the input impedance becomes more inductive [4–7]. This is illustrated in Figure 1.4, where the input impedance is given by $Z_{\text{in}} = R_{\text{in}} + jX_{\text{in}}$ at the resonant frequency f_0. In order to offset the inductive component of the input impedance, an alternative feeding mechanism to the direct probe feed is required.

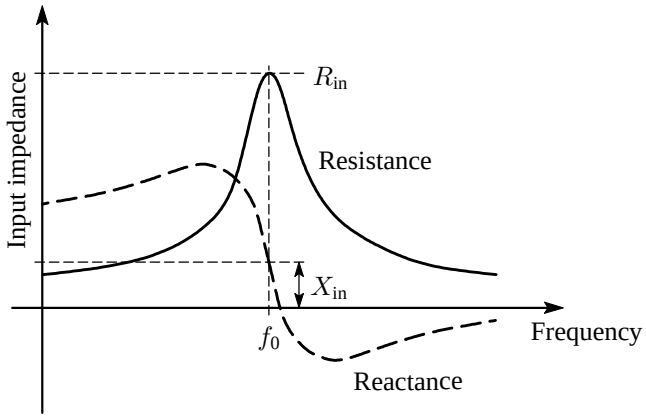

Figure 1.4 Illustrative input impedance of a probe-fed microstrip patch antenna on a thick substrate.

To this date, various feeding mechanisms, as well as various other approaches to enhance the impedance bandwidth of probe-fed microstrip patch antennas, have been suggested and implemented. These, for example, include wideband impedance-matching networks, edge-coupled patches, stacked patches, shaped probes, capacitive coupling and slotted patches. However, not all of these solutions fulfill the requirements that are imposed by modern-day wireless communications systems. Some of the solutions are not suitable for array applications, some require multiple substrate layers, some are very complex to design, while others are very sensitive to alignment errors and manufacturing tolerances. As such, the research into wideband probe-fed microstrip patch antennas, which are suitable for modern-day wireless communications systems, is still a very relevant topic. The number of publications that still appear on this topic also confirms that it is indeed the case.

Another area of research, which is closely linked to advances in antenna development, is the field of computational electromagnetics. As antennas become more complex, the use of simple analytical modelling techniques is not sufficient anymore. The use of more sophisticated numerical methods, such as full-wave modelling techniques, has therefore become inevitable. However, with these methods, the modelling of complex antenna configurations, and especially large antenna arrays, can become very computationally expensive and can easily exceed the capabilities of most personal computers. As such, the search for techniques that can reduce the computational complexity of these methods, is currently a very important research area and much progress has indeed been made during recent years.

Most of the research into new antenna elements and numerical modelling techniques has been performed independently from one another. This has resulted in general-purpose numerical modelling techniques, which is good per se, but which can require extensive computational resources for modelling electrically large antennas. The aim of this thesis is therefore firstly the develop-

ment of a new wideband probe-fed microstrip antenna element, which on the one hand, fulfills the requirements of modern-day wireless communication systems and improves on the shortcomings of previous approaches, but which on the other hand, also lends itself to more efficient numerical modelling techniques. The second aim of the thesis is then the formulation and implementation of a numerical modelling technique that can be used for the analysis and design of such antennas without resorting to excessive computational resources. In the next section, the specific objectives and scope of the study will be formulated in more detail.

1.2 OBJECTIVES AND SCOPE

As mentioned in the previous paragraph, the focus of this study is in two main areas. These are the development of new wideband probe-fed microstrip patch antenna elements and arrays, as well as the development of numerical modelling techniques for the efficient analysis and design of such antennas. The specific objectives and scope of the research are described in the bullets that follow.

- The first objective of this research is the development of a feeding mechanism for wideband probe-fed microstrip patch antenna elements. Modern wireless communication systems, such as the Global System for Mobile (GSM) Communications and the Universal Mobile Telecommunications System (UMTS), typically require bandwidths of approximately 10% to 15%. For this research, the base station antennas are of particular interest and therefore the new antenna elements should be suitable for use within various array configurations, while still retaining the benefits of low cost, light weight, low profile, as well as ease of design and manufacture. As microwave substrates can be relatively expensive for large arrays, it would be beneficial to minimise the number of substrate layers. Furthermore, in order to enhance the efficiency of the numerical modelling, the radiating patch elements will be restricted to rectangular shapes. The scope of this study will also be limited to single-band antenna elements only.

- An objective that follows from the previous bullet, is to verify the performance of the new antenna element, to characterise it, and to show how it can be used in various applications. This will be achieved through numerical modelling as well as through actual experimental measurements.

- Another major objective of this study is the formulation and implementation of an efficient numerical modelling technique, which can be used for the analysis and design of antenna elements and arrays that are based on the new antenna element. Here, the focus is primarily on minimising the amount of computer memory that is required. This is very important for the analysis of large antenna arrays. In terms of accuracy, the numerical model should compare well to commercial codes. It should handle multiple substrate layers as well as planar and vertical currents.[2] The analysis of arbitrarily-orientated antenna elements should

[2] Vertical currents are required to model the probe feeds, while horizontal currents are confined to specific planar layers. This is commonly referred to as a so-called 2.5D formulation.

also be possible (i.e. it should not be restricted to configurations where the antenna elements are all aligned to a rectangular grid). The scope of the numerical model will be limited to the antenna elements only. Feed networks can be implemented in many ways and can usually be designed effectively with existing modelling techniques. Also, for probe-fed antennas, the feed network is well isolated from the antenna elements and therefore any coupling between the feed network and the antenna elements can be ignored.

- Finally, an important objective is the validation of the numerical model as well as various examples to illustrate its performance and benefits. For this purpose, the results of the numerical formulation will be compared to published results, measurements, as well as the simulation results of two commercial codes.

1.3 ORIGINAL CONTRIBUTIONS

This study has resulted in a number of original contributions, of which some have already been published by the author [8–14]. In summary, the principal contributions of this study include the development of a new capacitive feeding mechanism for wideband probe-fed microstrip patch antennas as well as the implementation of a spectral-domain moment-method formulation for the efficient analysis of large, finite arrays of these elements. Such antenna configurations are very useful in the wireless communications industry, but extremely difficult to analyse with commercially available software. The detailed contributions are described in the bullets that follow.

- A novel feeding mechanism has been developed for probe-fed microstrip patch antennas on thick substrates, which, in principle, can be used with any shape of radiating element. As shown in Figure 1.5, the feeding mechanism consists of a small probe-fed patch that is capacitively coupled to the radiating element, thereby overcoming the inductance usually associated with a probe in a thick substrate. It has been demonstrated, both through numerical modelling and measurements, how this concept can be applied to rectangular as well as circular and annular-ring radiating elements. These elements have all been characterised and it turns out that this feeding mechanism is very easy to design and optimise. It has also been shown how these elements can be used in various array configurations.

- A new full-wave model, based on the spectral-domain moment-method (SDMM), has been developed to analyse these structures in multilayered substrates. This model is based on a unique combination of subdomain and entire-domain basis functions, leading to considerable savings in computer-memory requirements when compared to commercial codes (both in the spectral and spatial domains) that normally only use subdomain basis functions.

- Commercial SDMM codes are normally based on an underlying rectangular grid, implying that the modelled structure often has to be modified in order to fit into the grid. This new model allows for arbitrary-sized basis functions that can also have an arbitrary orientation with respect to each other. There is therefore no need to modify the geometry of the actual structure.

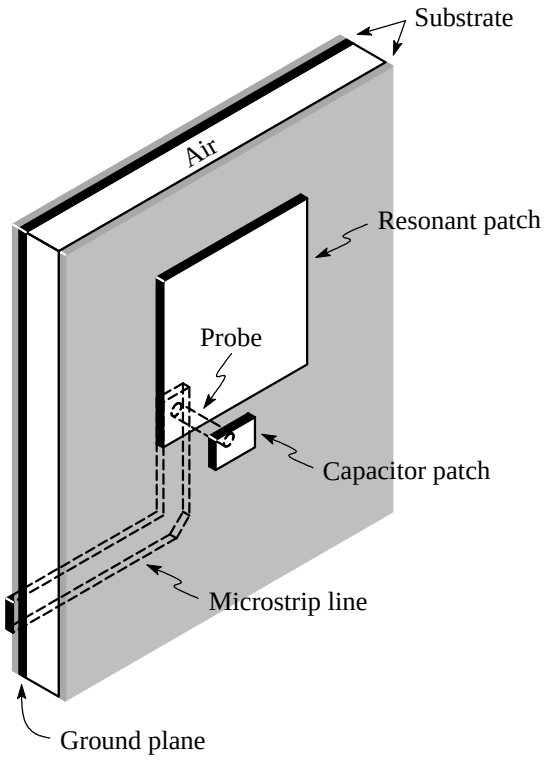

Figure 1.5 New wideband microstrip patch antenna with the capacitive feed probe.

- A very important type of basis function, which is required when a probe is connected to a microstrip patch, is the so-called attachment mode. In the literature, various subdomain and entire-domain attachment modes have been proposed for the SDMM, but it was not clear as to what the limitations of each one are. Some of these modes have been studied in various situations, resulting in a better understanding of where they are applicable. The circular attachment mode has also been extended for a more accurate description of the electric current density on small circular probe-fed capacitor patches.

- One of the difficulties associated with the SDMM, is the highly oscillating nature of the interaction integrands for basis and testing functions that are widely separated. A recent publication dealt with this issue by proposing a new integration path in the complex plane, over which the integrand decays exponentially. However, this method becomes less efficient as the basis and testing functions move closer to each other, even more so for thick substrates. During this study, the method has been extended and can now also be used in situations where the basis and testing functions are relatively close to each other on a relatively thick substrate. The conditions under which this method is valid, have also been refined.

- When using the moment method (MM), the interactions between all basis and testing functions have to be calculated. However, depending on the implementation, there are often identical interactions that have to be calculated repeatedly. On a rectangular grid, these

duplicate entries can easily be identified and eliminated, but becomes much more difficult with a mixture of lower-order and higher-order basis functions that are arbitrarily orientated. Special algorithms have been developed to deal with such a mixture of basis functions and proves to speed up the solution significantly.

1.4 OVERVIEW OF THE THESIS

This chapter presented some background information on microstrip patch antennas and the various feeding techniques that can be used. It was pointed out why the probe feed is of particular interest for wireless communications systems and what the challenges are when wideband operation of these antennas is required. The shortcomings of existing approaches, in terms of antenna elements and modelling techniques, were also briefly pointed out. With these in mind, the main objectives and scope of the study were formulated. In short, it includes the development of new wideband probe-fed microstrip antenna elements and arrays, as well as the development of numerical modelling techniques for the efficient analysis and design of such antennas. The original contributions that followed, were also summarised. A short overview of the remaining chapters will now follow.

Chapter 2 starts off by presenting an overview of various techniques that have been used thus far for the bandwidth-enhancement of probe-fed microstrip patch antennas. The performance as well as the advantages and disadvantages of the most practical approaches is also discussed. This is followed by presenting the new microstrip patch antenna element with the capacitive feed probe. Chapter 2 then also gives an overview of various modelling techniques that can be used for the analysis and design of probe-fed microstrip patch antennas. These range from simple approximate methods to advanced full-wave methods. The strengths and weaknesses of each method is also addressed. Finally, the chapter is concluded by an overview of the formulation that was implemented for the purposes of this study. The formulation is based on the SDMM.

Chapter 3 deals with the implementation of the SDMM formulation. It starts off with a general overview of the MM and shows how it can be formulated in the spectral domain. The Green's function for planarly multilayered media is discussed in detail, as are the various basis functions that were used. Various numerical integration strategies were implemented. These, together with algorithms that were implemented to minimise duplicate calculations, are also presented with the necessary detail. In short, Chapter 3 covers all the computational aspects of the formulation that was implemented. These also include the evaluation of the different network parameters and far fields.

Chapter 4 contains all the numerical and experimental results. It starts off with a validation of the SDMM formulation that was implemented. This is followed by a characterisation of the new antenna element in order to determine the effect of the various geometrical parameters. A number of applications are also presented. These include vertically and horizontally polarised arrays, as well as $\pm 45^{\circ}$ slant-polarised arrays. Finally, it is shown how the new feeding mechanism can be

used for microstrip patches where the resonant patch is not necessarily rectangular in shape.

Chapter 5 contains general conclusions regarding this study and concludes the thesis with some recommendations that can be considered for future work.

CHAPTER 2

Wideband Probe-Fed Microstrip Patch Antennas and Modelling Techniques

2.1 INTRODUCTORY REMARKS

During recent years, much effort has gone into bandwidth enhancement techniques for microstrip antennas in general. As such, there is a great amount of information in the open literature and it covers a very broad range of solutions that have been proposed thus far [1]. The entire spectrum of approaches that have been suggested is too comprehensive to discuss here and therefore the discussion in this chapter will be restricted to techniques that have been applied to enhance the bandwidth of probe-fed microstrip patch antennas in particular. In this chapter, a broad overview will be given in terms of the various techniques that are currently available to enhance the bandwidth of probe-fed microstrip patch antennas. The performance, advantages and disadvantages of the most practical approaches will also be discussed. With these in mind, the new antenna element that forms the basis of this study, will be presented.

Another field in which there has been a tremendous amount of activity during recent years, is that of computational electromagnetics [15, 16]. These tools are essential for an accurate analysis and design of complex antenna elements and arrays. Although probe-fed microstrip patch antennas are structurally quite simple, an accurate analysis of their various characteristics proves to be rather intricate. This is partly due to the singular and rapidly-varying nature of the current in the vicinity of the probe-to-patch junction and also due to the presence of a multilayered substrate. This chapter will give a brief overview of the methods that are currently available, together with their associated strengths and shortcomings. Once again, with these in mind, an overview of the formulation that was implemented for the purposes of this study, will also be presented.

In this chapter, Section 2.2 gives an overview of wideband probe-fed microstrip antennas, while Section 2.3 presents the new wideband microstrip antenna elements, employing capacitive feed probes. Section 2.4 gives an overview of the modelling techniques that are currently available, while Section 2.5 presents the basic aspects of the theoretical formulation that was implemented for the purposes of this study.

2.2 OVERVIEW OF WIDEBAND PROBE-FED MICROSTRIP PATCH ANTENNAS

The impedance bandwidth of microstrip patch antennas is usually much smaller than the pattern bandwidth [17]. This discussion on bandwidth-enhancement techniques will therefore focus on input impedance rather than radiation patterns. There are a number of ways in which the impedance bandwidth of probe-fed microstrip patch antennas can be enhanced. According to Pozar [18], the various bandwidth-enhancement techniques can be categorised into three broad approaches: impedance matching; the use of multiple resonances; and the use of lossy materials. For the purpose of this overview, it has been decided to rather categorise the different approaches in terms of the antenna structures that are normally used. These include: wideband impedance-matching networks; edge-coupled patches; stacked elements; shaped probes; and finally capacitive coupling and slotted patches. In terms of Pozar's categories, all these approaches can be identified as making use of either impedance matching or multiple resonances. In practice, lossy materials are not frequently used as it limits the radiation efficiency of the antenna. It will therefore not be considered here.

2.2.1 Wideband Impedance-Matching Networks

One of the most direct ways to improve the impedance bandwidth of probe-fed microstrip antennas, without altering the antenna element itself, is to use a reactive matching network that compensates for the rapid frequency variations of the input impedance. As shown in Figure 2.1, this can typically be implemented in microstrip form below the ground plane of the antenna element. The method is not restricted to antenna elements on either thin or a thick substrates, but the thick substrate will of course add some extra bandwidth.

Pues and Van de Capelle [19] implemented the method by modelling the antenna as a simple resonant circuit. A procedure, similar to the design of a bandpass filter, is then used to synthesise the matching network. With this approach, they have managed to increase the bandwidth from 4.2% to 12% for a voltage standing-wave ratio (VSWR) of 2:1. Subsequently to that, An *et al.* [20] used the simplified real frequency technique in order to design the matching network for a probe-fed microstrip patch antenna. They have managed to increase the bandwidth of one antenna element from 5.7% to 11.1% for a VSWR of 1.5:1, and that of another from 9.4% to 16.8% for a VSWR of 2:1. Recently, De Haaij *et al.* [21] have shown how a parallel resonant circuit can increase the bandwidth from 3.2% to 6.9% for a VSWR of 1.5:1.

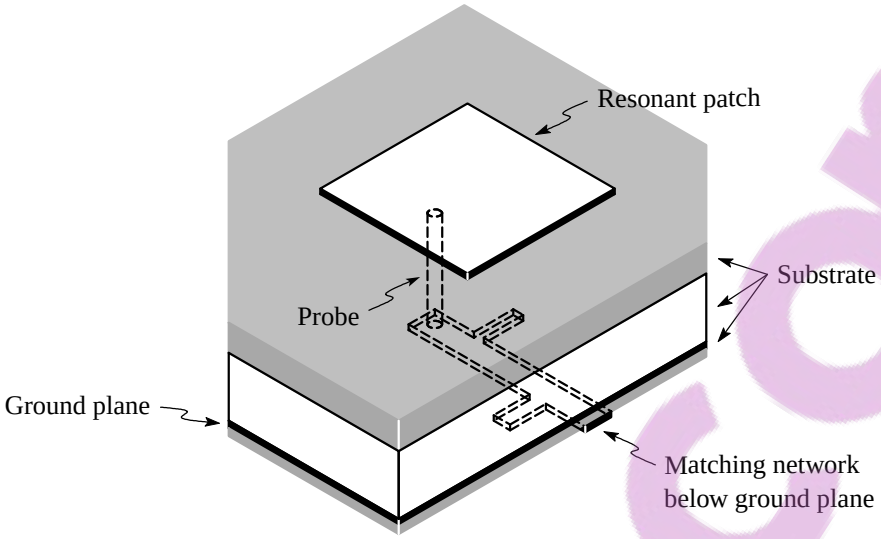

Figure 2.1 Geometry of a probe-fed microstrip patch antenna with a wideband impedance-matching network.

The advantages of using impedance-matching networks are that the antenna elements do not get altered and that the matching network can be placed behind the antenna's ground plane. As such, the radiation characteristics of the antenna element stay unchanged, while radiation from the matching network is also minimised. The drawback of this method is that the matching network can potentially take up space that is very limited when microstrip feed networks are used to excite the individual elements in an antenna array. Another drawback is that, for single-element antennas, more than one substrate layer is required to support the antenna element and the matching network.

2.2.2 Edge-Coupled Patches

The basic idea behind edge-coupled patches, is to increase the impedance bandwidth of a microstrip patch through the introduction of additional resonant patches. By doing so, a few closely-spaced resonances can be created. Only one of the elements is driven directly. The other patches are coupled through proximity effects. An example of such an arrangement is shown in Figure 2.2.

This approach has been investigated by Wood [22] as well as Kumar and Gupta [23–25]. The parasitic patches can be coupled to either the radiating edges, the non-radiating edges or to both pairs of edges. The approach in [25] uses short transmission lines to couple the parasitic patches directly to the driven patch. With the edge-coupled approach, impedance bandwidths of up to 25.8% have been obtained for a VSWR of 2:1. This was achieved with four parasitic patches coupled to the driven patch.

The advantages of the edge-coupled approach include the fact that the structure is coplanar in nature and that it can be fabricated on a single-layer substrate. However, this approach also has

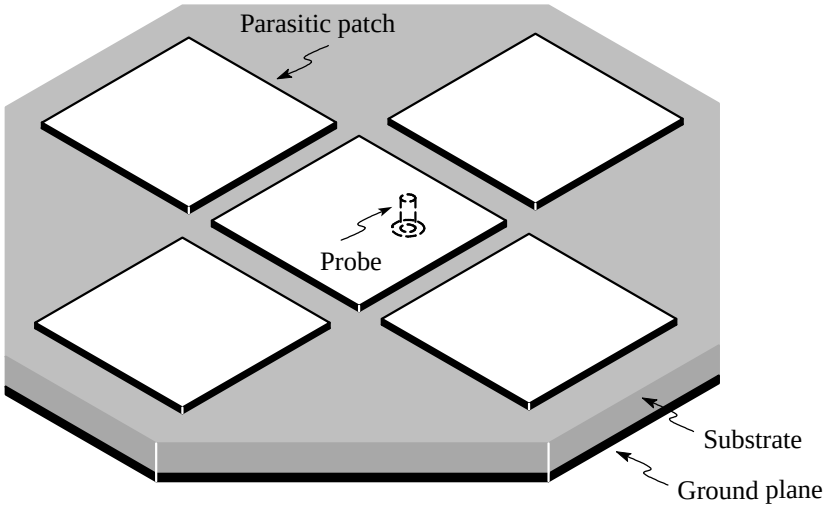

Figure 2.2 Geometry of a probe-fed microstrip patch element that is edge-coupled to the parasitic patches.

a few drawbacks. Due to the fact that the different patches radiate with different amplitudes and phases at different frequencies, the radiation patterns change significantly over the operating frequencies. The enlarged size of the structure can also be a potential handicap in many applications. For example, in phased-array applications, the large separation distances between elements can introduce grating lobes.

2.2.3 Stacked Patches

A very popular technique, which is often used to increase the impedance bandwidth of microstrip patch antennas, is to stack two or more resonant patches on top of each other [2]. As with the edge-coupled resonators, this technique also relies on closely-spaced multiple resonances. However, in this case, the elements take up less surface area due to the fact that they are not arranged in a coplanar configuration. Figure 2.3 shows the geometry of such an antenna element where the bottom patch is driven by a probe and the top patch, which is located on a different substrate layer, is proximity-coupled to the bottom one.

In practice, the patches are usually very close in size so that the generation of two distinct resonances can be avoided. Different shapes of patches can be used. These commonly include rectangular patches [26, 27], circular patches [26, 28, 29] and annular-ring patches [26, 30]. It has also been shown how a combination of shapes can be used [31, 32]. As far as impedance bandwidth goes, Waterhouse [26] reported a 26% 10 dB return-loss bandwidth for rectangular patches, Mitchell *et al.* [29] reported a 33% 10 dB return-loss bandwidth for circular patches, while Kokotoff *et al.* [30] reported a 22% 10 dB return-loss bandwidth for annular-ring patches. These bandwidths were all obtained for two patches stacked on top of each other. It is possible to stack more patches, but the performance may not be much better than with only two patches [2,18].

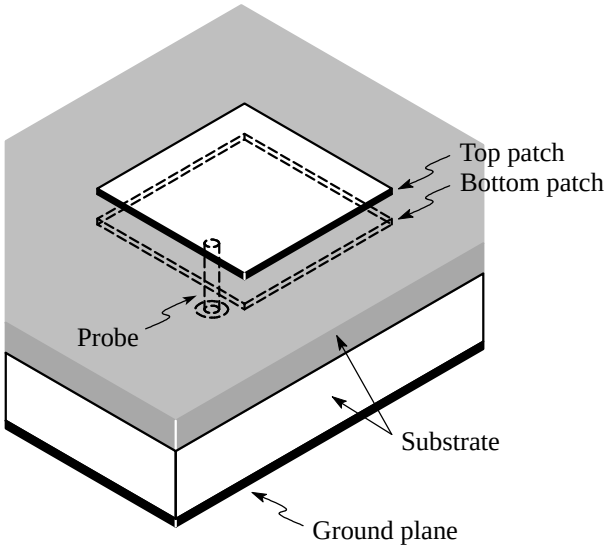

Figure 2.3 Geometry of a probe-fed stacked microstrip patch antenna.

Instead of aligning the patches vertically, some researchers have also used a horizontal offset between the patches [33]. However, due to the structural asymmetry, these configurations exhibit beam dispersion.

The stacked-patch configuration has a number of advantages over the edge-coupled configuration. Since it does not increase the surface area of the element, it can be used in array configurations without the danger of creating grating lobes. Its radiation patterns and phase centre also remains relatively constant over the operating frequency band. It has a large number of parameters that can be used for optimisation. However, due to this, the design and optimisation process can also be very complex. Another drawback of stacked patches, is that it requires more than one substrate layer to support the patches.

2.2.4 Shaped Probes

As was shown in Chapter 1, a thick substrate can be used to enhance the impedance bandwidth of microstrip patch antennas. However, the input impedance of probe-fed microstrip patch antennas become more inductive as the substrate thickness is increased. In order to offset this inductance, some capacitance is needed in the antenna's feeding structure. One way to implement such a capacitive feed is to alter the shape of the probe. There are basically two approaches. In one approach, the probe is connected directly to the patch [34, 35], while in the other approach, the probe is not connected to the patch at all [36–39].

The direct feed can be implemented as shown in Figure 2.4(a), where the feeding structure consists of a stepped probe. The horizontal part of the probe couples capacitively to the patch. Chen and Chia [34] reported an impedance bandwidth of 19.5% for a VSWR of 2:1. Another option is to

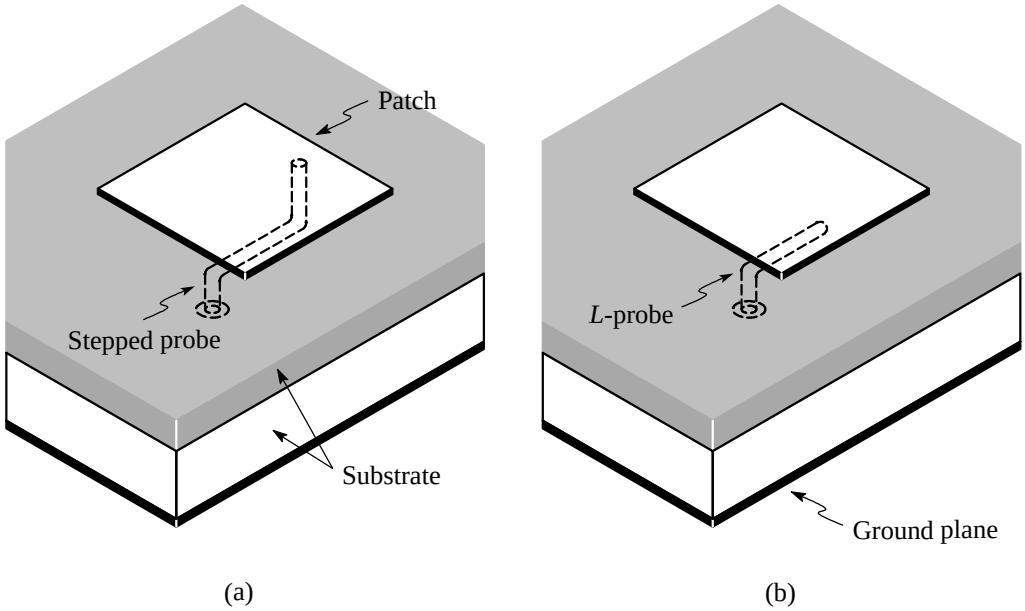

Figure 2.4 Geometries of microstrip patch antennas with shaped probes. (a) Stepped probe. (b) *L*-shaped probe.

add a stub to one of the radiating edges of the patch and to feed the stub directly with a probe. For such an approach, Chen and Chia [35] reported an impedance bandwidth of 25%, once again for a VSWR of 2:1.

The proximity-coupled probe is implemented as shown in Figure 2.4(b), where the probe is bent into a *L*-shape. The horizontal part of the probe runs underneath the patch and also couples capacitively to it. This solution has been implemented for a variety of patch shapes. Mak *et al.* reported an impedance bandwidth of 36% for a rectangular patch in [36] and 42% for a triangular patch in [39], while Guo *et al.* reported an impedance bandwidth of 27% for an annular-ring patch in [38]. These bandwidth figures were all quoted for a VSWR of 2:1. Instead of a *L*-shaped probe, Mak *et al.* [40] also used a *T*-shaped probe and managed to achieve an impedance bandwidth of 40% for a VSWR of 2:1.

A microstrip patch antenna with a shaped probe, be it directly driven or not, can usually be supported on a single substrate layer. This makes it extremely suitable for antenna arrays where cost has to be minimised. Most of these elements have radiation patterns with a slight squint in the *E*-plane and slightly high cross-polarisation levels in the *H*-plane. These are characteristics of probe-fed microstrip patch antennas on thick substrates. The stepped probe, though, exhibits somewhat lower cross-polarisation levels. The patches that are directly driven should be more robust that those with the proximity coupled probes. For the latter ones, care has to be taken with respect to the proper alignment of the pathes and probes. Another advantage of both approaches is that, since they do not increase the surface area of the element, they can be used in array config-

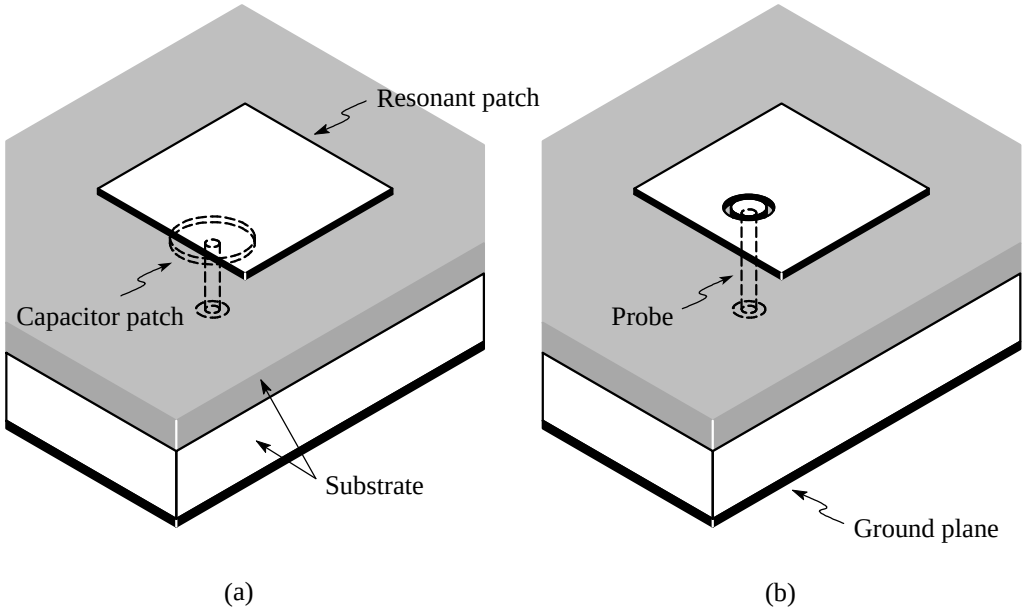

Figure 2.5 Geometries of probe-fed microstrip patch antennas where capacitive coupling and slots are used. (a) Capacitive coupling. (b) Slot in the surface of the patch.

urations without the danger of creating grating lobes.

2.2.5 Capacitive Coupling and Slotted Patches

There are two alternative approaches that can also be used to overcome the inductive nature of the input impedance associated with a probe-fed patch on a thick substrate. These are capacitive coupling or the use of slots within the surface of the patch element. Examples of such approaches are shown in Figures 2.5(a) and (b) respectively. It can be argued that these two approaches are structurally quite similar. The approach in Figure 2.5(a) has a small probe-fed capacitor patch, which is situated below the resonant patch [41–43]. The gap between them acts as a series capacitor. Similarly, the annular slot in Figure 2.5(b) separates the patch into a small probe-fed capacitor patch and a resonant patch [44, 45]. In this case, the slot also acts as a series capacitor. In principle, both of these approaches employ some sort of capacitive coupling and are functionally also, to some degree, equivalent to the *L*-probe and *T*-probe as described in Section 2.2.4.

Liu *et al.* [46] combined the capacitively-coupled feed probe with stacked patches and reported a impedance bandwidth of 25.7% for a VSWR of 2:1. To achieve this, they used two stacked patches with a small probe-fed patch below the bottom resonant patch. In another approach, González *et al.* [47] placed a resonant patch, together with the small probe-fed capacitor patch just below it, into a metallic cavity. With this configuration, they managed to obtain a impedance bandwidth of 35.3% for a VSWR of 2:1.

As far as the slotted patches go, Hall [44] showed that, for a circular resonant patch with a annular

slot around a small circular probe-fed capacitor patch in the surface of the resonant patch, a 10 dB return-loss bandwidth of 13.2% could be obtained for the TM_{11} mode and 15.8% for the TM_{21} mode. Anguera *et al.* [45] used a rectangular resonant patch, also with a small circular probe-fed capacitor patch in the surface of the resonant patch, and managed to achieve an impedance bandwidth of 21.7% for a VSWR of 1.5:1. Chen and Chia [48] used a small rectangular probe-fed capacitor patch, located within a notch that was cut into the surface of the resonant patch. They managed to obtain an impedance bandwidth of 36% for a VSWR of 2:1. Some authors also used a rectangular resonant patch with a *U*-slot in its surface. The metallic area inside the slot is then driven directly with a probe. Here, Tong *et al.* [49] reported a impedance bandwidth of 27% for a VSWR of 2:1, while Weigand *et al.* [50] reported an impedance bandwidth of 39%, also for a VSWR of 2:1. In yet another approach, Nie *et al.* [51] placed a circular probe-fed patch within a annular-ring patch, with the circular patch exciting higher-order modes on the annular-ring patch. They managed to obtain a 8 dB return-loss bandwidth of 20%. Kokotoff *et al.* [52] placed a small shorted circular probe-fed patch within a annular-ring patch, but with the circular patch exciting the dominant TM_{11} mode on the annular-ring patch. They reported a 10 dB return-loss of 6.6%.

The advantage of the approach where the capacitor patch is located below the resonant patch, is that the cross-polarisation levels in the *H*-plane are lower than what can be achieved with the approach where the capacitor patch is located within the surface of the resonant patch. However, in order to support the capacitor patch below the resonant patch, an additional substrate layer might be required. In contrast, only one substrate layer is required to support the configuration where the capacitor patch is located inside the surface of the resonant patch. Furthermore, the capacitor patch below the resonant patch is prone to alignment errors and can complicate the fabrication process. On the other hand, when using a capacitor patch within the surface area of a resonant patch, there can potentially be many design parameters that can complicate the design of such antenna elements. Here also, an advantage of both approaches is that, since they do not increase the surface area of the element, they can be used in array configurations without the danger of creating grating lobes.

2.3 NEW WIDEBAND MICROSTRIP PATCH ANTENNAS WITH CAPACITIVE FEED PROBES

As was stated earlier on, the basis of this study is a new wideband microstrip patch antenna element with a capacitive feed probe. Figure 2.6 shows the general geometry of the new antenna structure. As can be seen, it consists of a rectangular resonant patch with a small probe-fed capacitor patch right next to it. Both patches reside on the same substrate layer. For this study, both circular and rectangular capacitor patches, as shown in Figures 2.6(a) and (b) respectively, were used.

For wideband applications, the two patches can be manufactured on a thin substrate with a thick low-loss substrate, such as air, right below it. The antenna element is functionally very similar to most other capacitively-coupled elements. The gap between the resonant patch and the capacitor

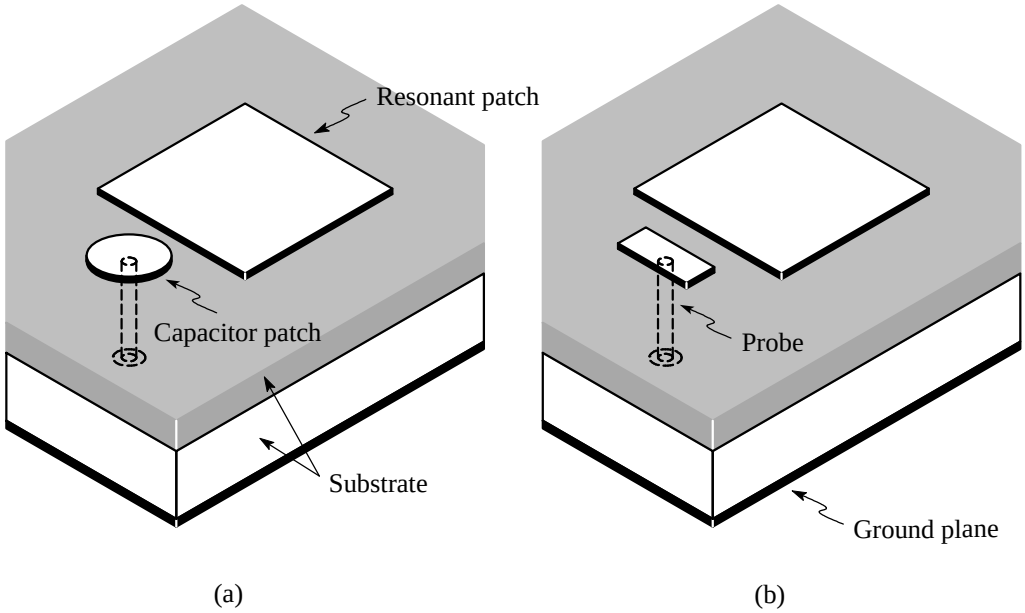

Figure 2.6 Geometries of the new wideband microstrip patch antennas employing capacitive feed probes. (a) Circular capacitor patch. (b) Rectangular capacitor patch.

patch acts as a series capacitor, thereby offsetting the inductance of the long probe. Once the size of the resonant patch and the thickness of the substrate have been fixed for a certain operating frequency and impedance bandwidth, there are basically two parameters that can be used to control the input impedance of the antenna element. These are the size of the capacitor patch and the size of the gap between the two patches. In Chapter 4, it will be shown how these parameters affect the input impedance.

Given that most of the approaches for wideband probe-fed microstrip patch antennas have been described in Section 2.2, the structural properties of the new antenna element can be viewed in context. First of all, the new antenna element can be manufactured on a single substrate layer due to both the resonant patch and the capacitor patch residing on the same layer. This is very important for large antenna arrays where laminates can be very expensive. The fact that the capacitor patch is driven directly by a probe, gives the structure some rigidity. The structure is also less prone to alignment errors, which can be a factor for antenna elements where the probe does not make physical contact with any of the patches or where the capacitor patch is located on a different layer than the resonant patch. The surface area of the element is not much larger than that of a resonant patch and therefore it is very suitable for use within antenna arrays. An advantage that might not be very obvious at first, is that the antenna element, as opposed to slotted antenna elements, consists of parts that are canonical in shape. As will be shown in Section 2.5, it has huge benefits for the analysis of such antennas, especially for large antenna arrays. Finally, the design of such an antenna element, as well as tuning of the input impedance, is very straightforward due to the few parameters that have to be adjusted. In terms of performance, it is expected that the new antenna

element should be comparable to other probe-fed patch antennas on thick substrates. This will be investigated thoroughly in Chapter 4.

2.4 OVERVIEW OF MODELLING TECHNIQUES

There are a number of methods that can be used for the analysis of probe-fed microstrip patch antennas. Most of these methods fall into one of two broad categories: approximate methods and full-wave methods [1]. The approximate methods are based on simplifying assumptions and therefore they have a number of limitations and are usually less accurate. They are almost always used to analyse single antenna elements as it is very difficult to model coupling between elements with these methods. However, where applicable, they normally do provide good physical insight and the solution times are usually very small. The full-wave methods include all relevant wave mechanisms and rely heavily upon the use of efficient numerical algorithms. When applied properly, the full-wave methods are very accurate and can be used to model a wide variety of antenna configurations, including antenna arrays. These methods tend to be much more complex than the approximate methods and also provide less physical insight. Very often they also require much computational resources and extensive solution times.

In the remainder of this section, an overview of both approximate and full-wave methods will be given. Since the full-wave moment method, also known as the method of moments, is arguably the most popular method for the analysis of microstrip antennas, it will be discussed separately. The moment method can be implemented in either the spatial domain or the spectral domain. Both of these will be considered.

2.4.1 Approximate Methods

Some of the popular approximate models include the *transmission-line model*, the *cavity model* and the *segmentation model*. These models usually treat the microstrip patch as a transmission line or as a cavity resonator.

The **transmission-line model** represents the antenna by radiating slots that are separated by a length of low-impedance transmission line [4, 53–57]. A good implementation of this model is the one by Pues and Van de Capelle [57]. Each radiating slot is represented by a parallel equivalent admittance. The analysis then basically boils down to normal circuit theory. This method is the simplest method for the analysis and design of microstrip patch antennas, but often yields the least accurate results and also lacks versatility. It can be used to calculate the resonant frequency and input resistance of an antenna element. With this method, it is difficult to model the coupling between antenna elements, although it has been done successfully [55, 58]. The method only works reasonably well for antennas with thin substrates and low dielectric constants, while it becomes increasingly less accurate as either the substrate thickness or dielectric constant is increased [1]. The transmission-line model has mostly been applied to directly-driven rectangular patches.

Some of the drawbacks associated with the transmission-line model can be overcome with the **cavity model**. The cavity model is a modal-expansion analysis technique whereby the patch is viewed as a thin cavity with electric conductors above and below it, and with magnetic walls along its perimeter [56, 59, 60]. With this method, the electric field between the patch and the ground plane is expanded in terms of a series of cavity resonant modes or eigenfunctions, along with its eigenvalues or resonant frequencies associated with each mode. Due to the cavity being thin, only transverse magnetic (TM) field configurations, with respect to the height of the cavity, are considered. The field variation along the height of the cavity is also assumed to be constant. Furthermore, due to the fact that a lossless cavity cannot radiate and exhibits a purely reactive input impedance, the radiation effect is modelled by introducing an artificially-increased loss tangent for the substrate. The cavity model can model the resonant frequency and input impedance more accurately than the transmission-line model, but it is also limited to patch shapes for which the two-dimensional Helmholtz equation admits an analytical solution [61]. As with the transmission-line model, the cavity model also becomes less accurate as the substrate thickness or dielectric constant is increased [1]. It does not take into account the effect of guided waves in the substrate. It is difficult to model mutual coupling with the cavity model, although it has been done successfully [62, 63]. Gómez-Tagle and Christodoulou [64] even used it successfully for the modelling of stacked patches in a multilayered substrate. Microstrip patch antennas are often represented by an equivalent network model [43, 45, 65, 66]. In such a model, the values of the lumped elements can be determined by using the cavity model [67].

The **segmentation method** is more versatile than both the transmission-line model and the cavity model, especially in terms of its ability to treat patches with arbitrary shapes. It is an extension of the cavity model, but instead of treating the patch as a single cavity, the patch is segmented into sections of regular shapes. The cavity model is then applied to each section, after which the multiport-connection method is used to connect the individual sections. This method has been used, for example, by Palanisamy and Garg [68] for the modelling of a square-ring patch, while Kumar and Gupta [23–25] used it for the modelling of edge-coupled patches. As with the other approximate methods that have been described, this method also works best for thin, low dielectric-constant substrates.

2.4.2 Full-Wave Methods

Three very popular full-wave methods that can be used to model probe-fed microstrip patch antennas, are the *moment method* (MM), the *finite-element method* (FEM) and the *finite-difference time-domain* (FDTD) *method*. These are the three major paradigms of full-wave electromagnetic modelling techniques [69]. Unlike the approximate methods, these methods include all the relevant wave mechanisms and are potentially very accurate. They all incorporate the idea of discretising some unknown electromagnetic property. For the MM, it is the current density, while for the FEM and FDTD, it is normally the electric field (also the magnetic field for the FDTD method). The discretisation process results in the electromagnetic property of interest being approximated

by a set of smaller elements, but of which the complex amplitudes are initially unknown. The amplitudes are determined by applying the full-wave method of choice to the agglomeration of elements. Usually, the approximation becomes more accurate as the number of elements is increased. Although these methods all share the idea of discretisation, their implementations are very different and therefore each of the three methods will now be considered in some more detail.

The **MM** is undoubtedly the most widely-used full-wave method for the analysis of microstrip antennas [69]. It is synonymous with the method of weighted residuals and was popularised by Harrington [70–72] who first demonstrated its power and flexibility for the solution of electromagnetic problems in the 1960s. This method is mostly applied in the frequency domain, where only a single frequency is considered at any one time.

When using the MM, the current density on the antenna is usually the working variable from which all the other antenna parameters are derived. The method is implemented by replacing the antenna with an equivalent surface current density. The surface current density is then discretised into a set of appropriate current-density elements, also known as basis functions (or expansion functions), with variable amplitudes. For example, these elements can take the form of wire segments and surface patches. Now, the Green's function for the problem is used to express the electric and/or magnetic fields everywhere in terms of the current-density elements on the surface of the antenna. Boundary conditions for the electric and/or magnetic fields are then enforced on the surface of the antenna by using testing functions (also known as weighting functions). This process is often called the testing procedure and results in a system of linear integral equations (IEs). This system of equations can be expressed in matrix form, where the interaction between each basis (expansion) function and each testing (weighting) function is taken into account. For most MM implementations, this matrix, also known as the interaction matrix, is usually a dense matrix. If the basis functions and testing functions are chosen to be the same set of functions, the method is known as the Galerkin method. Finally, the system of linear equations is solved to yield the amplitudes of the current-density elements. After the surface current density on the surface of the antenna has been solved for, the other antenna parameters, such as the input impedance, radiation patterns and gain, can easily be derived. For more detailed descriptions of the MM, texts such as those by Balanis [4, 73], Stutzman and Thiele [74], as well as Sarkar *et al.* [75], can be consulted.

A major advantage of the MM, when compared to other full-wave methods, is its efficient treatment of highly conducting surfaces. With the MM, only the surface current density is discretised and not the fields in the surrounding medium. Furthermore, it inherently includes the far-field radiation condition, while antennas that are embedded in multilayered media, can be simulated efficiently when using the appropriate Green's function for such a configuration. On the down side, the MM is not very well suited for the efficient analysis of problems that include electromagnetically penetrable materials. Also, while the formulations for multilayered media are very

powerful, they are very intricate and complex to implement. For an efficient multilayered-media formulation, an infinite ground plane and laterally infinite layers have to be assumed. The implementation for finite ground planes and layers is much more inefficient as the substrate and ground plane also have to be discretised.

Despite some of its drawbacks, the MM is still the preferred method for frequency-domain problems that involve highly conducting surfaces [15]. For the analysis of microstrip antennas, the method can either be implemented in the so-called spatial domain or the so-called spectral domain. Due to the fact that these two implementations have been used so extensively for the analysis of microstrip antennas, they will be considered separately in Sections 2.4.3 and 2.4.4 respectively.

The **FEM** is widely used in structural mechanics and thermodynamics. It was introduced to the electromagnetic community towards the end of the 1960s [15, 69]. Since then, great progress has been made in terms of its application to electromagnetic problems. As is the case with the MM, the FEM is also mostly applied in the frequency domain. What makes the FEM very attractive, is its inherent ability to handle inhomogeneous media.

When using the FEM for electromagnetic problems, the electric field is the unknown variable that has to be solved for. The method is implemented by discretising the entire volume over which the electric field exists, together with its bounding surface, into small elements. Triangular elements are typically used on surfaces, while tetrahedrons can be used for the volumetric elements. Simple linear or higher-order functions on the nodes, along the edges or on the faces of the elements, are used to model the electric field. For antenna problems, the volume over which the electric field exists, will have one boundary on the antenna and another boundary some distance away from the antenna. The latter boundary is an absorbing boundary, which is needed to truncate the volume. One viewpoint from which the FEM can be derived, is that of variational analysis [15]. This method starts with the partial differential equation (PDE) form of Maxwell's equations and finds a variational functional for which the minimum (or extremal point) corresponds with the solution of the PDE, subject to the boundary conditions. An example of such a functional is the energy functional, which is an expression describing all the energy associated with the configuration being analysed, in terms of the electric field [76]. After the boundary conditions have been enforced, a matrix equation is obtained. This equation can then be solved to yield the amplitudes that are associated with the functions on the elements used to model the electric field. The matrix associated with the FEM, is a sparse matrix due to the fact that every element only interacts with the elements in its own neighbourhood. Other parameters, such as the magnetic field, induced currents and power loss, can be obtained from the electric field. For more detailed descriptions of the FEM, texts such as those by Jin [77], Silvester and Ferrari [78], Volakis *et al.* [79], as well as Peterson *et al.* [80], can be consulted.

The major advantage of the FEM is that the electrical and geometrical properties of each element

can be defined independently [76]. Therefore, very complicated geometries and inhomogeneous materials can be treated with relative ease. This implies that the analysis of microstrip antennas with finite ground planes and layers is also possible. However, the FEM has a few weak points when compared to methods such as the MM. The fact that the entire volume between the antenna surface and the absorbing boundary has to discretised, makes the FEM very inefficient for the analysis of highly conducting radiators. Also, for large three-dimensional structures, the generation of the mesh, into which the problem is discretised, can become very complex and time-consuming.

The FEM is usually not the preferred method for the analysis of most antenna problems, but is frequently used for the simulation of microwave devices and eigenvalue problems. An interesting approach is where the FEM is hybridised with the MM. These methods are very useful for the analysis of microstrip antennas inside cavities [47, 81]. Like most other full-wave modelling techniques, the FEM has been implemented in a few commercial codes. A typical example is HFSS from Ansoft.

The **FDTD method**, which was introduced by Yee [82] in 1966, is also very well suited for the analysis of problems that contain inhomogeneous media. However, unlike the MM and the FEM, the FDTD method is a time-domain method and is not restricted to a single frequency at any one time. As compared to the MM and the FEM, the FDTD method is much easier to implement as it makes limited demands on higher mathematics [15].

The FDTD method is also a PDE-based method. However, unlike the FEM, it does not make use of variational analysis, but directly approximates the space- and time-differential operators in Maxwell's time-dependant curl equations with central-difference schemes. This is facilitated by modelling the region of interest with two spatially interleaved grids of discrete points [76]. One grid contains the points at which the electric field is evaluated, while the other grid contains the points at which the magnetic field is evaluated. A time-stepping procedure is used where the electric and magnetic fields are calculated alternatively. The field values at the next time step are calculated by using those at the current and previous time steps. In such a way, the fields are then effectively propagated throughout the grid. The time stepping is continued until a steady-state solution is obtained. The source that drives the problem is of course also some time-dependant function. Frequency-domain results can be obtained by applying a discrete Fourier transform to the time-domain results. Unlike the MM and the FEM, no system of linear equations has to be solved and therefore no matrix has to be stored. As with the FEM, the grid has to be terminated with an absorbing boundary. For more detailed descriptions of the FDTD method, texts such as those by Taflove [83, 84] and Elsherbeni *et al.* [85] can be consulted.

The FDTD method has a number of attractive features, which include its relatively simple implementation, its straightforward treatment of inhomogeneous materials, its ability to generate wideband data from a single run and the fact that no system of linear equations need to be solved.

The analysis of microstrip antennas with finite ground planes and layers is of course also possible. On the down side, however, the regular orthogonal grid that is normally used, is not very flexible. This implies that curved surfaces have to be approximated with a staircase approach. For configurations with sharp edges, such an approach may require a very fine grid and therefore many field points. As with the FEM, the fact that the volume around the antenna is discretised, makes the FDTD inefficient for the analysis of highly conductive radiators.

Like the FEM, the FDTD method is usually not the preferred method for the analysis of most antenna problems, but it is very useful for wideband systems and in situations where time-domain solutions are required. Despite of this, the FDTD method has been used for the analysis of probe-fed microstrip patch antennas [49, 85, 86] and can indeed yield very accurate results. The FDTD method has been implemented in a few commercial codes. Typical examples of these are Fidelity from Zeland Software and XFDTD from Remcom.

As has already been mentioned, the MM is by far the most widely-used method for the analysis of microstrip antennas. There are two broad implementations of this method: the spatial-domain implementation and the spectral-domain implementation. Each of these implementations has its own advantages and will now be discussed in Sections 2.4.3 and 2.4.4 respectively.

2.4.3 Spatial-Domain Moment Method

As the name indicates, the spatial-domain MM is characterised by the fact that all the entries in the interaction matrix are expressed in terms of spatial variables. As mentioned before, each entry in the interaction matrix represents the interaction between a basis (expansion) function and a testing (weighting) function. This is accomplished by using the Green's function for the problem at hand. Of course, in this case, it would be the Green's function for a grounded planarly multilayered medium. The Green's function for planarly multilayered media is available in closed form, but only in the spectral domain. Its spatial-domain counterparts are then commonly obtained by applying an inverse Fourier-Bessel transform (also known as a Sommerfeld integral) to the spectral-domain Green's function. Apart from this, each entry in the interaction matrix also contains two surface integrals. One integral is associated with the convolution between the basis function and the Green's function, in order to find the electric field due to the basis function, while the other integral is associated with the testing procedure, in order to apply the relevant boundary conditions over the support (footprint) of the testing function.

In the spatial domain, the so-called mixed-potential form of the electric-field integral-equation (EFIE), or in short, the MPIE, is usually preferred for the analysis of microstrip antennas embedded in planarly multilayered media [42, 87–95]. With the MPIE formulation, the electric field is expressed in terms of the induced current density and induced charge density through the vector and scalar potentials respectively. The MPIE is preferred due to the fact that the potential forms of the Green's function are less singular than the field forms [96]. This becomes more apparent

when the interaction between two very closely-spaced basis and testing functions is calculated. The evaluation of the Sommerfeld integrals, which are required to find the spatial-domain Green's function, is usually a very laborious process due to the integrand being highly oscillatory and slowly decaying. As such, much effort has been invested into finding methods to speed up the evaluation of this type of integral. One popular approach is to integrate along the Sommerfeld integration path [97] and to use techniques such as the partition-extrapolation method to speed up the integration [98]. An approach that has become very popular recently, is to derive closed-form expressions for the Green's function [99–103]. The basic idea behind this approach is to approximate the Green's function by a sum of complex exponentials to which the Sommerfeld identity can be applied, resulting in closed-form expressions for the Green's function. However, the process is not entirely trivial as it involves the extraction of surface-wave contributions that are associated with the poles of the Green's function. Another technique that can be used with any of the aforementioned approaches, is to precompute the integrals, whereafter interpolation techniques can be used on the precomputed values.

The spatial-domain MM is well suited for the use of subdomain basis functions (i.e. basis functions that exist only over a small part of the total surface area to be modelled). This is due to the fact that the two surface integrals, which are associated with each entry in the interaction matrix, can be evaluated much more easily for a simple function over a small support than for a complex function over a much larger support. Two types of subdomain basis functions that are often used on surfaces, are rooftop functions with rectangular support [87] and Rao, Wilton and Glisson (RWG) basis functions with triangular support [104]. The RWG basis functions are very useful for the modelling of geometries with arbitrary shapes [97, 105]. Special basis functions, known as attachment modes, are required to model the current behaviour at junctions between wires and surface patches. A number of attachment modes have been developed for use within the spatial-domain MM. For some of them, the attachment point has to coincide with the corners of the surface basis functions [87, 90], while for others, the attachment point can be anywhere on the surface basis functions [89, 106–108].

Due to the use of subdomain basis functions in the spatial-domain MM, the number of basis functions that are required to model the current on a structure, increases very rapidly with the size of the structure. This implies that the interaction matrix can very easily become quite large, resulting in potentially very large computer-memory requirements for storage of the interaction matrix. For large problems, the bottleneck in the spatial-domain approach is the solution time associated with the matrix equation. It usually exceeds the time that is required to set up the interaction matrix. In this area too, many efforts have led to more efficient methods of solving the matrix equation [109]. Some of the approaches include: the conjugate-gradient (CG) method combined with the fast Fourier transform (FFT) [110–113]; the fast-multipole method (FMM) [114]; and the impedance-matrix localisation (IML) method [115].

The spatial-domain MM is the method of choice for most commercial MM codes. Typical examples of these are IE3D from Zeland Software, Ensemble from Ansoft and FEKO from EM Software and Systems. For the modelling of surfaces, IE3D uses basis functions with both rectangular and triangular support, while Ensemble and FEKO only use basis functions with triangular support.

2.4.4 Spectral-Domain Moment Method

The spectral-domain MM is characterised by the fact that the entries in the interaction matrix are expressed in terms of spectral variables rather than spatial variables [116]. This is achieved by applying a two-dimensional Fourier transform to the basis functions, the testing functions and the Green's function. In effect, the two transverse spatial variables are transformed to their spectral counterparts. These spectral variables are actually two wavenumbers that are associated with the same directions as the spatial variables. A general entry in the interaction matrix would now contain two infinite integrals over the two spectral variables. As has already been mentioned, the spectral-domain Green's function can be found in closed form [117]. However, the spectral-domain formulation do place certain requirements on the basis functions and testing functions that can be used. One of these is that the two-dimensional Fourier transforms of the basis functions should be available in closed form. Another is that the two-dimensional Fourier transforms of the basis functions should decay faster than what the Green's function grows asymptotically [118, 119].

In the spectral domain, the Green's function does not become singular for small separation distances between the basis functions. Therefore, the electric field is usually expressed directly in terms of the induced current density through the EFIE [120]. Furthermore, the spectral-domain MM is well suited for the use of entire-domain basis functions (i.e. basis functions that exist over the entire surface area to be modelled). This is due to the fact that a function with a larger support in the spatial domain, transforms to a function that decays faster in the spectral domain. An example of such an entire-domain basis function, is the set of resonant modes that would be excited on a microstrip patch [31, 121–125]. These basis functions may not be as versatile as the subdomain basis functions, but the solution can be very efficient if the antenna structure mainly consists of canonical shapes. As with the spatial-domain approach, various kinds of attachment modes have also been developed to model the current behaviour at junctions between wires and surface patches [30, 126–135] or between wires and microstrip lines [136]. In the spectral-domain, however, it might be harder to find an attachment mode that models the current density at the junction accurately and of which the two-dimensional Fourier transform can be found in closed form. Subdomain basis functions can also be used with the spectral-domain formulation [137–142]. Some codes use volumetric currents for vertical connections [140–143]. The use of such basis functions, however, place a restriction on probe lengths that can be modelled accurately.

The most computationally-intensive part of the spectral-domain MM is the evaluation of the two

infinite integrals over the spectral variables for each entry in the interaction matrix. This is mainly due to the integrand becoming more oscillatory as the separation distance between the basis and testing function is increased. The integrand also exhibits poles, branch points and branch cuts that further complicate the evaluation of the integrals. The efficient evaluation of these integrals have been the topic of many research papers and, as such, various methods have been developed to deal with these integrals. One approach is to transform the spectral variables to a polar coordinate system [123, 144, 145]. By doing so, the two infinite integrals are transformed to one finite integral and one semi-infinite integral. Numerical integration algorithms, which take advantage of the cancellation effect that is associated with a fast oscillating integrand, can then be used to speed up the evaluation of the semi-infinite integral [146, 147]. It is also possible to use asymptotic extraction techniques [61, 125, 140–142, 148–159]. In both cases, however, it is important to realise that, for the semi-infinite integral, the contributions from the poles and branch points have to be extracted or the integration path has to be deformed so as to avoid these singularities [123, 160]. Another approach is to leave the spectral variables in a rectangular coordinate system. The separation of variables can then be used to speed up the evaluation of the integrals [161–163]. However, this method places some restrictions on the basis functions and testing functions that can be used. Another method is to use complex integration paths that dampens the oscillatory nature of the integrand [164–168]. The FFT can also be used to speed up numerical integration, but it implies that the basis functions should all be of equal size and should be spaced on a underlying rectangular grid [150, 169, 170]. Although the spectral-domain formulation has been used for the analysis of finite arrays on a uniform grid [125, 171–173], it is often used to model antenna arrays of infinite size by only analysing one unit cell of the array [129, 131, 174, 175].

When entire-domain basis functions are used with the spectral-domain MM, the interaction matrix is usually much smaller than with subdomain basis functions. In contrast with the spatial-domain MM, the bottleneck is not the solution time associated with the matrix equation, but rather the processing time that is required to set up the interaction matrix. This is due to the spectral integrations that have to be evaluated numerically.

The spectral-domain MM has been implemented in some commercial codes. Typical examples of these are Sonnet from Sonnet Software and EMSight from Applied Wave Research. These codes use subdomain basis functions on an underlying rectangular grid.

2.5 PROPOSED FORMULATION

From the previous discussion on analysis techniques, it is clear that the approximate methods are inappropriate for the modelling of the new antenna elements and also for antenna arrays that are based on these elements. This is partly due to the thick multilayered substrate as well as the fact that accurate coupling calculations between the various patches are crucial. As for the full-wave methods, the FEM and FDTD method are usually not one of the first choices when it comes to the modelling of microstrip antennas. This is of course due to the huge number of elements

that is needed to discretise the region around the antennas. The MM is far more efficient for such analyses as it only discretises the surface of the antenna. As was mentioned in the previous section, the spectral-domain MM formulation is very well suited for the analysis of problems that involve canonical shapes. Canonical shapes permit the usage of entire-domain basis functions that brings about significant savings in computer-memory requirements. The new antenna elements consist entirely of canonically-shaped patches and therefore naturally lend themselves to the use of the spectral-domain MM. A brief overview of the spectral-domain MM formulation that was implemented, will now be given. The details of the implementation can be found in Chapter 3.

As was explained in Section 2.3, the bandwidth of the new antenna element is obtained by introducing a low-loss substrate, such as air, between the patch laminate and the ground plane. The analysis of such a structure calls for the use of the planarly multilayered Green's function. In the spectral domain, the EFIE, which relates the electric field directly to the current density on the antenna, is normally used. For the purposes of this study, the Green's function was calculated as reported by Chen [6] and Lee *et al.* [176]. As the currents on the antenna structure can flow both in a horizontal and vertical direction, all nine components of the dyadic Green's function are required. A point to note here is that the currents flow either in a completely horizontal direction or a completely vertical direction (i.e. there are no oblique current flow through the layers of the substrate). The analysis of such a problem is often termed a two-and-one-half-dimensional analysis.

An antenna array basically consists of antenna elements and a feed network. With probe-fed antennas, the feed network is usually situated below the ground plane and is therefore isolated from the antenna elements. If an infinite ground plane is assumed, as is the case with the planarly multilayered Greens's functions, there will be no coupling between the feed network and the antenna elements, neither will there be any radiation from the feed network. Due to this, the formulation that was implemented, only models the antenna elements and not the feed network. The feed network can take on many forms and can usually be modelled quite effectively with most full-wave electromagnetic simulators. The feed network will of course excite the antenna elements in a certain way and there will also be certain impedance-matching issues between the feed network and the antenna elements. This can, however, be handled very easily if the scattering parameters of both the antenna elements and the feed network are connected by means of network-analysis techniques.[1]

In terms of basis functions, the proposed formulation draws on the benefits of entire-domain functions, while subdomain functions are only used on small features of the antenna elements. It is assumed that the patches are infinitely thin, but that the probes have finite radii that can be specified. The electric current density on each rectangular resonant patch is modelled by a set of entire-domain sinusoidal functions. These functions originate from a cavity-model analysis of

[1] Commercial codes, such as IE3D and Sonnet, have specific modules that are capable of network analyses.

rectangular patch antennas [125]. They account for most of the memory savings that are associated with this formulation. It has been found that the current density on each circular capacitor patch, as well as the current density at the junction where it connects to the probe, can be modelled with an extension to the circular attachment mode of Pinhas and Shtrikman [127]. The same attachment mode, together with subdomain rooftop basis functions, are used to model the current density on each rectangular capacitor patch. In this study, a rectangular attachment mode [6, 7, 129, 132] was also investigated, but as will be shown in Chapter 4, it is not as versatile as the circular one. Finally, due to the probes being fairly long, the current density on each probe is modelled by piecewise-sinusoidal functions along the length of the probe. The basis functions on the probes take the probe radii into account, but it is assumed that the current density on the probes has no axial variation. The piecewise-sinusoidal functions along the length of each probe have been used instead of piecewise-linear functions that are normally used [6,7,125]. This choice ensures that the analytical integration associated with terms in the interaction matrix that contain vertical currents, are much simpler.

Due to the many different basis and testing functions that are used to model the current density on different parts of the antenna elements, the MM interaction matrix contains entries for many different types of interactions. The spectral integrations that are associated with the different types of interactions do not all behave in a similar manner and therefore different integration strategies had to be implemented. The integrations associated with entries that describe the interaction between basis and testing functions on the probes and/or circular attachment modes, can be reduced to a single integral. The integration path for this integral is slightly deformed in order to avoid any singularities. When the basis functions are laterally separated, the method of averages [146, 177] is used to speed up the numerical integration process. The integration strategy for the remaining entries depends on whether the basis functions overlap or not. For basis functions that overlap, the integrand is smooth and can usually be evaluated quite easily. In this formulation, these integrals are evaluated by transforming to a polar coordinate system. For basis functions that are widely separated, the integrand is highly oscillatory and not easy to evaluate. These integrals are evaluated in a rectangular coordinate system, where the integration path is deformed in an appropriate way so that the oscillations in the integrand are damped. This is an extension to the work of Sereno-Garino *et al.* [164–168]. Unlike most other spectral-domain formulations, the basis functions in this formulation can be arbitrarily orientated and positioned. This implies that methods such as the FFT, cannot easily be used to speed up the numerical integrations. These methods require basis functions that are aligned on a rectangular grid. Given that the basis functions are not necessarily aligned and that there are many different types of interactions, it is impractical to use asymptotic extraction techniques to speed up the integrations. In previous work, the analytical parts associated with these techniques, have only been derived for the interaction between specific types of basis and testing functions, and for the special case where they are all aligned.

Another method that was used to speed up the process of setting up the interaction matrix, is to

eliminate the recalculation of any duplicate entries. As a first step in this direction, the Galerkin method was used, ensuring that the interaction matrix is symmetric. For the remaining entries, special algorithms were developed to identify all duplicates before the interaction matrix is actually generated. Due to the different types of basis functions and their arbitrary orientations, this is not a trivial process. However, especially for the analysis of antenna arrays, this process saves a huge amount of computational time.

Due to the choice of basis functions, the interaction matrix is usually relatively small and therefore the matrix equation can be solved by direct inversion of the interaction matrix. In this case, Gaussian elimination was used. The excitation for each antenna element is modelled with the delta-gap model at the base of each probe. With this excitation model, the Y-parameters associated with the antenna can be calculated directly once the basis-function coefficients have been solved for. The radiation patterns are calculated by using the stationary-phase method [6, 141].

Many of the ideas that have been used in this formulation, have been implemented separately to some extent before. However, this formulation combines these ideas, together with some new ones, in a unique way, thereby resulting in an efficient analysis of the new antenna elements and associated antenna arrays.

2.6 CONCLUDING REMARKS

This chapter presented a broad overview of several approaches that can be used to enhance the impedance bandwidth of probe-fed microstrip patch antennas, as well as the different techniques that can be used for the modelling of these antennas. The new antenna element, which forms the basis of this study, has also been introduced, together with a qualitative description of the theoretical formulation that was implemented for the modelling thereof. The new antenna element makes use of capacitive coupling in its feed structure, but unlike other approaches, the capacitor patch is positioned next to the resonant patch. This has several advantages: all the patches can be manufactured on a single laminate and is therefore relatively cheap and easy to manufacture; the input impedance can be controlled by adjusting only two parameters; and the fact that all the patches have canonical shapes, lends itself to more efficient modelling techniques. The theoretical formulation that was implemented for the analysis of these new antenna elements and arrays, is based on the spectral-domain MM that implements the planarly multilayered Green's function as well as a mixture of entire-domain and subdomain basis functions. The details of this implementation will be addressed in Chapter 3.

CHAPTER 3

Implementation of the Spectral-Domain Moment-Method Formulation

3.1 INTRODUCTORY REMARKS

This chapter presents a detailed exposition of the theoretical formulation that was implemented for the rigorous analysis of microstrip patch antennas with capacitive feed probes. The basic antenna geometries under consideration are shown in Figure 3.1. In its general form, it consists of one or more rectangular (or square) resonant patch elements that are capacitively coupled to smaller probe-fed capacitor patches. The capacitor patches can either be circular or rectangular in shape. The patches do not necessary have to be aligned, but can be orientated arbitrarily. All of the patches and probes reside within a grounded, planarly multilayered substrate. It is assumed that the patches, probes and ground plane are all perfect electric conductors (PECs) and that the multilayered substrate is isotropic, but possibly lossy. The analysis excludes the feed network as it can usually be analysed separately for probe-fed microstrip antennas.

The present analysis is based on a Green's function/moment method (MM) approach, where the electric-field integral-equation (EFIE), representing the boundary condition that the total tangential electric field must vanish on the PEC parts of the structure, is discretised by the Galerkin method. The unknown coefficients are evaluated by solving the resulting matrix equation. Although probe-fed patch antennas have enjoyed extensive theoretical analysis, the present analysis relies on a unique combination of entire-domain and subdomain basis functions and therefore introduces unique numerical requirements.

Section 3.2 presents a general overview of the MM formulation that was implemented, while

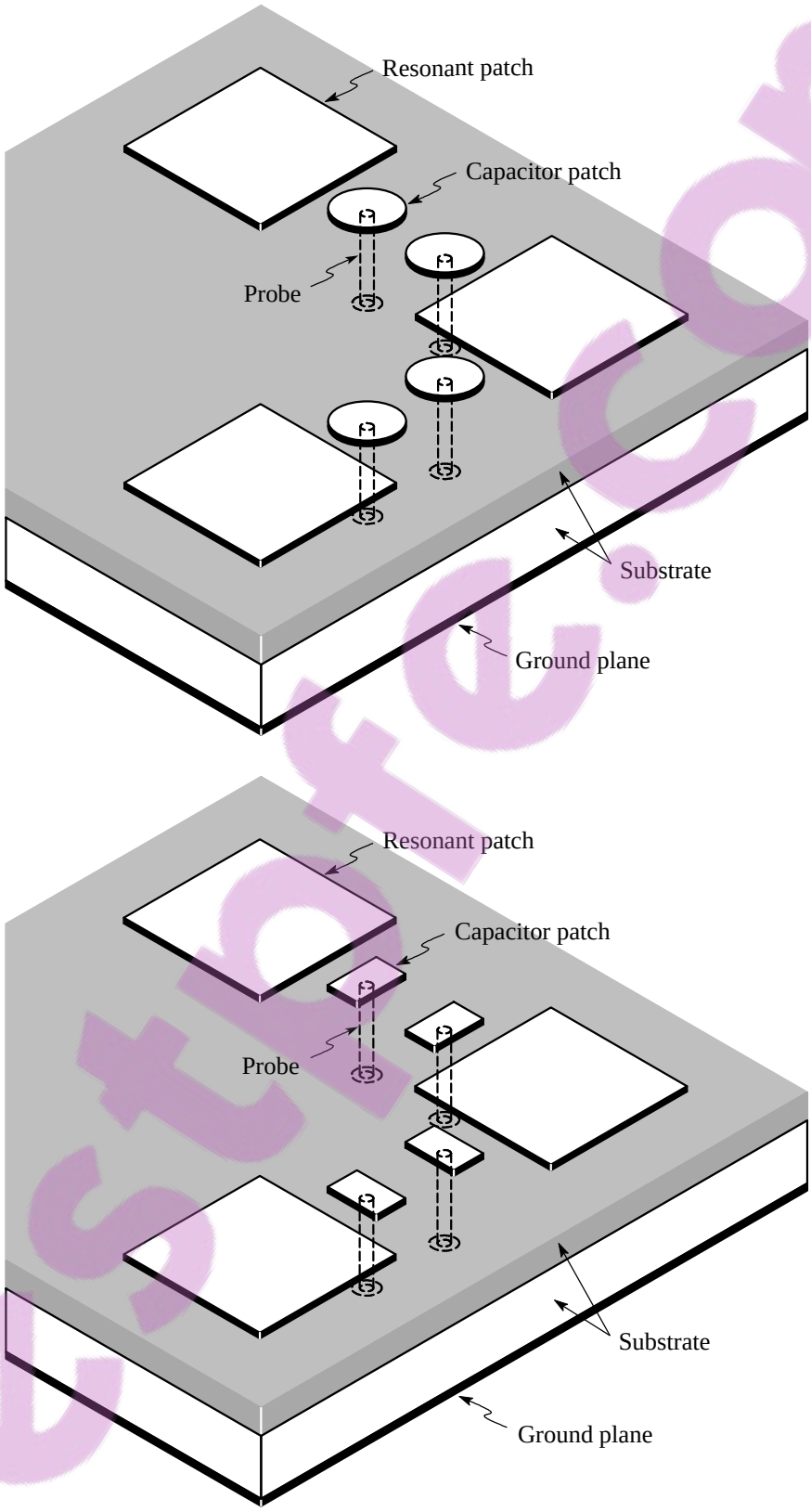

Figure 3.1 Basic antenna geometries.

Section 3.3 shows how the MM formulation can be cast into its spectral-domain form. The multilayered-media Green's function and basis functions are addressed in Sections 3.4 and 3.5 respectively. Section 3.6 deals with attachment modes, which are special basis functions required to model the singular and rapidly varying nature of the surface current density in the vicinity of each probe-to-patch junction. Section 3.8 deals with issues surrounding the evaluation of interaction-matrix elements, while Section 3.9 describes different integration strategies that have been used to evaluate these matrix elements. One of the difficulties associated with the spectral-domain MM (SDMM) is the highly oscillating nature of integrands for basis and testing functions that are widely separated. In Section 3.9, a recently-published method is extended to handle both situations where the basis and testing functions are closely spaced or widely separated. When using the MM, the interactions between all basis and testing functions have to be calculated. However, depending on the implementation, there are often identical interactions that have to be calculated repeatedly. On a rectangular grid, these duplicate entries can easily be identified and eliminated, but it becomes much more difficult with a mixture of lower-order and higher-order basis functions that are arbitrarily orientated. Special algorithms have been developed to deal with such a mixture of basis and testing functions, and are addressed in Section 3.10. Section 3.11 deals with the evaluation of the excitation-vector elements, while Section 3.12 addresses the solution of the matrix equation to yield the unknown current-density coefficients. The evaluation of the various network parameters for an array of antenna elements, is addressed in Section 3.13, while Section 3.14 deals with the evaluation of the far fields.

3.2 GENERAL FORMULATION

The general problem to be solved here, is shown in Figure 3.2(a). It consists of a PEC structure that is embedded within a grounded multilayered medium. For purposes of generalisation and illustration, the PEC structure is represented by an arbitrary shape, but in practice it would represent the patches and probes of the microstrip antenna. The excitation is due to impressed electric and magnetic current sources, $\mathbf{J}^{\text{imp}}$ and $\mathbf{M}^{\text{imp}}$, that radiate known incident electric and magnetic fields, $\mathbf{E}^{\text{inc}}$ and $\mathbf{H}^{\text{inc}}$, in the presence of the grounded multilayered medium, but in the absence of the PEC structure.[1] These fields, that impinge upon the surface of the PEC structure, induce on it an electric current density $\mathbf{J}$, which in turn radiates the scattered fields $\mathbf{E}^{\text{scat}}$ and $\mathbf{H}^{\text{scat}}$. Therefore, at every point $\mathbf{r}$, the total electric and magnetic fields, $\mathbf{E}^{\text{tot}}$ and $\mathbf{H}^{\text{tot}}$, existing in the presence of the patches, probes and grounded multilayered medium, can be expressed as

$$\mathbf{E}^{\text{tot}}(\mathbf{r}) = \mathbf{E}^{\text{inc}}(\mathbf{r}) + \mathbf{E}^{\text{scat}}(\mathbf{r}) \tag{3.1}$$

and

$$\mathbf{H}^{\text{tot}}(\mathbf{r}) = \mathbf{H}^{\text{inc}}(\mathbf{r}) + \mathbf{H}^{\text{scat}}(\mathbf{r}). \tag{3.2}$$

[1] In the case of probe-fed microstrip antennas, $\mathbf{H}^{\text{inc}}$ can be thought of as the equivalent magnetic current density in the aperture, where the probe passes through the ground plane.

Now, the EFIE is based on the fact that, on the surface of the PEC structure, the total tangential electric field must vanish. This can be expressed as

$$\begin{aligned}\mathbf{E}^{\text{tot}}_{\text{tan}}(\mathbf{r}) &= \hat{n} \times \mathbf{E}^{\text{tot}}(\mathbf{r}) \\ &= \hat{n} \times \mathbf{E}^{\text{inc}}(\mathbf{r}) + \hat{n} \times \mathbf{E}^{\text{scat}}(\mathbf{r}) \qquad (3.3) \\ &= \mathbf{E}^{\text{inc}}_{\text{tan}}(\mathbf{r}) + \mathbf{E}^{\text{scat}}_{\text{tan}}(\mathbf{r}) = 0, \qquad (3.4)\end{aligned}$$

where $\hat{n}$ is the normal vector at position $\mathbf{r}$ on the surface of the PEC structure. It then follows that

$$\mathbf{E}^{\text{scat}}_{\text{tan}}(\mathbf{r}) = -\mathbf{E}^{\text{inc}}_{\text{tan}}(\mathbf{r}), \qquad (3.5)$$

where $\mathbf{E}^{\text{inc}}_{\text{tan}}$ represents the incident electric field, tangential to the structure at $\mathbf{r}$, and $\mathbf{E}^{\text{scat}}_{\text{tan}}$ represents the scattered electric field, also tangential to the structure at $\mathbf{r}$.

The *surface equivalence theorem* [73] can be used to replace the PEC structure with an equivalent electric current density $\mathbf{J}$, as shown in Figure 3.2(b). The representation in Figure 3.2(b) is also known as the *physical equivalent* of the problem in Figure 3.2(a). In practice, the patches are normally assumed to be infinitely thin and therefore $\mathbf{J}$ will be the vector sum of the true current densities on the top and bottom surfaces of the patches. The scattered fields are radiated by $\mathbf{J}$ in the presence of the grounded multilayered medium (but not the embedded PEC structure) and can be expressed as

$$\mathbf{E}^{\text{scat}}_{\text{tan}}(\mathbf{r}) = \iint_{\mathcal{S}} \bar{\mathbf{G}}(\mathbf{r}|\mathbf{r}') \cdot \mathbf{J}(\mathbf{r}')\, ds', \qquad (3.6)$$

where $\bar{\mathbf{G}}$ is the dyadic Green's function for a grounded multilayered medium, relating the electric field $\mathbf{E}^{\text{scat}}_{\text{tan}}$ at the *observation* position $\mathbf{r}$ to the surface current density $\mathbf{J}$ at the *source* position $\mathbf{r}'$. In (3.6), $\mathcal{S}$ represents the surface area over which $\mathbf{J}$ extends and is also known as the *support* of $\mathbf{J}$. The EFIE in (3.5) can now be written as

$$\iint_{\mathcal{S}} \bar{\mathbf{G}}(\mathbf{r}|\mathbf{r}') \cdot \mathbf{J}(\mathbf{r}')\, ds' = -\mathbf{E}^{\text{inc}}_{\text{tan}}(\mathbf{r}), \qquad (3.7)$$

which is a Fredholm integral equation of the first kind. In (3.7), $\bar{\mathbf{G}}$ is the *kernel* of the equation, $\mathbf{E}^{\text{inc}}_{\text{tan}}$ is the known *excitation* and $\mathbf{J}$ is the unknown *response* to be determined.

The first step in the solution of (3.7), via the MM, is to approximate the unknown current density $\mathbf{J}$ on the patches and probes by a set of N vector *basis functions* with unknown amplitude coefficients. It can be expanded as

$$\mathbf{J}(\mathbf{r}') = \sum_{n=1}^{N} I_n\, \mathbf{f}_n(\mathbf{r}'), \qquad (3.8)$$

where $\mathbf{f}$ refers to the vector basis functions (also known as expansion functions) and I refers to

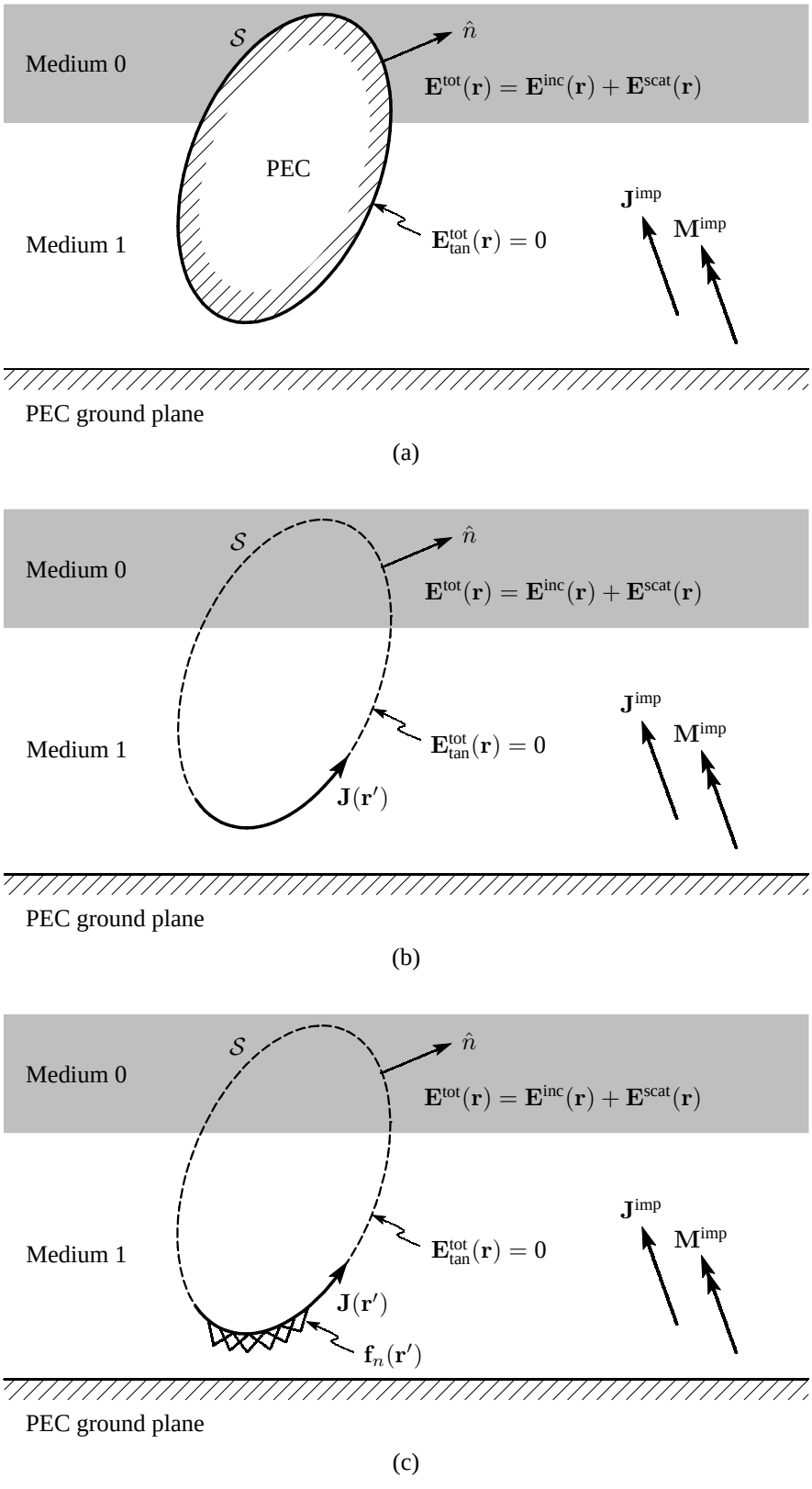

Figure 3.2 Development of the EFIE. (a) Actual problem. (b) Physical equivalent. (c) Basis functions.

the unknown amplitude coefficients (which are generally complex numbers). This is illustrated in Figure 3.2(c).

Exploiting the linearity of the operator on the left-hand side of (3.7), leads to

$$\sum_{n=1}^{N} I_n \iint_{\mathcal{S}} \bar{\mathbf{G}}(\mathbf{r}|\mathbf{r}') \cdot \mathbf{f}_n(\mathbf{r}')\, ds' = -\mathbf{E}^{\text{inc}}_{\text{tan}}(\mathbf{r}), \tag{3.9}$$

which is one equation with N unknowns. It alone is not sufficient to determine the N unknown amplitude coefficients. To resolve the N amplitude coefficients, it is necessary to have N linearly independent equations. This can be achieved by defining a symmetric product

$$\langle \mathbf{a}, \mathbf{b} \rangle = \iint_{\mathcal{S}_a} \mathbf{a} \cdot \mathbf{b}\, ds, \tag{3.10}$$

where $\mathbf{a}$ is used to *test* $\mathbf{b}$ over the domain $\mathcal{S}_a$. In (3.10), $\mathbf{a}$ is a vector function, also known as the *testing function* (or weighting function) with associated support $\mathcal{S}_a$. By using Galerkin's method [4, 73, 74], both basis and testing functions are chosen to be the same set of functions. Therefore, the same set of vector basis functions in (3.8) are also used to test (3.9), yielding a set of simultaneous equations that can be solved by standard linear algebra techniques. The boundary condition in (3.9) then becomes

$$\iint_{\mathcal{S}_m} \mathbf{f}_m(\mathbf{r}) \cdot \sum_{n=1}^{N} I_n \iint_{\mathcal{S}_n} \bar{\mathbf{G}}(\mathbf{r}|\mathbf{r}') \cdot \mathbf{f}_n(\mathbf{r}')\, ds' ds = -\iint_{\mathcal{S}_m} \mathbf{f}_m(\mathbf{r}) \cdot \mathbf{E}^{\text{inc}}_{\text{tan}}(\mathbf{r})\, ds, \quad m = 1, 2, \ldots, N \tag{3.11}$$

or

$$\sum_{n=1}^{N} I_n \big\langle \mathbf{f}_m, \mathbf{E}^{\text{scat}}_{\text{tan}}(\mathbf{f}_n) \big\rangle = -\big\langle \mathbf{f}_m, \mathbf{E}^{\text{inc}}_{\text{tan}} \big\rangle, \quad m = 1, 2, \ldots, N. \tag{3.12}$$

The resulting system of linear equations can also be expressed in matrix notation as

$$[Z_{m,n}]\,\{I_n\} = \{V_m\}, \tag{3.13}$$

in which $[Z_{m,n}]$ is the $N \times N$-dimensional *interaction matrix* with elements

$$Z_{m,n} = \big\langle \mathbf{f}_m, \mathbf{E}^{\text{scat}}_{\text{tan}}(\mathbf{f}_n) \big\rangle \tag{3.14}$$

and $\{V_m\}$ is the N-dimensional *excitation vector* with elements

$$V_m = -\big\langle \mathbf{f}_m, \mathbf{E}^{\text{inc}}_{\text{tan}} \big\rangle. \tag{3.15}$$

In (3.13), $\{I_n\}$ is the N-dimensional vector that contains the unknown amplitude coefficients of

(3.8). The problem can be solved as

$$\{I_n\} = [Z_{m,n}]^{-1}\{V_m\} \tag{3.16}$$

through any of the standard numerical techniques. Once the unknown amplitude coefficients have been resolved, the electric current density **J** is essentially known and all other quantities of interest can then also be calculated.

In the next section, it will now be shown how the interaction-matrix elements can be calculated in the spectral domain.

3.3 SPECTRAL-DOMAIN FORMULATION

It is often more convenient to calculate the elements of the interaction matrix in the spectral domain rather than in the spatial domain. This is due to the fact that, in the spectral domain, the dyadic Green's function for a grounded multilayered medium can be derived in closed form. Usually it requires that the Fourier transforms of the basis and testing functions should also be available in closed form, thereby limiting the choice of basis and testing functions somewhat. However, the spectral-domain formulation can be very efficient if these expressions are available.

In the spatial domain, the elements of the interaction matrix can be expressed as

$$\begin{aligned} Z_{m,n} &= \iint_{\mathcal{S}_m} \iint_{\mathcal{S}_n} \mathbf{f}_m(\mathbf{r}) \cdot \bar{\mathbf{G}}(\mathbf{r}|\mathbf{r}') \cdot \mathbf{f}_n(\mathbf{r}')\, ds' ds \\ &= \int_z \int_y \int_x \mathbf{f}_m(x,y,z) \cdot \int_{z'} \int_{y'} \int_{x'} \bar{\mathbf{G}}(x,y,z|x',y',z') \cdot \mathbf{f}_n(x',y',z')\, dx'dy'dz'\, dxdydz, \end{aligned} \tag{3.17}$$

where all the variables are shown in Figure 3.3, which in turn depicts the general coordinate system for the theoretical analysis that follows. A two-dimensional Fourier-transform pair can now be defined as

$$\tilde{f}(k_x,k_y) = \mathcal{F}\Big\{f(x,y)\Big\} = \int_{-\infty}^{\infty}\int_{-\infty}^{\infty} f(x,y)\, e^{-jk_x x}\, e^{-jk_y y}\, dxdy \tag{3.18}$$

$$f(x,y) = \mathcal{F}^{-1}\Big\{\tilde{f}(k_x,k_y)\Big\} = \frac{1}{4\pi^2}\int_{-\infty}^{\infty}\int_{-\infty}^{\infty} \tilde{f}(k_x,k_y)\, e^{jk_x x}\, e^{jk_y y}\, dk_x dk_y \tag{3.19}$$

in order to transform between a general function $f(x,y)$ and its spectral counterpart $\tilde{f}(k_x,k_y)$. By using the definition in (3.19), the dyadic Green's function $\bar{\mathbf{G}}$ in (3.17) can be related to its spectral domain counterpart $\bar{\tilde{\mathbf{G}}}$ through

$$\bar{\mathbf{G}}(x,y,z|x',y',z') = \frac{1}{4\pi^2}\int_{-\infty}^{\infty}\int_{-\infty}^{\infty} \bar{\tilde{\mathbf{G}}}(k_x,k_y,z|z')\, e^{jk_x(x-x')}\, e^{jk_y(y-y')}\, dk_x dk_y. \tag{3.20}$$

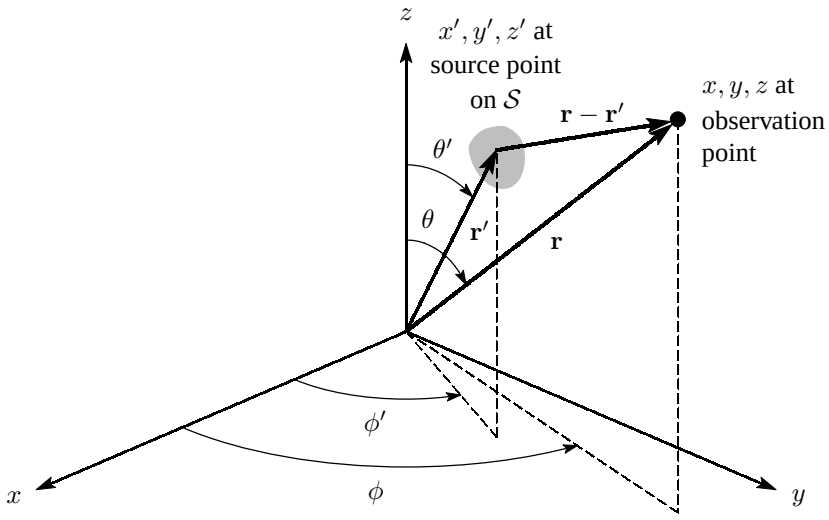

Figure 3.3 Coordinate system for the theoretical analysis.

This allows (3.17) to be written, after some reorganisation of the terms and operators, as

$$Z_{m,n} = \frac{1}{4\pi^2}\int_{k_y}\int_{k_x}\int_{z}\int_{z'}\left[\int_{y}\int_{x}\mathbf{f}_m(x,y,z)\,e^{jk_x x}\,e^{jk_y y}\,dxdy\right] \cdot \tilde{\tilde{\mathbf{G}}}(k_x,k_y,z|z')\cdot\left[\int_{y'}\int_{x'}\mathbf{f}_n(x',y',z')\,e^{-jk_x x'}\,e^{-jk_y y'}\,dx'dy'\right]dz'dz\,dk_x dk_y. \quad (3.21)$$

The expressions between the two pairs of square brackets in (3.21) can be recognised as two-dimensional Fourier transforms, similar to the definition in (3.18). The expression in (3.21) can therefore finally be simplified to

$$Z_{m,n} = \frac{1}{4\pi^2}\int_{k_y}\int_{k_x}\int_{z}\int_{z'}\tilde{\mathbf{f}}_m(-k_x,-k_y,z)\cdot\tilde{\tilde{\mathbf{G}}}(k_x,k_y,z|z')\cdot\tilde{\mathbf{f}}_n(k_x,k_y,z')\,dz'dz\,dk_x dk_y. \quad (3.22)$$

As is evident from this discussion, the spectral-domain forms of both the dyadic Green's function and the basis functions (per implication, also the testing functions) need to be found. These will now be addressed in the sections that follow.

3.4 GREEN'S FUNCTION

Consider the grounded, planarly multilayered medium as shown in Figure 3.4. It is assumed that there are $T+1$ layers and that they are numbered from 0 to T, starting with 0 at the top layer and ending with T at the bottom layer. The top layer (layer 0), which is normally assumed to be free space, extends to infinity along the z direction, while the bottom layer (layer T) is bounded by a PEC ground plane right below it. All the layers are also assumed to have infinite dimensions along the x and y directions. The interface between layers t and $t+1$ is at $z = d_{(t)}$, while the thickness of layer t is $h_{(t)} = d_{(t-1)} - d_{(t)}$.

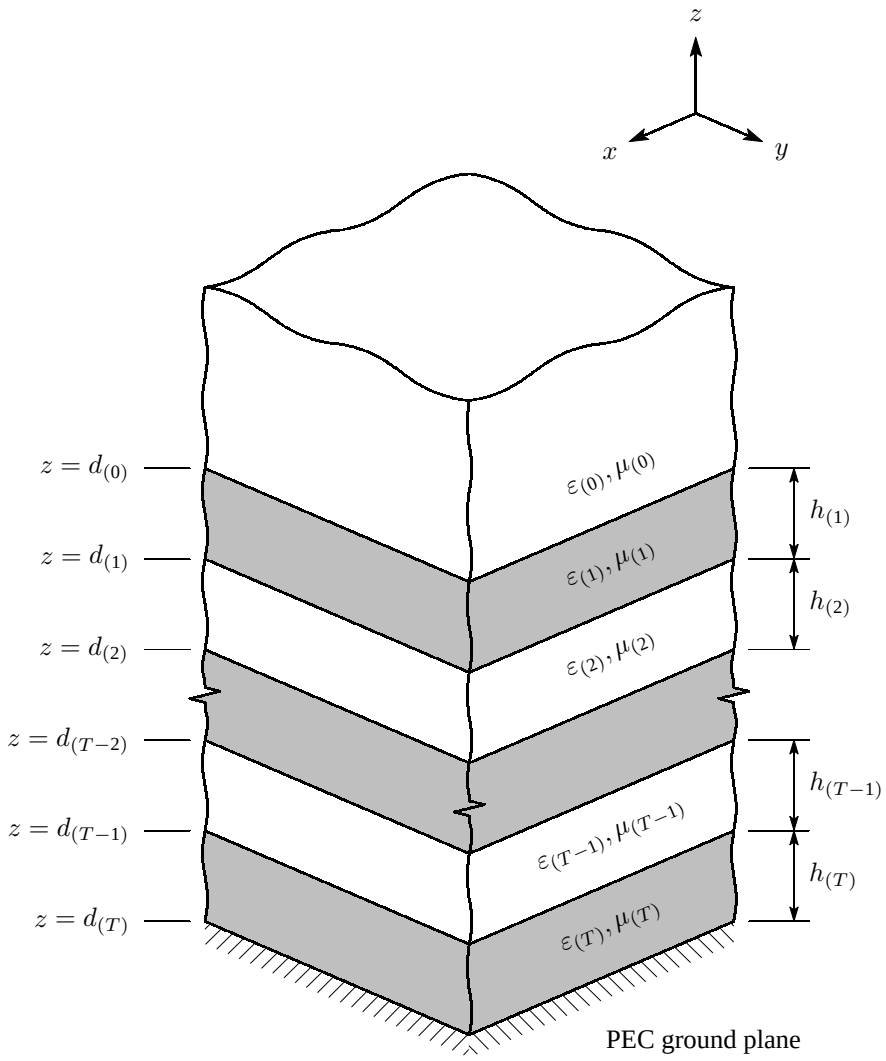

Figure 3.4 Grounded, planarly multilayered medium.

The complex permittivity $\varepsilon_{(t)}$ and complex permeability $\mu_{(t)}$ of layer t can be expressed as

$$\varepsilon_{(t)} = \varepsilon_0 \varepsilon_{r(t)} \left[1 - j \tan \delta_{\varepsilon(t)}\right] \tag{3.23}$$

and

$$\mu_{(t)} = \mu_0 \mu_{r(t)} \left[1 - j \tan \delta_{\mu(t)}\right], \tag{3.24}$$

where:

$\varepsilon_0 = 8.854 \cdot 10^{-12}$ F/m is the permittivity of free space;

$\mu_0 = 4\pi \cdot 10^{-7}$ H/m is the permeability of free space;

$\varepsilon_{r(t)}$ is the relative permittivity of layer t;

$\mu_{r(t)}$ is the relative permeability of layer t;

$\tan \delta_{\varepsilon(t)}$ is the electric loss tangent of layer t;

$\tan\delta_{\mu(t)}$ is the magnetic loss tangent of layer t.

The wavenumber in the z direction can be expressed as

$$k_{z(t)} = \sqrt{k_{(t)}^2 - k_\rho^2}, \quad \Im\mathrm{m}\{k_{z(t)} \leq 0\}, \tag{3.25}$$

where k_ρ is the wavenumber in the radial direction, given by

$$k_\rho^2 = k_x^2 + k_y^2. \tag{3.26}$$

Here, k_x and k_y are the wavenumbers in the x and y directions respectively. Furthermore, $k_{(t)}$ is the wavenumber in layer t, given by

$$k_{(t)} = \omega\sqrt{\mu_{(t)}\varepsilon_{(t)}}, \tag{3.27}$$

with $\omega = 2\pi f$ the radial frequency and f the frequency.

In order to derive the expressions for the components of the Green's function, which relate the electric field in one layer to the electric current density in another layer, the vector wave functions, which depend on the reflection coefficients at the interfaces between layers, as well as the wave amplitudes within the various layers, have to be found [6, 7, 178]. For an isotropic medium, where ε and μ vary only in one direction (the z direction in this case), the vector wave equations can be reduced to two scalar equations that are decoupled from each other [178]. They characterise two types of waves, namely the *transverse electric* (TE) and *transverse magnetic* (TM) waves. In the case of the TE waves, the electric field is transverse to the z direction, while in the case of the TM waves, the magnetic field is transverse to the z direction. The reflection coefficients, wave amplitudes and wave functions associated with both these types of waves, will now be addressed in the following sections.

3.4.1 Reflection Coefficients

First consider a half-space (i.e. there are only two semi-infinite planar layers) with layers t and $t+1$, or alternatively, layers $t-1$ and t. If a wave now travels from layer t to $t+1$ or from layer t to layer $t-1$, there will be both incident and reflected waves in layer t, but only a transmitted wave in layer $t \pm 1$. Now, at the interface between the two layers, t and $t \pm 1$, the *Fresnel reflection coefficients* are defined as

$$R^{\mathrm{TE}}_{(t),(t\pm1)} = \frac{\mu_{(t\pm1)}k_{z(t)} - \mu_{(t)}k_{z(t\pm1)}}{\mu_{(t\pm1)}k_{z(t)} + \mu_{(t)}k_{z(t\pm1)}} \tag{3.28}$$

and

$$R^{\mathrm{TM}}_{(t),(t\pm1)} = \frac{\varepsilon_{(t\pm1)}k_{z(t)} - \varepsilon_{(t)}k_{z(t\pm1)}}{\varepsilon_{(t\pm1)}k_{z(t)} + \varepsilon_{(t)}k_{z(t\pm1)}} \tag{3.29}$$

for the TE and TM cases respectively. In (3.28), $R^{\text{TE}}_{(t),(t\pm1)}$ can be interpreted as the ratio of the amplitude of the reflected TE wave in layer $t\pm1$ to the amplitude of the incident TE wave in layer t. The same goes for $R^{\text{TM}}_{(t),(t\pm1)}$ in (3.29), except that it is associated with a TM wave. In multilayered media, the Fresnel reflection coefficients can be calculated at each boundary by considering only the two layers adjacent to the boundary. There are however two special cases. These are at the top of layer 0, where there is effectively no boundary and at the bottom of layer T, where it is bounded by a PEC ground plane. At the top of layer 0, (3.28) and (3.29) reduce to

$$R^{\text{TE}}_{(0),(-1)} = 0 \tag{3.30}$$

and

$$R^{\text{TM}}_{(0),(-1)} = 0 \tag{3.31}$$

respectively, while at the lower boundary of layer T, they become

$$R^{\text{TE}}_{(T),(T+1)} = -1 \tag{3.32}$$

and

$$R^{\text{TM}}_{(T),(T+1)} = 1 \tag{3.33}$$

respectively. Layers -1 and $T+1$ are merely imaginary layers.

In a multilayered medium, there will of course be multiple reflections at each interface between two adjacent layers. In such a case it is more convenient to work with the *generalised reflection coefficients*. These are reflection coefficients that relate the amplitude of the reflected wave to the amplitude of the incident wave at a specific layer, but also include the effect of subsurface reflections. In the case of TE waves, they are given by

$$\check{R}^{\text{TE}}_{(t),(t-1)} = \begin{cases} R^{\text{TE}}_{(t),(t-1)}, & t = 0 \\ \dfrac{R^{\text{TE}}_{(t),(t-1)} + \check{R}^{\text{TE}}_{(t-1),(t-2)}\, e^{-j2k_{z(t-1)}h_{(t-1)}}}{1 + R^{\text{TE}}_{(t),(t-1)}\check{R}^{\text{TE}}_{(t-1),(t-2)}\, e^{-j2k_{z(t-1)}h_{(t-1)}}}, & t = 1, 2, \ldots, T \end{cases} \tag{3.34}$$

and

$$\check{R}^{\text{TE}}_{(t),(t+1)} = \begin{cases} R^{\text{TE}}_{(t),(t+1)}, & t = T \\ \dfrac{R^{\text{TE}}_{(t),(t+1)} + \check{R}^{\text{TE}}_{(t+1),(t+2)}\, e^{-j2k_{z(t+1)}h_{(t+1)}}}{1 + R^{\text{TE}}_{(t),(t+1)}\check{R}^{\text{TE}}_{(t+1),(t+2)}\, e^{-j2k_{z(t+1)}h_{(t+1)}}}, & t = T-1, T-2, \ldots, 0, \end{cases} \tag{3.35}$$

where $\check{R}^{\text{TE}}_{(t),(t-1)}$ is the generalised reflection coefficient at the interface between layers t and $t-1$, associated with an incident TE wave travelling from layer t to layer $t-1$. Similarly, $\check{R}^{\text{TE}}_{(t),(t+1)}$ is associated with an incident TE wave, travelling from layer t to layer $t+1$. By considering the

expressions in (3.34) and (3.35) carefully, one can see that they define recursive relationships. For example, $\check{R}^{\mathrm{TE}}_{(t),(t-1)}$ is dependant on $\check{R}^{\mathrm{TE}}_{(t-1),(t-2)}$ and so on, up to the top layer. Therefore in order to find $\check{R}^{\mathrm{TE}}_{(t),(t-1)}$, one would start at the top layer and work your way down the layers. Similarly, in order to find $\check{R}^{\mathrm{TE}}_{(t),(t+1)}$, one would start at the bottom layer and work your way upwards.

In the case of TM waves, the generalised reflection coefficients are given by

$$\check{R}^{\mathrm{TM}}_{(t),(t-1)} = \begin{cases} R^{\mathrm{TM}}_{(t),(t-1)}, & t = 0 \\ \dfrac{R^{\mathrm{TM}}_{(t),(t-1)} + \check{R}^{\mathrm{TM}}_{(t-1),(t-2)}\, e^{-j2k_{z(t-1)}h_{(t-1)}}}{1 + R^{\mathrm{TM}}_{(t),(t-1)}\check{R}^{\mathrm{TM}}_{(t-1),(t-2)}\, e^{-j2k_{z(t-1)}h_{(t-1)}}}, & t = 1, 2, \ldots, T \end{cases} \tag{3.36}$$

and

$$\check{R}^{\mathrm{TM}}_{(t),(t+1)} = \begin{cases} R^{\mathrm{TM}}_{(t),(t+1)}, & t = T \\ \dfrac{R^{\mathrm{TM}}_{(t),(t+1)} + \check{R}^{\mathrm{TM}}_{(t+1),(t+2)}\, e^{-j2k_{z(t+1)}h_{(t+1)}}}{1 + R^{\mathrm{TM}}_{(t),(t+1)}\check{R}^{\mathrm{TM}}_{(t+1),(t+2)}\, e^{-j2k_{z(t+1)}h_{(t+1)}}}, & t = T-1, T-2, \ldots, 0. \end{cases} \tag{3.37}$$

3.4.2 Wave Amplitudes

Let $t = \ell$ denote the layer containing the observation point and $t = \ell'$ denote the layer containing the source point. The wave amplitude in the source layer ℓ' can then be expressed as

$$A^{\mathrm{TE}}_{(\ell')} = \frac{1}{1 - \check{R}^{\mathrm{TE}}_{(\ell'),(\ell'-1)}\check{R}^{\mathrm{TE}}_{(\ell'),(\ell'+1)}\, e^{-j2k_{z(\ell')}h_{(\ell')}}} \tag{3.38}$$

for TE waves and as

$$A^{\mathrm{TM}}_{(\ell')} = \frac{1}{1 - \check{R}^{\mathrm{TM}}_{(\ell'),(\ell'-1)}\check{R}^{\mathrm{TM}}_{(\ell'),(\ell'+1)}\, e^{-j2k_{z(\ell')}h_{(\ell')}}} \tag{3.39}$$

for TM waves. The wave amplitude in the observation layer can now also be found through a recursive process. Let $A^{\mathrm{TE}}_{(\ell)+}$ or $A^{\mathrm{TM}}_{(\ell)+}$ denote the wave amplitude in the observation layer for $z \geq z'$ (i.e. the observation point above or equal to the source point), while $A^{\mathrm{TE}}_{(\ell)-}$ or $A^{\mathrm{TM}}_{(\ell)-}$ denote the wave amplitude in the observation layer for $z < z'$ (i.e. the observation point below the source point). $A^{\mathrm{TE}}_{(\ell)+}$ or $A^{\mathrm{TM}}_{(\ell)+}$ can be found by starting at the source layer with either (3.38) or (3.39) and applying either

$$A^{\mathrm{TE}}_{(t)+} = A^{\mathrm{TE}}_{(t+1)+}\, e^{j[k_{z(t)} - k_{z(t+1)}]d_{(t)}} \frac{1 - R^{\mathrm{TE}}_{(t),(t+1)}}{1 - R^{\mathrm{TE}}_{(t),(t+1)}\check{R}^{\mathrm{TE}}_{(t),(t-1)}\, e^{-j2k_{z(t)}h_{(t)}}}, \quad t = \ell' - 1, \ell' - 2, \ldots, \ell \tag{3.40}$$

or

$$A^{\mathrm{TM}}_{(t)+} = A^{\mathrm{TM}}_{(t+1)+}\, e^{j[k_{z(t)}-k_{z(t+1)}]d_{(t)}} \frac{1-R^{\mathrm{TM}}_{(t),(t+1)}}{1-R^{\mathrm{TM}}_{(t),(t+1)}\check{R}^{\mathrm{TM}}_{(t),(t-1)}\, e^{-j2k_{z(t)}h_{(t)}}}, \qquad t=\ell'-1,\ell'-2,\ldots,\ell \quad (3.41)$$

for each consecutive layer up to the observation layer. Similarly, $A^{\mathrm{TE}}_{(\ell)-}$ or $A^{\mathrm{TM}}_{(\ell)-}$ can be found by starting at the source layer with either (3.38) or (3.39) and applying either

$$A^{\mathrm{TE}}_{(t)-} = A^{\mathrm{TE}}_{(t-1)-}\, e^{j[k_{z(t-1)}-k_{z(t)}]d_{(t-1)}} \frac{1-R^{\mathrm{TE}}_{(t),(t-1)}}{1-R^{\mathrm{TE}}_{(t),(t-1)}\check{R}^{\mathrm{TE}}_{(t),(t+1)}\, e^{-j2k_{z(t)}h_{(t)}}}, \qquad t=\ell'+1,\ell'+2,\ldots,\ell \quad (3.42)$$

or

$$A^{\mathrm{TM}}_{(t)-} = A^{\mathrm{TM}}_{(t-1)-}\, e^{j[k_{z(t-1)}-k_{z(t)}]d_{(t-1)}} \frac{1-R^{\mathrm{TM}}_{(t),(t-1)}}{1-R^{\mathrm{TM}}_{(t),(t-1)}\check{R}^{\mathrm{TM}}_{(t),(t+1)}\, e^{-j2k_{z(t)}h_{(t)}}}, \qquad t=\ell'+1,\ell'+2,\ldots,\ell \quad (3.43)$$

for each consecutive layer down to the observation layer.

3.4.3 Wave Functions

The wave function, for an observation point at z in layer ℓ due to a source at z' in layer ℓ', can then be expressed as a superposition of upgoing and downgoing waves. For TE waves, the wave function can be expressed as

$$F^{\mathrm{TE}}_{(\ell)+}(z,z') = A^{\mathrm{TE}}_{(\ell)+}\left\{e^{jk_{z(\ell')}z'} + \check{R}^{\mathrm{TE}}_{(\ell'),(\ell'+1)}\, e^{j2k_{z(\ell')}d_{(\ell')}}\, e^{-jk_{z(\ell')}z'}\right\} \cdot\left\{e^{-jk_{z(\ell)}z} + \check{R}^{\mathrm{TE}}_{(\ell),(\ell-1)}\, e^{-j2k_{z(\ell)}d_{(\ell-1)}}\, e^{jk_{z(\ell)}z}\right\} \quad (3.44)$$

if $z \geq z'$, and as

$$F^{\mathrm{TE}}_{(\ell)-}(z,z') = A^{\mathrm{TE}}_{(\ell)-}\left\{e^{jk_{z(\ell)}z} + \check{R}^{\mathrm{TE}}_{(\ell),(\ell+1)}\, e^{j2k_{z(\ell)}d_{(\ell)}}\, e^{-jk_{z(\ell)}z}\right\} \cdot\left\{e^{-jk_{z(\ell')}z'} + \check{R}^{\mathrm{TE}}_{(\ell'),(\ell'-1)}\, e^{-j2k_{z(\ell')}d_{(\ell'-1)}}\, e^{jk_{z(\ell')}z'}\right\} \quad (3.45)$$

if $z < z'$. Similarly, for TM waves, the wave function can be expressed as

$$F^{\mathrm{TM}}_{(\ell)+}(z,z') = A^{\mathrm{TM}}_{(\ell)+}\left\{e^{jk_{z(\ell')}z'} + \check{R}^{\mathrm{TM}}_{(\ell'),(\ell'+1)}\, e^{j2k_{z(\ell')}d_{(\ell')}}\, e^{-jk_{z(\ell')}z'}\right\} \cdot\left\{e^{-jk_{z(\ell)}z} + \check{R}^{\mathrm{TM}}_{(\ell),(\ell-1)}\, e^{-j2k_{z(\ell)}d_{(\ell-1)}}\, e^{jk_{z(\ell)}z}\right\} \quad (3.46)$$

if $z \geq z'$, and as

$$F^{\mathrm{TM}}_{(\ell)-}(z,z') = A^{\mathrm{TM}}_{(\ell)-}\left\{e^{jk_{z(\ell)}z} + \check{R}^{\mathrm{TM}}_{(\ell),(\ell+1)}\, e^{j2k_{z(\ell)}d_{(\ell)}}\, e^{-jk_{z(\ell)}z}\right\} \cdot \left\{e^{-jk_{z(\ell')}z'} + \check{R}^{\mathrm{TM}}_{(\ell'),(\ell'-1)}\, e^{-j2k_{z(\ell')}d_{(\ell'-1)}}\, e^{jk_{z(\ell')}z'}\right\} \quad (3.47)$$

if $z < z'$. The derivatives and double derivatives of F^{TM}_{+} and F^{TM}_{-} with respect to z and z' are also required in the expressions for the Green's function. After some straightforward manipulation, they are given by

$$\frac{\partial}{\partial z} F^{\mathrm{TM}}_{(\ell)+}(z,z') = jk_{z(\ell)} A^{\mathrm{TM}}_{(\ell)+}\left\{e^{jk_{z(\ell')}z'} + \check{R}^{\mathrm{TM}}_{(\ell'),(\ell'+1)}\, e^{j2k_{z(\ell')}d_{(\ell')}}\, e^{-jk_{z(\ell')}z'}\right\} \cdot \left\{-e^{-jk_{z(\ell)}z} + \check{R}^{\mathrm{TM}}_{(\ell),(\ell-1)}\, e^{-j2k_{z(\ell)}d_{(\ell-1)}}\, e^{jk_{z(\ell)}z}\right\}, \quad (3.48)$$

$$\frac{\partial}{\partial z} F^{\mathrm{TM}}_{(\ell)-}(z,z') = jk_{z(\ell)} A^{\mathrm{TM}}_{(\ell)-}\left\{e^{jk_{z(\ell)}z} - \check{R}^{\mathrm{TM}}_{(\ell),(\ell+1)}\, e^{j2k_{z(\ell)}d_{(\ell)}}\, e^{-jk_{z(\ell)}z}\right\} \cdot \left\{e^{-jk_{z(\ell')}z'} + \check{R}^{\mathrm{TM}}_{(\ell'),(\ell'-1)}\, e^{-j2k_{z(\ell')}d_{(\ell'-1)}}\, e^{jk_{z(\ell')}z'}\right\}, \quad (3.49)$$

$$\frac{\partial}{\partial z'} F^{\mathrm{TM}}_{(\ell)+}(z,z') = jk_{z(\ell')} A^{\mathrm{TM}}_{(\ell)+}\left\{e^{jk_{z(\ell')}z'} - \check{R}^{\mathrm{TM}}_{(\ell'),(\ell'+1)}\, e^{j2k_{z(\ell')}d_{(\ell')}}\, e^{-jk_{z(\ell')}z'}\right\} \cdot \left\{e^{-jk_{z(\ell)}z} + \check{R}^{\mathrm{TM}}_{(\ell),(\ell-1)}\, e^{-j2k_{z(\ell)}d_{(\ell-1)}}\, e^{jk_{z(\ell)}z}\right\}, \quad (3.50)$$

$$\frac{\partial}{\partial z'} F^{\mathrm{TM}}_{(\ell)-}(z,z') = jk_{z(\ell')} A^{\mathrm{TM}}_{(\ell)-}\left\{e^{jk_{z(\ell)}z} + \check{R}^{\mathrm{TM}}_{(\ell),(\ell+1)}\, e^{j2k_{z(\ell)}d_{(\ell)}}\, e^{-jk_{z(\ell)}z}\right\} \cdot \left\{-e^{-jk_{z(\ell')}z'} + \check{R}^{\mathrm{TM}}_{(\ell'),(\ell'-1)}\, e^{-j2k_{z(\ell')}d_{(\ell'-1)}}\, e^{jk_{z(\ell')}z'}\right\}, \quad (3.51)$$

$$\frac{\partial^2}{\partial z' \partial z} F^{\mathrm{TM}}_{(\ell)+}(z,z') = -k_{z(\ell')}k_{z(\ell)} A^{\mathrm{TM}}_{(\ell)+}\left\{e^{jk_{z(\ell')}z'} - \check{R}^{\mathrm{TM}}_{(\ell'),(\ell'+1)}\, e^{j2k_{z(\ell')}d_{(\ell')}}\, e^{-jk_{z(\ell')}z'}\right\} \cdot \left\{-e^{-jk_{z(\ell)}z} + \check{R}^{\mathrm{TM}}_{(\ell),(\ell-1)}\, e^{-j2k_{z(\ell)}d_{(\ell-1)}}\, e^{jk_{z(\ell)}z}\right\} \quad (3.52)$$

and

$$\frac{\partial^2}{\partial z' \partial z} F^{\mathrm{TM}}_{(\ell)-}(z,z') = -k_{z(\ell')}k_{z(\ell)} A^{\mathrm{TM}}_{(\ell)-}\left\{e^{jk_{z(\ell)}z} - \check{R}^{\mathrm{TM}}_{(\ell),(\ell+1)}\, e^{j2k_{z(\ell)}d_{(\ell)}}\, e^{-jk_{z(\ell)}z}\right\} \cdot \left\{-e^{-jk_{z(\ell')}z'} + \check{R}^{\mathrm{TM}}_{(\ell'),(\ell'-1)}\, e^{-j2k_{z(\ell')}d_{(\ell'-1)}}\, e^{jk_{z(\ell')}z'}\right\}. \quad (3.53)$$

The terms between brackets in (3.44) to (3.53) should be multiplied out in order to avoid numerical overflow for large values of k_ρ, which in turn results in large negative imaginary values for k_z.

3.4.4 Components of the Green's Function

Figure 3.5 shows the various current-density components that have to be taken into account for the purposes of this analysis. In general then, the current density can be expanded in terms of its individual components as

$$\mathbf{J}(x,y,z) = J_x(x,y)\,\hat{x} + J_y(x,y)\,\hat{y} + J_z(z)\,\hat{z}. \tag{3.54}$$

Due to the fact that the current density is either horizontal or vertical, but not oblique, this kind of problem is often referred to as two-and-one-half-dimensional (2.5D) as opposed to a full three-dimensional problem (3D). The analysis of 2.5D electromagnetic problems, however, still requires knowledge of all nine components of the dyadic Green's function that relates the electric field to the electric current density.

Now, the dyadic Green's function can be expressed in terms of its spectral-domain components as

$$\tilde{\tilde{\mathbf{G}}} = \hat{x}\,\tilde{G}_{xx}\,\hat{x} + \hat{x}\,\tilde{G}_{xy}\,\hat{y} + \hat{x}\,\tilde{G}_{xz}\,\hat{z} + \hat{y}\,\tilde{G}_{yx}\,\hat{x} + \hat{y}\,\tilde{G}_{yy}\,\hat{y} + \hat{y}\,\tilde{G}_{yz}\,\hat{z} + \hat{z}\,\tilde{G}_{zx}\,\hat{x} + \hat{z}\,\tilde{G}_{zy}\,\hat{y} + \hat{z}\,\tilde{G}_{zz}\,\hat{z}, \tag{3.55}$$

where, for example, the $\tilde{G}_{xy}$ component provides the x-directed component of the electric field due to the y-directed component of the electric current density.

The nine components of (3.55) are given by

$$\tilde{G}_{xx}(k_x,k_y,z|z') = \frac{-\omega\mu_{(\ell')}}{2k_{z(\ell')}k_\rho^2}\left[k_y^2 F^{\text{TE}}_{(\ell)\pm}(z,z') + \frac{k_x^2}{\omega^2\mu_{(\ell')}\varepsilon_{(\ell)}}\,\frac{\partial^2}{\partial z'\partial z}\,F^{\text{TM}}_{(\ell)\pm}(z,z')\right], \tag{3.56}$$

$$\tilde{G}_{yy}(k_x,k_y,z|z') = \frac{-\omega\mu_{(\ell')}}{2k_{z(\ell')}k_\rho^2}\left[k_x^2 F^{\text{TE}}_{(\ell)\pm}(z,z') + \frac{k_y^2}{\omega^2\mu_{(\ell')}\varepsilon_{(\ell)}}\,\frac{\partial^2}{\partial z'\partial z}\,F^{\text{TM}}_{(\ell)\pm}(z,z')\right], \tag{3.57}$$

$$\begin{aligned}\tilde{G}_{xy}(k_x,k_y,z|z') &= \tilde{G}_{yx}(k_x,k_y,z|z') \\ &= \frac{-\omega\mu_{(\ell')}}{2k_{z(\ell')}k_\rho^2}\,k_xk_y\left[-F^{\text{TE}}_{(\ell)\pm}(z,z') + \frac{1}{\omega^2\mu_{(\ell')}\varepsilon_{(\ell)}}\,\frac{\partial^2}{\partial z'\partial z}\,F^{\text{TM}}_{(\ell)\pm}(z,z')\right],\end{aligned} \tag{3.58}$$

$$\tilde{G}_{xz}(k_x,k_y,z|z') = \frac{jk_x}{2k_{z(\ell')}\omega\varepsilon_{(\ell)}}\,\frac{\partial}{\partial z}\,F^{\text{TM}}_{(\ell)\pm}(z,z'), \tag{3.59}$$

$$\tilde{G}_{yz}(k_x,k_y,z|z') = \frac{jk_y}{2k_{z(\ell')}\omega\varepsilon_{(\ell)}}\,\frac{\partial}{\partial z}\,F^{\text{TM}}_{(\ell)\pm}(z,z'), \tag{3.60}$$

$$\tilde{G}_{zx}(k_x,k_y,z|z') = \frac{-jk_x}{2k_{z(\ell')}\omega\varepsilon_{(\ell)}}\,\frac{\partial}{\partial z'}\,F^{\text{TM}}_{(\ell)\pm}(z,z'), \tag{3.61}$$

$$\tilde{G}_{zy}(k_x,k_y,z|z') = \frac{-jk_y}{2k_{z(\ell')}\omega\varepsilon_{(\ell)}}\,\frac{\partial}{\partial z'}\,F^{\text{TM}}_{(\ell)\pm}(z,z') \tag{3.62}$$

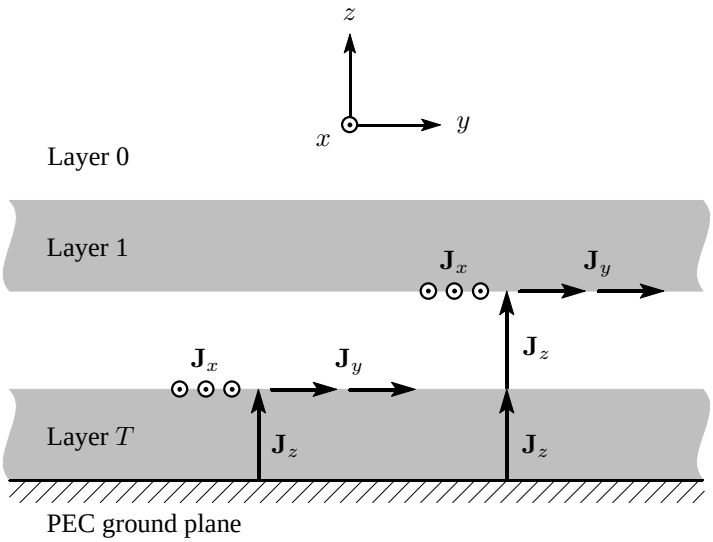

Figure 3.5 Current-density components.

and

$$\tilde{G}_{zz}(k_x, k_y, z|z') = \frac{-k_\rho^2}{2k_{z(\ell')}\omega\varepsilon_{(\ell)}} F^{\mathrm{TM}}_{(\ell)\pm}(z, z') - \frac{1}{j\omega\varepsilon_{(\ell')}}\delta(z - z'). \tag{3.63}$$

In Appendix A, it is shown how these Green's-function components can be derived. The Green's-function components for two [128, 129], three [132, 175] and four layers [28] are available in the literature, but are often limited to the case where the probe only passes through one of the substrate layers. For a more general analysis, also including an arbitrary number of substrate layers, the recursive method becomes inevitable.

The next step in the analysis is to define appropriate basis functions (testing functions are similar) over which to expand the electric current density. This will be dealt with in the section that follows.

3.5 BASIS FUNCTIONS

As mentioned earlier on, the antenna structure basically consists of probes, capacitor patches (which can either be circular or rectangular) and rectangular (or square) resonant pathes. In order to obtain an efficient computational solution, the current density over each of these parts has to be approximated by as few a number of basis functions as possible. This can be achieved by using entire-domain basis functions on the rectangular resonant patches, which account for most of the antenna size, while resorting to subdomain basis functions only on the probes and capacitor patches. The latter are usually quite small when compared to a wavelength and therefore should require relatively few subdomain basis functions. Furthermore, during the analysis of some antenna configurations, it might happen that the individual basis functions are not always aligned to one another, but that they have different orientations. In order to simplify the analysis of such an arrangement, it is necessary to define a local coordinate system for each basis function as shown in Figure 3.6. These local coordinate systems are denoted by u and v axes, as opposed to the x

and y axes for the global coordinate system.

In mathematical notation, the complete set of basis functions, which is used for the analysis of microstrip patch antennas with capacitive feed probes, can be expressed as

$$\begin{aligned}\mathbf{J} &= \sum_{n=1}^{N} I_n \, \mathbf{f}_n \\ &= \underbrace{\sum_{np=1}^{N_P} \sum_{nz=1}^{N_{np}^{PZ}} I_{np:nz}^{PZ} \, \mathbf{f}_{np:nz}^{PZ}}_{\text{PWS basis functions on probes}} + \underbrace{\sum_{na=1}^{N_A} I_{na}^{A} \left(\mathbf{f}_{na}^{AZ} + \mathbf{f}_{na}^{AP} \right)}_{\text{attachment modes}} \\ &\quad + \underbrace{\sum_{ns=1}^{N_S} \left(\sum_{nu=1}^{N_{ns}^{SU}} I_{ns:nu}^{SU} \, \mathbf{f}_{ns:nu}^{SU} + \sum_{nv=1}^{N_{ns}^{SV}} I_{ns:nv}^{SV} \, \mathbf{f}_{ns:nv}^{SV} \right)}_{\text{subdomain rooftop basis functions on rectangular capacitor patches}} \\ &\quad + \underbrace{\sum_{ne=1}^{N_E} \left(\sum_{nu=1}^{N_{ne}^{EU}} I_{ne:nu}^{EU} \, \mathbf{f}_{ne:nu}^{EU} + \sum_{nv=1}^{N_{ne}^{EV}} I_{ne:nv}^{EV} \, \mathbf{f}_{ne:nv}^{EV} \right)}_{\text{entire-domain sinusoidal basis functions on resonant patches}} . \end{aligned} \tag{3.64}$$

Here, $\mathbf{f}$ refers to the different vector basis functions, while I refers to the unknown current-density coefficients.

The basis functions on the N_P probes are taken to be overlapping piecewise-sinusoidal (PWS) functions and also take into account the finite radii of the probes. They are represented by $\mathbf{f}_{np:nz}^{PZ}$, which is the nz-th of N_{np}^{PZ} basis functions on the np-th probe.

The N_A attachment modes (being either circular or rectangular) all have two parts: one part, $\mathbf{f}_{na}^{AZ}$, residing on the probe and one part, $\mathbf{f}_{na}^{AP}$, residing on the patch. The probe part of each attachment mode is modelled by one half of a PWS function right below the probe-to-patch junction. The patch part (which differs for the circular and rectangular attachment modes) is described in more detail in Section 3.6. The patch part of the circular attachment mode alone is sufficient for modelling the electric current density on the circular capacitor patches, whereas the remaining current density on the rectangular capacitor patches is approximated by overlapping rooftop basis functions.

Rooftop basis functions yield more flexibility in the modelling of the patch current and are usually more convenient for small patch sizes, while entire-domain sinusoidal basis functions (usually expressed in terms of sine and cosine functions) yield a smaller number of unknowns in the solution and are therefore more efficient for resonant pathes. The overlapping rooftop basis functions on the N_S rectangular capacitor patches are then represented by $\mathbf{f}_{ns:nu}^{SU}$ and $\mathbf{f}_{ns:nv}^{SV}$, where $\mathbf{f}_{ns:nu}^{SU}$ is the nu-th of N_{ns}^{SU} u-directed basis functions on the ns-th rectangular capacitor patch and $\mathbf{f}_{ns:nv}^{SV}$ is the

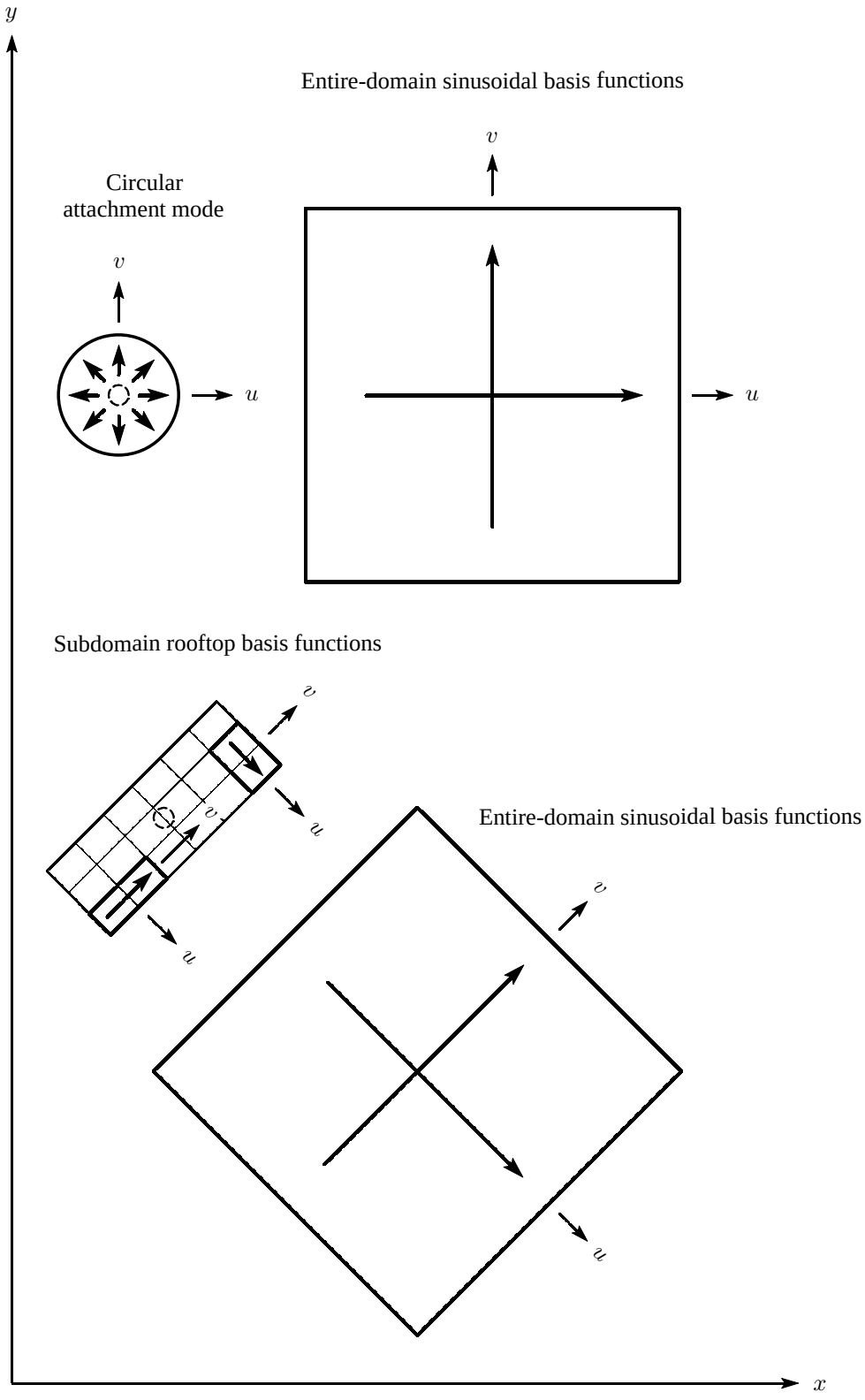

Figure 3.6 Local coordinate systems for some of the basis functions.

nv-th of N_{ns}^{SV} v-directed basis functions on the ns-th rectangular capacitor patch. Similarly, the entire-domain sinusoidal basis functions on the N_E rectangular resonant patches are represented by $\mathbf{f}_{ne:nu}^{EU}$ and $\mathbf{f}_{ne:nv}^{EV}$, where $\mathbf{f}_{ne:nu}^{EU}$ is the nu-th of N_{ne}^{EU} u-directed basis functions on the ne-th rectangular resonant patch and $\mathbf{f}_{ne:nv}^{EV}$ is the nv-th of N_{ne}^{EV} v-directed basis functions on the ne-th rectangular resonant patch.

If the complete set of basis functions is used in an analysis, the total number of basis functions on the structure, N, can be calculated as

$$N = \sum_{np=1}^{N_P} N_{np}^{PZ} + N_A + \sum_{ns=1}^{N_S} \left(N_{ns}^{SU} + N_{ns}^{SV} \right) + \sum_{ne=1}^{N_E} \left(N_{ne}^{EU} + N_{ne}^{EV} \right). \tag{3.65}$$

Note that it is not always necessary to use the complete set of basis functions. For example, if the structure does not comprise of rectangular capacitor patches, the rooftop basis functions are not required.

Each of the different basis functions, as have just been discussed, will now be described in somewhat more detail in the sections that follow. Section 3.5.1 addresses the PWS basis functions on the probes, Section 3.5.2 the subdomain rooftop basis functions on the rectangular capacitor patches and Section 3.5.3 the entire-domain sinusoidal basis functions on the rectangular resonant patches. The attachment modes are somewhat more specialised and are therefore described separately in Section 3.6.

3.5.1 Piecewise-Sinusoidal Basis Functions on the Probes

In a thick substrate, the electric current density on the surface of the probes will generally vary along the length of the probes. Furthermore, if the probes are thin, which is usually the case, the electric current density should have minimal angular variation around the probe. As shown in Figure 3.7, the electric current density on the probes can be modelled by a set of PWS basis functions, residing on the surface of every probe. These basis functions are used to model the electric current density along the length of each probe. In most approaches [6, 7, 125], piecewise-linear basis functions are normally used, but these functions result in very complicated expressions for the interaction-matrix entries where integration over the length of the probe is required. The PWS functions can approximate piecewise-linear functions very well, but result in much simpler expressions for the interaction-matrix entries.

In a coordinate system that is local to each probe, the basis functions can be expressed as

$$\mathbf{f}_{np:nz}^{PZ}(u, v, z) = \frac{1}{2\pi a_{np}} f_{nz}^{PZ}(z)\, \hat{z} \Big|_{u^2+v^2=a_{np}^2}, \tag{3.66}$$

where $\mathbf{f}_{np:nz}^{PZ}$ refers to the nz-th basis function on the np-th probe. The basis functions on the np-

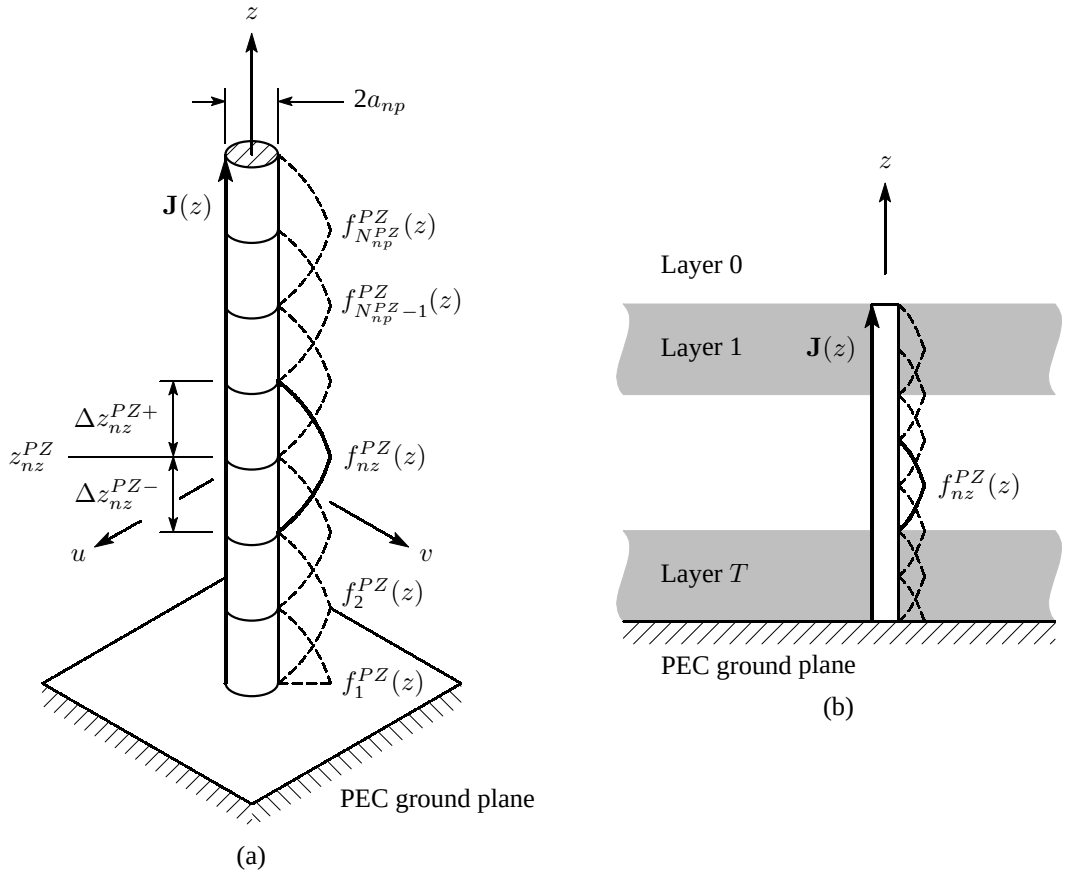

Figure 3.7 Piecewise-sinusoidal basis functions on probe np. (a) Isolated probe. (b) Probe in a multilayered substrate.

th probe are numbered from 1 for the bottom-most basis function to N_{np}^{PZ} for the top-most basis function. The radius of the np-th probe is denoted by a_{np}.

The PWS parts of the basis functions are given by

$$f_{nz}^{PZ}(z) = \begin{cases} \dfrac{\sin[k_F(z_{nz}^{PZ} + \Delta z_{nz}^{PZ+} - z)]}{\sin(k_F \Delta z_{nz}^{PZ+})} & nz \geq 1,\ z_{nz}^{PZ} \leq z \leq z_{nz}^{PZ} + \Delta z_{nz}^{PZ+} \\ \dfrac{\sin[k_F(z - z_{nz}^{PZ} + \Delta z_{nz}^{PZ-})]}{\sin(k_F \Delta z_{nz}^{PZ-})} & nz \geq 2,\ z_{nz}^{PZ} - \Delta z_{nz}^{PZ-} \leq z \leq z_{nz}^{PZ}. \end{cases} \tag{3.67}$$

Here, z_{nz}^{PZ} is the z position of the nz-th PWS function, while Δz_{nz}^{PZ+} and Δz_{nz}^{PZ-} are the segment sizes just above and below z_{nz}^{PZ}, as shown in Figure 3.7(a).

In order to closely approximate piecewise-linear basis functions, the value of k_F is chosen as

$$k_F = \frac{1}{100 \cdot \max\left(\Delta z_1^{PZ+}, \Delta z_2^{PZ+}, \ldots, \Delta z_{N_{\max}^{PZ}}^{PZ+}\right)}, \tag{3.68}$$

where

$$N_{\max}^{PZ} = \max\left(N_1^{PZ}, N_2^{PZ}, \ldots, N_{N_P}^{PZ}\right). \tag{3.69}$$

By using the value of k_F in (3.68), the PWS functions deviate only very slightly from piecewise-linear functions over the same support.

In the spectral domain, the probe basis functions can be expressed as

$$\tilde{\mathbf{f}}_{np:nz}^{PZ}(k_u, k_v, z) = f_{nz}^{PZ}(z)\, J_0(k_\rho a_{np})\, \hat{z} \tag{3.70}$$

where $J_0(\cdot)$ is the Bessel function of the first kind of order 0 and

$$k_\rho^2 = k_u^2 + k_v^2 = k_x^2 + k_y^2. \tag{3.71}$$

In Appendix B, it is shown how the spectral-domain form of these basis functions can be derived.

3.5.2 Rooftop Basis Functions on the Rectangular Capacitor Patches

Due to the probe-to-patch junction on capacitor patches, the electric current density on the rectangular capacitor patches has to be partially modelled by an attachment mode. However, the patch part of the attachment mode alone is not sufficient to model the electric current density on the rectangular capacitor patches and therefore it has to be augmented with other basis functions. Due to the geometry of the rectangular capacitor patch, and its relative small size, subdomain rooftop basis functions [137–139] are a good choice. Figure 3.8 illustrates the use of subdomain rooftop basis functions on a rectangular capacitor patch.

In a coordinate system that is local to each rooftop basis function, the rooftop basis functions are expressed as

$$\mathbf{f}_{ns:nu}^{SU}(u, v) = \left(1 - \frac{|u|}{\Delta l_{ns}}\right) \text{rect}\left(\frac{v}{\Delta w_{ns}}\right) \hat{u}, \quad |u| \leq \Delta l_{ns},\ z = z_{ns}^S \tag{3.72}$$

for the u-directed basis functions and as

$$\mathbf{f}_{ns:nv}^{SV}(u, v) = \left(1 - \frac{|v|}{\Delta w_{ns}}\right) \text{rect}\left(\frac{u}{\Delta l_{ns}}\right) \hat{v}, \quad |v| \leq \Delta w_{ns},\ z = z_{ns}^S \tag{3.73}$$

for the v-directed basis functions. Here, $\mathbf{f}_{ns:nu}^{SU}$ refers to the nu-th u-directed basis function on the ns-th rectangular capacitor patch, while $\mathbf{f}_{ns:nv}^{SV}$ refers to the nv-th v-directed basis function on the ns-th rectangular capacitor patch. Also, z_{ns}^S is the z position of the ns-th rectangular capacitor patch.

As shown in Figure 3.8, $\hat{u}$ and $\hat{v}$ point along the local u and v directions for the ns-th capacitor patch. The ns-th rectangular capacitor patch has dimensions of l_{ns} and w_{ns} along the u and v

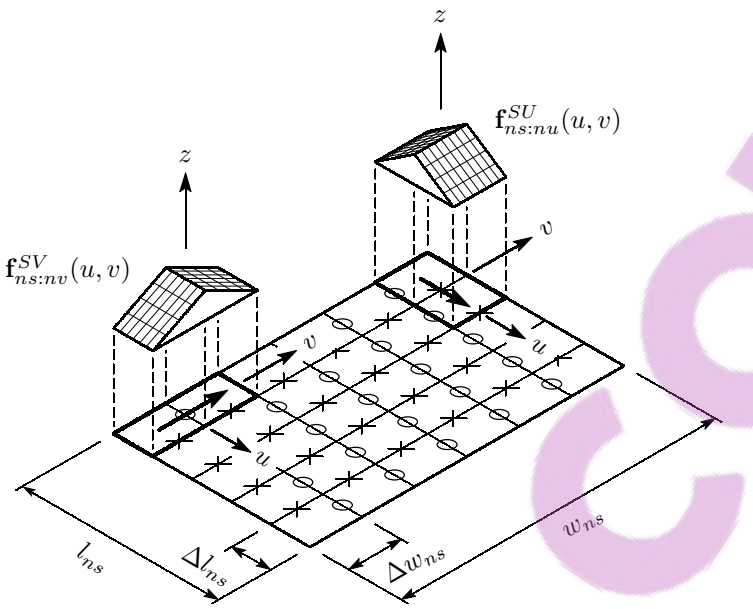

Figure 3.8 Subdomain rooftop basis functions on rectangular capacitor patch ns.

directions respectively. Each capacitor patch is also divided into a grid of cells, where the size of a single cell is Δl_{ns} by Δw_{ns}. As shown in Figure 3.8, each rooftop basis function then spans two such cells.

In the spectral domain, the subdomain rooftop basis functions can be expressed as

$$\tilde{\mathbf{f}}^{SU}_{ns:nu}(k_u,k_v) = \frac{8}{\Delta l_{ns} k_u^2 k_v} \sin^2\left(\frac{k_u \Delta l_{ns}}{2}\right) \sin\left(\frac{k_v \Delta w_{ns}}{2}\right) \hat{u}, \quad z = z^S_{ns} \tag{3.74}$$

and

$$\tilde{\mathbf{f}}^{SV}_{ns:nv}(k_u,k_v) = \frac{8}{\Delta w_{ns} k_v^2 k_u} \sin^2\left(\frac{k_v \Delta w_{ns}}{2}\right) \sin\left(\frac{k_u \Delta l_{ns}}{2}\right) \hat{v}, \quad z = z^S_{ns} \tag{3.75}$$

respectively. In Appendix B, it is shown how the spectral-domain form of these basis functions can be derived.

3.5.3 Sinusoidal Basis Functions on the Resonant Patches

As the rectangular resonant patches are not directly coupled to any other part of the structure, entire-domain sinusoidal basis functions [31, 123–125], which normally originate from a cavity-model analysis of rectangular patch antennas, should be sufficient to model the electric current density on these patches. The entire-domain sinusoidal basis functions are illustrated in Figure 3.9.

In a coordinate system that is local to each rectangular resonant patch, the entire-domain sinusoidal

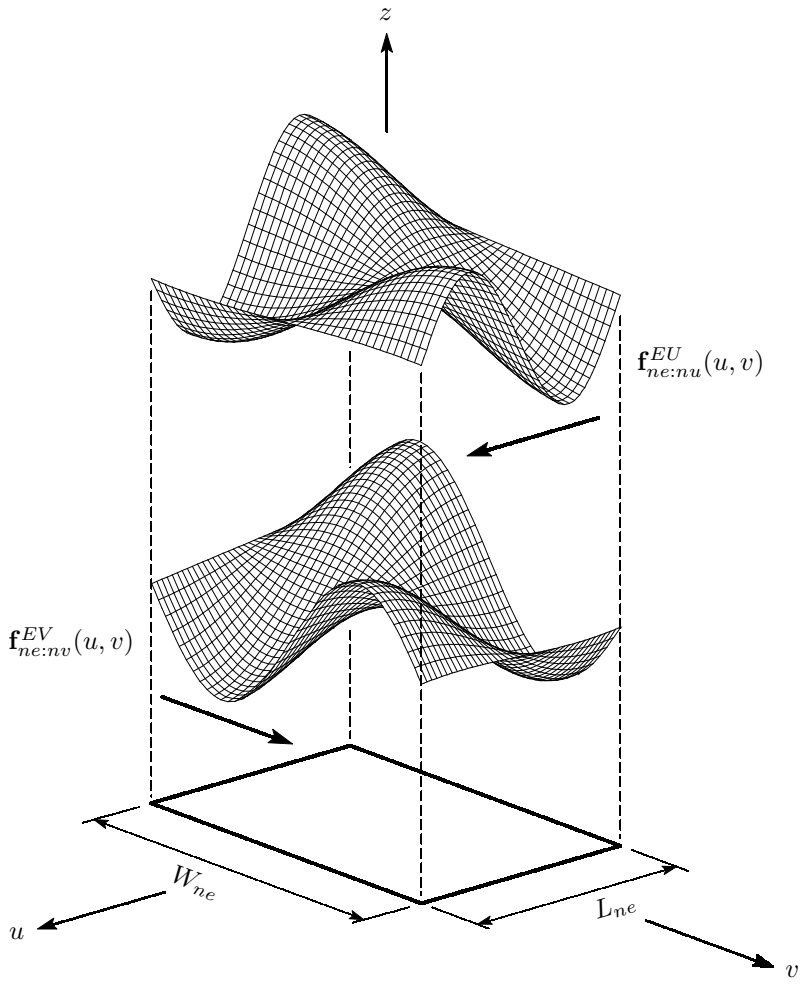

Figure 3.9 Entire-domain sinusoidal basis functions on rectangular resonant patch ne. Here, $p^{EU}_{ne:nu} = 2$ and $q^{EU}_{ne:nu} = 1$, while $p^{EV}_{ne:nv} = 2$ and $q^{EV}_{ne:nv} = 1$.

basis functions are expressed as

$$\mathbf{f}^{EU}_{ne:nu}(u,v) = \sin\left[\frac{p^{EU}_{ne:nu}\pi}{L_{ne}}\left(u+\frac{L_{ne}}{2}\right)\right]\cos\left[\frac{q^{EU}_{ne:nu}\pi}{W_{ne}}\left(v+\frac{W_{ne}}{2}\right)\right]\hat{u}, \quad |u| \leq \frac{L_{ne}}{2},\ |v| \leq \frac{W_{ne}}{2},\ z = z^E_{ne} \tag{3.76}$$

for the u-directed basis functions and as

$$\mathbf{f}^{EV}_{ne:nv}(u,v) = \sin\left[\frac{p^{EV}_{ne:nv}\pi}{W_{ne}}\left(v+\frac{W_{ne}}{2}\right)\right]\cos\left[\frac{q^{EV}_{ne:nv}\pi}{L_{ne}}\left(u+\frac{L_{ne}}{2}\right)\right]\hat{v}, \quad |u| \leq \frac{L_{ne}}{2},\ |v| \leq \frac{W_{ne}}{2},\ z = z^E_{ne} \tag{3.77}$$

for the v-directed basis functions. Here, $\mathbf{f}^{EU}_{ne:nu}$ refers to the nu-th u-directed basis function on the ne-th rectangular resonant patch, while $\mathbf{f}^{EV}_{ne:nv}$ refers to the nv-th v-directed basis function on

the ne-th rectangular resonant patch. Also, z_{ne}^{E} is the z position of the ne-th rectangular resonant patch.

As shown in Figure 3.9, $\hat{u}$ and $\hat{v}$ point along the local u and v directions for the ne-th resonant patch. The patch has dimensions of L_{ne} along the u direction and W_{ne} along the v direction. The $(p_{ne:nu}^{EU}, q_{ne:nu}^{EU})$ mode is associated with the nu-th u-directed basis function on the ne-th rectangular resonant patch, while the $(p_{ne:nv}^{EV}, q_{ne:nv}^{EV})$ mode is associated with the nv-th v-directed basis function. Here, $p_{ne:nu}^{EU}$ and $p_{ne:nv}^{EV}$ can take on values of $1, 2, \ldots$, while $q_{ne:nu}^{EU}$ and $q_{ne:nv}^{EV}$ can take on values of $0, 1, 2, \ldots$.

In the spectral domain, the entire-domain sinusoidal basis functions can be expressed as

$$\tilde{\mathbf{f}}_{ne:nu}^{EU}(k_u, k_v) = \frac{p_{ne:nu}^{EU}\pi/L_{ne}}{k_u^2 - (p_{ne:nu}^{EU}\pi/L_{ne})^2}\left[(-1)^{p_{ne:nu}^{EU}} e^{-jk_uL_{ne}/2} - e^{jk_uL_{ne}/2}\right] \cdot \frac{jk_v}{k_v^2 - (q_{ne:nu}^{EU}\pi/W_{ne})^2}\left[(-1)^{q_{ne:nu}^{EU}} e^{-jk_vW_{ne}/2} - e^{jk_vW_{ne}/2}\right]\hat{u}, \quad z = z_{ne}^{E} \tag{3.78}$$

and

$$\tilde{\mathbf{f}}_{ne:nv}^{EV}(k_u, k_v) = \frac{p_{ne:nv}^{EV}\pi/W_{ne}}{k_v^2 - (p_{ne:nv}^{EV}\pi/W_{ne})^2}\left[(-1)^{p_{ne:nv}^{EV}} e^{-jk_vW_{ne}/2} - e^{jk_vW_{ne}/2}\right] \cdot \frac{jk_u}{k_u^2 - (q_{ne:nv}^{EV}\pi/L_{ne})^2}\left[(-1)^{q_{ne:nv}^{EV}} e^{-jk_uL_{ne}/2} - e^{jk_uL_{ne}/2}\right]\hat{v}, \quad z = z_{ne}^{E} \tag{3.79}$$

respectively. As with the other basis functions, the derivation of these expressions can be found in Appendix B.

3.6 ATTACHMENT MODES

As mentioned before, the attachment modes are special basis functions that are used to accurately model probe-to-patch transitions. They ensure the continuity of the electric current at the junction and also model the singular behaviour of the electric current density at the junction. In this section, two types of attachment modes will be addressed. These will be referred to as the rectangular and circular attachment modes respectively.[2] Both approaches have been used by different researchers, mainly for the analysis of probes connected to resonant patches on a thin substrate. From the literature, it is not clear whether they can be used for probes in thick substrates and for patches that are well below resonant size. Therefore, both of these approaches will be investigated to determine which one is the most appropriate. As they differ substantially, they will be considered separately.

[2] The two attachment modes are not formally known as rectangular and circular attachment modes, but are termed so here in order to distinguish between them.

3.6.1 Rectangular Attachment Mode

The rectangular attachment mode can only be used to model probe-to-patch junctions for rectangular patches. This attachment mode was first proposed by Aberle and Pozar [129, 132], and has since been extended by Chen and Lee [6, 7]. As shown in Figure 3.10(a), the probe part of the attachment mode can be modelled by one half of a PWS function right below every probe-to-patch junction. In a coordinate system that is local to each patch on which an attachment mode resides, the probe part of each attachment mode can therefore be expressed as

$$\mathbf{f}_{na}^{AZ}(u,v,z) = \frac{1}{2\pi a_{na}} f_{na}^{AZ}(z)\,\hat{z}\,\Big|_{(u-u_{na}^{AZ})^2+(v-v_{na}^{AZ})^2=a_{na}^2}, \tag{3.80}$$

where $\mathbf{f}_{na}^{AZ}$ refers to the probe part of the na-th attachment mode. If the current density on the probe, associated with the attachment mode, is approximated by N_{np}^{PZ} PWS basis functions, the probe part of the attachment mode can also be viewed as the $(N_{np}^{PZ}+1)$-th basis function on the probe. The radius of the probe associated with the attachment mode, is denoted by a_{na}, while its position relative to the centre of the patch, is denoted by $(u_{na}^{AZ}, v_{na}^{AZ})$.

The PWS part of the basis function is given by

$$f_{na}^{AZ}(z) = \frac{\sin[k_F(z - z_{na}^{A} + \Delta z_{na}^{A-})]}{\sin(k_F \Delta z_{na}^{A-})}, \quad z_{na}^{A} - \Delta z_{na}^{A-} \leq z \leq z_{na}^{A}, \tag{3.81}$$

where z_{na}^{A} is the z position of the na-th attachment mode (i.e. the top of the associated probe) and Δz_{na}^{A-} is the segment size just below z_{na}^{A}, as shown in Figure 3.10(a). The value of k_F is given by (3.68).

In the spectral domain, the probe part of each attachment mode can be expressed as

$$\tilde{\mathbf{f}}_{na}^{AZ}(k_u, k_v, z) = f_{na}^{AZ}(z)\, J_0(k_\rho a_{na})\, e^{-j(k_u u_{na}^{AZ} + k_v v_{na}^{AZ})}\,\hat{z}. \tag{3.82}$$

It is derived in a similar way as the spectral-domain form of the other PWS basis functions on the probe.

The patch part of the entire-domain attachment mode is based on the the eigenmodes of the magnetic-wall cavity model for a rectangular patch with an uniform current filament source. In a coordinate system that is local to each patch on which an attachment mode resides, the patch part of the attachment mode can be written as [6, 7]

$$\mathbf{f}_{na}^{AP}(u,v) = \frac{1}{2\pi}\int_0^{2\pi} \mathbf{J}_{na}^{AP}(u,v,\dot{u}_{na}^{AZ},\dot{v}_{na}^{AZ})\,d\phi, \tag{3.83}$$

where

$$\dot{u}_{na}^{AZ} = u_{na}^{AZ} + a_{na}\cos(\phi) \tag{3.84}$$

and

$$\dot{v}_{na}^{AZ} = v_{na}^{AZ} + a_{na}\sin(\phi) \tag{3.85}$$

are the coordinates for any position on the surface of the probe. In (3.83), $\mathbf{J}_{na}^{AP}(u, v, \dot{u}_{na}^{AZ}, \dot{v}_{na}^{AZ})$ is the electric current density that would exist at (u, v) on the patch due to a current filament at $(\dot{u}_{na}^{AZ}, \dot{v}_{na}^{AZ})$. Therefore, in order to find the electric current density that would exist at (u, v) due to the total current on the probe, $\mathbf{J}_{na}^{AP}(u, v, \dot{u}_{na}^{AZ}, \dot{v}_{na}^{AZ})$ has to be integrated over the circumference of the probe.

After some manipulation, which is shown in Appendix B, $\mathbf{J}_{na}^{AP}(u, v, \dot{u}_{na}^{AZ}, \dot{v}_{na}^{AZ})$ can be expressed as [6, 7, 129, 132]

$$\mathbf{J}_{na}^{AP}(u, v, \dot{u}_{na}^{AZ}, \dot{v}_{na}^{AZ}) = \frac{-1}{2W_{na}} \sum_{i=0}^{\infty} \epsilon_i \cos\left[\frac{i\pi}{W_{na}}\left(\dot{v}_{na}^{AZ} + \frac{W_{na}}{2}\right)\right]$$
$$\cdot \left\{ g_s(\beta, L_{na}, \dot{u}_{na}^{AZ}, u) f_c(i, W_{na}, v)\, \hat{u} + \left(\frac{i\pi}{W_{na}}\right) g_c(\beta, L_{na}, \dot{u}_{na}^{AZ}, u) f_s(i, W_{na}, v)\, \hat{v} \right\},$$
$$|u| \leq \frac{L_{na}}{2},\ |v| \leq \frac{W_{na}}{2},\ z = z_{na}^{A}, \tag{3.86}$$

where

$$g_s(\beta, L_{na}, \dot{u}_{na}^{AZ}, u) = \frac{\sin[\beta(u + \dot{u}_{na}^{AZ})] - \text{sgn}(u - \dot{u}_{na}^{AZ})\sin[\beta(L_{na} - |u - \dot{u}_{na}^{AZ}|)]}{\sin(\beta L_{na})}, \tag{3.87}$$

$$g_c(\beta, L_{na}, \dot{u}_{na}^{AZ}, u) = \frac{\cos[\beta(u + \dot{u}_{na}^{AZ})] + \cos[\beta(L_{na} - |u - \dot{u}_{na}^{AZ}|)]}{\beta \sin(\beta L_{na})}, \tag{3.88}$$

$$f_s(i, W_{na}, v) = \sin\left[\frac{i\pi}{W_{na}}\left(v + \frac{W_{na}}{2}\right)\right] \tag{3.89}$$

and

$$f_c(i, W_{na}, v) = \cos\left[\frac{i\pi}{W_{na}}\left(v + \frac{W_{na}}{2}\right)\right], \tag{3.90}$$

with

$$\text{sgn}(u) = \begin{cases} 1, & u > 0 \\ 0, & u = 0 \\ -1, & u < 0 \end{cases}, \tag{3.91}$$

$$\beta = \sqrt{\varepsilon_{r(\text{eff})} k_0^2 - \left(\frac{i\pi}{W_{na}}\right)^2} \tag{3.92}$$

and the Neumann numbers

$$\epsilon_i = \begin{cases} 1, & i = 0 \\ 2, & i > 0. \end{cases} \tag{3.93}$$

In (3.92), $k_0 = 2\pi/\lambda_0$, where λ_0 is the free-space wavelength. Also, $\varepsilon_{r(\text{eff})}$ is the effective relative

permittivity of the layers below the patch. For two layers between the probe-fed patch and the ground plane, it can be calculated as [65, 66, 179]

$$\varepsilon_{r(\text{eff})} = \frac{\varepsilon_{r(1)}\varepsilon_{r(2)}\left[h_{(1)}+h_{(2)}\right]}{\varepsilon_{r(1)}h_{(2)}+\varepsilon_{r(2)}h_{(1)}}\left[1-\tan\delta_{\varepsilon(1)}\tan\delta_{\varepsilon(2)}\right]. \tag{3.94}$$

Figure 3.10(b) shows the patch part of the attachment mode where the patch size is small as compared to a wavelength, while Figure 3.10(c) shows the same for a resonant patch.[3] From these two figures it can clearly be seen that, when the patch is small, the attachment mode basically only models the singular nature of the electric current density at the junction position, but when the patch is of a resonant size, the attachment mode also includes the resonant modes.

In the spectral domain, the patch part of the attachment mode can be expressed as

$$\begin{aligned}\tilde{\mathbf{f}}_{na}^{AP}(k_u,k_v) = {} & \frac{j(k_u\,\hat{u}+k_v\,\hat{v})}{k_{z(\text{eff})}^2}\,J_0(k_\rho a_{na})\,e^{-j(k_u u_{na}^{AZ}+k_v v_{na}^{AZ})} \\ & -\frac{(k_u k_v\,\hat{u}+k_\alpha^2\,\hat{v})}{k_{z(\text{eff})}^2}\,A(k_\alpha)J_0(\sqrt{\varepsilon_{r(\text{eff})}}k_0 a_{na})\,e^{-jk_u u_{na}^{AZ}} \\ & -\frac{1}{W_{na}}\sum_{i=0}^{\infty}\epsilon_i\cos\left[\frac{i\pi}{W_{na}}\left(v_{na}^{AZ}+\frac{W_{na}}{2}\right)\right]\frac{(-1)^i e^{-jk_v W_{na}/2}-e^{jk_v W_{na}/2}}{[k_v^2-(i\pi/W_{na})^2][k_u^2-\beta^2]} \\ & \cdot\left[k_v\,\hat{u}+k_u\frac{(i\pi/W_{na})^2}{\beta^2}\,\hat{v}\right]\left[\frac{\beta\cos(\beta u_{na}^{AZ})\sin(k_u L_{na}/2)}{\sin(\beta L_{na}/2)}\right. \\ & \left.-j\frac{\beta\sin(\beta x_{na}^{AZ})\cos(k_u L_{na}/2)}{\cos(\beta L_{na}/2)}\right]J_0(\sqrt{\varepsilon_{r(\text{eff})}}k_0 a_{na}),\quad z=z_{na}^{A},\end{aligned} \tag{3.95}$$

where

$$A(k_\alpha)=\frac{j}{k_\alpha}\left[\frac{\cos(k_\alpha v_{na}^{AZ})\sin(k_v W_{na}/2)}{\sin(k_\alpha W_{na}/2)}-j\frac{\sin(k_\alpha v_{na}^{AZ})\cos(k_v W_{na}/2)}{\cos(k_\alpha W_{na}/2)}\right], \tag{3.96}$$

$$k_\alpha^2=\varepsilon_{r(\text{eff})}k_0^2-k_u^2 \tag{3.97}$$

and

$$k_{z(\text{eff})}^2=\left[\varepsilon_{r(\text{eff})}k_0^2-k_u^2-k_v^2\right]=-\left(k_v^2-k_\alpha^2\right). \tag{3.98}$$

The derivation of the spectral-domain form of the patch part of the rectangular attachment mode can be found in [6,7], but is also included in Appendix B for completeness sake. Also, in [6,7], the resonant mode is subtracted from the electric current density on the patch, while angular variation of the electric current density on the probe is also taken into account. This is not done here and therefore the expressions are not exactly the same as those in [6, 7].

[3] Although the new antenna elements do not include resonant patches that are driven directly with probes, such configurations will be studied in Chapter 4 in order to establish the abilities of the attachment mode.

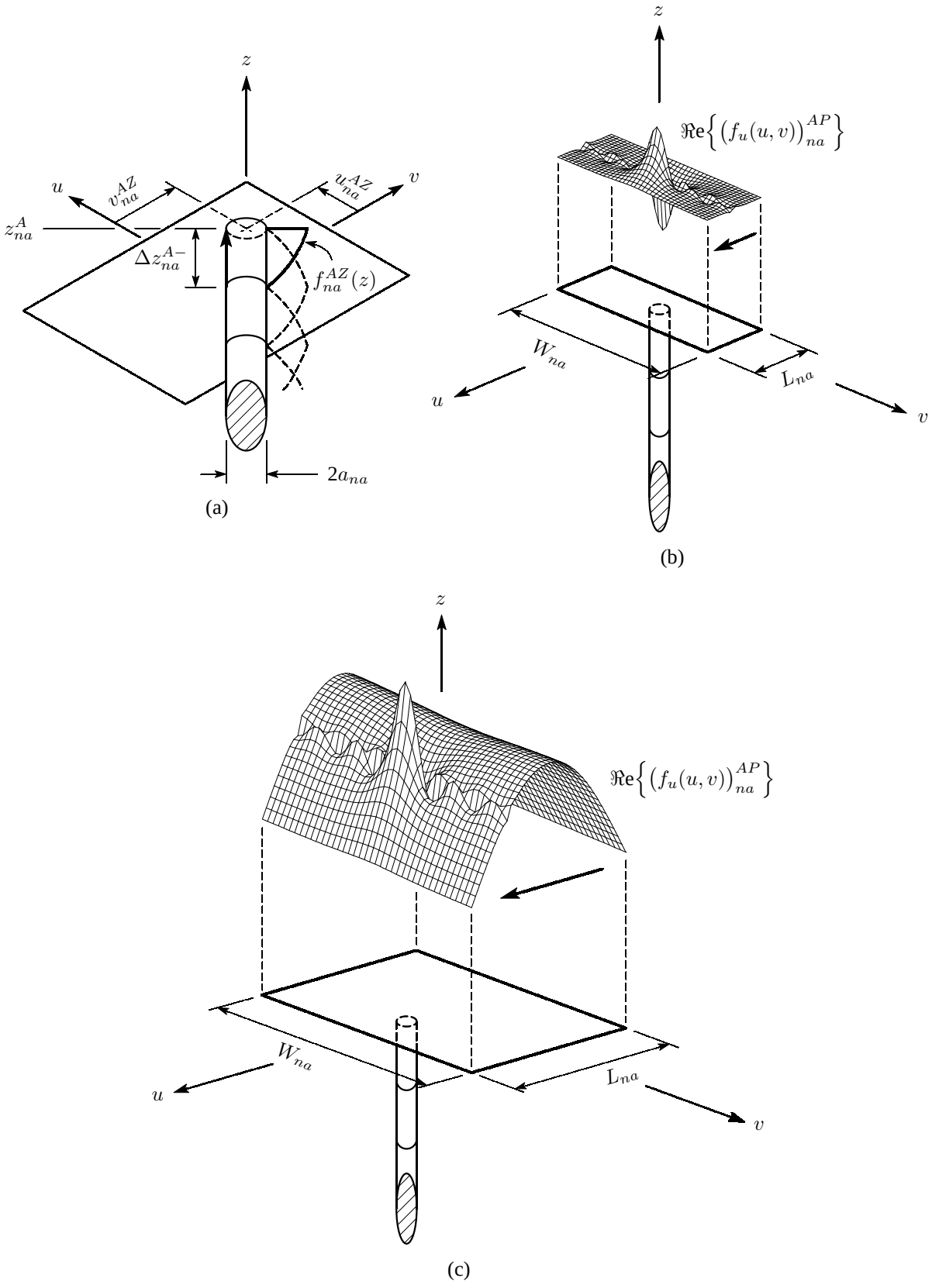

Figure 3.10 Rectangular attachment mode na. (a) Probe part of the attachment mode. (b) Patch part of the attachment mode for a small patch. (c) Patch part of the attachment mode for a resonant patch.

3.6.2 Circular Attachment Mode

In order to model the probe-to-patch transitions for circular patches, it is necessary to use circular attachment modes. Such an attachment mode was developed by Pinhas and Shtrikman [127], and has since also been used for the analysis of rectangular probe-fed patches [124, 125]. As shown in Figure 3.11(a), the probe part of the circular attachment mode can also be modelled by one half of a PWS function right below every probe-to-patch junction. In a coordinate system that is local to the top of the probe associated with the attachment mode, the probe part of each attachment mode can therefore be expressed as

$$\mathbf{f}_{na}^{AZ}(u,v,z) = \frac{1}{2\pi a_{na}} f_{na}^{AZ}(z)\,\hat{z}\Big|_{u^2+v^2=a_{na}}, \tag{3.99}$$

where $\mathbf{f}_{na}^{AZ}$ refers to the probe part of the na-th attachment mode. If the current density on the probe associated with the attachment mode, is approximated by N_{np}^{PZ} PWS basis functions, the probe part of the attachment mode can also be viewed as the $(N_{np}^{PZ}+1)$-th basis function on the probe. The radius of the probe associated with the attachment mode is denoted by a_{na}.

The PWS part of the basis function is given by

$$f_{na}^{AZ}(z) = \frac{\sin[k_F(z - z_{na}^{A} + \Delta z_{na}^{A-})]}{\sin(k_F \Delta z_{na}^{A-})}, \quad z_{na}^{A} - \Delta z_{na}^{A-} \le z \le z_{na}^{A}, \tag{3.100}$$

where z_{na}^{A} is the z position of the na-th attachment mode (i.e. the top of the associated probe) and Δz_{na}^{A-} is the segment size just below z_{na}^{A}, as shown in Figure 3.11(a). The value of k_F is given by (3.68).

In the spectral domain, the probe part of the attachment mode can be expressed as

$$\tilde{\mathbf{f}}_{na}^{AZ}(k_u,k_v,z) = f_{na}^{AZ}(z)\,J_0(k_\rho a_{na})\,\hat{z}. \tag{3.101}$$

It is derived in a similar way as the spectral-domain form of the other PWS basis functions on the probe.

The patch part of the circular attachment mode is represented by a radial current density, spreading over a small fictitious disk with radius b_{na}, concentric with the probe. It can be written as [127]

$$\mathbf{f}_{na}^{AP}(u,v) = \begin{cases} \dfrac{-\rho}{2\pi b_{na}^2}\,\hat{\rho}, & 0 \le \rho < a_{na},\ z = z_{na}^{A} \\ \left(\dfrac{-\rho}{2\pi b_{na}^2} + \dfrac{1}{2\pi\rho}\right)\hat{\rho}, & a_{na} \le \rho \le b_{na},\ z = z_{na}^{A} \\ 0, & \rho > b_{na},\ z = z_{na}^{A}, \end{cases} \tag{3.102}$$

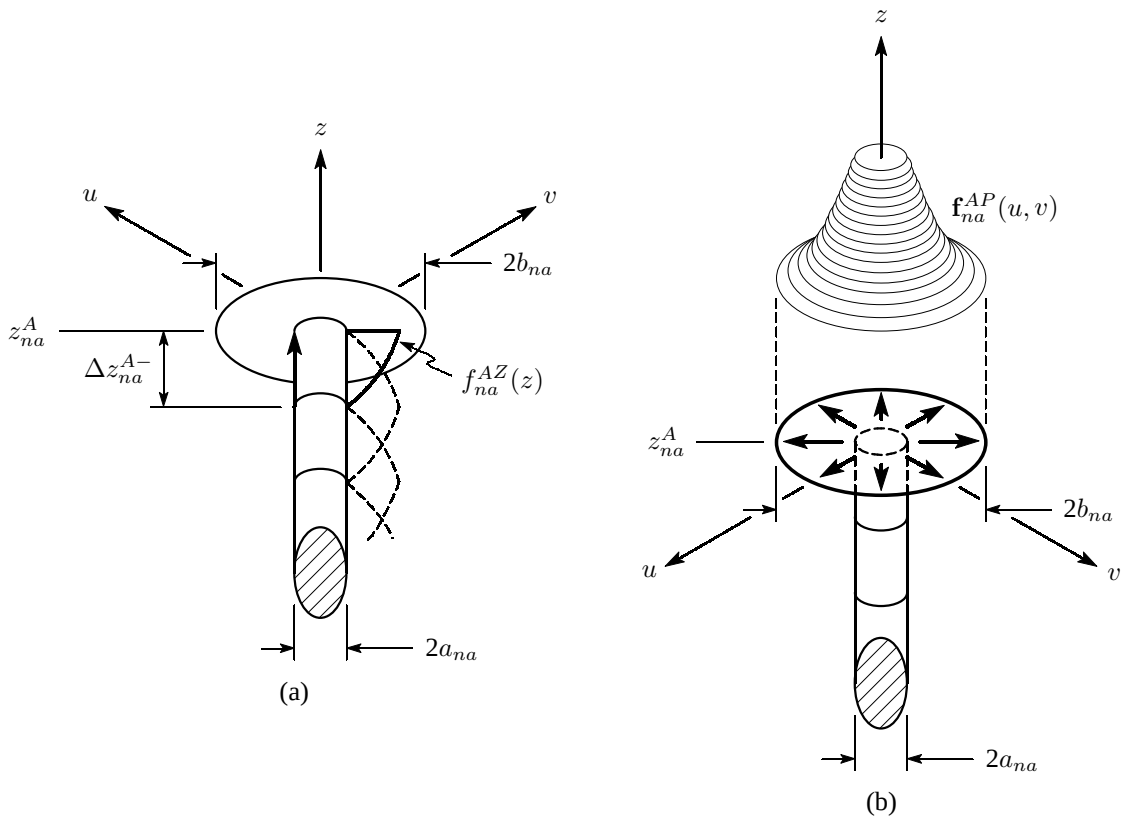

Figure 3.11 Circular attachment mode na. (a) Probe part of the attachment mode. (b) Patch part of the attachment mode.

where

$$\rho = \sqrt{u^2 + v^2} \tag{3.103}$$

and

$$\hat{\rho} = u\,\hat{u} + v\,\hat{v}. \tag{3.104}$$

As is shown in Figure 3.11(b), it has a maximum value at the probe-to-patch junction and then tapers off towards zero at the edge of the attachment mode.

In the spectral domain, the patch part of the attachment mode can be expressed as

$$\begin{aligned}\tilde{\mathbf{f}}_{na}^{AP}(k_u, k_v) &= \left[\frac{jJ_2(k_\rho b_{na})}{k_\rho} - \frac{jJ_0(k_\rho a_{na})}{k_\rho} + \frac{jJ_0(k_\rho b_{na})}{k_\rho}\right]\left[\frac{k_u}{k_\rho}\,\hat{u} + \frac{k_v}{k_\rho}\,\hat{v}\right] \\ &= \left[\frac{j2J_1(k_\rho b_{na})}{k_\rho^2 b_{na}} - \frac{jJ_0(k_\rho a_{na})}{k_\rho}\right]\left[\frac{k_u}{k_\rho}\,\hat{u} + \frac{k_v}{k_\rho}\,\hat{v}\right], \quad z = z_{na}^A,\end{aligned} \tag{3.105}$$

where $J_1(\cdot)$ is the Bessel function of the first kind of order 1 and $J_2(\cdot)$ is the Bessel function of the first kind of order 2. In order to avoid numerical overflow problems for very small values of k_ρ, it is advisable to use the first form in (3.105) together with the small-argument form of $J_2(\cdot)$.

The term associated with $J_2(\cdot)$ can then be approximated as

$$\frac{jJ_2(k_\rho b_{na})}{k_\rho} \overset{k_\rho \to 0}{\simeq} \frac{jk_\rho b_{na}^2}{8}. \tag{3.106}$$

The derivation of (3.105) can be found in Appendix B.

The circular attachment mode can be used to model the complete electric current density on the circular capacitor patches. However, in the next section a higher-order circular attachment mode will be presented that appears to be somewhat more accurate, especially when only the attachment mode is used to model the electric current density on a circular capacitor patch.

3.6.3 Higher-Order Circular Attachment Mode

The probe part of the higher-order circular attachment mode is exactly the same as the one described in the previous section. The patch part of the higher-order circular attachment mode is also represented by a radial current density, spreading over a small fictitious disk with radius b_{na} and which is concentric with the probe. However, on the surface of the patch, the current that flows towards the centre of the patch, is smaller than that for the normal circular attachment mode, which was presented in the previous section. The patch part of the higher-order circular attachment mode can be written as

$$\mathbf{f}_{na}^{AP}(u,v) = \begin{cases} \dfrac{-\rho^3}{2\pi b_{na}^4}\,\hat{\rho}, & 0 \le \rho < a_{na},\ z = z_{na}^A \\ \left(\dfrac{-\rho^3}{2\pi b_{na}^4} + \dfrac{1}{2\pi\rho}\right)\hat{\rho}, & a_{na} \le \rho \le b_{na},\ z = z_{na}^A \\ 0, & \rho > b_{na},\ z = z_{na}^A. \end{cases} \tag{3.107}$$

Here, the higher-order terms force the current density that flows inwards, towards the centre of the attachment mode, to be lower relative to the current density that flows outwards, towards the edge of the attachment mode. It is important to note that not just any functions can be chosen to achieve the desired effect. The current must be continuous across the junction, while the Fourier transform of the attachment mode must also be available in closed form.

In the spectral domain, the patch part of the higher-order circular attachment mode can be expressed as

$$\begin{aligned} &\tilde{\mathbf{f}}_{na}^{AP}(k_u,k_v) \\ &= \left[\frac{-jJ_4(k_\rho b_{na})}{k_\rho} + \frac{j4J_3(k_\rho b_{na})}{k_\rho^2 b_{na}} - \frac{jJ_0(k_\rho a_{na})}{k_\rho} + \frac{jJ_0(k_\rho b_{na})}{k_\rho}\right]\left[\frac{k_u}{k_\rho}\,\hat{u} + \frac{k_v}{k_\rho}\,\hat{v}\right] \\ &= \left[\frac{-j16J_1(k_\rho b_{na})}{k_\rho^4 b_{na}^3} + \frac{j4J_1(k_\rho b_{na})}{k_\rho^2 b_{na}} + \frac{j8J_0(k_\rho b_{na})}{k_\rho^2 b_{na}^2} - \frac{jJ_0(k_\rho a_{na})}{k_\rho}\right]\left[\frac{k_u}{k_\rho}\,\hat{u} + \frac{k_v}{k_\rho}\,\hat{v}\right],\ z = z_{na}^A, \end{aligned} \tag{3.108}$$

where $J_3(\cdot)$ is the Bessel function of the first kind of order 3 and $J_4(\cdot)$ is the Bessel function of the first kind of order 4. In order to avoid numerical overflow problems for very small values of k_ρ, it is advisable to use the first form in (3.108) together with the small-argument forms of $J_3(\cdot)$ and $J_4(\cdot)$. The terms associated with $J_3(\cdot)$ and $J_4(\cdot)$ can then be approximated as

$$\frac{-jJ_4(k_\rho b_{na})}{k_\rho} + \frac{j4J_3(k_\rho b_{na})}{k_\rho^2 b_{na}} \overset{k_\rho \to 0}{\simeq} \frac{-jk_\rho^3 b_{na}^4}{384} + \frac{jk_\rho b_{na}^2}{12}. \tag{3.109}$$

As with the other basis functions, the derivation of (3.108) can be found in Appendix B.

The complete set of basis functions has now been defined. In the following section, it will be shown how the system of linear independent equations can be constructed by making use of the dyadic Green's function and various vector basis and testing functions.

3.7 SYSTEM OF LINEAR EQUATIONS

In Section 3.2, it has been shown that the system of linear equations can be represented in matrix notation as

$$[Z_{m,n}]\,\{I_n\} = \{V_m\}, \tag{3.110}$$

where the subscript m is associated with the testing functions and the subscript n is associated with the basis functions. This system can be expanded as

$$\begin{bmatrix}
\left[Z^{PZ,PZ}_{mp:mz,np:nz}\right] & \left[Z^{PZ,A}_{mp:mz,na}\right] & \left[Z^{PZ,SU}_{mp:mz,ns:nu}\right] & \left[Z^{PZ,SV}_{mp:mz,ns:nv}\right] & \cdots \\
\left[Z^{A,PZ}_{ma,np:nz}\right] & \left[Z^{A,A}_{ma,na}\right] & \left[Z^{A,SU}_{ma,ns:nu}\right] & \left[Z^{A,SV}_{ma,ns:nv}\right] & \cdots \\
\left[Z^{SU,PZ}_{ms:mu,np:nz}\right] & \left[Z^{SU,A}_{ms:mu,na}\right] & \left[Z^{SU,SU}_{ms:mu,ns:nu}\right] & \left[Z^{SU,SV}_{ms:mu,ns:nv}\right] & \cdots \\
\left[Z^{SV,PZ}_{ms:mv,np:nz}\right] & \left[Z^{SV,A}_{ms:mv,na}\right] & \left[Z^{SV,SU}_{ms:mv,ns:nu}\right] & \left[Z^{SV,SV}_{ms:mv,ns:nv}\right] & \cdots \\
\left[Z^{EU,PZ}_{me:mu,np:nz}\right] & \left[Z^{EU,A}_{me:mu,na}\right] & \left[Z^{EU,SU}_{me:mu,ns:nu}\right] & \left[Z^{EU,SV}_{me:mu,ns:nv}\right] & \cdots \\
\left[Z^{EV,PZ}_{me:mv,np:nz}\right] & \left[Z^{EV,A}_{me:mv,na}\right] & \left[Z^{EV,SU}_{me:mv,ns:nu}\right] & \left[Z^{EV,SV}_{me:mv,ns:nv}\right] & \cdots
\end{bmatrix}$$

$$\begin{bmatrix}
\cdots & \left[Z^{PZ,EU}_{mp:mz,ne:nu}\right] & \left[Z^{PZ,EV}_{mp:mz,ne:nv}\right] \\
\cdots & \left[Z^{A,EU}_{ma,ne:nu}\right] & \left[Z^{A,EV}_{ma,ne:nv}\right] \\
\cdots & \left[Z^{SU,EU}_{ms:mu,ne:nu}\right] & \left[Z^{SU,EV}_{ms:mu,ne:nv}\right] \\
\cdots & \left[Z^{SV,EU}_{ms:mv,ne:nu}\right] & \left[Z^{SV,EV}_{ms:mv,ne:nv}\right] \\
\cdots & \left[Z^{EU,EU}_{me:mu,ne:nu}\right] & \left[Z^{EU,EV}_{me:mu,ne:nv}\right] \\
\cdots & \left[Z^{EV,EU}_{me:mv,ne:nu}\right] & \left[Z^{EV,EV}_{me:mv,ne:nv}\right]
\end{bmatrix} \cdot \begin{Bmatrix} \{I^{PZ}_{np:nz}\} \\ \{I^{A}_{na}\} \\ \{I^{SU}_{ns:nu}\} \\ \{I^{SV}_{ns:nv}\} \\ \{I^{EU}_{ne:nu}\} \\ \{I^{EV}_{ne:nv}\} \end{Bmatrix} = \begin{Bmatrix} \{V^{PZ}_{mp:mz}\} \\ \{0\} \\ \{0\} \\ \{0\} \\ \{0\} \\ \{0\} \end{Bmatrix} \tag{3.111}$$

by inserting the six different types of basis functions, as defined in (3.64), into (3.110). As can be seen, the interaction matrix consists of 36 submatrices, where the entries in each submatrix describe the interaction between a specific type of basis function and testing function. For example, in (3.111), $Z^{SU,EV}_{ms:mu,ne:nv}$ refers to the interaction between the mu-th u-directed subdomain rooftop testing function on the ms-th rectangular capacitor patch and the nv-th v-directed entire-domain sinusoidal basis function on the ne-th rectangular resonant patch. Due to the fact that the Galerkin method is used (i.e. the testing functions and basis functions are chosen to be the same set of functions), the interaction matrix in (3.111) is symmetric and therefore only slightly more than half of the total number of entries in the matrix have to be calculated. More specifically, if N is the total number of basis functions, only $(N^2+N)/2$ of the matrix entries have to be calculated, as opposed to N^2 if the matrix were not symmetric.

The submatrix elements in (3.110) that have to be calculated, are given by

$$Z^{PZ,PZ}_{mp:mz,np:nz} = \left\langle \mathbf{f}^{PZ}_{mp:mz}, \mathbf{E}^{\text{scat}}_{\tan}(\mathbf{f}^{PZ}_{np:nz}) \right\rangle,$$
$$mp = 1,2,\ldots,N_P,\ mz = 1,2,\ldots,N^{PZ}_{mp},\ np = 1,2,\ldots,N_P,\ nz = 1,2,\ldots,N^{PZ}_{np}, \quad (3.112)$$

$$Z^{PZ,A}_{mp:mz,na} = \left\langle \mathbf{f}^{PZ}_{mp:mz}, \mathbf{E}^{\text{scat}}_{\tan}(\mathbf{f}^{AZ}_{na} + \mathbf{f}^{AP}_{na}) \right\rangle,$$
$$mp = 1,2,\ldots,N_P,\ mz = 1,2,\ldots,N^{PZ}_{mp},\ na = 1,2,\ldots,N_A, \quad (3.113)$$

$$Z^{A,A}_{ma,na} = \left\langle \mathbf{f}^{AZ}_{ma} + \mathbf{f}^{AP}_{ma}, \mathbf{E}^{\text{scat}}_{\tan}(\mathbf{f}^{AZ}_{na} + \mathbf{f}^{AP}_{na}) \right\rangle,$$
$$ma = 1,2,\ldots,N_A,\ na = 1,2,\ldots,N_A, \quad (3.114)$$

$$Z^{PZ,SU}_{mp:mz,ns:nu} = \left\langle \mathbf{f}^{PZ}_{mp:mz}, \mathbf{E}^{\text{scat}}_{\tan}(\mathbf{f}^{SU}_{ns:nu}) \right\rangle,$$
$$mp = 1,2,\ldots,N_P,\ mz = 1,2,\ldots,N^{PZ}_{mp},\ ns = 1,2,\ldots,N_S,\ nu = 1,2,\ldots,N^{SU}_{ns}, \quad (3.115)$$

$$Z^{A,SU}_{ma,ns:nu} = \left\langle \mathbf{f}^{AZ}_{ma} + \mathbf{f}^{AP}_{ma}, \mathbf{E}^{\text{scat}}_{\tan}(\mathbf{f}^{SU}_{ns:nu}) \right\rangle,$$
$$ma = 1,2,\ldots,N_A,\ ns = 1,2,\ldots,N_S,\ nu = 1,2,\ldots,N^{SU}_{ns}, \quad (3.116)$$

$$Z^{SU,SU}_{ms:mu,ns:nu} = \left\langle \mathbf{f}^{SU}_{ms:mu}, \mathbf{E}^{\text{scat}}_{\tan}(\mathbf{f}^{SU}_{ns:nu}) \right\rangle,$$
$$ms = 1,2,\ldots,N_S,\ mu = 1,2,\ldots,N^{SU}_{ms},\ ns = 1,2,\ldots,N_S,\ nu = 1,2,\ldots,N^{SU}_{ns}, \quad (3.117)$$

$$Z^{PZ,SV}_{mp:mz,ns:nv} = \left\langle \mathbf{f}^{PZ}_{mp:mz}, \mathbf{E}^{\text{scat}}_{\tan}(\mathbf{f}^{SV}_{ns:nv}) \right\rangle,$$
$$mp = 1,2,\ldots,N_P,\ mz = 1,2,\ldots,N^{PZ}_{mp},\ ns = 1,2,\ldots,N_S,\ nv = 1,2,\ldots,N^{SV}_{ns}, \quad (3.118)$$

$$Z^{A,SV}_{ma,ns:nv} = \langle \mathbf{f}^{AZ}_{ma} + \mathbf{f}^{AP}_{ma}, \mathbf{E}^{\text{scat}}_{\text{tan}}(\mathbf{f}^{SV}_{ns:nv}) \rangle,$$
$$ma = 1, 2, \ldots, N_A,\ ns = 1, 2, \ldots, N_S,\ nv = 1, 2, \ldots, N^{SV}_{ns}, \quad (3.119)$$

$$Z^{SU,SV}_{ms:mu,ns:nv} = \langle \mathbf{f}^{SU}_{ms:mu}, \mathbf{E}^{\text{scat}}_{\text{tan}}(\mathbf{f}^{SV}_{ns:nv}) \rangle,$$
$$ms = 1, 2, \ldots, N_S,\ mu = 1, 2, \ldots, N^{SU}_{ms},\ ns = 1, 2, \ldots, N_S,\ nv = 1, 2, \ldots, N^{SV}_{ns}, \quad (3.120)$$

$$Z^{SV,SV}_{ms:mv,ns:nv} = \langle \mathbf{f}^{SV}_{ms:mv}, \mathbf{E}^{\text{scat}}_{\text{tan}}(\mathbf{f}^{SV}_{ns:nv}) \rangle,$$
$$ms = 1, 2, \ldots, N_S,\ mv = 1, 2, \ldots, N^{SV}_{ms},\ ns = 1, 2, \ldots, N_S,\ nv = 1, 2, \ldots, N^{SV}_{ns}, \quad (3.121)$$

$$Z^{PZ,EU}_{mp:mz,ne:nu} = \langle \mathbf{f}^{PZ}_{mp:mz}, \mathbf{E}^{\text{scat}}_{\text{tan}}(\mathbf{f}^{EU}_{ne:nu}) \rangle,$$
$$mp = 1, 2, \ldots, N_P,\ mz = 1, 2, \ldots, N^{PZ}_{mp},\ ne = 1, 2, \ldots, N_E,\ nu = 1, 2, \ldots, N^{EU}_{ne}, \quad (3.122)$$

$$Z^{A,EU}_{na,me:mu} = \langle \mathbf{f}^{AZ}_{ma} + \mathbf{f}^{AP}_{ma}, \mathbf{E}^{\text{scat}}_{\text{tan}}(\mathbf{f}^{EU}_{ne:nu}) \rangle,$$
$$ma = 1, 2, \ldots, N_A,\ ne = 1, 2, \ldots, N_E,\ nu = 1, 2, \ldots, N^{EU}_{ne}, \quad (3.123)$$

$$Z^{SU,EU}_{ms:mu,ne:nu} = \langle \mathbf{f}^{SU}_{ms:mu}, \mathbf{E}^{\text{scat}}_{\text{tan}}(\mathbf{f}^{EU}_{ne:nu}) \rangle,$$
$$ms = 1, 2, \ldots, N_S,\ mu = 1, 2, \ldots, N^{SU}_{ms},\ ne = 1, 2, \ldots, N_E,\ nu = 1, 2, \ldots, N^{EU}_{ne}, \quad (3.124)$$

$$Z^{SV,EU}_{ms:mv,ne:nu} = \langle \mathbf{f}^{SV}_{ms:mv}, \mathbf{E}^{\text{scat}}_{\text{tan}}(\mathbf{f}^{EU}_{ne:nu}) \rangle,$$
$$ms = 1, 2, \ldots, N_S,\ mv = 1, 2, \ldots, N^{SV}_{ms},\ ne = 1, 2, \ldots, N_E,\ nu = 1, 2, \ldots, N^{EU}_{ne}, \quad (3.125)$$

$$Z^{EU,EU}_{me:mu,ne:nu} = \langle \mathbf{f}^{EU}_{me:mu}, \mathbf{E}^{\text{scat}}_{\text{tan}}(\mathbf{f}^{EU}_{ne:nu}) \rangle,$$
$$me = 1, 2, \ldots, N_E,\ mu = 1, 2, \ldots, N^{EU}_{me},\ ne = 1, 2, \ldots, N_E,\ nu = 1, 2, \ldots, N^{EU}_{ne}, \quad (3.126)$$

$$Z^{PZ,EV}_{mp:mz,ne:nv} = \langle \mathbf{f}^{PZ}_{mp:mz}, \mathbf{E}^{\text{scat}}_{\text{tan}}(\mathbf{f}^{EV}_{ne:nv}) \rangle,$$
$$mp = 1, 2, \ldots, N_P,\ mz = 1, 2, \ldots, N^{PZ}_{mp},\ ne = 1, 2, \ldots, N_E,\ nv = 1, 2, \ldots, N^{EV}_{ne}, \quad (3.127)$$

$$Z^{A,EV}_{ma,ne:nv} = \langle \mathbf{f}^{AZ}_{ma} + \mathbf{f}^{AP}_{ma}, \mathbf{E}^{\text{scat}}_{\text{tan}}(\mathbf{f}^{EV}_{ne:nv}) \rangle,$$
$$ma = 1, 2, \ldots, N_A,\ ne = 1, 2, \ldots, N_E,\ nv = 1, 2, \ldots, N^{EV}_{ne}, \quad (3.128)$$

$$Z^{SU,EV}_{ms:mu,ne:nv} = \left\langle \mathbf{f}^{SU}_{ms:mu}, \mathbf{E}^{\text{scat}}_{\tan}(\mathbf{f}^{EV}_{ne:nv}) \right\rangle,$$
$$ms = 1, 2, \ldots, N_S,\ mu = 1, 2, \ldots, N^{SU}_{ms},\ ne = 1, 2, \ldots, N_E,\ nv = 1, 2, \ldots, N^{EV}_{ne}, \quad (3.129)$$

$$Z^{SV,EV}_{ms:mv,ne:nv} = \left\langle \mathbf{f}^{SV}_{ms:mv}, \mathbf{E}^{\text{scat}}_{\tan}(\mathbf{f}^{EV}_{ne:nv}) \right\rangle,$$
$$ms = 1, 2, \ldots, N_S,\ mv = 1, 2, \ldots, N^{SV}_{ms},\ ne = 1, 2, \ldots, N_E,\ nv = 1, 2, \ldots, N^{EV}_{ne}, \quad (3.130)$$

$$Z^{EU,EV}_{me:mu,ne:nv} = \left\langle \mathbf{f}^{EU}_{me:mu}, \mathbf{E}^{\text{scat}}_{\tan}(\mathbf{f}^{EV}_{ne:nv}) \right\rangle,$$
$$me = 1, 2, \ldots, N_E,\ mu = 1, 2, \ldots, N^{EU}_{me},\ ne = 1, 2, \ldots, N_E,\ nv = 1, 2, \ldots, N^{EV}_{ne} \quad (3.131)$$

and

$$Z^{EV,EV}_{me:mv,ne:nv} = \left\langle \mathbf{f}^{EV}_{me:mv}, \mathbf{E}^{\text{scat}}_{\tan}(\mathbf{f}^{EV}_{ne:nv}) \right\rangle,$$
$$me = 1, 2, \ldots, N_E,\ mv = 1, 2, \ldots, N^{EV}_{me},\ ne = 1, 2, \ldots, N_E,\ nv = 1, 2, \ldots, N^{EV}_{ne}. \quad (3.132)$$

The remaining submatrix elements can be found by making use of symmetry. Also, note that the diagonal submatrices of the interaction matrix are themselves symmetric and therefore some of their entries can also be found by making use of symmetry within the submatrix.

The excitation vector only has one subvector to calculate. Its non-zero elements can be expressed as

$$V^{PZ}_{mp:mz} = -\left\langle \mathbf{f}^{PZ}_{mp:mz}, \mathbf{E}^{\text{inc}}_{\tan} \right\rangle, \quad mp = 1, 2, \ldots, N_P,\ mz = 1. \quad (3.133)$$

The actual evaluation of the interaction-matrix entries accounts for most of the computational burden and will now be addressed in the section that follows.

3.8 EVALUATION OF THE INTERACTION-MATRIX ENTRIES

As is evident from (3.22), the evaluation of each entry in the interaction matrix requires integration over the k_x and k_y wavenumbers, as well as possible integration over the z and z' variables. The integrations over z and z' can be done analytically, but the integrations over k_x and k_y require numerical integration in the complex plane, where special care has to be taken with respect to poles, branch points and branch cuts.

As will be explained later, it is more convenient to follow the approach in [164–168] and to define a new coordinate system, as shown in Figure 3.12.[4] This new coordinate system is represented by the ξ and ζ axes, which is chosen in such a way that the ξ axis starts from the centre of the testing

[4] The new coordinate system was previously used to calculate the interaction between basis and testing functions that are widely separated [164–168]. Here, it is used for all interactions.

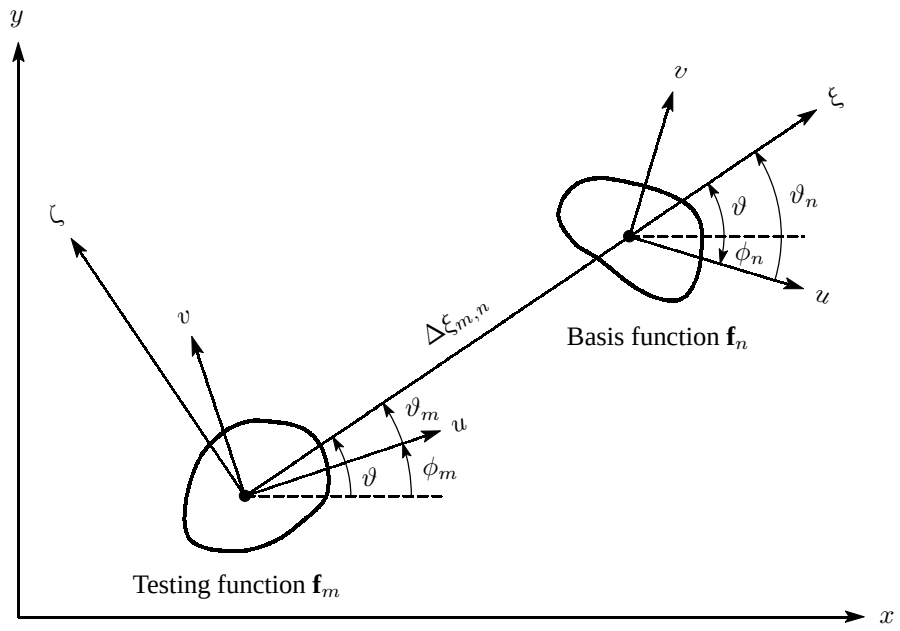

Figure 3.12 Coordinate system used for the evaluation of the interaction-matrix entries.

function and runs through the centre of the basis function. Between the two functions, there is therefore a displacement of $\Delta\xi_{m,n}$ along the ξ axis, while there is no displacement along the ζ axis. In the rest of this section, it will now be shown how the expression in (3.22) can be cast into a new form so that the integration is performed over the k_ξ and k_ζ wavenumbers, as opposed to the k_x and k_y wavenumbers. The benefit of this change in variables is explained in Section 3.9, which deals with integration strategies.

In the new coordinate system of Figure 3.12, the interaction-matrix entries can be expressed as

$$Z_{m,n} = \frac{1}{4\pi^2} \int_{k_\zeta} \int_{k_\xi} \int_z \int_{z'} \tilde{\mathbf{f}}_m(-k_\xi, -k_\zeta, z) \cdot \tilde{\bar{\mathbf{G}}}(k_\xi, k_\zeta, z|z') \cdot \tilde{\mathbf{f}}_n(k_\xi, k_\zeta, z')\, dz' dz\, dk_\xi dk_\zeta, \tag{3.134}$$

where the expressions for $\tilde{\bar{\mathbf{G}}}(k_\xi, k_\zeta, z|z')$, $\tilde{\mathbf{f}}_n(k_\xi, k_\zeta, z')$ and $\tilde{\mathbf{f}}_m(k_\xi, k_\zeta, z)$ still have to be determined.

The expression for $\tilde{\bar{\mathbf{G}}}(k_\xi, k_\zeta, z|z')$ is very straightforward to derive. It can simply be done by rotating the x and y axes until the x axis coincides with the ξ axis. Now, in terms of its individual components, the dyadic Green's function can be expressed as

$$\tilde{\bar{\mathbf{G}}} = \hat{\xi}\,\tilde{G}_{\xi\xi}\,\hat{\xi} + \hat{\xi}\,\tilde{G}_{\xi\zeta}\,\hat{\zeta} + \hat{\xi}\,\tilde{G}_{\xi z}\,\hat{z} + \hat{\zeta}\,\tilde{G}_{\zeta\xi}\,\hat{\xi} + \hat{\zeta}\,\tilde{G}_{\zeta\zeta}\,\hat{\zeta} + \hat{\zeta}\,\tilde{G}_{\zeta z}\,\hat{z} + \hat{z}\,\tilde{G}_{z\xi}\,\hat{\xi} + \hat{z}\,\tilde{G}_{z\zeta}\,\hat{\zeta} + \hat{z}\,\tilde{G}_{zz}\,\hat{z}, \tag{3.135}$$

where the individual components are given by

$$\tilde{G}_{\xi\xi}(k_\xi, k_\zeta, z|z') = \tilde{G}_{xx}(k_x = k_\xi, k_y = k_\zeta, z|z'), \tag{3.136}$$

$$\tilde{G}_{\xi\zeta}(k_\xi, k_\zeta, z|z') = \tilde{G}_{xy}(k_x = k_\xi, k_y = k_\zeta, z|z'), \tag{3.137}$$

$$\tilde{G}_{\xi z}(k_\xi, k_\zeta, z|z') = \tilde{G}_{xz}(k_x = k_\xi, k_y = k_\zeta, z|z'), \tag{3.138}$$

$$\tilde{G}_{\zeta\xi}(k_\xi, k_\zeta, z|z') = \tilde{G}_{yx}(k_x = k_\xi, k_y = k_\zeta, z|z'), \tag{3.139}$$

$$\tilde{G}_{\zeta\zeta}(k_\xi, k_\zeta, z|z') = \tilde{G}_{yy}(k_x = k_\xi, k_y = k_\zeta, z|z'), \tag{3.140}$$

$$\tilde{G}_{\zeta z}(k_\xi, k_\zeta, z|z') = \tilde{G}_{yz}(k_x = k_\xi, k_y = k_\zeta, z|z'), \tag{3.141}$$

$$\tilde{G}_{z\xi}(k_\xi, k_\zeta, z|z') = \tilde{G}_{zx}(k_x = k_\xi, k_y = k_\zeta, z|z'), \tag{3.142}$$

$$\tilde{G}_{z\zeta}(k_\xi, k_\zeta, z|z') = \tilde{G}_{zy}(k_x = k_\xi, k_y = k_\zeta, z|z') \tag{3.143}$$

and

$$\tilde{G}_{zz}(k_\xi, k_\zeta, z|z') = \tilde{G}_{zz}(k_x = k_\xi, k_y = k_\zeta, z|z'). \tag{3.144}$$

The vector basis function $\tilde{\mathbf{f}}_n(k_\xi, k_\zeta, z')$ can be expressed in terms of its three components as

$$\tilde{\mathbf{f}}_n(k_\xi, k_\zeta, z') = \left(\tilde{f}_\xi(k_\xi, k_\zeta, z')\right)_n \hat{\xi} + \left(\tilde{f}_\zeta(k_\xi, k_\zeta, z')\right)_n \hat{\zeta} + \left(\tilde{f}_z(k_\xi, k_\zeta, z')\right)_n \hat{z}, \tag{3.145}$$

where

$$\begin{aligned}
&\left(\tilde{f}_\xi(k_\xi, k_\zeta, z')\right)_n \\
&= \left(\tilde{f}_u\big(k_u = k_\xi \cos(-\vartheta_n) + k_\zeta \sin(-\vartheta_n), k_v = -k_\xi \sin(-\vartheta_n) + k_\zeta \cos(-\vartheta_n), z'\big)\right)_n \\
&\quad \cdot \cos(\vartheta_n)\, e^{-jk_\xi \Delta\xi_{m,n}} \\
&+ \left(\tilde{f}_v\big(k_u = k_\xi \cos(-\vartheta_n) + k_\zeta \sin(-\vartheta_n), k_v = -k_\xi \sin(-\vartheta_n) + k_\zeta \cos(-\vartheta_n), z'\big)\right)_n \\
&\quad \cdot \sin(\vartheta_n)\, e^{-jk_\xi \Delta\xi_{m,n}},
\end{aligned} \tag{3.146}$$

$$\begin{aligned}
&\left(\tilde{f}_\zeta(k_\xi, k_\zeta, z')\right)_n \\
&= -\left(\tilde{f}_u\big(k_u = k_\xi \cos(-\vartheta_n) + k_\zeta \sin(-\vartheta_n), k_v = -k_\xi \sin(-\vartheta_n) + k_\zeta \cos(-\vartheta_n), z'\big)\right)_n \\
&\quad \cdot \sin(\vartheta_n)\, e^{-jk_\xi \Delta\xi_{m,n}} \\
&+ \left(\tilde{f}_v\big(k_u = k_\xi \cos(-\vartheta_n) + k_\zeta \sin(-\vartheta_n), k_v = -k_\xi \sin(-\vartheta_n) + k_\zeta \cos(-\vartheta_n), z'\big)\right)_n \\
&\quad \cdot \cos(\vartheta_n)\, e^{-jk_\xi \Delta\xi_{m,n}}
\end{aligned} \tag{3.147}$$

and

$$\left(\tilde{f}_z(k_\xi, k_\zeta, z')\right)_n = \left(\tilde{f}_z(k_u = k_\xi, k_v = k_\zeta, z')\right)_n e^{-jk_\xi \Delta\xi_{m,n}}. \tag{3.148}$$

Here, ϑ_n is the angle from the u axis (associated with the basis function) to the ξ axis. It can be calculated as

$$\vartheta_n = \vartheta - \phi_n, \tag{3.149}$$

where ϕ_n is the rotation angle, of the local coordinate system of the testing function, with respect

to the (x, y) coordinate system. Furthermore, ϑ is the rotation angle of the (ξ, ζ) coordinate system with respect to the (x, y) coordinate system. All these angles are illustrated in Figure 3.12. Through (3.146) and (3.147), the two-dimensional Fourier transform of the testing function is basically rotated through an angle of $(-\vartheta_n)$.[5] Furthermore, the expressions in (3.151) to (3.153) all contain a $e^{-jk_\xi \Delta\xi_{m,n}}$ term due to the $\Delta\xi_{m,n}$ displacement of the testing function along the ξ axis.

In a similarly way, the vector testing function $\tilde{\mathbf{f}}_m(k_\xi, k_\zeta, z)$ can be expressed in terms of its three components as

$$\tilde{\mathbf{f}}_m(k_\xi, k_\zeta, z) = \left(\tilde{f}_\xi(k_\xi, k_\zeta, z)\right)_m \hat{\xi} + \left(\tilde{f}_\zeta(k_\xi, k_\zeta, z)\right)_m \hat{\zeta} + \left(\tilde{f}_z(k_\xi, k_\zeta, z)\right)_m \hat{z}, \tag{3.150}$$

where

$$\begin{aligned}
&\left(\tilde{f}_\xi(k_\xi, k_\zeta, z)\right)_m \\
&= \left(\tilde{f}_u\big(k_u = k_\xi \cos(-\vartheta_m) + k_\zeta \sin(-\vartheta_m), k_v = -k_\xi \sin(-\vartheta_m) + k_\zeta \cos(-\vartheta_m), z\big)\right)_m \\
&\quad \cdot \cos(\vartheta_m) \\
&+ \left(\tilde{f}_v\big(k_u = k_\xi \cos(-\vartheta_m) + k_\zeta \sin(-\vartheta_m), k_v = -k_\xi \sin(-\vartheta_m) + k_\zeta \cos(-\vartheta_m), z\big)\right)_m \\
&\quad \cdot \sin(\vartheta_m),
\end{aligned} \tag{3.151}$$

$$\begin{aligned}
&\left(\tilde{f}_\zeta(k_\xi, k_\zeta, z)\right)_m \\
&= -\left(\tilde{f}_u\big(k_u = k_\xi \cos(-\vartheta_m) + k_\zeta \sin(-\vartheta_m), k_v = -k_\xi \sin(-\vartheta_m) + k_\zeta \cos(-\vartheta_m), z\big)\right)_m \\
&\quad \cdot \sin(\vartheta_m) \\
&+ \left(\tilde{f}_v\big(k_u = k_\xi \cos(-\vartheta_m) + k_\zeta \sin(-\vartheta_m), k_v = -k_\xi \sin(-\vartheta_m) + k_\zeta \cos(-\vartheta_m), z\big)\right)_m \\
&\quad \cdot \cos(\vartheta_m)
\end{aligned} \tag{3.152}$$

and

$$\left(\tilde{f}_z(k_\xi, k_\zeta, z)\right)_m = \left(\tilde{f}_z(k_u = k_\xi, k_v = k_\zeta, z)\right)_m. \tag{3.153}$$

In this case, ϑ_m is the angle from the u axis (associated with the testing function) to the ξ axis. It can be calculated as

$$\vartheta_m = \vartheta - \phi_m, \tag{3.154}$$

where ϕ_m is the rotation angle, of the local coordinate system of the testing function, with respect to the (x, y) coordinate system.

In general then, for basis function n and testing function m, both with ξ, ζ and z components, the

[5] If a two-dimensional function is rotated through an angle $(-\vartheta_n)$, its two-dimensional Fourier transform is also rotated through $(-\vartheta_n)$ [180].

interaction between them can be expressed as

$$
\begin{aligned}
Z_{m,n} = \frac{1}{4\pi^2}\int_{k_\zeta}\int_{k_\xi}\Big[& \big(\tilde{f}_\xi(-k_\xi,-k_\zeta,z)\big)_m \tilde{G}_{\xi\xi}(k_\xi,k_\zeta,z|z')\big(\tilde{f}_\xi(k_\xi,k_\zeta,z')\big)_n \\
& + \big(\tilde{f}_\xi(-k_\xi,-k_\zeta,z)\big)_m \tilde{G}_{\xi\zeta}(k_\xi,k_\zeta,z|z')\big(\tilde{f}_\zeta(k_\xi,k_\zeta,z')\big)_n \\
& + \big(\tilde{f}_\zeta(-k_\xi,-k_\zeta,z)\big)_m \tilde{G}_{\zeta\xi}(k_\xi,k_\zeta,z|z')\big(\tilde{f}_\xi(k_\xi,k_\zeta,z')\big)_n \\
& + \big(\tilde{f}_\zeta(-k_\xi,-k_\zeta,z)\big)_m \tilde{G}_{\zeta\zeta}(k_\xi,k_\zeta,z|z')\big(\tilde{f}_\zeta(k_\xi,k_\zeta,z')\big)_n \\
& + \big(\tilde{f}_z(-k_\xi,-k_\zeta)\big)_m \tilde{G}^I_{z\xi}(k_\xi,k_\zeta,z')\big(\tilde{f}_\xi(k_\xi,k_\zeta,z')\big)_n \\
& + \big(\tilde{f}_z(-k_\xi,-k_\zeta)\big)_m \tilde{G}^I_{z\zeta}(k_\xi,k_\zeta,z')\big(\tilde{f}_\zeta(k_\xi,k_\zeta,z')\big)_n \\
& + \big(\tilde{f}_z(-k_\xi,-k_\zeta)\big)_m \tilde{G}^{II}_{zz}(k_\xi,k_\zeta)\big(\tilde{f}_z(k_\xi,k_\zeta)\big)_n\Big]\, dk_\xi dk_\zeta, \qquad (3.155)
\end{aligned}
$$

where

$$
\tilde{G}^I_{z\xi}(k_\xi,k_\zeta,z') = \int_z \big(f_z(z)\big)_m \tilde{G}_{z\xi}(k_\xi,k_\zeta,z|z')\, dz', \qquad (3.156)
$$

$$
\tilde{G}^I_{z\zeta}(k_\xi,k_\zeta,z') = \int_z \big(f_z(z)\big)_m \tilde{G}_{z\zeta}(k_\xi,k_\zeta,z|z')\, dz' \qquad (3.157)
$$

and

$$
\tilde{G}^{II}_{zz}(k_\xi,k_\zeta) = \int_z\int_{z'} \big(f_z(z)\big)_m \tilde{G}_{z\zeta}(k_\xi,k_\zeta,z|z')\big(f_z(z')\big)_n\, dz'dz. \qquad (3.158)
$$

The expressions in (3.156) to (3.158) will be referred to as *expanded Green's-function components* for the purposes of this analysis. This is due to the fact that they contain integrations that have to be performed over z and/or z'. In Appendix A, it is shown how they can be evaluated.

The numerical integration over k_ξ and k_ζ in (3.155) is a rather formidable task and will now be addressed in the section that follows.

3.9 INTEGRATION STRATEGIES

Fast numerical integration methods, which are required for the efficient evaluation of the entries in the interaction matrix, have been and still seem to be the topic of intensive research. This is understandable when realising that most of the computational time goes into the evaluation of these integrals, especially in the spectral domain.

For the purposes of this study, a few different integration strategies have been implemented. Their usage depends on the separation distance between basis and testing functions, as well as on types of basis and testing functions that are used. There is a common integration strategy that is used for all cases where there is overlap of the basis and testing functions, while two different integra-

tion strategies were implemented for cases where the basis and testing functions are completely separated. The usage of the latter two depends on whether the basis and testing functions are axisymmetric (i.e. no angular variation) or not. Each of the integration strategies will now be considered in more detail.

3.9.1 Integration Strategy for Overlapping Basis and Testing Functions

A general entry of the interaction matrix can be expressed in a compact form as

$$Z_{m,n} = \frac{1}{4\pi^2} \int_{-\infty}^{\infty} \int_{-\infty}^{\infty} \psi_{m,n}(k_\xi, k_\zeta)\, e^{-jk_\xi \Delta\xi_{m,n}}\, dk_\xi dk_\zeta, \tag{3.159}$$

where $\psi_{m,n}(k_\xi, k_\zeta)$ is a smooth function and $e^{-jk_\xi \Delta\xi_{m,n}}$ is the shift exponential due to the separation between the basis and testing functions. The integrals in (3.159) can be simplified by changing to polar coordinates. This is facilitated by setting

$$k_\xi = k_\rho \cos(\varphi) \tag{3.160}$$

and

$$k_\zeta = k_\rho \sin(\varphi). \tag{3.161}$$

Here, k_ρ is the wavenumber in a radial direction and φ is the angular variable. By making this change of variables, the expression in (3.159) can now be written as

$$Z_{m,n} = \frac{1}{4\pi^2} \int_{0}^{2\pi} \int_{0}^{\infty} \psi_{m,n}(k_\rho, \varphi)\, e^{-jk_\rho \Delta\xi_{m,n} \cos(\varphi)} k_\rho\, dk_\rho d\varphi. \tag{3.162}$$

As can be seen, the double infinite integrals in (3.159) have now been replaced by one finite integral and one semi-infinite integral. For numerical integration purposes, this form of the interaction-matrix entries, is usually preferred over the form in (3.159) [123, 144].

The finite integration over φ in (3.162) can usually be performed without any difficulty, provided that the integrand is not very oscillatory. However, the integration over k_ρ is much more involved and requires a very careful treatment. This is due to poles, branch points and branch cuts in the complex k_ρ plane. They are associated with the multilayered Green's function and appear in the fourth quadrant of the complex k_ρ plane (they also appear in the second quadrant, but these are not of importance here), as shown in Figure 3.13. In the lossless case, the singularities move onto the real k_ρ axis. They are however bounded by two values on the real axis, $k_{\rho,1}$ and $k_{\rho,2}$. These are given by [95, 178]

$$k_{\rho,1} = k_0 \sqrt{\min\left[\mu_{r(0)}\varepsilon_{r(0)}, \mu_{r(1)}\varepsilon_{r(1)}, \ldots, \mu_{r(T)}\varepsilon_{r(T)}\right]} \tag{3.163}$$

and

$$k_{\rho,2} = k_0 \sqrt{\max\left[\mu_{r(0)}\varepsilon_{r(0)}, \mu_{r(1)}\varepsilon_{r(1)}, \ldots, \mu_{r(T)}\varepsilon_{r(T)}\right]}. \tag{3.164}$$

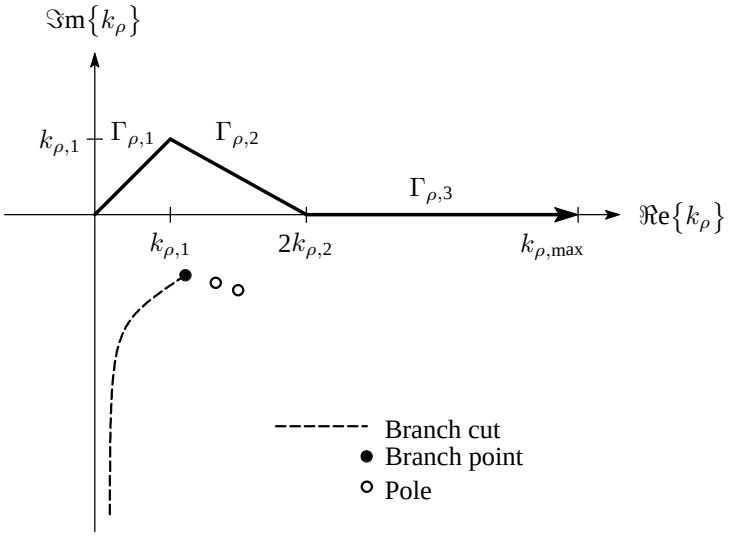

Figure 3.13 Integration path in the complex k_ρ plane for overlapping basis and testing functions.

In order to avoid the singularities on the real k_ρ axis, the integration contour is deformed into the first quadrant of the complex k_ρ plane [61, 151], as shown in Figure 3.13. The integration contour is divided into three parts: $\Gamma_{\rho,1}$, $\Gamma_{\rho,2}$ and $\Gamma_{\rho,3}$. In theory, $\Gamma_{\rho,3}$ runs along the real k_ρ axis up to infinity, but for the purposes of numerical integration, it has to be terminated at some value $k_{\rho,\max}$. The value of $k_{\rho,\max}$ depends on the basis and testing functions that are used. Its value for the different combinations of basis and testing functions has been found through extensive numerical experimentation and is presented in Table 3.1. The deformation of the integration path should be large enough to avoid the singularities, but also not too large, since the integrand grows exponentially away from the real axis. Also, the evaluation of Bessel functions with large complex arguments, becomes very difficult [181, 182]. Another possibility is not to deform the integration path at all, but to use residue extraction at the singularities [146, 183]. However, a thick substrate is usually associated with many surface-waves poles and, as such, the pole-tracking can be become extremely tedious. Therefore, this method will not be considered here.

The numerical integration along each part of the k_ρ integration contour is performed through Gaussian quadrature. The three parts of the integration contour, $\Gamma_{\rho,1}$, $\Gamma_{\rho,2}$ and $\Gamma_{\rho,3}$, are divided into $I_{\Gamma_{\rho,1}}$, $I_{\Gamma_{\rho,2}}$ and $I_{\Gamma_{\rho,3}}$ intervals respectively. Subsequently, $N_{\Gamma_{\rho,1}}$, $N_{\Gamma_{\rho,2}}$ and $N_{\Gamma_{\rho,3}}$ point Gauss-Legendre quadrature formulas are then applied to each interval on the three parts of the integration contour. Similarly, the φ integration contour is divided into I_φ intervals with N_φ point Gaussian-Legendre quadrature applied to each interval. Once again, the number of integration intervals and points required for the Gaussian quadrature, has also been determined through numerical experimentation, and is presented in Table 3.2.

The present integration method only works well for basis and testing functions that overlap or

Table 3.1
Value of $k_{\rho,\max}$ for (k_ρ, φ) integration.

Interaction	$k_{\rho,\max}$
$Z_{mp:mz,np:nz}^{PZ,PZ}$	$\max\{\min[80/\sqrt{\max(a_{mp},a_{np})\max(\Delta z_{mz},\Delta z_{nz})}, 320/\lvert z_{mp}-z_{np}\rvert], 4k_{\rho,2}\}$
$Z_{mp:mz,na}^{PZ,A}$	$\max\{\min[80/\sqrt{\max(a_{ma},a_{np})\max(\Delta z_{ma},\Delta z_{nz})}, 80/\lvert z_{mp}-z_{na}\rvert], 4k_{\rho,2}\}$
$Z_{ma,na}^{A,A}$	$\max(500/\sqrt{\max(a_{ma},a_{np})}, 4k_{\rho,2})$
$Z_{mp:mz,ns:nu}^{PZ,SU}$	$\max\{\min[\min(80/\sqrt{a_{mp}\Delta z_{mp}}, 20\pi/\Delta l_{ns}), 20/\lvert z_{mp}-z_{ns}\rvert], 4k_{\rho,2}\}$
$Z_{ma,ns:nu}^{A,SU}$	$\max\{\min[\min(500/\sqrt{a_{ma}}, 20\pi/\Delta l_{ns}), 20/\lvert z_{ma}-z_{ns}\rvert], 4k_{\rho,2}\}$
$Z_{ms:mu,ns:nu}^{SU,SU}$	$\max\{\min[20\pi/\min(\Delta l_{ms},\Delta l_{ns}), 20/\lvert z_{ms}-z_{ns}\rvert], 4k_{\rho,2}\}$
$Z_{mp:mz,ns:nv}^{PZ,SV}$	$\max\{\min[\min(80/\sqrt{a_{mp}\Delta z_{mp}}, 20\pi/\Delta w_{ns}), 20/\lvert z_{mp}-z_{ns}\rvert], 4k_{\rho,2}\}$
$Z_{ma,ns:nv}^{A,SV}$	$\max\{\min[\min(500/\sqrt{a_{ma}}, 20\pi/\Delta w_{ns}), 20/\lvert z_{ma}-z_{ns}\rvert], 4k_{\rho,2}\}$
$Z_{ms:mu,ns:nv}^{SU,SV}$	$\max\{\min[20\pi/\min(\Delta l_{ms},\Delta l_{ns},\Delta w_{ms},\Delta w_{ns}), 20/\lvert z_{ms}-z_{ns}\rvert], 4k_{\rho,2}\}$
$Z_{ms:mv,ns:nv}^{SV,SV}$	$\max\{\min[20\pi/\min(\Delta w_{ms},\Delta w_{ns}), 20/\lvert z_{ms}-z_{ns}\rvert], 4k_{\rho,2}\}$
$Z_{mp:mz,ne:nu}^{PZ,EU}$	$\max\{\min[\min(40/\sqrt{a_{mp}\Delta z_{mp}}, \sqrt{(p_{ne:nu}^{EU}\pi/L_{ne})^2+(q_{ne:nu}^{EU}\pi/W_{ne})^2}$ $+10\pi\sqrt{(1/L_{ne})^2+(1/W_{ne})^2}), 20/\lvert z_{mp}-z_{ne}\rvert], 4k_{\rho,2}\}$
$Z_{na,me:mu}^{A,EU}$	$\max\{\min[\min(500/\sqrt{a_{ma}}, \sqrt{(p_{ne:nu}^{EU}\pi/L_{ne})^2+(q_{ne:nu}^{EU}\pi/W_{ne})^2}$ $+10\pi\sqrt{(1/L_{ne})^2+(1/W_{ne})^2}), 20/\lvert z_{ma}-z_{ne}\rvert], 4k_{\rho,2}\}$
$Z_{ms:mu,ne:nu}^{SU,EU}$	$\max\{\min[\min(10\pi/\Delta l_{ms}, \sqrt{(p_{ne:nu}^{EU}\pi/L_{ne})^2+(q_{ne:nu}^{EU}\pi/W_{ne})^2}$ $+10\pi\sqrt{(1/L_{ne})^2+(1/W_{ne})^2}), 20/\lvert z_{ms}-z_{ne}\rvert], 4k_{\rho,2}\}$
$Z_{ms:mv,ne:nu}^{SV,EU}$	$\max\{\min[\min(10\pi/\Delta w_{ms}, \sqrt{(p_{ne:nu}^{EU}\pi/L_{ne})^2+(q_{ne:nu}^{EU}\pi/W_{ne})^2}$ $+10\pi\sqrt{(1/L_{ne})^2+(1/W_{ne})^2}), 20/\lvert z_{ms}-z_{ne}\rvert], 4k_{\rho,2}\}$
$Z_{me:mu,ne:nu}^{EU,EU}$	$\max\{\min[\max(\sqrt{(p_{me:mu}^{EU}\pi/L_{ne})^2+(q_{me:mu}^{EU}\pi/W_{ne})^2},$ $\sqrt{(p_{ne:nu}^{EU}\pi/L_{ne})^2+(q_{ne:nu}^{EU}\pi/W_{ne})^2})$ $+10\pi\sqrt{(1/L_{ne})^2+(1/W_{ne})^2}, 20/\lvert z_{me}-z_{ne}\rvert], 4k_{\rho,2}\}$
$Z_{mp:mz,ne:nv}^{PZ,EV}$	$\max\{\min[\min(40/\sqrt{a_{mp}\Delta z_{mp}}, \sqrt{(p_{ne:nv}^{EV}\pi/W_{ne})^2+(q_{ne:nv}^{EV}\pi/L_{ne})^2}$ $+10\pi\sqrt{(1/L_{ne})^2+(1/W_{ne})^2}), 20/\lvert z_{mp}-z_{ne}\rvert], 4k_{\rho,2}\}$
$Z_{na,me:mv}^{A,EV}$	$\max\{\min[\min(500/\sqrt{a_{ma}}, \sqrt{(p_{ne:nv}^{EV}\pi/W_{ne})^2+(q_{ne:nv}^{EV}\pi/L_{ne})^2}$ $+10\pi\sqrt{(1/L_{ne})^2+(1/W_{ne})^2}), 20/\lvert z_{ma}-z_{ne}\rvert], 4k_{\rho,2}\}$
$Z_{ms:mu,ne:nv}^{SU,EV}$	$\max\{\min[\min(10\pi/\Delta l_{ms}, \sqrt{(p_{ne:nv}^{EV}\pi/W_{ne})^2+(q_{ne:nv}^{EV}\pi/L_{ne})^2}$ $+10\pi\sqrt{(1/L_{ne})^2+(1/W_{ne})^2}), 20/\lvert z_{ms}-z_{ne}\rvert], 4k_{\rho,2}\}$
$Z_{ms:mv,ne:nv}^{SV,EV}$	$\max\{\min[\min(10\pi/\Delta w_{ms}, \sqrt{(p_{ne:nv}^{EV}\pi/W_{ne})^2+(q_{ne:nv}^{EV}\pi/L_{ne})^2}$ $+10\pi\sqrt{(1/L_{ne})^2+(1/W_{ne})^2}), 20/\lvert z_{ms}-z_{ne}\rvert], 4k_{\rho,2}\}$
$Z_{me:mu,ne:nv}^{EU,EV}$	$\max\{\min[\max(\sqrt{(p_{me:mu}^{EU}\pi/L_{ne})^2+(q_{me:mu}^{EU}\pi/W_{ne})^2},$ $\sqrt{(p_{ne:nv}^{EV}\pi/W_{ne})^2+(q_{ne:nv}^{EV}\pi/L_{ne})^2})$ $+10\pi\sqrt{(1/L_{ne})^2+(1/W_{ne})^2}, 20/\lvert z_{me}-z_{ne}\rvert], 4k_{\rho,2}\}$
$Z_{me:mv,ne:nv}^{EV,EV}$	$\max\{\min[\max(\sqrt{(p_{me:mv}^{EV}\pi/W_{ne})^2+(q_{me:mv}^{EV}\pi/L_{ne})^2},$ $\sqrt{(p_{ne:nv}^{EV}\pi/W_{ne})^2+(q_{ne:nv}^{EV}\pi/L_{ne})^2})$ $+10\pi\sqrt{(1/L_{ne})^2+(1/W_{ne})^2}, 20/\lvert z_{me}-z_{ne}\rvert], 4k_{\rho,2}\}$

Note: the terms containing $|z_m - z_n|$ should only be used if $|z_m - z_n| \neq 0$.

Table 3.2
Integration intervals and points for (k_ρ, φ) integration.

Interaction	I_φ	N_φ	$I_{\Gamma_{\rho,1}}$	$I_{\Gamma_{\rho,2}}$	$I_{\Gamma_{\rho,3}}$	$N_{\Gamma_{\rho,1}}$	$N_{\Gamma_{\rho,2}}$	$N_{\Gamma_{\rho,3}}$
$Z^{PZ,PZ}_{mp:mz,np:nz}$	n/a *	n/a *	1	4	$4\left\lceil \frac{k_{\rho,\max} a_{\max}}{\pi} + \frac{1}{4} \right\rceil$	4	4	12
$Z^{PZ,A}_{mp:mz,na}$	n/a *	n/a *	1	4	$4\left\lceil \frac{k_{\rho,\max} a_{\max}}{\pi} + \frac{1}{4} \right\rceil$	4	4	12
$Z^{A,A}_{ma,na}$	n/a *	n/a *	1	4	$4\left\lceil \frac{k_{\rho,\max} a_{\max}}{\pi} + \frac{1}{4} \right\rceil$	4	4	12
$Z^{PZ,SU}_{mp:mz,ns:nu}$	8	4	1	4	$\left\lceil \frac{k_{\rho,\max} \Delta l_{ns}}{2\pi} \right\rceil$	4	4	12
$Z^{A,SU}_{ma,ns:nu}$	8	8	1	4	$\left\lceil \frac{k_{\rho,\max} \Delta l_{ns}}{2\pi} \right\rceil$	4	4	20
$Z^{SU,SU}_{ms:mu,ns:nu}$	8	1	1	4	$\left\lceil \frac{k_{\rho,\max} \Delta l_{\max}}{2\pi} \right\rceil$	4	4	12
$Z^{PZ,SV}_{mp:mz,ns:nv}$	8	4	1	4	$\left\lceil \frac{k_{\rho,\max} \Delta w_{ns}}{2\pi} \right\rceil$	4	4	12
$Z^{A,SV}_{ma,ns:nv}$	8	8	1	4	$\left\lceil \frac{k_{\rho,\max} \Delta w_{ns}}{2\pi} \right\rceil$	4	4	20
$Z^{SU,SV}_{ms:mu,ns:nv}$	8	8	1	4	$\left\lceil \frac{k_{\rho,\max} \Delta l \Delta w_{\max}}{2\pi} \right\rceil$	4	4	12
$Z^{SV,SV}_{ms:mv,ns:nv}$	8	8	1	4	$\left\lceil \frac{k_{\rho,\max} \Delta w_{\max}}{2\pi} \right\rceil$	4	4	12
$Z^{PZ,EU}_{mp:mz,ne:nu}$	$\max(pq^{EU}_n, 8)$	4	1	4	$\left\lceil \frac{k_{\rho,\max} L_{ne}}{2\pi} \right\rceil$	4	4	12
$Z^{A,EU}_{na,me:mu}$	$\max(pq^{EU}_n, 8)$	4	1	4	$\left\lceil \frac{k_{\rho,\max} L_{ne}}{2\pi} \right\rceil$	4	4	12
$Z^{SU,EU}_{ms:mu,ne:nu}$	$\max(pq^{EU}_n, 8)$	4	1	4	$\left\lceil \frac{k_{\rho,\max} L_{ne}}{2\pi} \right\rceil$	4	4	12
$Z^{SV,EU}_{ms:mv,ne:nu}$	$\max(pq^{EU}_n, 8)$	4	1	4	$\left\lceil \frac{k_{\rho,\max} L_{ne}}{2\pi} \right\rceil$	4	4	12
$Z^{EU,EU}_{me:mu,ne:nu}$	$\max(pq^{EU}_m, pq^{EU}_n, 8)$	4	1	4	$\left\lceil \frac{k_{\rho,\max} L_{\max}}{2\pi} \right\rceil$	4	4	12
$Z^{PZ,EV}_{mp:mz,ne:nv}$	$\max(pq^{EV}_n, 8)$	4	1	4	$\left\lceil \frac{k_{\rho,\max} W_{ne}}{2\pi} \right\rceil$	4	4	12
$Z^{A,EV}_{na,me:mv}$	$\max(pq^{EV}_n, 8)$	4	1	4	$\left\lceil \frac{k_{\rho,\max} W_{ne}}{2\pi} \right\rceil$	4	4	12
$Z^{SU,EV}_{ms:mu,ne:nv}$	$\max(pq^{EV}_n, 8)$	4	1	4	$\left\lceil \frac{k_{\rho,\max} W_{ne}}{2\pi} \right\rceil$	4	4	12
$Z^{SV,EV}_{ms:mv,ne:nv}$	$\max(pq^{EV}_n, 8)$	4	1	4	$\left\lceil \frac{k_{\rho,\max} W_{ne}}{2\pi} \right\rceil$	4	4	12
$Z^{EU,EV}_{me:mu,ne:nv}$	$\max(pq^{EU}_m, pq^{EV}_n, 8)$	4	1	4	$\left\lceil \frac{k_{\rho,\max} LW_{\max}}{2\pi} \right\rceil$	4	4	12
$Z^{EV,EV}_{me:mv,ne:nv}$	$\max(pq^{EV}_m, pq^{EV}_n, 8)$	4	1	4	$\left\lceil \frac{k_{\rho,\max} W_{\max}}{2\pi} \right\rceil$	4	4	12

Note:

$pq^{EU}_m = 2(p^{EU}_{me:mu} + q^{EU}_{me:mu})$ and $pq^{EU}_n = 2(p^{EU}_{ne:nu} + q^{EU}_{ne:nu})$.

$pq^{EV}_m = 2(p^{EV}_{me:mv} + q^{EV}_{me:mv})$ and $pq^{EV}_n = 2(p^{EV}_{ne:nv} + q^{EV}_{ne:nv})$.

$\Delta a_{\max} = \max(a_{mp}, a_{np}, a_{ma}, a_{na})$ where applicable.

$\Delta l_{\max} = \max(\Delta l_{ms}, \Delta l_{ns})$ and $\Delta w_{\max} = \max(\Delta w_{ms}, \Delta w_{ns})$.

$\Delta l \Delta w_{\max} = \max(\Delta l_{ms}, \Delta l_{ns}, \Delta w_{ms}, \Delta w_{ns})$.

$L_{\max} = \max(L_{me}, L_{ne})$ and $W_{\max} = \max(W_{me}, W_{ne})$.

$LW_{\max} = \max(L_{me}, L_{ne}, W_{me}, W_{ne})$.

* due to symmetry, no φ integration is required for axisymmetric basis and testing functions.

where the separation between them is very small. The method becomes more and more inefficient as the basis and testing functions are moved further apart. To illustrate this, consider the behaviour of the two integrands in Figures 3.14(a) and (b). The integrand in Figure 3.14(a) is for the interaction between basis and testing functions with no separation between them, while the integrand in Figure 3.14(b) is for the interaction between basis and testing functions with a finite separation distance between them. It can be seen that the integrand in Figure 3.14(a) is fairly smooth, but that the shift exponential causes the integrand in Figure 3.14(b) to be oscillatory. These oscillations become more severe as the separation distance is increased and therefore the present method becomes less and less efficient. In order to efficiently integrate the integrand associated with widely-separated basis and testing functions, one has to resort to other more appropriate methods. These will now be discussed in more detail.

3.9.2 Integration Strategy for Separated Basis and Testing Functions

A new technique has recently been developed by Sereno-Garino *et al.* [164–168] for a more efficient analysis of the interaction integrals when the basis and testing functions are widely separated. It makes use of integration-contour deformation in order to avoid the oscillations that are caused by the shift exponential.

A general entry of the interaction matrix can once again be expressed in its compact form as

$$Z_{m,n} = \frac{1}{4\pi^2} \int_{-\infty}^{\infty} \int_{-\infty}^{\infty} \psi_{m,n}(k_\xi, k_\zeta)\, e^{-jk_\xi \Delta\xi_{m,n}}\, dk_\xi dk_\zeta, \tag{3.165}$$

where $\psi_{m,n}(k_\xi, k_\zeta)$ is a smooth function and $e^{-jk_\xi \Delta\xi_{m,n}}$ is the shift exponential due to the separation between the basis and testing functions. In this case, however, the integration variables are not substituted with their polar counterparts, as in the previous section, but are left in rectangular coordinates. The new technique can best be described by expressing (3.165) as

$$Z_{m,n} = \frac{1}{4\pi^2} \int_{-\infty}^{\infty} \Psi_{m,n}(k_\xi)\, e^{-jk_\xi \Delta\xi_{m,n}}\, dk_\xi, \tag{3.166}$$

where

$$\Psi_{m,n}(k_\xi) = \int_{-\infty}^{\infty} \psi_{m,n}(k_\xi, k_\zeta)\, dk_\zeta. \tag{3.167}$$

Here, it can be seen what benefit the new coordinate system in Figure 3.12 adds to the evaluation of the integrals. The inner integration over k_ζ can be evaluated without much trouble as there is no separation between the basis and testing functions along the ζ direction. This then in turn also implies that $\Psi_{m,n}(k_\xi)$ is a smooth function without any oscillations due to the shift exponential. The integration over k_ξ can be facilitated by choosing an integration contour over which the shift exponential decays.

Sereno-Garino *et al.* suggested that the k_ζ integration contour should stay close to the real k_ζ axis,

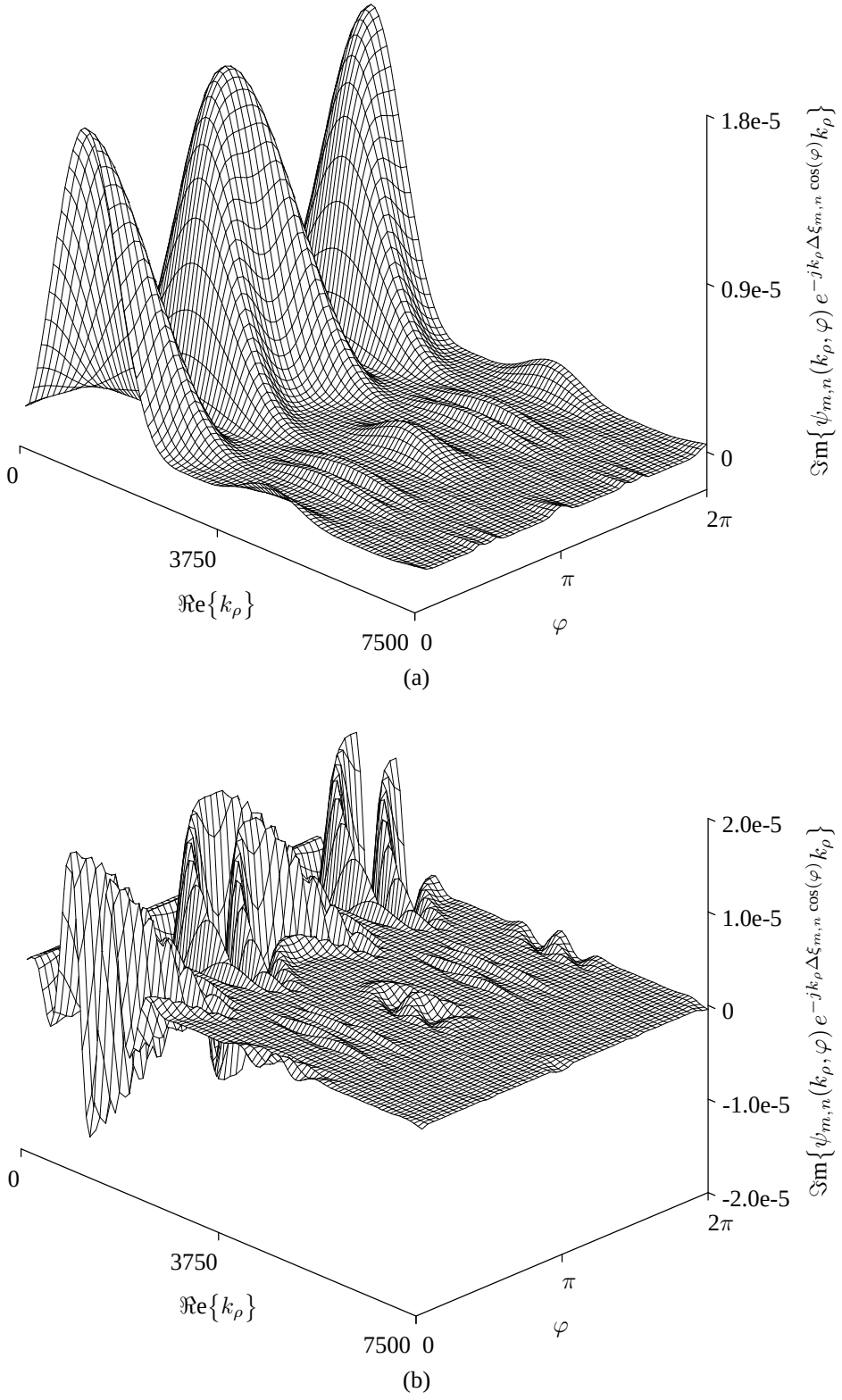

Figure 3.14 Integrand of $Z_{m,n}$, as a function of $\Re\mathrm{e}\{k_\rho\}$ (but evaluated over the deformed k_ρ integration contour) and φ, for rooftop basis and testing functions with: $\Delta l_{ns} = \Delta w_{ns} = \Delta l_{ms} = \Delta w_{ms}$ = 2 mm, $\phi_n = \phi_m = \vartheta = 0$, $h_{(1)}$ = 1.6 mm, $h_{(2)}$ = 15 mm, $\varepsilon_{r(0)} = \varepsilon_{r(2)} = 1$, $\varepsilon_{r(1)}$ = 4.25, $\tan\delta_{\varepsilon(0)} = \tan\delta_{\varepsilon(2)} = 0$, $\tan\delta_{\varepsilon(1)}$ = 0.02 and f = 1.8 GHz. (a) Completely overlapping basis and testing functions ($\Delta\xi_{m,n} = 0$). (b) Separated basis and testing functions with $\Delta\xi_{m,n}$ = 8 mm.

while the k_ξ integration contour should run up along the left-hand side of the negative imaginary k_ξ axis, go through the origin, go around the branch points and poles, and then come down the right-hand side of the negative imaginary k_ξ axis. This has the wanted effect that the shift exponential $e^{-jk_\xi \Delta\xi_{m,n}}$ decays to zero along the negative imaginary k_ξ axis.

For the purposes of this study, however, the integration contours as shown in Figure 3.15 were used instead. Now, before discussing the benefit of this choice, it has to be realised that the k_ξ and k_ζ integration contours cannot just be chosen at will and neither can they be considered independently. The k_ζ integration contour affects the location of the singularities in the complex k_ξ plane and therefore these two contours have to be considered simultaneously. The k_ζ integration contour, as shown in Figure 3.15(b), is basically similar to the one suggested by Sereno-Garino *et al.* and stays on the real k_ζ axis, except for small deformations to avoid singularities that would appear at the origin of the complex k_ξ plane when $k_{\rho,1} \leq k_\zeta \leq k_{\rho,2}$. The k_ξ integration contour, as shown in Figure 3.15(a), which consists of four parts, $\Gamma_{\xi,1}$, $\Gamma_{\xi,2}$, $\Gamma_{\xi,3}$ and $\Gamma_{\xi,4}$, mainly differs from the one suggested by Sereno-Garino *et al.* in that the $\Gamma_{\xi,1}$ and $\Gamma_{\xi,4}$ parts of the contour do not approach the negative imaginary k_ξ axis at the start and end points of the contour, but instead they move away from the negative imaginary k_ξ axis at angle of 45°. The reason for this choice will soon be explained.

First consider the behaviour of the integrand of $Z_{m,n}$ for two separated rooftop basis and testing functions over parts $\Gamma_{\xi,1}$, $\Gamma_{\xi,2}$, $\Gamma_{\xi,3}$ and $\Gamma_{\xi,4}$, as shown in Figures 3.16(a) to (d). From these figures it can be seen that the integrand is fairly smooth over k_ζ and that the corresponding integral can therefore be evaluated without much trouble. In order to motivate the usage of the k_ξ integration contour in Figure 3.15(a), consider the behaviour of the integrand in Figures 3.17(a) and (b). The integrand in Figure 3.17(a) is for the interaction between basis and testing functions with a small separation distance between them, while the integrand in Figure 3.17(b) is for the interaction between basis and testing functions with a larger separation distance between them. Now, as can be seen from these two figures, the integrand along the the negative imaginary k_ξ axis is only smooth for larger separation distances between basis and testing functions, but becomes very ragged for small separation distances (this behaviour also becomes more apparent for thicker substrates). This implies that the integration contour, as suggested by Sereno-Garino *et al.*, would be troublesome for small separation distances. However, in both Figures 3.17(a) and (b), it can be seen that the k_ξ integration contour in Figure 3.15(a) always result in a smooth integrand, regardless of the separation distance (except for overlap) between the basis and testing functions.

For numerical integration purposes, the k_ξ integration contour starts at $(-k_{\xi,\max}, -k_{\xi,\max})$ and ends at $(2k_{\rho,2} + k_{\xi,\max}, -k_{\xi,\max})$, while the k_ζ integration contour starts at $(-k_{\zeta,\max}, 0)$ and ends at $(k_{\zeta,\max}, 0)$. A value of $15/\Delta\xi_{m,n}$ for $k_{\xi,\max}$ has been found to work sufficiently well for all combinations of basis and testing functions, while the values for $k_{\zeta,\max}$ are summarised in Table 3.3. These have also been found through extensive numerical experimentation.

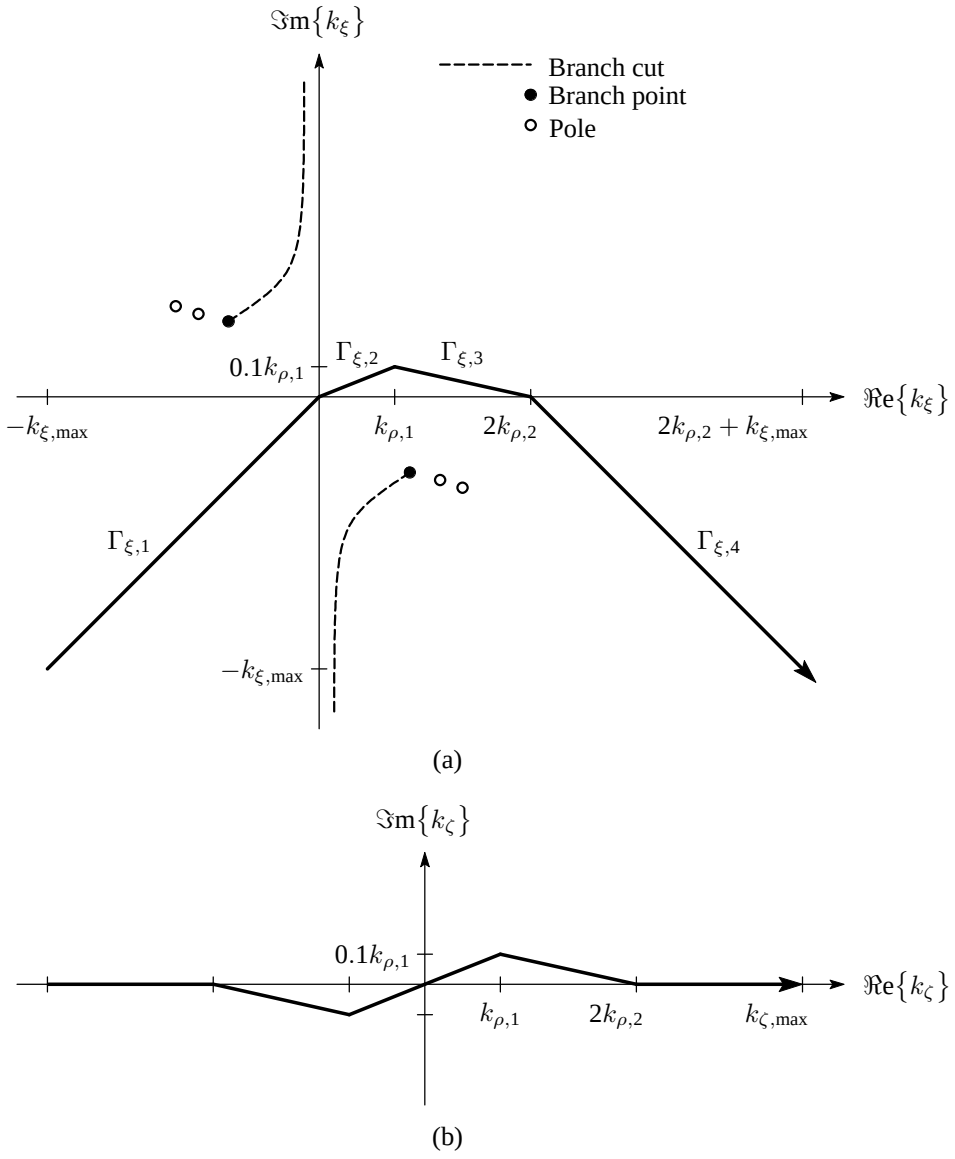

Figure 3.15 Integration path in the complex k_ξ and k_ζ planes for non-overlapping basis and testing functions. (a) The k_ξ plane. (b) The k_ζ plane.

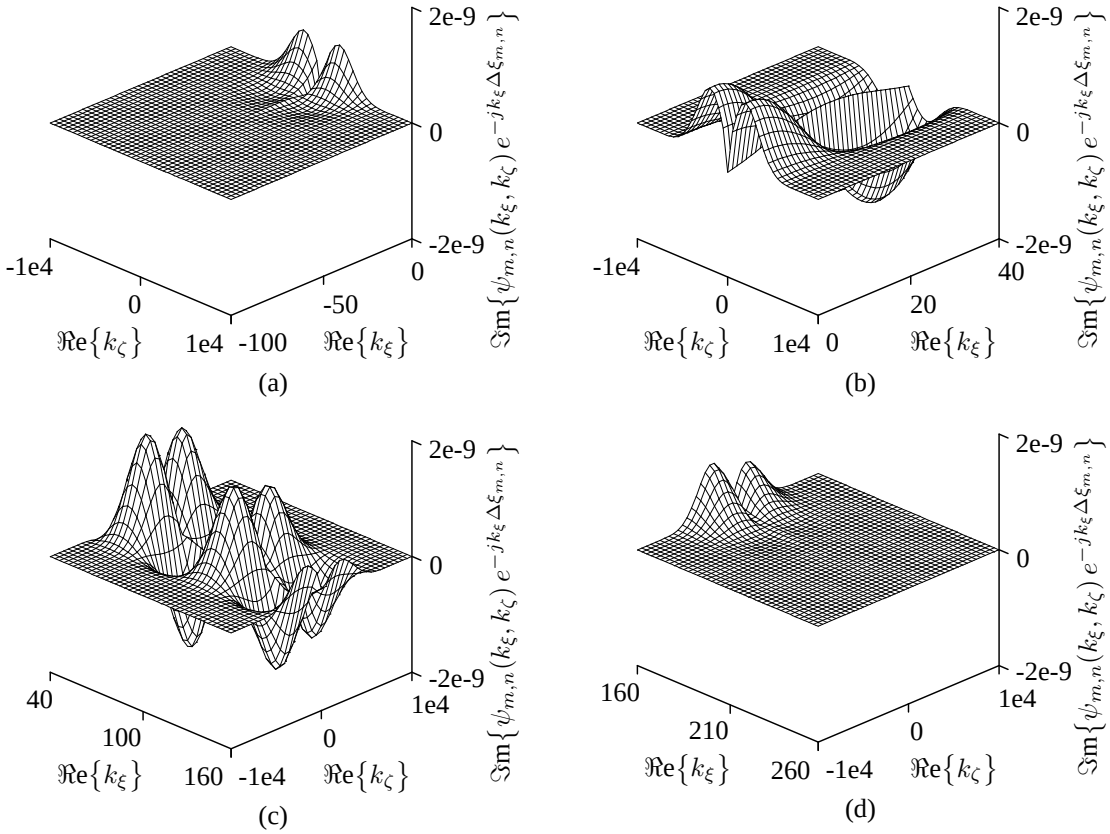

Figure 3.16 Integrand of $Z_{m,n}$, as a function of $\Re\mathrm{e}\{k_\xi\}$ and $\Re\mathrm{e}\{k_\zeta\}$ (but evaluated over the deformed k_ζ integration contour), for rooftop basis and testing functions with: $\Delta l_{ns} = \Delta w_{ns} = \Delta l_{ms} = \Delta w_{ms} = 1$ mm, $\phi_n = \phi_m = 0$, $\vartheta = 45°$, $\Delta\xi_{m,n} = 113.14$ mm, $h_{(1)} = 1.6$ mm, $h_{(2)} = 15$ mm, $\varepsilon_{r(0)} = \varepsilon_{r(2)} = 1$, $\varepsilon_{r(1)} = 4$, $\tan\delta_{\varepsilon(0)} = \tan\delta_{\varepsilon(1)} = \tan\delta_{\varepsilon(2)} = 0$ and $f = 1.91$ GHz. (a) $\Gamma_{\xi,1}$ part of k_ξ integration contour. (b) $\Gamma_{\xi,2}$ part of k_ξ integration contour. (c) $\Gamma_{\xi,3}$ part of k_ξ integration contour. (d) $\Gamma_{\xi,4}$ part of k_ξ integration contour.

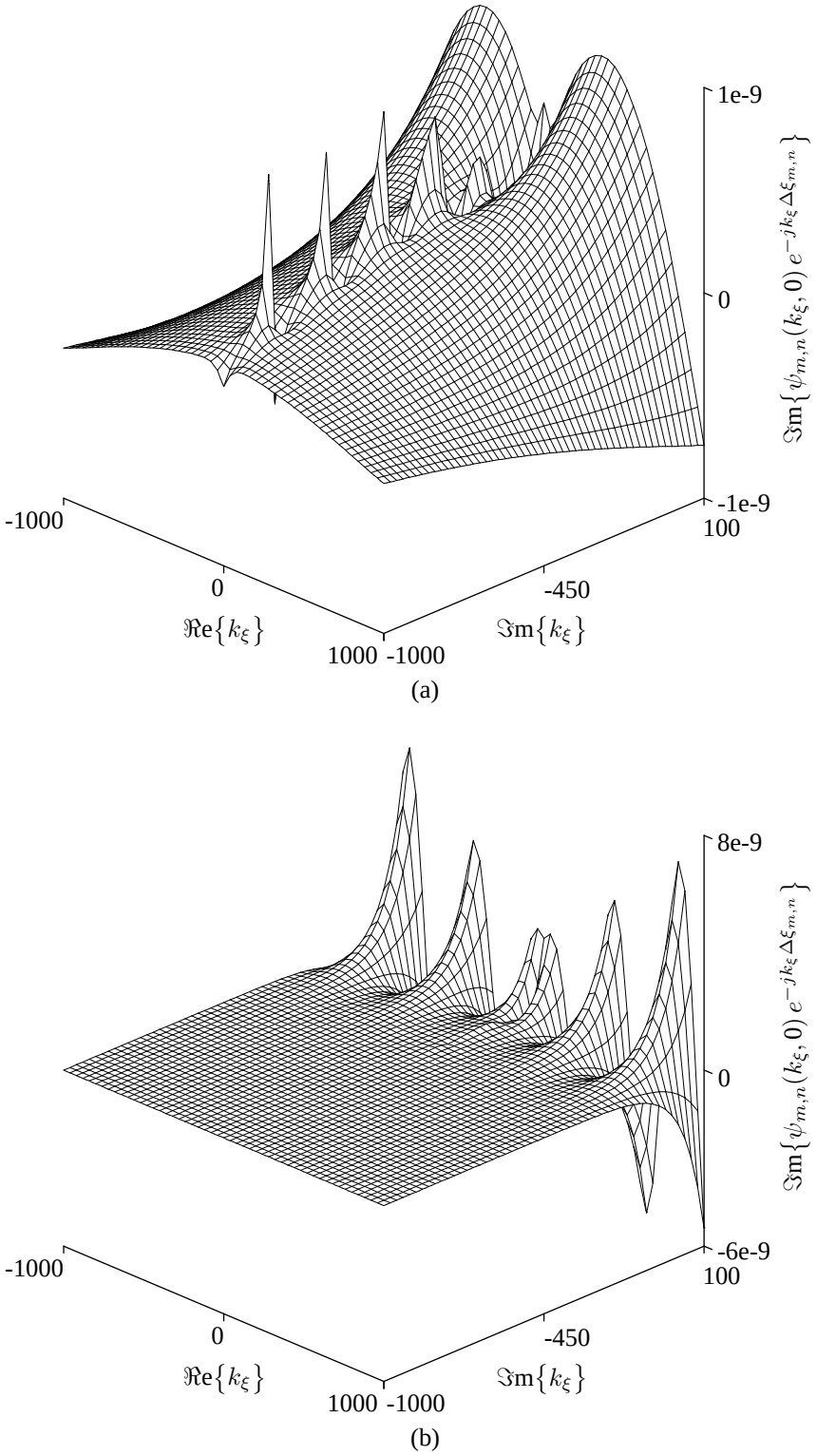

Figure 3.17 Integrand of $Z_{m,n}$ over the complex k_ξ plane (at $k_\zeta = 0$) for rooftop basis and testing functions with: $\Delta l_{ns} = \Delta w_{ns} = \Delta l_{ms} = \Delta w_{ms} = 1$ mm, $\phi_n = \phi_m = 0$, $\vartheta = 45°$, $h_{(1)} = 1.6$ mm, $h_{(2)} = 15$ mm, $\varepsilon_{r(0)} = \varepsilon_{r(2)} = 1$, $\varepsilon_{r(1)} = 4$, $\tan\delta_{\varepsilon(0)} = \tan\delta_{\varepsilon(1)} = \tan\delta_{\varepsilon(2)} = 0$ and $f = 1.91$ GHz. (a) Closely-spaced basis and testing functions with $\Delta\xi_{m,n} = 2.83$ mm. (b) Widely-separated basis and testing functions with $\Delta\xi_{m,n} = 21.21$ mm.

Table 3.3
Value of $k_{\zeta,\max}$ for (k_ξ, k_ζ) integration.

Interaction	$k_{\zeta,\max}$
$Z^{PZ,PZ}_{mp:mz,np:nz}$	not applicable
$Z^{PZ,A}_{mp:mz,na}$	not applicable
$Z^{A,A}_{ma,na}$	not applicable
$Z^{PZ,SU}_{mp:mz,ns:nu}$	$\max\{\min[\min(200/\sqrt{a_{mp}}, 4\pi/\min(\Delta l_{ns}, \Delta w_{ns})), 20/\lvert z_{mp}-z_{ns}\rvert], 4k_{\rho,2}\}$
$Z^{A,SU}_{ma,ns:nu}$	$\max\{\min[\min(200/\sqrt{a_{mp}}, 4\pi/\min(\Delta l_{ns}, \Delta w_{ns})), 20/\lvert z_{mp}-z_{ns}\rvert], 4k_{\rho,2}\}$
$Z^{SU,SU}_{ms:mu,ns:nu}$	$\max\{\min[4\pi/\min(\Delta l_{ms}, \Delta w_{ms}, \Delta l_{ns}, \Delta w_{ns}), 20/\lvert z_{mp}-z_{ns}\rvert], 4k_{\rho,2}\}$
$Z^{PZ,SV}_{mp:mz,ns:nv}$	$\max\{\min[\min(200/\sqrt{a_{mp}}, 4\pi/\min(\Delta l_{ns}, \Delta w_{ns})), 20/\lvert z_{mp}-z_{ns}\rvert], 4k_{\rho,2}\}$
$Z^{A,SV}_{ma,ns:nv}$	$\max\{\min[\min(200/\sqrt{a_{mp}}, 4\pi/\min(\Delta l_{ns}, \Delta w_{ns})), 20/\lvert z_{mp}-z_{ns}\rvert], 4k_{\rho,2}\}$
$Z^{SU,SV}_{ms:mu,ns:nv}$	$\max\{\min[4\pi/\min(\Delta l_{ms}, \Delta w_{ms}, \Delta l_{ns}, \Delta w_{ns}), 20/\lvert z_{mp}-z_{ns}\rvert], 4k_{\rho,2}\}$
$Z^{SV,SV}_{ms:mv,ns:nv}$	$\max\{\min[4\pi/\min(\Delta l_{ms}, \Delta w_{ms}, \Delta l_{ns}, \Delta w_{ns}), 20/\lvert z_{mp}-z_{ns}\rvert], 4k_{\rho,2}\}$
$Z^{PZ,EU}_{mp:mz,ne:nu}$	$\max\{\min[\min(200/\sqrt{a_{mp}}, 2\pi\sqrt{(p^{EU}_{ne:nu}\pi/L_{ne})^2+(q^{EU}_{ne:nu}\pi/W_{ne})^2}$ $+20\pi^2\sqrt{(1/L_{ne})^2+(1/W_{ne})^2}), 20/\lvert z_{mp}-z_{ne}\rvert], 4k_{\rho,2}\}$
$Z^{A,EU}_{na,me:mu}$	$\max\{\min[\min(200/\sqrt{a_{mp}}, 2\pi\sqrt{(p^{EU}_{ne:nu}\pi/L_{ne})^2+(q^{EU}_{ne:nu}\pi/W_{ne})^2}$ $+20\pi^2\sqrt{(1/L_{ne})^2+(1/W_{ne})^2}), 20/\lvert z_{ma}-z_{ne}\rvert], 4k_{\rho,2}\}$
$Z^{SU,EU}_{ms:mu,ne:nu}$	$\max\{\min[\min(4\pi/\Delta l_{ms}, 2\pi\sqrt{(p^{EU}_{ne:nu}\pi/L_{ne})^2+(q^{EU}_{ne:nu}\pi/W_{ne})^2}$ $+20\pi^2\sqrt{(1/L_{ne})^2+(1/W_{ne})^2}), 20/\lvert z_{ms}-z_{ne}\rvert], 4k_{\rho,2}\}$
$Z^{SV,EU}_{ms:mv,ne:nu}$	$\max\{\min[\min(4\pi/\Delta w_{ms}, 2\pi\sqrt{(p^{EU}_{ne:nu}\pi/L_{ne})^2+(q^{EU}_{ne:nu}\pi/W_{ne})^2}$ $+20\pi^2\sqrt{(1/L_{ne})^2+(1/W_{ne})^2}), 20/\lvert z_{ms}-z_{ne}\rvert], 4k_{\rho,2}\}$
$Z^{EU,EU}_{me:mu,ne:nu}$	$\max\{\min[\max(2\pi\sqrt{(p^{EU}_{me:mu}\pi/L_{ne})^2+(q^{EU}_{me:mu}\pi/W_{ne})^2},$ $2\pi\sqrt{(p^{EU}_{ne:nu}\pi/L_{ne})^2+(q^{EU}_{ne:nu}\pi/W_{ne})^2})$ $+20\pi^2\sqrt{(1/L_{ne})^2+(1/W_{ne})^2}, 20/\lvert z_{me}-z_{ne}\rvert], 4k_{\rho,2}\}$
$Z^{PZ,EV}_{mp:mz,ne:nv}$	$\max\{\min[\min(200/\sqrt{a_{mp}}, 2\pi\sqrt{(p^{EV}_{ne:nv}\pi/W_{ne})^2+(q^{EV}_{ne:nv}\pi/L_{ne})^2}$ $+20\pi^2\sqrt{(1/L_{ne})^2+(1/W_{ne})^2}), 20/\lvert z_{mp}-z_{ne}\rvert], 4k_{\rho,2}\}$
$Z^{A,EV}_{na,me:mv}$	$\max\{\min[\min(200/\sqrt{a_{mp}}, 2\pi\sqrt{(p^{EV}_{ne:nv}\pi/W_{ne})^2+(q^{EV}_{ne:nv}\pi/L_{ne})^2}$ $+20\pi^2\sqrt{(1/L_{ne})^2+(1/W_{ne})^2}), 20/\lvert z_{ma}-z_{ne}\rvert], 4k_{\rho,2}\}$
$Z^{SU,EV}_{ms:mu,ne:nv}$	$\max\{\min[\min(4\pi/\Delta l_{ms}, 2\pi\sqrt{(p^{EV}_{ne:nv}\pi/W_{ne})^2+(q^{EV}_{ne:nv}\pi/L_{ne})^2}$ $+20\pi^2\sqrt{(1/L_{ne})^2+(1/W_{ne})^2}), 20/\lvert z_{ms}-z_{ne}\rvert], 4k_{\rho,2}\}$
$Z^{SV,EV}_{ms:mv,ne:nv}$	$\max\{\min[\min(4\pi/\Delta w_{ms}, 2\pi\sqrt{(p^{EV}_{ne:nv}\pi/W_{ne})^2+(q^{EV}_{ne:nv}\pi/L_{ne})^2}$ $+20\pi^2\sqrt{(1/L_{ne})^2+(1/W_{ne})^2}), 20/\lvert z_{ms}-z_{ne}\rvert], 4k_{\rho,2}\}$
$Z^{EU,EV}_{me:mu,ne:nv}$	$\max\{\min[\max(2\pi\sqrt{(p^{EU}_{me:mu}\pi/L_{ne})^2+(q^{EU}_{me:mu}\pi/W_{ne})^2},$ $2\pi\sqrt{(p^{EV}_{ne:nv}\pi/W_{ne})^2+(q^{EV}_{ne:nv}\pi/L_{ne})^2})$ $+20\pi^2\sqrt{(1/L_{ne})^2+(1/W_{ne})^2}, 20/\lvert z_{me}-z_{ne}\rvert], 4k_{\rho,2}\}$
$Z^{EV,EV}_{me:mv,ne:nv}$	$\max\{\min[\max(2\pi\sqrt{(p^{EV}_{me:mv}\pi/W_{ne})^2+(q^{EV}_{me:mv}\pi/L_{ne})^2},$ $2\pi\sqrt{(p^{EV}_{ne:nv}\pi/W_{ne})^2+(q^{EV}_{ne:nv}\pi/L_{ne})^2})$ $+20\pi^2\sqrt{(1/L_{ne})^2+(1/W_{ne})^2}, 20/\lvert z_{me}-z_{ne}\rvert], 4k_{\rho,2}\}$

Note: the terms containing $|z_m - z_n|$ should only be used if $|z_m - z_n| \neq 0$.

For the actual implementation of this method, adaptive Romberg integration was used for the evaluation of the inner integral, which is defined in (3.167). The evaluation of the outer integral, as defined in (3.166), can also be accelerated, especially over parts $\Gamma_{\xi,2}$ and $\Gamma_{\xi,3}$ of the k_ξ integration contour where $\Psi_{m,n}(k_\xi)e^{-jk_\xi\Delta\xi_{m,n}}$ can be very oscillatory for large separation distances. Due to the fact that $\Psi_{m,n}(k_\xi)$ has a smooth behaviour over the k_ξ integration contour, it can be approximated with cubic-spline interpolation over each part of the k_ξ integration contour and the integration can therefore be carried out analytically. If $\Psi_{m,n}(k_\xi)$ is evaluated in a reduced set of points, then between the points k_{ξ_i} and $k_{\xi_{i+1}}$, $\Psi_{m,n}(k_\xi)$ can be approximated as

$$\Psi_{m,n}(k_\xi) \simeq A_i\big(k_\xi - k_{\xi_i}\big)^3 + B_i\big(k_\xi - k_{\xi_i}\big)^2 + C_i\big(k_\xi - k_{\xi_i}\big) + D_i, \tag{3.168}$$

where A_i, B_i, C_i and D_i are the cubic-spline coefficients. The integral of $\Psi_{m,n}(k_\xi)e^{-jk_\xi\Delta\xi_{m,n}}$, over the interval between k_{ξ_i} and $k_{\xi_{i+1}}$, can then be evaluated as

$$\begin{aligned}
&\int_{k_{\xi_i}}^{k_{\xi_{i+1}}} \Psi_{m,n}(k_\xi)\, e^{-jk_\xi\Delta\xi_{m,n}}\, dk_\xi \\
&\simeq \int_{k_{\xi_i}}^{k_{\xi_{i+1}}} \left[A_i\big(k_\xi - k_{\xi_i}\big)^3 + B_i\big(k_\xi - k_{\xi_i}\big)^2 + C_i\big(k_\xi - k_{\xi_i}\big) + D_i\right] e^{-jk_\xi\Delta\xi_{m,n}}\, dk_\xi \\
&= \left\{A_i\left[\frac{-(k_{\xi_{i+1}} - k_{\xi_i})^3}{j\Delta\xi_{m,n}} + \frac{3(k_{\xi_{i+1}} - k_{\xi_i})^2}{(\Delta\xi_{m,n})^2} + \frac{6(k_{\xi_{i+1}} - k_{\xi_i})}{j(\Delta\xi_{m,n})^3} - \frac{6}{(\Delta\xi_{m,n})^4}\right]\right. \\
&\quad + B_i\left[\frac{-(k_{\xi_{i+1}} - k_{\xi_i})^2}{j\Delta\xi_{m,n}} + \frac{2(k_{\xi_{i+1}} - k_{\xi_i})}{(\Delta\xi_{m,n})^2} + \frac{2}{j(\Delta\xi_{m,n})^3}\right] + C_i\left[\frac{-(k_{\xi_{i+1}} - k_{\xi_i})}{j\Delta\xi_{m,n}} + \frac{1}{(\Delta\xi_{m,n})^2}\right] \\
&\quad \left. + D_i\left[\frac{-1}{j\Delta\xi_{m,n}}\right]\right\} e^{-jk_{\xi_i}\Delta\xi_{m,n}}\, e^{-j(k_{\xi_{i+1}} - k_{\xi_i})\Delta\xi_{m,n}} \\
&\quad - \left\{A_i\left[\frac{-6}{(\Delta\xi_{m,n})^4}\right] + B_i\left[\frac{2}{j(\Delta\xi_{m,n})^3}\right] + C_i\left[\frac{1}{(\Delta\xi_{m,n})^2}\right] + D_i\left[\frac{-1}{j\Delta\xi_{m,n}}\right]\right\} e^{-jk_{\xi_i}\Delta\xi_{m,n}}.
\end{aligned} \tag{3.169}$$

After some numerical experimentation, it was found that the number of interpolation points that are required for sufficient accuracy, amounts to 16 on parts $\Gamma_{\xi,1}$ and $\Gamma_{\xi,4}$ of the k_ξ integration contour, while 6 points are needed on parts $\Gamma_{\xi,2}$ and $\Gamma_{\xi,3}$. Another observation regarding $\Psi_{m,n}(k_\xi)$, is that it is not dependent on the separation distance $\Delta\xi_{m,n}$, and therefore it only has to be computed once. Thereafter it can be used with any value of $\Delta\xi_{m,n}$, provided that the relative alignment of the basis and testing functions stays the same. This is often the case when analysing antenna arrays.

An important point, that has to be kept in mind when using this integration technique, is that it cannot be used for the case where there is any overlap between the basis and testing functions. The reason therefore is that the shift exponential does not decay to zero in the negative imaginary k_ξ plane, but instead grows exponentially. Sereno-Garino *et al.* pointed out that there should be no physical overlap between the basis and testing functions when using this method. However, during

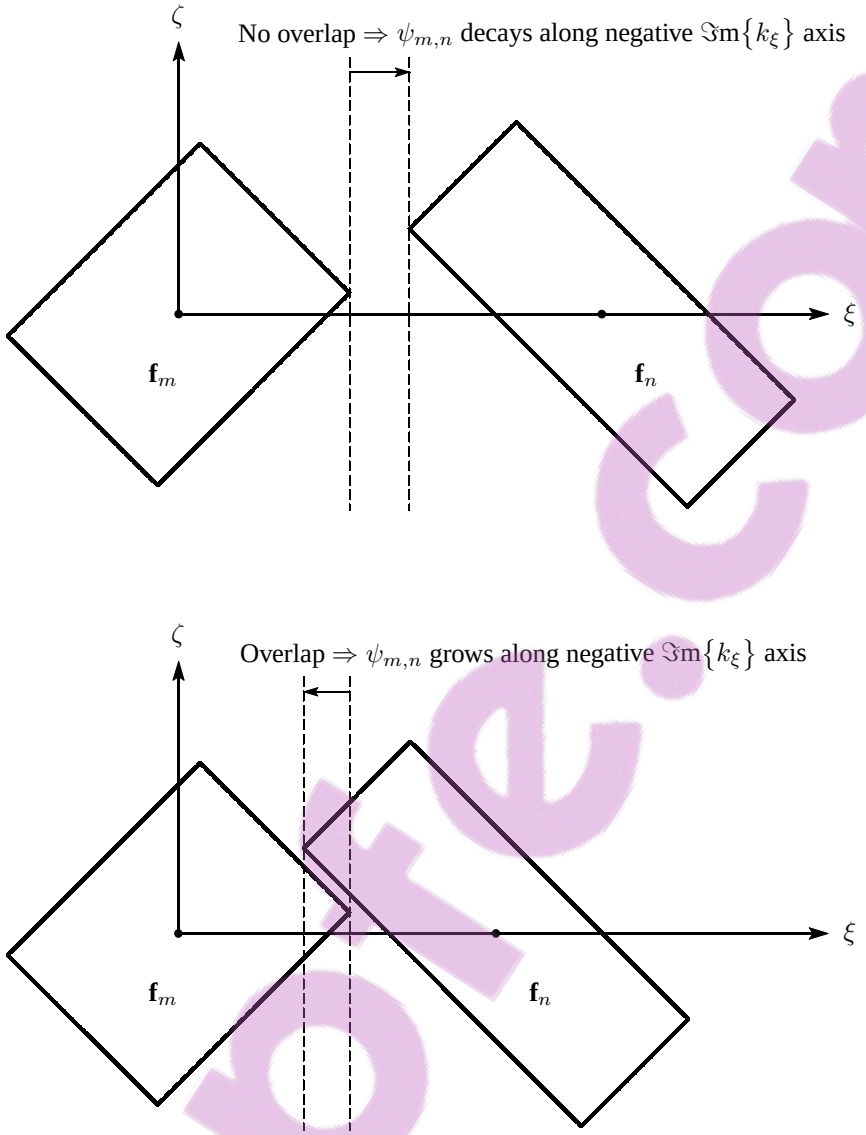

Figure 3.18 Condition for integration along the negative imaginary k_ξ axis.

this study, it has been found that this condition alone is not sufficient. It has been found, through numerical experimentation, that for this integration technique to work, there should be no overlap between the basis and testing functions in the ξ direction. This is illustrated in Figure 3.18, where it can be seen that, although there might not be any physical overlap between the two functions, it is still possible to have overlap in the ξ direction. Note that this situation does not occur for basis and testing functions with circular support, but only occurs when one of the functions does not have circular support. In such a situation, one would be forced to use the less efficient integration method in Section 3.9.1.

Even though this technique is much more efficient than the one in the previous section, for basis and testing functions that are widely separated, there is still a more efficient method for axisymmetric functions. This will now be addressed in the section that follows.

3.9.3 Integration Strategy for Separated Axisymmetric Basis and Testing Functions

The interaction integrals for axisymmetric basis and testing functions that are separated, can be evaluated very efficiently. These functions include the PWS basis functions on the probes, as well as the circular attachment modes. They are both characterised by the fact that, in a polar coordinate system, they have no angular variation (i.e. they are only functions of k_ρ). The advantage of this is that the double integrals in (3.162) can be reduced to a single integral.

For basis and testing functions with no angular variation (note that the Green's function has no angular variation either), the expression in (3.162) can be written as

$$Z_{m,n} = \frac{1}{4\pi^2} \int_0^{2\pi} \int_0^{\infty} \psi_{m,n}(k_\rho)\, e^{-jk_\rho \Delta\xi_{m,n} \cos(\varphi)} k_\rho \, dk_\rho d\varphi. \tag{3.170}$$

Then, by realising that

$$J_0(k_\rho \Delta\xi_{m,n}) = \frac{1}{2\pi} \int_0^{2\pi} e^{-jk_\rho \Delta\xi_{m,n} \cos(\varphi)} \, d\varphi, \tag{3.171}$$

(3.170) can be reduced to

$$Z_{m,n} = \frac{1}{2\pi} \int_0^{\infty} \psi_{m,n}(k_\rho) J_0(k_\rho \Delta\xi_{m,n}) k_\rho \, dk_\rho. \tag{3.172}$$

The integrand in (3.172) can be broken up into of a smooth part, $\psi_{m,n}(k_\rho)k_\rho$, as well as an oscillating part, $J_0(k_\rho \Delta\xi_{m,n})$. Such integrals can be evaluated very efficiently by using the *method of averages* [146,177]. With this method, the integral is approximated by a summation of integrations over half cycles of the integrand. An acceleration device, such as Shanks' nonlinear transformation, is then used to speed up the summation. The deformed integration contour of Figure 3.13 is also used in this case.

An additional method that can be used to speed up the overall analysis, is to identify all entries in the interaction matrix that are duplicates and to avoid calculating them more than once. This will now be addressed in the section that follows.

3.10 IDENTIFICATION OF DUPLICATE ENTRIES IN THE INTERACTION MATRIX

Usually, there are many entries in the interaction matrix that are duplicates. This is especially so when an antenna array is analysed. A tremendous amount of computational time can be saved if these entries are identified beforehand and not calculated more than once. In Section 3.7, it has already been pointed out that the interaction matrix is symmetric and that close to half of the entries need not be calculated right from the outset. Depending on the antenna geometry and choice of basis functions, the remaining number of entries that has to be calculated, can further be

reduced by an order of magnitude or so.

As have been shown in Section 3.7, the interaction matrix consists of a number of submatrices where each submatrix contains the entries associated with a specific combination of basis and testing functions. The process of finding the duplicate entries is implemented by first initialising all the entries in the interaction matrix. A set of certain geometric parameters is then calculated for the first entry in a specific submatrix. This entry then becomes the reference entry. The same set of parameters is now calculated in turn for every other entry in the submatrix. Wherever these two sets correspond, the address of the reference entry is stored in the other entry's location. After the geometric parameters of all the entries in the submatrix have been compared to that of the reference entry, the reference entry is changed to the second entry (or to the next entry where an address of a reference entry has not been stored yet) in the submatrix and the process of comparing the geometric parameters of the other entries to that of the reference entry, is repeated again for each remaining entry. Of course, if an address of a reference entry has already been stored for a specific entry, that entry does not have to be checked again. Also, the number of entries that have to be checked against the reference entry, becomes smaller as the process is repeated, due to the fact that the previous reference entries do not have to be checked again. This process, as has just been described, is followed for each submatrix in the interaction matrix. Finally, only the entries with no address information are actually calculated, while the other values are simply fetched from the corresponding address that is stored in that entry's location. The process of finding all the duplicate entries only have to be performed once as it is independent of frequency. It is therefore advisable to store the matrix with the address information off line so that it can be reused again.

It is possible that some entries in one submatrix can correspond to entries in another submatrix. Therefore, some of the submatrices are grouped together during the process of finding the duplicate entries. The submatrices that can be grouped together are:

- $\left[Z^{PZ,SU}_{mp:mz,ns:nu}\right]$ and $\left[Z^{PZ,SV}_{mp:mz,ns:nv}\right]$;
- $\left[Z^{A,SU}_{ma,ns:nu}\right]$ and $\left[Z^{A,SV}_{ma,ns:nv}\right]$;
- $\left[Z^{PZ,EU}_{mp:mz,ne:nu}\right]$ and $\left[Z^{PZ,EV}_{mp:mz,ne:nv}\right]$;
- $\left[Z^{A,EU}_{ma,ne:nu}\right]$ and $\left[Z^{A,EV}_{ma,ne:nv}\right]$;
- $\left[Z^{SU,SU}_{ms:mu,ns:nu}\right]$, $\left[Z^{SU,SV}_{ms:mu,ns:nv}\right]$ and $\left[Z^{SV,SV}_{ms:mv,ns:nv}\right]$;
- $\left[Z^{SU,EU}_{ms:mu,ne:nu}\right]$, $\left[Z^{SU,EV}_{ms:mu,ne:nv}\right]$, $\left[Z^{SV,EU}_{ms:mv,ne:nu}\right]$ and $\left[Z^{SV,EV}_{ms:mv,ne:nv}\right]$;
- $\left[Z^{EU,EU}_{me:mu,ne:nu}\right]$, $\left[Z^{EU,EV}_{me:mu,ne:nv}\right]$ and $\left[Z^{EV,EV}_{me:mv,ne:nv}\right]$.

All the interaction-matrix entries can basically be divided into three groups for the purpose of finding the duplicate entries. Firstly, there are entries for which both the basis and testing functions are axisymmetric. These include the $Z^{PZ,PS}_{mp:mz,np:nz}$, $Z^{PZ,A}_{mp:mz,na}$ and $Z^{A,A}_{ma,na}$ entries. Secondly, there are entries for which the basis functions have rectangular support, and for which the testing func-

tions are axisymmetric. These include the $Z^{PZ,SU}_{mp:mz,ns:nu}$, $Z^{PZ,SV}_{mp:mz,ns:nv}$, $Z^{A,SU}_{ma,ns:nu}$ and $Z^{A,SV}_{ma,ns:nv}$ entries. Thirdly and finally, there are entries for which both the basis and testing functions have rectangular support. These include the $Z^{SU,SU}_{ms:mu,ns:nu}$, $Z^{SU,SV}_{ms:mu,ns:nv}$ and $Z^{SV,SV}_{ms:mv,ns:nv}$ entries, the $Z^{SU,EU}_{ms:mu,ne:nu}$, $Z^{SU,EV}_{ms:mu,ne:nv}$, $Z^{SV,EU}_{ms:mv,ne:nu}$ and $Z^{SV,EV}_{ms:mv,ne:nv}$ entries, as well as the $Z^{EU,EU}_{me:mu,ne:nu}$, $Z^{EU,EV}_{me:mu,ne:nv}$ and $Z^{EV,EV}_{me:mv,ne:nv}$ entries. The algorithms that were developed to determine whether two entries are duplicates, are not trivial and therefore each of them, together with the geometric parameters that need to be compared for entries in each of the three groups, will be discussed separately.

Before the different algorithms are discussed, it is necessary to define two new functions that will be used. The first one is $\text{ang}_{\pm\pi}(\phi)$. It takes the angle ϕ as argument and returns the same angle, but limited between $-\pi$ and π. The function can be defined as

$$\text{ang}_{\pm\pi}(\phi) = \begin{cases} \phi - 2\pi \,\text{int}\left(\dfrac{\phi}{2\pi}\right) - 2\pi, & \phi - 2\pi \,\text{int}\left(\dfrac{\phi}{2\pi}\right) > \pi \\ \phi - 2\pi \,\text{int}\left(\dfrac{\phi}{2\pi}\right) + 2\pi, & \phi - 2\pi \,\text{int}\left(\dfrac{\phi}{2\pi}\right) \leq -\pi \\ \phi, & \text{otherwise.} \end{cases} \tag{3.173}$$

The second function, $\text{and}_{\pm 1}(a, b)$, is a special "and" function that takes two arguments, a and b. The function is defined as

$$\text{and}_{\pm 1}(a, b) = \begin{cases} 1, & |a| = 0,\ |b| = 0 \\ 1, & |a| > 0,\ |b| > 0 \\ -1, & \text{otherwise.} \end{cases} \tag{3.174}$$

3.10.1 Interaction between Axisymmetric Functions

The identification of duplicate interaction-matrix entries, where both basis and testing functions are axisymmetric, is the most simple case of all. Let $Z_{m,n}$ be the reference entry and $Z_{m',n'}$ the entry being compared to the reference entry. Furthermore, let a_m and a_n be the radii of the testing and basis functions associated with $Z_{m,n}$, while $a_{m'}$ and $a_{n'}$ are associated with $Z_{m',n'}$. The testing and basis functions associated with $Z_{m,n}$, are located at z_m and z_n along the z direction, while those associated with $Z_{m,n}$, are located at $z_{m'}$ and $z_{n'}$. For $Z_{m,n}$, the separation distance between basis and testing functions is $\Delta\xi_{m,n}$, while for $Z_{m',n'}$, the separation distance is $\Delta\xi_{m',n'}$. The interactions $Z_{m',n'}$ and $Z_{m,n}$, can then be checked for equality through the following algorithm:

IF $\Delta\xi_{m',n'} = \Delta\xi_{m,n}$ THEN

  IF $(z_{m'} = z_m$ AND $z_{n'} = z_n)$ OR $(z_{m'} = z_n$ AND $z_{n'} = z_m)$ THEN

    IF $(a_{m'} = a_m$ AND $a_{n'} = a_n)$ OR $(a_{m'} = a_n$ AND $a_{n'} = a_m)$ THEN

    $\boxed{Z_{m',n'} \Leftarrow Z_{m,n}}$

END IF

END IF

END IF

3.10.2 Interaction between Axisymmetric Functions and Functions with Rectangular Support

Figure 3.19 shows the reference interaction $Z_{m,n}$ and the interaction $Z_{m',n'}$ being compared to the reference interaction for the case where the testing function is axisymmetric and where the basis function has rectangular support. Once again, let a_m be the radius of the testing function associated with $Z_{m,n}$, and $a_{m'}$ the radius of the testing function associated with $Z_{m',n'}$. The dimensions of the rectangular patch associated with $Z_{m,n}$, are L_n and W_n, while those associated with $Z_{m',n'}$, are $L_{n'}$ and $W_{n'}$. The angles ϑ_n and $\vartheta_{n'}$, correspond to those in Figure 3.12. The testing and basis functions associated with $Z_{m,n}$, are located at z_m and z_n along the z direction, while those associated with $Z_{m,n}$, are located at $z_{m'}$ and $z_{n'}$. For $Z_{m,n}$, the separation distance between basis and testing functions is $\Delta\xi_{m,n}$, while for $Z_{m',n'}$, the separation distance is $\Delta\xi_{m',n'}$. Furthermore, (p_n, q_n) is the set of modes on the basis function associated with $Z_{m,n}$, while $(p_{n'}, q_{n'})$ is the set of modes on the basis function associated with $Z_{m',n'}$. The interactions $Z_{m',n'}$ and $Z_{m,n}$, can then be checked for equality through the following algorithm:

IF $\Delta\xi_{m',n'} = \Delta\xi_{m,n}$ THEN

IF $(z_{m'} = z_m$ AND $z_{n'} = z_n)$ THEN

IF $a_{m'} = a_m$ AND $L_{n'} = L_n$ AND $W_{n'} = W_n$ AND $p_{n'} = p_n$ AND $q_{n'} = q_n$ THEN

IF $|\text{ang}_{\pm\pi}(\vartheta_{n'}) - \text{ang}_{\pm\pi}(\vartheta_n)| = (0$ OR $\pi)$ THEN

IF $(p_{n'} + q_{n'})$ mod $2 = 0$ THEN

SIGN $\Leftarrow 1$

ELSE

SIGN $\Leftarrow \text{and}_{\pm 1}(|\text{ang}_{\pm\pi}(\vartheta_{n'}) - \text{ang}_{\pm\pi}(\vartheta_n)|, 0)$

END IF

$\boxed{Z_{m',n'} \Leftarrow \text{SIGN} \cdot Z_{m,n}}$

ELSE IF $|\text{ang}_{\pm\pi}(\vartheta_{n'}) + \text{ang}_{\pm\pi}(\vartheta_n)| = (0$ OR $\pi)$ THEN

IF $(p_{n'} + q_{n'})$ mod $2 = 0$ THEN

SIGN $\Leftarrow 1$

ELSE

SIGN $\Leftarrow \text{and}_{\pm 1}(|\text{ang}_{\pm\pi}(\vartheta_{n'}) + \text{ang}_{\pm\pi}(\vartheta_n)|, 0)$

END IF

SIGN $\Leftarrow \text{SIGN} \cdot \text{and}_{\pm 1}(q_{n'}$ mod $2, 0)$

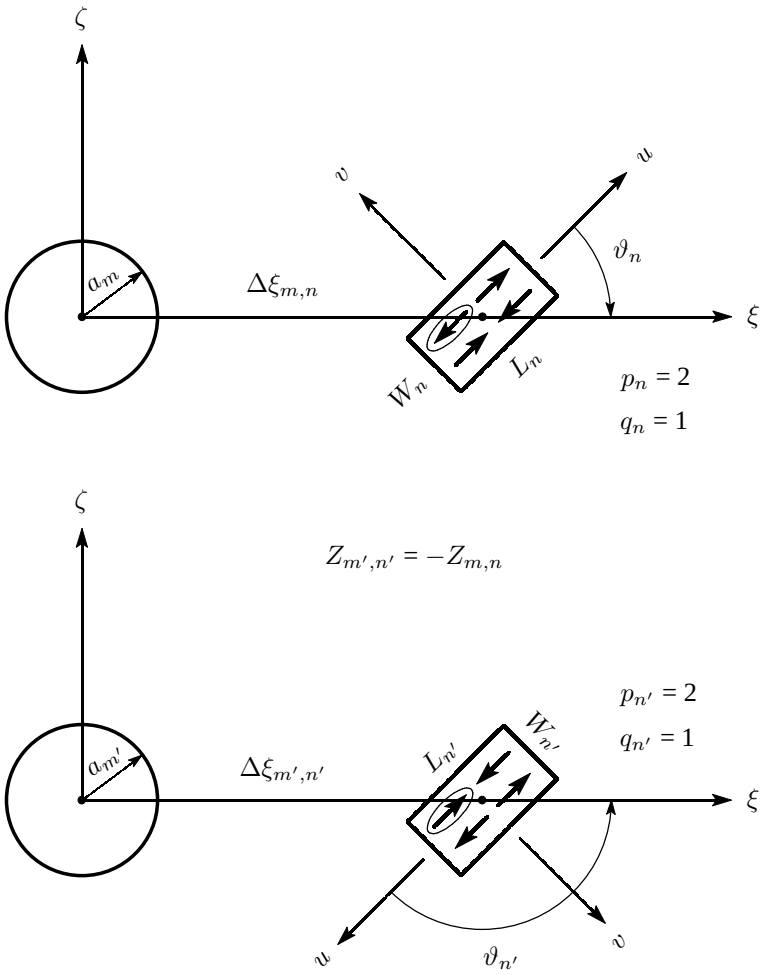

Figure 3.19 Checking $Z_{m',n'}$ and $Z_{m,n}$ for equality where axisymmetric basis functions and basis functions with rectangular support are involved.

$$\boxed{Z_{m',n'} \Leftarrow \text{SIGN} \cdot Z_{m,n}}$$

END IF

END IF

END IF

END IF

To visually illustrate what this algorithm does, consider the situation depicted in Figure 3.19. It can be seen that the circled current component (which is the nearest current component to the axisymmetric function) associated with the $Z_{m,n}$ interaction, points towards a fictitious line that is orthogonal to itself and that goes through the centre of the testing function. On the other hand, the circled current component associated with the $Z_{m',n'}$ interaction, points away from a similar virtual line. Given that the other dimensions, modes and angles correspond, $Z_{m,n}$ is therefore equal to $-Z_{m',n'}$. Furthermore, if $\Delta\xi_{m,n} = 0$ and $\Delta\xi_{m',n'} = 0$, and given that all the relevant

dimension, mode and angle requirements are satisfied in the algorithm, $Z_{m,n}$ is always equal to $Z_{m',n'}$, and the SIGN does not need to be calculated.

Another point that has to be noted here is that, for the purposes of this algorithm, a subdomain rooftop basis function can be considered to be a special case of the entire-domain sinusoidal basis function with the $(p = 1, q = 0)$ set of modes. Also, as have been noted earlier on, there are submatrices in the interaction matrix with entries that are equal. In this case, for example, the $Z_{m,n}$ interaction can be that between a circular attachment mode and a u-directed entire-domain sinusoidal basis function, while the $Z_{m',n'}$ interaction can be that between a circular attachment mode and a v-directed entire-domain sinusoidal basis function. Now, in the previous algorithm, if the basis function associated with $Z_{m,n}$, is u-directed, while the basis function associated with $Z_{m',n'}$, is v-directed, an angle of $(\vartheta_{n'} + \pi/2)$ has to be used in the place of $\vartheta_{n'}$. On the other hand, if the basis function associated with $Z_{m,n}$, is v-directed, while the basis function associated with $Z_{m',n'}$, is u-directed, an angle of $(\vartheta_{n'} - \pi/2)$ has to be used in the place of $\vartheta_{n'}$.

3.10.3 Interaction between Functions with Rectangular Support

Figure 3.20 shows the reference interaction $Z_{m,n}$ and the interaction $Z_{m',n'}$ being compared to the reference interaction for the case where both the testing function and the basis function have rectangular support. The dimensions and angles are the same as in the previous discussion, except that both functions have rectangular support in this case. The interactions $Z_{m',n'}$ and $Z_{m,n}$, can then be checked for equality through the following algorithm:

IF $\Delta\xi_{m',n'} = \Delta\xi_{m,n}$ THEN
  IF $(z_{m'} = z_m$ AND $z_{n'} = z_n)$ OR $(z_{m'} = z_n$ AND $z_{n'} = z_m)$ THEN
    IF $L_{m'} = L_m$ AND $W_{m'} = W_m$ AND $p_{m'} = p_m$ AND $q_{m'} = q_m$
    AND $L_{n'} = L_n$ AND $W_{n'} = W_n$ AND $p_{n'} = p_n$ AND $q_{n'} = q_n$ THEN
      IF $|\text{ang}_{\pm\pi}(\vartheta_{m'}) - \text{ang}_{\pm\pi}(\vartheta_m)| = (0$ OR $\pi)$
      AND $|\text{ang}_{\pm\pi}(\vartheta_{n'}) - \text{ang}_{\pm\pi}(\vartheta_n)| = (0$ OR $\pi)$ THEN
        IF $(p_{m'} + q_{m'})$ mod $2 = 0$ THEN
          SIGN $\Leftarrow 1$
        ELSE
          SIGN $\Leftarrow \text{and}_{\pm 1}(|\text{ang}_{\pm\pi}(\vartheta_{m'}) - \text{ang}_{\pm\pi}(\vartheta_m)|, 0)$
        END IF
        IF $(p_{n'} + q_{n'})$ mod $2 = 0$ THEN
          SIGN $\Leftarrow$ SIGN $\cdot\, 1$
        ELSE
          SIGN $\Leftarrow$ SIGN $\cdot\, \text{and}_{\pm 1}(|\text{ang}_{\pm\pi}(\vartheta_{n'}) - \text{ang}_{\pm\pi}(\vartheta_n)|, 0)$

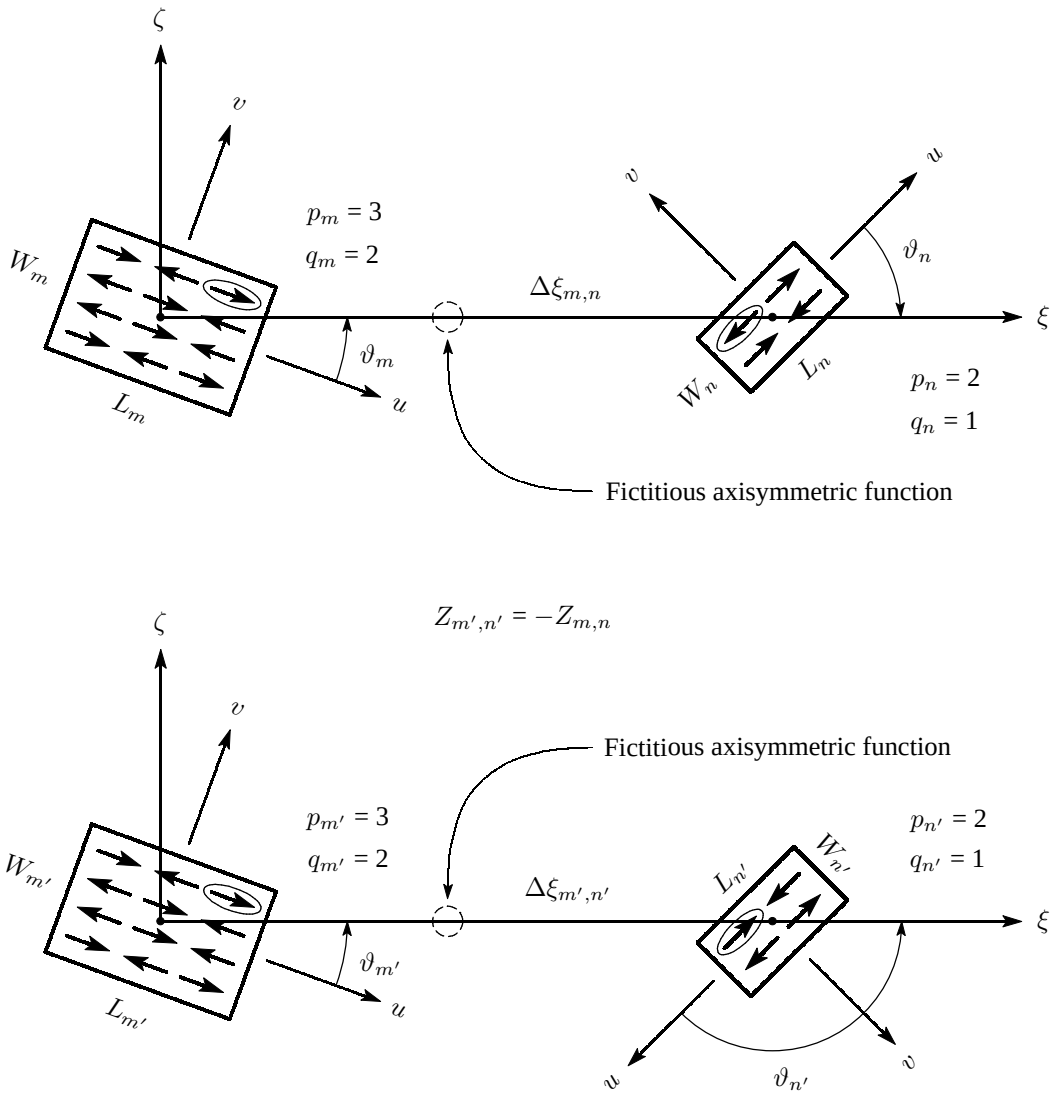

Figure 3.20 Checking $Z_{m',n'}$ and $Z_{m,n}$ for equality where two basis functions with rectangular support are involved.

END IF

$\boxed{Z_{m',n'} \Leftarrow \text{SIGN} \cdot Z_{m,n}}$

ELSE IF $|\text{ang}_{\pm\pi}(\vartheta_{m'}) + \text{ang}_{\pm\pi}(\vartheta_m)| = (0 \text{ OR } \pi)$

AND $|\text{ang}_{\pm\pi}(\vartheta_{n'}) + \text{ang}_{\pm\pi}(\vartheta_n)| = (0 \text{ OR } \pi)$ THEN

IF $(p_{m'} + q_{m'}) \bmod 2 = 0$ THEN

SIGN $\Leftarrow 1$

ELSE

SIGN $\Leftarrow \text{and}_{\pm 1}(|\text{ang}_{\pm\pi}(\vartheta_{m'}) + \text{ang}_{\pm\pi}(\vartheta_m)|, 0)$

END IF

IF $(p_{n'} + q_{n'}) \bmod 2 = 0$ THEN

SIGN $\Leftarrow$ SIGN $\cdot\, 1$

ELSE

SIGN $\Leftarrow$ SIGN $\cdot\, \text{and}_{\pm 1}(|\text{ang}_{\pm\pi}(\vartheta_{n'}) + \text{ang}_{\pm\pi}(\vartheta_n)|, 0)$

END IF

SIGN $\Leftarrow$ SIGN $\cdot\, \text{and}_{\pm 1}(q_{m'} \bmod 2, 0)$

SIGN $\Leftarrow$ SIGN $\cdot\, \text{and}_{\pm 1}(q_{n'} \bmod 2, 0)$

$\boxed{Z_{m',n'} \Leftarrow \text{SIGN} \cdot Z_{m,n}}$

END IF

END IF

ELSE IF $L_{m'} = L_n$ AND $W_{m'} = W_n$ AND $p_{m'} = p_n$ AND $q_{m'} = q_n$

AND $L_{n'} = L_m$ AND $W_{n'} = W_m$ AND $p_{n'} = p_m$ AND $q_{n'} = q_m$ THEN

IF $|\text{ang}_{\pm\pi}(\vartheta_{m'}) - \text{ang}_{\pm\pi}(\vartheta_n)| = (0 \text{ OR } \pi)$

AND $|\text{ang}_{\pm\pi}(\vartheta_{n'}) - \text{ang}_{\pm\pi}(\vartheta_m)| = (0 \text{ OR } \pi)$ THEN

IF $(p_{m'} + q_{m'}) \bmod 2 = 0$ THEN

SIGN $\Leftarrow 1$

ELSE

SIGN $\Leftarrow \text{and}_{\pm 1}(|\text{ang}_{\pm\pi}(\vartheta_{m'}) - \text{ang}_{\pm\pi}(\vartheta_n)|, \pi)$

END IF

IF $(p_{n'} + q_{n'}) \bmod 2 = 0$ THEN

SIGN $\Leftarrow$ SIGN $\cdot\, 1$

ELSE

SIGN $\Leftarrow$ SIGN $\cdot\, \text{and}_{\pm 1}(|\text{ang}_{\pm\pi}(\vartheta_{n'}) - \text{ang}_{\pm\pi}(\vartheta_m)|, \pi)$

END IF

$\boxed{Z_{m',n'} \Leftarrow \text{SIGN} \cdot Z_{m,n}}$

ELSE IF $|\text{ang}_{\pm\pi}(\vartheta_{m'}) + \text{ang}_{\pm\pi}(\vartheta_n)| = (0 \text{ OR } \pi)$

AND $|\text{ang}_{\pm\pi}(\vartheta_{n'}) + \text{ang}_{\pm\pi}(\vartheta_m)| = (0 \text{ OR } \pi)$ THEN

IF $(p_{m'} + q_{m'}) \bmod 2 = 0$ THEN

SIGN $\Leftarrow 1$

ELSE

SIGN $\Leftarrow \text{and}_{\pm 1}(|\text{ang}_{\pm\pi}(\vartheta_{m'}) + \text{ang}_{\pm\pi}(\vartheta_n)|, \pi)$

END IF

IF $(p_{n'} + q_{n'})$ mod $2 = 0$ THEN

SIGN $\Leftarrow$ SIGN $\cdot\ 1$

ELSE

SIGN $\Leftarrow$ SIGN $\cdot$ and$_{\pm 1}(|\text{ang}_{\pm\pi}(\vartheta_{n'}) + \text{ang}_{\pm\pi}(\vartheta_m)|, \pi)$

END IF

SIGN $\Leftarrow$ SIGN $\cdot$ and$_{\pm 1}(q_{m'}$ mod $2, 0)$

SIGN $\Leftarrow$ SIGN $\cdot$ and$_{\pm 1}(q_{n'}$ mod $2, 0)$

$\boxed{Z_{m',n'} \Leftarrow \text{SIGN} \cdot Z_{m,n}}$

END IF

END IF

END IF

END IF

To visually illustrate what this algorithm does, consider the situation depicted in Figure 3.20. The interaction can be viewed as two separate interactions, namely the interaction between the testing function and a fictitious axisymmetric function, as well as the interaction between the basis function and the same fictitious axisymmetric function. Here, the fictitious axisymmetric function is located between the testing and basis functions. Now, consider the situation in Figure 3.20 for the $Z_{m,n}$ interaction. It can be seen that the circled current component (which is the nearest current component to the fictitious axisymmetric function) on the testing function points towards a fictitious line that is orthogonal to itself and that goes through the centre of the fictitious axisymmetric function. Similarly, the circled current component on the basis function, also points towards a similar virtual line. On the other hand, for the $Z_{m',n'}$ interaction, it can be seen that the circled current component on the testing function points towards the virtual line, but that the circled current component on the basis function, points away from the virtual line. Given that the other dimensions, modes and angles correspond, $Z_{m,n}$ is therefore equal to $-Z_{m',n'}$. Furthermore, if $\Delta\xi_{m,n} = 0$ and $\Delta\xi_{m',n'} = 0$, the same algorithm, as has just been described, can be used. However, the basis functions associated with the $Z_{m',n'}$ interaction are first rotated so that the basis function associated with $Z_{m',n'}$ points in the same direction as the basis function associated with $Z_{m,n}$. This is done to avoid problems when checking the angle requirements in the algorithm.

As in the previous discussion, it is also possible that, for example, the $Z_{m,n}$ interaction can have a u-directed entire-domain sinusoidal basis function, while the $Z_{m',n'}$ interaction can have a v-directed entire-domain sinusoidal basis function. In such a case, the same arguments (with respect to the angles) as in the previous discussion, can also be applied here. Another situation that has to be catered for in this case, is where the basis function in $Z_{m,n}$ is compared to the testing function in $Z_{m',n'}$ and vice versa. It is treated in a similar way as has just been described.

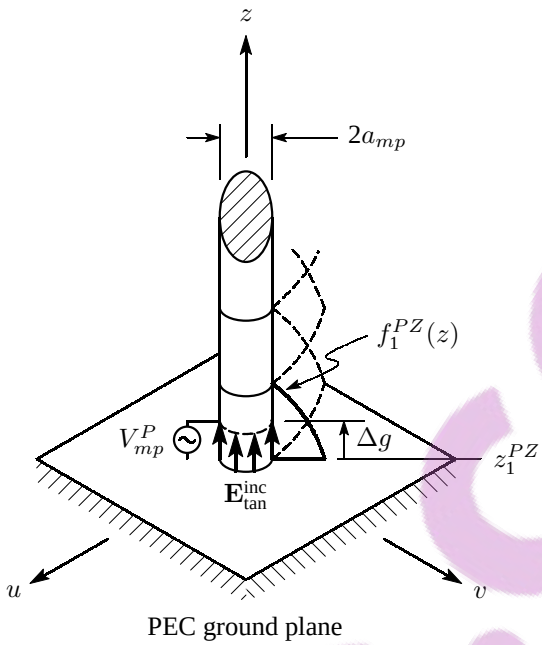

Figure 3.21 The source region on probe mp.

The only part of the system of linear equations in (3.13) that still needs to be addressed, is the evaluation of the excitation vector elements. This will now follow.

3.11 EVALUATION OF THE EXCITATION-VECTOR ELEMENTS

Assume that each probe is excited by a voltage source as shown in Figure 3.21. The source region can then be described by the so-called *delta-gap* model [4, 73]. Using the delta-gap model, it is assumed that a constant voltage of V_{mp}^P is applied over the narrow feed gap Δg of probe mp. The incident electric field $\mathbf{E}_{\tan}^{\text{inc}}$ is then also constant over the feed gap and zero elsewhere. It can be related to the feed-gap voltage and feed-gap width through

$$\mathbf{E}_{\tan}^{\text{inc}}(u,v,z) = \frac{V_{mp}^P}{\Delta g}\hat{z}\Big|_{u^2+v^2=a_{mp}^2}, \quad z_1^{PZ} \leq z \leq z_1^{PZ} + \Delta g. \tag{3.175}$$

Another way to visualise the delta-gap model, is to place a narrow band of impressed magnetic current density in the feed gap. This magnetic current density would flow in a ϕ direction around the probe and would set up the incident electric field across the feed gap. It would be related to the incident electric field through

$$\mathbf{M}^{\text{imp}}(u,v,z) = -\hat{n} \times \mathbf{E}_{\tan}^{\text{inc}}(u,v,z)\Big|_{u^2+v^2=a_{mp}^2}, \tag{3.176}$$

where $\hat{n}$ is the normal vector on the surface of the probe. This representation of the delta-gap model should not be confused with the magnetic-frill model [4, 73].

Each nonzero entry of the excitation vector can now be expressed as

$$V_{mp:mz}^{PZ} = -\iint_{\mathcal{S}_{mp:mz}} \mathbf{f}_{mp:mz}^{PZ}(\mathbf{r}) \cdot \mathbf{E}_{\tan}^{\text{inc}}(\mathbf{r})\, ds, \quad mp = 1, 2, \ldots, N_P,\ mz = 1, \tag{3.177}$$

where

$$\mathbf{f}_{mp:1}^{PZ}(u, v, z) = \frac{1}{2\pi a_{mp}} f_1^{PZ}(z)\, \hat{z} \Big|_{u^2+v^2=a_{mp}^2} \tag{3.178}$$

is the basis function at the bottom of probe mp. Here, $f_1^{PZ}(z)$ is one half of a PWS function as given by (3.67). The expression in (3.177) for the nonzero entries of the excitation vector can then be simplified to

$$\begin{aligned} V_{mp}^{PZ} &= \frac{-1}{2\pi a_{mp}} \int_0^{2\pi} \mathbf{f}_1^{PZ}(z = z_1^{PZ}) \frac{V_{mp}^P}{\Delta g}\, \Delta g\, a_{mp}\, d\phi \\ &= -V_{mp}^P, \quad mp = 1, 2, \ldots, N_P. \end{aligned} \tag{3.179}$$

All the elements that are required for the solution of the system in (3.13), have now been addressed. Some issues regarding the actual solution of the system of linear equations will now be discussed in the next section.

3.12 SOLUTION OF THE CURRENT-DENSITY COEFFICIENTS

Due to the fact that this formulation does not generate linear equations with an excessive number of unknowns, Gauss-Jordan elimination, LU decomposition or any similar method [184], can be used very effectively to solve for the unknown current-density coefficients I_n. If the antenna that is analysed, has more than one port, and if the network parameters are required, the system of linear equations will have to be solved once for every port of the antenna. This is due to separate excitation vectors that have to be set up for each port. In such a case, it would be advisable to also store a copy of the interaction matrix so that it can be reused. If this is not done, the interaction matrix would have to be recalculated for each excitation vector, thereby increasing the computation time excessively. Furthermore, for a multiport antenna, each solution of the linear system of equations would only provide the current-density coefficients that correspond to one excitation vector. However, when calculating the far fields of a multiport antenna, one would normally be interested in the fields that are generated due to a combination of port excitations. This can be done by setting up one excitation vector for all of the ports simultaneously or by summing the individual current-density coefficients in an appropriate way when the system of linear equations is solved for multiple excitation vectors. These are all factors that have to be kept in mind when implementing the formulation. The remaining sections will now deal with observables that can be calculated once the system of linear equations has been solved. These typically include the network parameters and far fields.

3.13 EVALUATION OF THE NETWORK PARAMETERS

In the analysis of antennas or antenna arrays, there is almost always a requirement to calculate the network parameters of the structure. These are usually expressed in terms of the *impedance matrix* $[Z^P]$, the *admittance matrix* $[Y^P]$ or the *scattering matrix* $[S^P]$. With the current formulation, it is most convenient to calculate the admittance matrix first and then to calculate the impedance matrix directly from the admittance matrix. Finally, the scattering matrix can then be calculated by making use of both the admittance and impedance matrices. The scattering matrix is normally used by software packages that are capable of microwave network analysis. Such packages can be used, for example, to analyse an antenna array together with its feed network. This is achieved by analysing the two structures separately, after which the scattering parameters of the two structures are connected to yield an overall scattering matrix for the entire structure. However, for such an analysis to be accurate, there should be no electromagnetic coupling between the two structures. This is usually the case for probe-fed microstrip antennas.

For the purposes of this analysis, it can be assumed that port mp is associated with probe mp, port np with probe np and so on. Therefore, the total number of ports will also be equal to the total number of probes N_P. Now, entry $Y^P_{mp,np}$ (which relates the current at port mp to the voltage at port np) of the admittance matrix can be calculated as

$$Y^P_{mp,np} = \frac{I^{PZ}_{mp:1}}{V^P_{np}}, \tag{3.180}$$

where $I^{PZ}_{mp:1}$ is the current at port mp (also the current-density coefficient of the bottommost basis function on probe mp) and V^P_{np} is the applied voltage at port np. After all entries of the admittance matrix have been calculated, the impedance matrix is simply calculated through

$$[Z^P] = [Y^P]^{-1}. \tag{3.181}$$

With both the admittance matrix and the impedance matrix known, the scattering matrix can be calculated as [185]

$$[S^P] = [Z^P_0]^{1/2}\left([Y^P_0] - [Y^P]\right)\left([Y^P_0] + [Y^P]\right)^{-1}[Z^P_0]^{1/2}, \tag{3.182}$$

where

$$[Z^P_0] = \begin{bmatrix} (Z^P_0)_1 & 0 & \cdots & 0 \\ 0 & (Z^P_0)_2 & \cdots & 0 \\ \vdots & \vdots & \ddots & \vdots \\ 0 & 0 & \cdots & (Z^P_0)_{N_P} \end{bmatrix} \tag{3.183}$$

is a diagonal matrix with the characteristic impedance $\left(Z_0^P\right)_{np}$ of each port on the diagonal of the matrix. Furthermore,

$$\left[Y_0^P\right] = \begin{bmatrix} \left(Y_0^P\right)_1 & 0 & \cdots & 0 \\ 0 & \left(Y_0^P\right)_2 & \cdots & 0 \\ \vdots & \vdots & \ddots & \vdots \\ 0 & 0 & \cdots & \left(Y_0^P\right)_{N_P} \end{bmatrix} \tag{3.184}$$

is a diagonal matrix with the characteristic admittance $\left(Y_0^P\right)_{np}$ of each port on the diagonal of the matrix. Here, $\left(Y_0^P\right)_{np} = 1/\left(Z_0^P\right)_{np}$. Also in (3.182),

$$\left[Z_0^P\right]^{1/2} = \begin{bmatrix} \sqrt{\left(Z_0^P\right)_1} & 0 & \cdots & 0 \\ 0 & \sqrt{\left(Z_0^P\right)_2} & \cdots & 0 \\ \vdots & \vdots & \ddots & \vdots \\ 0 & 0 & \cdots & \sqrt{\left(Z_0^P\right)_{N_P}} \end{bmatrix} \tag{3.185}$$

is a diagonal matrix with the square root of the characteristic impedance of each port on the diagonal of the matrix, while

$$\left[Y_0^P\right]^{1/2} = \begin{bmatrix} \sqrt{\left(Y_0^P\right)_1} & 0 & \cdots & 0 \\ 0 & \sqrt{\left(Y_0^P\right)_2} & \cdots & 0 \\ \vdots & \vdots & \ddots & \vdots \\ 0 & 0 & \cdots & \sqrt{\left(Y_0^P\right)_{N_P}} \end{bmatrix} \tag{3.186}$$

is a diagonal matrix with the square root of the characteristic admittance of each port on the diagonal of the matrix.

3.14 EVALUATION OF THE FAR FIELDS

In the spectral domain, the evaluation of the far fields is relatively straightforward. The far fields can be calculated by using the *method of stationary phase* [4, 178]. This method is commonly used for the evaluation of integrals where the integrand is highly oscillatory, but where the contributions to the integral mainly comes from the so-called stationary point and its surrounding

neighbourhood. The radiation integrals that are used to obtain the far fields of antennas, are typical of such integrals. The method of stationary phase essentially finds an asymptotic solution to such integrals.

In general, the far field $\mathbf{E}^{\text{scat}}$ at point $\mathbf{r}$ can be related to its spectral-domain counterpart, at position z_r along the z direction, through [6, 141]

$$\mathbf{E}^{\text{scat}}(\mathbf{r}) = \frac{-1}{j2\pi}\,\tilde{\mathbf{E}}^{\text{scat}}(k_{xs}, k_{ys}, z_r)\,k_{zs}e^{jk_{zs}z_r}\frac{e^{-jk_{(0)}r}}{r}. \tag{3.187}$$

The stationary point is defined by

$$k_{xs} = k_{(0)}\sin(\theta)\cos(\phi), \tag{3.188}$$

$$k_{ys} = k_{(0)}\sin(\theta)\sin(\phi) \tag{3.189}$$

and

$$k_{zs} = k_{(0)}\cos(\theta), \tag{3.190}$$

where (θ, ϕ) denotes the direction of the far field, and where $k_{(0)}$ is the wavenumber in the top layer that extends to infinity along the positive z direction. The far field can also be expressed as

$$\mathbf{E}^{\text{scat}}(\mathbf{r}) = \mathbf{E}^{\text{scat}}(r, \theta, \phi) = \mathbf{E}^{\text{scat}}(\theta, \phi)\frac{e^{-jk_{(0)}r}}{r}, \tag{3.191}$$

where one part is a function of angular position only and the other part is a function of distance only. The $e^{-jk_{(0)}r}/r$ part is often dropped from far-field expressions, leaving only the angular dependence of the far field. By making use of (3.187), this part can be expressed as

$$\mathbf{E}^{\text{scat}}(\theta, \phi) = \frac{-1}{j2\pi}\,\tilde{\mathbf{E}}^{\text{scat}}(k_{xs}, k_{ys}, z_r)\,k_{zs}e^{jk_{zs}z_r}. \tag{3.192}$$

The spectral-domain form of the scattered field $\tilde{\mathbf{E}}^{\text{scat}}(k_{xs}, k_{ys}, z_r)$ is now first expressed in terms of its spatial-domain counterpart by invoking the two-dimensional Fourier transform of (3.18). This then allows $\tilde{\mathbf{E}}^{\text{scat}}(k_{xs}, k_{ys}, z_r)$ to be expressed in terms of the spatial-domain current density on the structure, by making use of the spatial-domain Green's function. Mathematically, this is expressed as

$$\begin{aligned}\tilde{\mathbf{E}}^{\text{scat}}(k_{xs}, k_{ys}, z_r) &= \int_{-\infty}^{\infty}\int_{-\infty}^{\infty}\mathbf{E}^{\text{scat}}(x, y, z_r)\,e^{-jk_{xs}x}\,e^{-jk_{ys}y}\,dxdy \\ &= \int_y\int_x\left[\int_{z'}\int_{y'}\int_{x'}\bar{\mathbf{G}}(x, y, z_r|x', y', z')\cdot\mathbf{J}(x', y', z')\,dx'dy'dz'\right] \\ &\quad\cdot e^{-jk_{xs}x}\,e^{-jk_{ys}y}\,dxdy.\end{aligned} \tag{3.193}$$

Now, the Green's function can be written in terms of its spectral-domain counterpart, resulting in

$$\begin{aligned}\tilde{\mathbf{E}}^{\text{scat}}(k_{xs},k_{ys},z_r) = \int_{k_{ys}}\int_{k_{xs}} \Bigg\{ \int_y\int_x\int_{z'} \tilde{\bar{\mathbf{G}}}(k_{xs},k_{ys},z_r|z') \\ \cdot \left[\int_{y'}\int_{x'} \mathbf{J}(x',y',z')\, e^{-jk_{xs}x'}\, e^{-jk_{ys}y'}\, dx'dy'\right] dz'\, e^{-jk_{xs}x}\, e^{-jk_{ys}y}\, dxdy \Bigg\} \\ \cdot\, e^{jk_{xs}x}\, e^{jk_{ys}y}\, dk_{xs}dk_{ys}. \end{aligned} \tag{3.194}$$

The term is square brackets can be identified as a two-dimensional Fourier transform, enabling one to express $\tilde{\mathbf{E}}^{\text{scat}}(k_{xs},k_{ys},z_r)$ as

$$\begin{aligned}\tilde{\mathbf{E}}^{\text{scat}}(k_{xs},k_{ys},z_r) &= \int_{k_{ys}}\int_{k_{xs}} \left[\int_y\int_x\int_{z'} \tilde{\bar{\mathbf{G}}}(k_{xs},k_{ys},z_r|z')\cdot\tilde{\mathbf{J}}(k_{xs},k_{ys},z')\,dz' \right. \\ &\qquad \left. \cdot\, e^{-jk_{xs}x}\, e^{-jk_{ys}y}\, dxdy\right] e^{jk_{xs}x}\, e^{jk_{ys}y}\, dk_{xs}dk_{ys} \\ &= \int_{z'} \tilde{\bar{\mathbf{G}}}(k_{xs},k_{ys},z_r|z')\cdot\tilde{\mathbf{J}}(k_{xs},k_{ys},z')\,dz' \\ &= \sum_{n=1}^{N} I_n \int_{z'} \tilde{\bar{\mathbf{G}}}(k_{xs},k_{ys},z_r|z')\cdot\tilde{\mathbf{f}}_n(k_{xs},k_{ys},z')\,dz'. \end{aligned} \tag{3.195}$$

At this point, it is now convenient to express the far field $\mathbf{E}^{\text{scat}}(\theta,\phi)$ and the basis function $\tilde{\mathbf{f}}_n$ in terms of their components in the global (x,y,z) coordinate system. These are given by

$$\mathbf{E}^{\text{scat}}(\theta,\phi) = E_x^{\text{scat}}(\theta,\phi)\,\hat{x} + E_y^{\text{scat}}(\theta,\phi)\,\hat{y} + E_z^{\text{scat}}(\theta,\phi)\,\hat{z} \tag{3.196}$$

and

$$\tilde{\mathbf{f}}_n(k_{xs},k_{ys},z') = \left(\tilde{f}_x(k_{xs},k_{ys},z')\right)_n \hat{x} + \left(\tilde{f}_y(k_{xs},k_{ys},z')\right)_n \hat{y} + \left(\tilde{f}_z(k_{xs},k_{ys},z')\right)_n \hat{z} \tag{3.197}$$

respectively.

The basis-function components in the global (x,y,z) coordinate system can be determined from the components in each basis function's local (u,v,z) coordinate system. This is done through

$$\begin{aligned}&\left(\tilde{f}_x(k_{xs},k_{ys},z')\right)_n \\ &= \left(\tilde{f}_u\big(k_u = k_{xs}\cos(\phi_n) + k_{ys}\sin(\phi_n), k_v = -k_{xs}\sin(\phi_n) + k_{ys}\cos(\phi_n), z'\big)\right)_n \cos(-\phi_n) \\ &\quad \cdot\, e^{-jk_{xs}x_n}\, e^{-jk_{ys}y_n} \\ &- \left(\tilde{f}_v\big(k_u = k_{xs}\cos(\phi_n) + k_{ys}\sin(\phi_n), k_v = -k_{xs}\sin(\phi_n) + k_{ys}\cos(\phi_n), z'\big)\right)_n \sin(-\phi_n) \\ &\quad \cdot\, e^{-jk_{xs}x_n}\, e^{-jk_{ys}y_n}, \end{aligned} \tag{3.198}$$

$$
\begin{aligned}
&\left(\tilde{f}_y(k_{xs}, k_{ys}, z')\right)_n \\
&= \left(\tilde{f}_u\left(k_u = k_{xs}\cos(\phi_n) + k_{ys}\sin(\phi_n), k_v = -k_{xs}\sin(\phi_n) + k_{ys}\cos(\phi_n), z'\right)\right)_n \sin(-\phi_n) \\
&\quad \cdot e^{-jk_{xs}x_n}\, e^{-jk_{ys}y_n} \\
&+ \left(\tilde{f}_v\left(k_u = k_{xs}\cos(\phi_n) + k_{ys}\sin(\phi_n), k_v = -k_{xs}\sin(\phi_n) + k_{ys}\cos(\phi_n), z'\right)\right)_n \cos(-\phi_n) \\
&\quad \cdot e^{-jk_{xs}x_n}\, e^{-jk_{ys}y_n}
\end{aligned} \tag{3.199}
$$

and

$$
\left(\tilde{f}_z(k_{xs}, k_{ys}, z')\right)_n = \left(\tilde{f}_z(k_u = k_{xs}, k_v = k_{ys}, z')\right)_n e^{-jk_{xs}x_n}\, e^{-jk_{ys}y_n}, \tag{3.200}
$$

where x_n and y_n define the (x, y) position of the n-th basis function in the global (x, y, z) coordinate system and where the angle ϕ_n has already been defined in Figure 3.12.

By using (3.195) to (3.197), the three components of the far field can be expressed as

$$
\begin{aligned}
E_x^{\text{scat}}(\theta, \phi) = \sum_{n=1}^{N} I_n \Big[&\tilde{G}_{xx}(k_{xs}, k_{ys}, z_r|z')\left(\tilde{f}_x(k_{xs}, k_{ys}, z')\right)_n \\
&+\tilde{G}_{xy}(k_{xs}, k_{ys}, z_r|z')\left(\tilde{f}_y(k_{xs}, k_{ys}, z')\right)_n \\
&+\tilde{G}^I_{xz}(k_{xs}, k_{ys}, z_r)\left(\tilde{f}_z(k_{xs}, k_{ys})\right)_n \Big],
\end{aligned} \tag{3.201}
$$

$$
\begin{aligned}
E_y^{\text{scat}}(\theta, \phi) = \sum_{n=1}^{N} I_n \Big[&\tilde{G}_{yx}(k_{xs}, k_{ys}, z_r|z')\left(\tilde{f}_x(k_{xs}, k_{ys}, z')\right)_n \\
&+\tilde{G}_{yy}(k_{xs}, k_{ys}, z_r|z')\left(\tilde{f}_y(k_{xs}, k_{ys}, z')\right)_n \\
&+\tilde{G}^I_{yz}(k_{xs}, k_{ys}, z_r)\left(\tilde{f}_z(k_{xs}, k_{ys})\right)_n \Big]
\end{aligned} \tag{3.202}
$$

and

$$
\begin{aligned}
E_z^{\text{scat}}(\theta, \phi) = \sum_{n=1}^{N} I_n \Big[&\tilde{G}_{zx}(k_{xs}, k_{ys}, z_r|z')\left(\tilde{f}_x(k_{xs}, k_{ys}, z')\right)_n \\
&+\tilde{G}_{zy}(k_{xs}, k_{ys}, z_r|z')\left(\tilde{f}_y(k_{xs}, k_{ys}, z')\right)_n \\
&+\tilde{G}^I_{zz}(k_{xs}, k_{ys}, z_r)\left(\tilde{f}_z(k_{xs}, k_{ys})\right)_n \Big].
\end{aligned} \tag{3.203}
$$

In these, the expanded Green's-function components are given by

$$
\tilde{G}^I_{xz}(k_{xs}, k_{ys}, z_r) = \int_{z'} \tilde{G}^I_{xz}(k_{xs}, k_{ys}, z_r|z')\left(\tilde{f}_z(z')\right)_n dz', \tag{3.204}
$$

$$\tilde{G}^I_{yz}(k_{xs}, k_{ys}, z_r) = \int_{z'} \tilde{G}^I_{yz}(k_{xs}, k_{ys}, z_r|z') \left(\tilde{f}_z(z')\right)_n dz' \tag{3.205}$$

and

$$\tilde{G}^I_{zz}(k_{xs}, k_{ys}, z_r) = \int_{z'} \tilde{G}^I_{zz}(k_{xs}, k_{ys}, z_r|z') \left(\tilde{f}_z(z')\right)_n dz'. \tag{3.206}$$

In Appendix B, it is shown how these expanded Green's functions can be evaluated.

Far fields are most often expressed in spherical coordinates through

$$\mathbf{E}^{\text{scat}}(\theta, \phi) = E^{\text{scat}}_\theta(\theta, \phi)\, \hat{\theta} + E^{\text{scat}}_\phi(\theta, \phi)\, \hat{\phi}, \tag{3.207}$$

where the two components, E^{scat}_θ and E^{scat}_ϕ, can be determined from their counterparts in a rectangular coordinate system. This in done through

$$E^{\text{scat}}_\theta(\theta, \phi) = E^{\text{scat}}_x(\theta, \phi)\cos(\theta)\cos(\phi) + E^{\text{scat}}_y(\theta, \phi)\cos(\theta)\sin(\phi) - E^{\text{scat}}_z(\theta, \phi)\sin(\theta) \tag{3.208}$$

and

$$E^{\text{scat}}_\phi(\theta, \phi) = -E^{\text{scat}}_x(\theta, \phi)\sin(\phi) + E^{\text{scat}}_y(\theta, \phi)\cos(\phi). \tag{3.209}$$

Finally, the antenna gain associated with the two far-field components, can be calculated as

$$G_\theta(\theta, \phi) = \frac{4\pi |E^{\text{scat}}_\theta(\theta, \phi)|^2}{2\eta_{(0)} P_{\text{in}}} \tag{3.210}$$

and

$$G_\phi(\theta, \phi) = \frac{4\pi |E^{\text{scat}}_\phi(\theta, \phi)|^2}{2\eta_{(0)} P_{\text{in}}}, \tag{3.211}$$

where

$$\eta_{(0)} = \sqrt{\frac{\mu_{(0)}}{\varepsilon_{(0)}}} \tag{3.212}$$

is the intrinsic impedance of the top layer, and

$$P_{\text{in}} = \frac{1}{2}\, \Re\text{e}\left\{ \sum_{np=1}^{N_P} V^P_{np} \left(I^{PZ}_{np:1}\right)^* \right\} \tag{3.213}$$

is the total input power to the antenna.

3.15 CONCLUDING REMARKS

This chapter presented a detailed exposition of the theoretical formulation that was implemented for the analysis of microstrip patch antennas with capacitive feed probes. It started off with an overview of the general SDMM formulation for a structure that is embedded within a grounded multilayered medium. The various basis function were discussed at length, while a new higher-

order circular attachment mode was presented for the modelling of circular capacitor patches (the suitability of the various attachment modes will be investigated in the next chapter). It was shown how different integration strategies can be used to speed up the calculation of interaction integrals. Here, a new method for the calculation of the interaction between basis and testing functions that are widely separated, was modified to also handle small separation distances. A number of algorithms were developed to identify duplicate entries within the interaction matrix. This has a significant effect on the overall computational time that is required for the analysis. In the next chapter it will be shown how effective this method is. Finally, it was shown how observables such as the network parameters and far fields, can be calculated. To summarise, although parts of this analysis have been implemented and reported on before, this analysis as a whole is unique in the combination of basis functions and numerical methods that have been implemented. As such, no results for this analysis are available in the literature. In Chapter 4, this analysis will be applied to a variety of antenna configurations and the results will be compared to measurements, as well as the results of other commercial codes.

CHAPTER 4

Numerical and Experimental Results

4.1 INTRODUCTORY REMARKS

The spectral-domain moment-method (SDMM) formulation of Chapter 3 was implemented in the *C* programming language and, as such, this implementation can now be used to analyse any antenna configuration consisting of microstrip patches with capacitive feed probes. In this chapter, it is shown how this implementation can be applied to a variety of applications. Throughout most most of this chapter, the results of the SDMM are compared to those of two other commercial codes, as well as some measured results. The two commercial codes are IE3D from Zeland Software [186] and FEKO from EM Software and Systems [187], while the circuit analysis module of Sonnet, from Sonnet Software [188], was also used. The measurements were all performed at the Centre for Electromagnetism at the University of Pretoria. This facility houses a Scientific Atlanta compact antenna test range, integrated with a dedicated Hewlett-Packard 8510C vector network analyser. For more general *S*-parameter measurements, a Hewlett-Packard 8510B vector network analyser is also used. Antenna gain in this facility is typically measured by using the gain-transfer method.

The SDMM implementation is validated in Section 4.2 for isolated parts of the antenna structure. In Section 4.3, the new antenna elements are characterised in order to determine the effect of the various geometrical parameters on the behaviour of the different elements. In Section 4.4, a number of applications are presented. These include vertically- and horizontally-polarised arrays, as well as $\pm 45^{\circ}$ slant-polarised arrays. The latter are often required for cellular base-stations antennas. Finally, in Section 4.5, it is shown how the capacitive feed probes can be used with alternatively-shaped resonant patches.

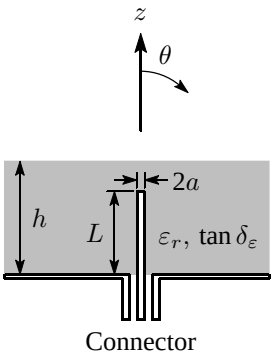

Figure 4.1 Geometry of a probe that is embedded within a grounded substrate.

4.2 VALIDATION OF THE SPECTRAL-DOMAIN MOMENT-METHOD IMPLEMENTATION

In order to validate the accuracy of the SDMM implementation, it is advisable to first analyse isolated parts of the antenna structure. In doing so, one can obtain a better understanding of the capabilities of the formulation. The input impedance is usually a sensitive parameter and can give a good indication of how well the code performs. As such, it is used as the basis for comparison throughout most of the validation process. A single probe that is embedded within a grounded substrate, is probably the most basic part of the structure and is therefore firstly considered. Thereafter, the structure is extended by adding a capacitor patch to the probe, and finally a resonant patch. This then would be the equivalent of a single antenna element. A detailed investigation into the capabilities of the various attachment modes also forms part of this validation.

4.2.1 Single Probe in a Grounded Substrate

Consider the probe of Figure 4.1, with length L and radius a, which is embedded within a grounded substrate of thickness h. The probe can be realised by extending the inner conductor of a coaxial cable through the ground plane into the substrate, while the outer conductor of the coaxial cable is connected to the ground plane. This problem has been addressed before and published results for the input impedance of such a probe are available within the open literature [189, 190].

Figure 4.2 shows simulated and published results for the input impedance versus normalised length of a probe that is totally embedded within a grounded substrate. For the SDMM formulation, between two and seven basis functions were used on the probe. It can be seen that the agreement between all the codes is very good and that it also compares exceptionally well with the published results.

Another interesting phenomena that can be validated here, is that far-field radiation towards the horizon (i.e. $\theta = \pm 90^{\circ}$) should always go down to zero, except under special conditions when the

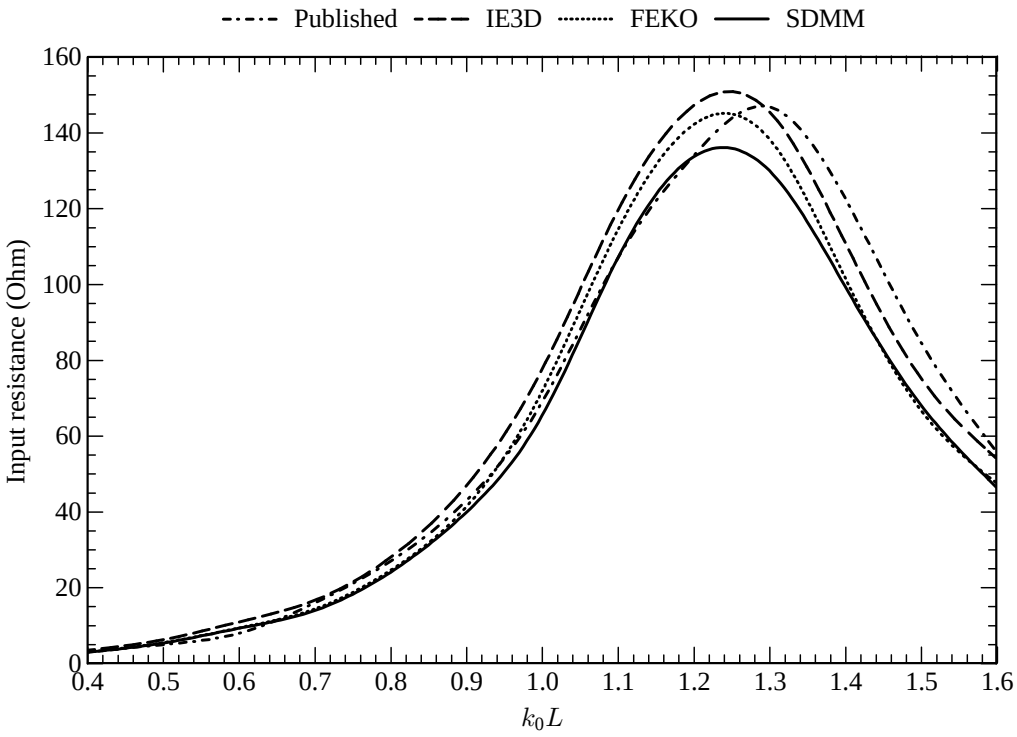

(a)

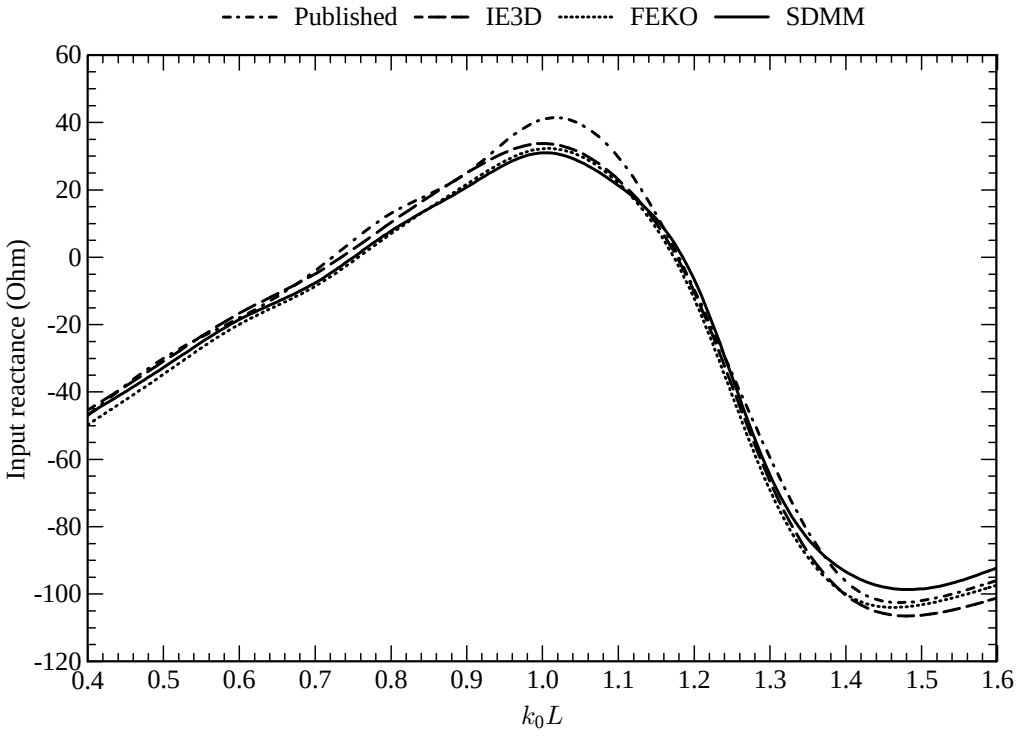

(b)

Figure 4.2 Input impedance of a probe that is embedded within a grounded substrate. Parameters: a = 1.5 mm, $h = 0.3\lambda_0$, ε_r = 3.9 and $\tan\delta_\varepsilon = 0$. (a) Input resistance. (b) Input reactance.

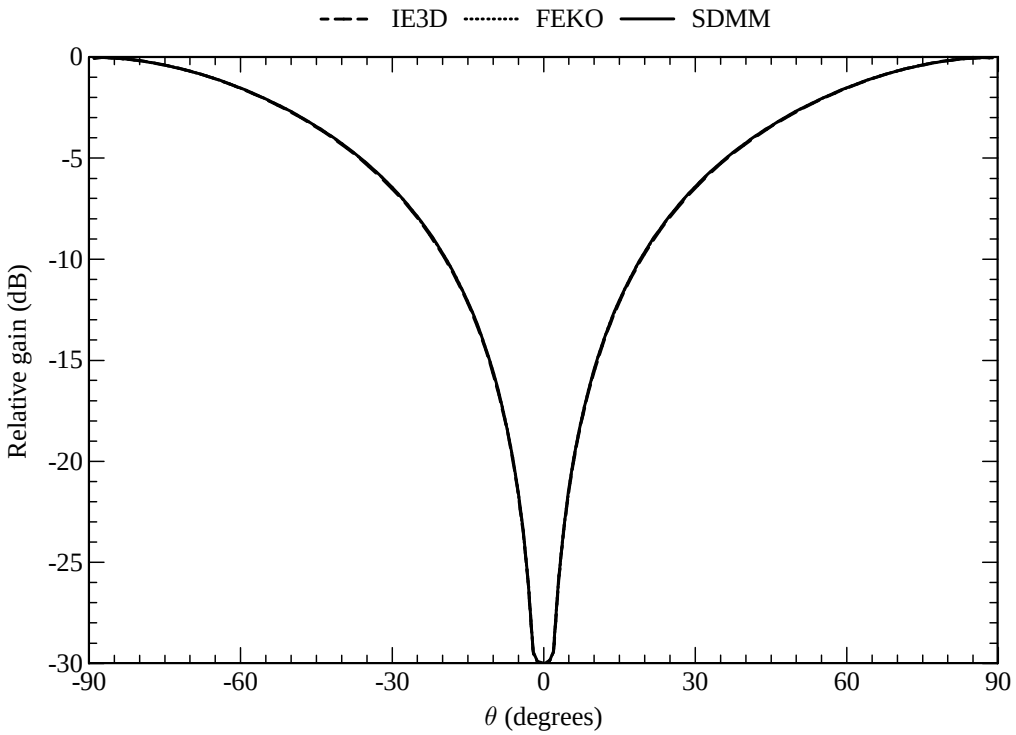

Figure 4.3 Radiation pattern of a probe that is embedded within a grounded substrate. Parameters: L = 48 mm, a = 1.5 mm, h = 90 mm, ε_r = 3.78, tan δ_ε = 0 and f = 1 GHz.

relation

$$h = \frac{i\lambda_0}{2\sqrt{\varepsilon_r - 1}}, \quad i = 1, 2, 3 \ldots \tag{4.1}$$

is satisfied [189, 191]. Figure 4.3 shows the radiation pattern for the case where $i = 1$. In this case, four basis functions were used on the probe. From this figure, it can indeed be seen that there is far-field radiation towards the horizon and that the results of the SDMM are virtually indistinguishable from those of the two commercial codes. Note that although there is radiation towards the horizon, all the codes give zero far fields at exactly $\theta = \pm 90^\circ$. This is due to the stationary-phase evaluation of the far fields.

From the results that have been presented here, it is clear that the SDMM, as implemented here, can model probes in multilayered substrates very successfully.

4.2.2 Circular Versus Rectangular Attachment Modes

In order to model the connection between a probe and a patch, a special basis function, also known as an attachment mode, is required. As discussed in Chapter 3, there are two common approaches: the rectangular attachment mode and the circular attachment mode. However, the performance of these attachment modes under a wide variety of geometrical parameters, is not well documented. In order to get a better understanding of the abilities of these two approaches, both of them are used

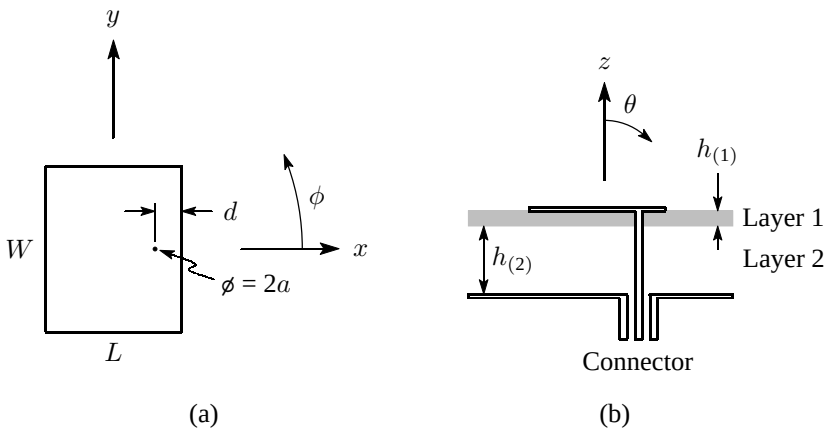

Figure 4.4 Geometry of a rectangular probe-fed patch. (a) Top view of the patch. (b) Side view of the multilayered substrate.

in this section to analyse various rectangular probe-fed patch configurations. The general geometry of such a patch is shown in Figure 4.4. The simulated results are then compared to experimental results, which have either been published or measured specifically for this study. The simulated results are first compared to published results for a conventional narrowband microstrip antenna on a thin substrate, in order to verify that both approaches yield the correct results as claimed in the literature. Both approaches are then tested for small and resonant probe-fed patches that reside on multilayered substrates of varying thickness.

Shaubert *et al.* [192], as well as Aberle *et al.* [132,133], have published input-impedance results for a narrowband probe-fed microstrip patch antenna on a thin substrate. Figure 4.5 shows the input impedance of this antenna, as measured by them, together with two sets of numerical results that were calculated by using the two different attachment-mode approaches. Both sets of calculated results were obtained by using nine entire-domain sinusoidal basis functions on the patch and one piecewise sinusoidal (PWS) basis function (excluding the one associated with the attachment mode) on the probe. For the entire-domain sinusoidal basis functions, the (1,0), (1,2), (2,0), (3,0), (5,0), (7,0) and (9,0) modes were used for the x-directed current, while the (2,0) and (2,1) modes were used for the y-directed current. The best results for the circular attachment mode were achieved by extending the radius of the attachment mode to the closest edge of the patch. As can be seen from the results in Figure 4.5, both approaches are capable of generating results that agree very well with measurements. This is specifically for the case of a resonant patch on a relatively thin substrate.

It is not clear from the literature how the attachment modes would perform for much smaller patch sizes and thick substrates. To gain a better understanding of how they would perform, two sets of patches were constructed, the one set having resonant patches (at frequencies between 1.4 GHz and 2.1 GHz) of 50 mm $\times$ 50 mm, and the other set having much smaller patches (below

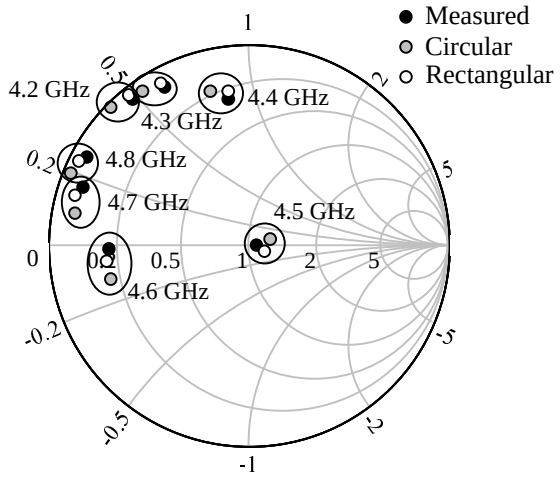

Figure 4.5 Input impedance (normalised to 50 Ω) of a rectangular probe-fed patch as modelled with the circular and rectangular attachment modes. Parameters: L = 9.5 mm, W = 12.5 mm, a = 0.45 mm, d = 3.2 mm, $h_{(1)}$ = 1.27 mm, $\varepsilon_{r(1)}$ = 10.53, tan $\delta_{\varepsilon(1)}$ = 0.002 and $h_{(2)}$ = 0.

resonance) at 5 mm × 10 mm. Both sets contained four patches and were etched on a 1.6 mm layer of FR-4. Three of the four patches contained air gaps, ranging from more or less 5 mm to 15 mm, between the FR-4 layer and the ground plane. The two sets of patches would therefore represent a combination of different sizes and substrate thicknesses.

Figure 4.6 shows the measured and calculated input-impedance results for the set of resonant patches. Both sets of calculated results were obtained by using nine entire-domain basis functions on the patches, and one to seven PWS basis functions (excluding the one associated with the attachment mode) on the probe, depending on the substrate thickness. Once again, for the entire-domain sinusoidal basis functions, the (1,0), (1,2), (2,0), (3,0), (5,0), (7,0) and (9,0) modes were used for the x-directed current, while the (2,0) and (2,1) modes were used for the y-directed current. It is apparent that both attachment-mode approaches yield results that compare very well with the measured results. It would therefore appear that both approaches can handle thick multilayered substrates with very good accuracy, provided that the patch is of a resonant size. A radius of 10 mm provided the best results for the circular attachment mode.

Figure 4.7 shows the measured and calculated input-impedance results for the set of small patches. In this case, both sets of calculated results were obtained by using forty-five subdomain rooftop basis functions on the patches, and one to seven piecewise sinusoidal basis functions (excluding the one associated with the attachment mode) on the probe, depending on the substrate thickness. In this case it is clear that the circular attachment mode still yields results that compare favourably with the measurements, but that the rectangular attachment mode has difficulty in modelling the small patches. For all of the substrate thicknesses, it would appear as though the rectangular

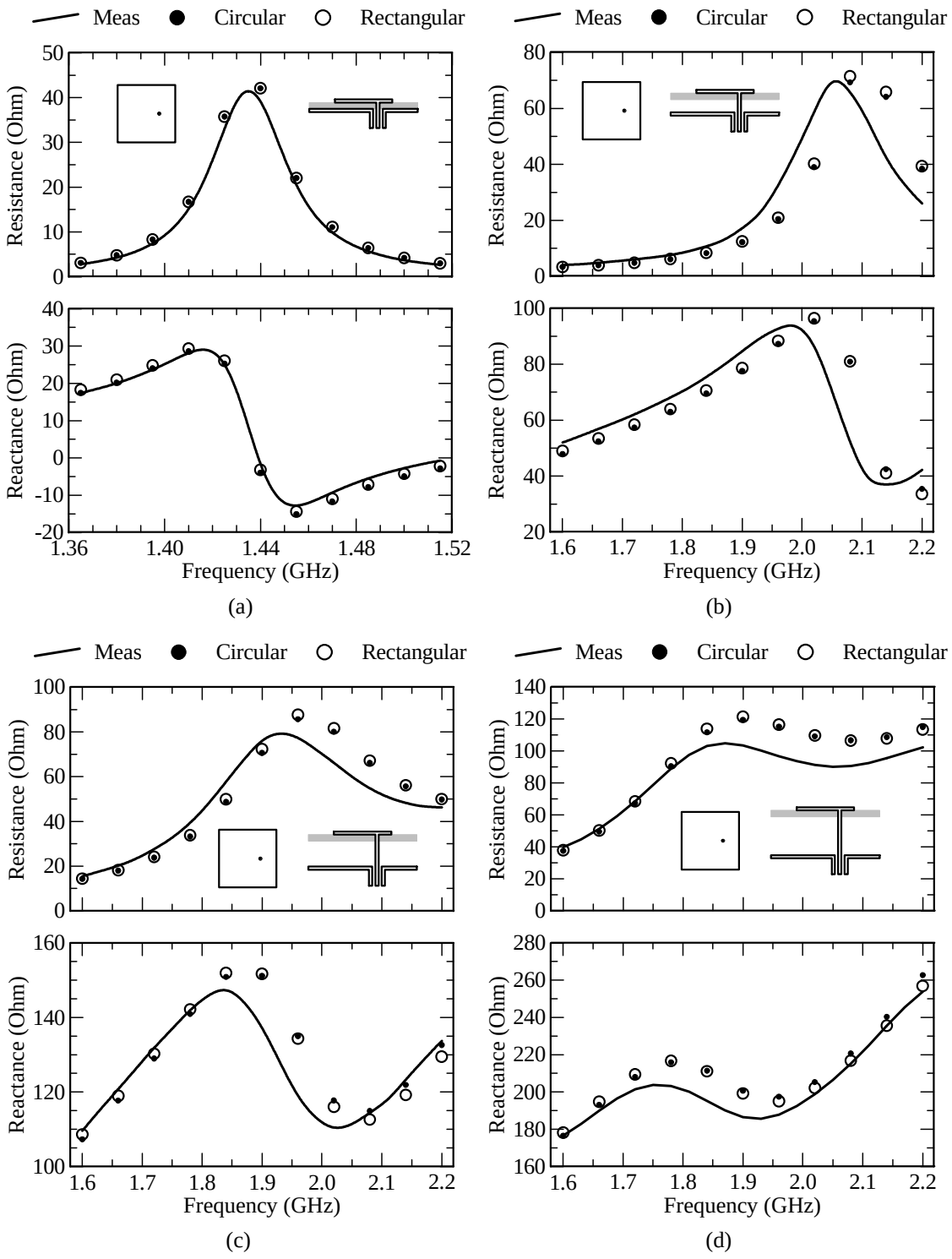

Figure 4.6 Input impedance of a square resonant probe-fed patch as modelled with the circular and rectangular attachment modes. Parameters: L = 50 mm, W = 50 mm, d = 15 mm, $h_{(1)}$ = 1.6 mm, $\varepsilon_{r(1)}$ = 4.25, $\tan\delta_{\varepsilon(1)}$ = 0.02 and $\tan\delta_{\varepsilon(2)}$ = 0. (a) $h_{(2)}$ = 0, a = 0.64 mm. (b) $h_{(2)}$ = 5.4 mm, a = 0.45 mm. (c) $h_{(2)}$ = 11.1 mm, a = 0.45 mm. (d) $h_{(2)}$ = 15.8 mm, a = 0.45 mm.

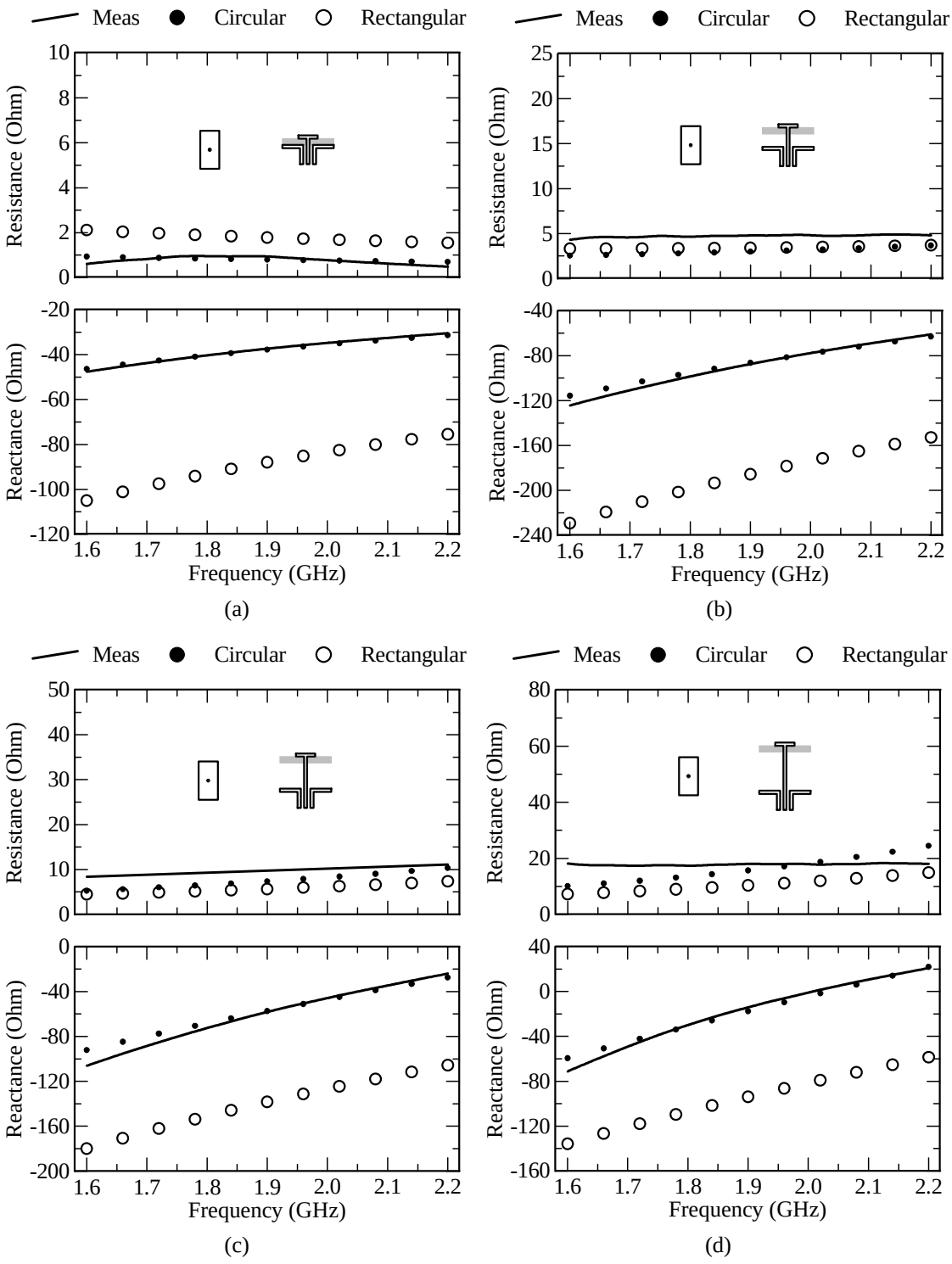

Figure 4.7 Input impedance of a small rectangular probe-fed patch as modelled with the circular and rectangular attachment modes. Parameters: L = 5 mm, W = 10 mm, d = 2.5 mm, $h_{(1)}$ = 1.6 mm, $\varepsilon_{r(1)}$ = 4.25, tan $\delta_{\varepsilon(1)}$ = 0.02 and tan $\delta_{\varepsilon(2)}$ = 0. (a) $h_{(2)}$ = 0, a = 0.64 mm. (b) $h_{(2)}$ = 5.3 mm, a = 0.45 mm. (c) $h_{(2)}$ = 10.2 mm, a = 0.45 mm. (d) $h_{(2)}$ = 15.3 mm, a = 0.45 mm.

attachment mode mainly yields an offset in the reactive part of the input impedance. In this case, the radius of the circular attachment mode was extended to the two closest edges for the best results.

This investigation was an attempt to gain a better understanding of the abilities of two widely-used attachment modes for a SDMM analysis of probe-fed microstrip patch antennas. It is clear from the results that have been presented here, that the circular attachment mode treats all patch sizes and substrate thicknesses with good accuracy, but that the rectangular attachment mode only works well for resonant patches, albeit it on thin and thick substrates. It would appear that the magnetic-wall cavity model with a uniform current filament source, upon which the rectangular attachment mode is based, is not a good approximation when dealing with very small patches, thereby resulting in the inaccuracies that have been observed. Some other benefits of the circular attachment mode over the rectangular attachment mode, is that it can be used with any shape of patch and that it is faster to evaluate. Furthermore, attachment modes, analogous to the rectangular attachment mode, which is based on the eigenmodes of the magnetic-wall cavity model, must be derived from scratch for other shapes of patches. One uncertainty related to the circular attachment mode, however, is the choice of the radius over which the current spreads on the surface of the patch. In all cases that were considered, the accuracy increased as the radius of the disk was increased. It has been stated by Taboada [108] that for triangular Rao, Wilton and Glisson (RWG) basis functions [104], the support of the attachment mode should be larger than the underlying subdomain basis functions. It also seems to be true in this case, implying that it should be possible to use a smaller radius for the attachment mode together with underlying subdomain basis functions, if these basis functions are also decreased in size. Finally, taking into account all of the observations, it would appear that the circular attachment mode is the more versatile of the two. The circular attachment mode, as well as a higher-order circular attachment mode that was developed in Chapter 3, will now be used to analyse both the circular and rectangular probe-fed capacitor patches.

4.2.3 Capacitor Patches

Following from the investigation into the attachment modes, it makes sense to retain only the circular attachment mode, as it is more versatile than the rectangular one. It will now be used to further validate the SDMM implementation in terms of its ability to model both the circular and rectangular probe-fed capacitor patches as shown in Figures 4.8 to 4.10.

Consider the circular capacitor patch as shown in Figure 4.8. The electric current density on the patch was modelled with only the circular attachment mode, having a radius of b, while the current density on the probe, having a radius of a, was modelled with four PWS basis functions (excluding the one associated with the attachment mode). Figure 4.11 shows the simulated input impedance of the circular capacitor patch, as a function of the probe radius. Additionally, it is also shown for two different radii of the capacitor patch. Here, SDMM refers to the implementation using the normal

circular attachment mode, while SDMM (HO) refers to the implementation using the higher-order circular attachment mode. It can be seen that the higher-order circular attachment mode predicts a slightly higher input reactance than the normal circular attachment mode. Furthermore, as far as the input reactance goes, the results for the higher-order circular attachment mode seem to follow the IE3D results rather closely, while the results of the normal circular attachment mode seem to be closer to the FEKO results. In general, however, all the results agree fairly well.

In order to make sure that the SDMM implementation can also calculate the coupling between two capacitor patches accurately, two probe-fed circular capacitor patches in fairly close proximity, were analysed. The geometry is shown in Figure 4.9. The same number of basis functions on each patch and probe was used as for the previous example. In this case, the higher-order circular attachment mode was used (the normal one basically gives the same results). Figure 4.12 shows the simulated coupling between the two capacitor patches. It can be seen that both the magnitude and the phase of the coupling, as predicted by the SDMM implementation, agrees very well with the results of both IE3D and FEKO.

Consider the rectangular capacitor patch as shown in Figure 4.10. The electric current density on the patch, having a size of $l \times w$, was modelled with subdomain rooftop basis functions, while the current density on the probe, having a radius of a, was modelled with four piecewise sinusoidal basis functions (excluding the one associated with the attachment mode). Figure 4.13 shows the simulated input impedance of the rectangular capacitor patch, as a function of the probe radius. Additionally, it is also shown for two sizes of the rectangular patch. For the patch size of 5 mm $\times$ 5 mm, twelve subdomain rooftop basis were used on the patch, while for the patch size of 5 mm $\times$ 20 mm, forty-seven were used. In both cases, a radius of 2.5 mm was used for the circular attachment mode. Once again, SDMM refers to the implementation using the normal circular attachment mode, while SDMM (HO) refers to the implementation using the higher-order circular attachment mode. In this case it can be seen that, apart from a small difference in the input reactance for the larger patch, there is not much difference between the results of the normal circular attachment mode and the higher-order version. For the small patch, there is good agreement between the various codes, but for the larger patch, there seem to be more variation in the results. Overall though, it would appear that the agreement is not far off.

The results in this section have shown that the SDMM implementation can model the probe-fed capacitor patches quite successfully. The validation will now continue by adding a square resonant patch to the structure, resulting in a single patch antenna element with a capacitive feed probe.

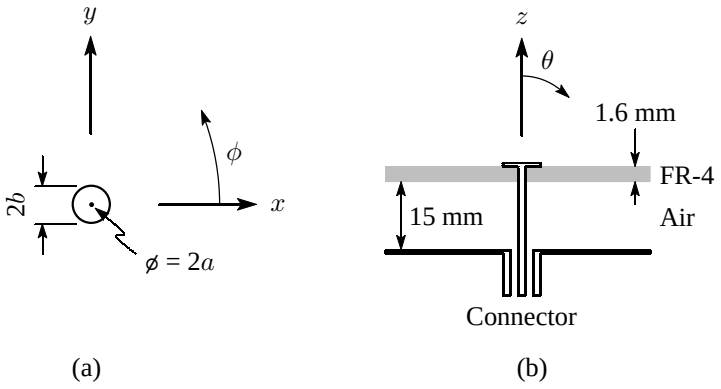

Figure 4.8 Geometry of the circular capacitor patch. (a) Top view of the patch. (b) Side view of the multilayered substrate with $\varepsilon_r = 4.25$ and $\tan\delta_\varepsilon = 0.02$ for the FR-4 layer and with $\varepsilon_r = 1$ and $\tan\delta_\varepsilon = 0$ for the air layer.

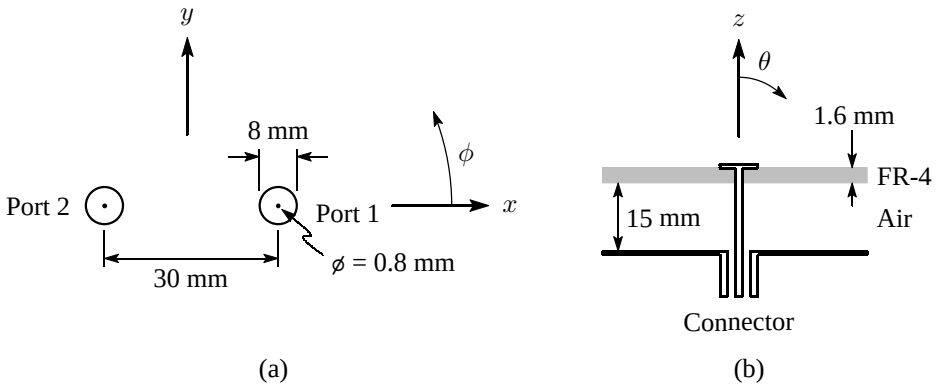

Figure 4.9 Geometry of two circular capacitor patches in close proximity. (a) Top view of the patches. (b) Side view of the multilayered substrate with $\varepsilon_r = 4.25$ and $\tan\delta_\varepsilon = 0.02$ for the FR-4 layer and with $\varepsilon_r = 1$ and $\tan\delta_\varepsilon = 0$ for the air layer.

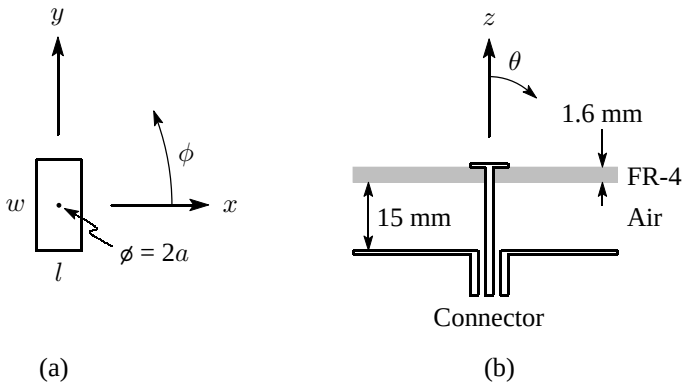

Figure 4.10 Geometry of the rectangular capacitor patch. (a) Top view of the patch. (b) Side view of the multilayered substrate with $\varepsilon_r = 4.25$ and $\tan\delta_\varepsilon = 0.02$ for the FR-4 layer and with $\varepsilon_r = 1$ and $\tan\delta_\varepsilon = 0$ for the air layer.

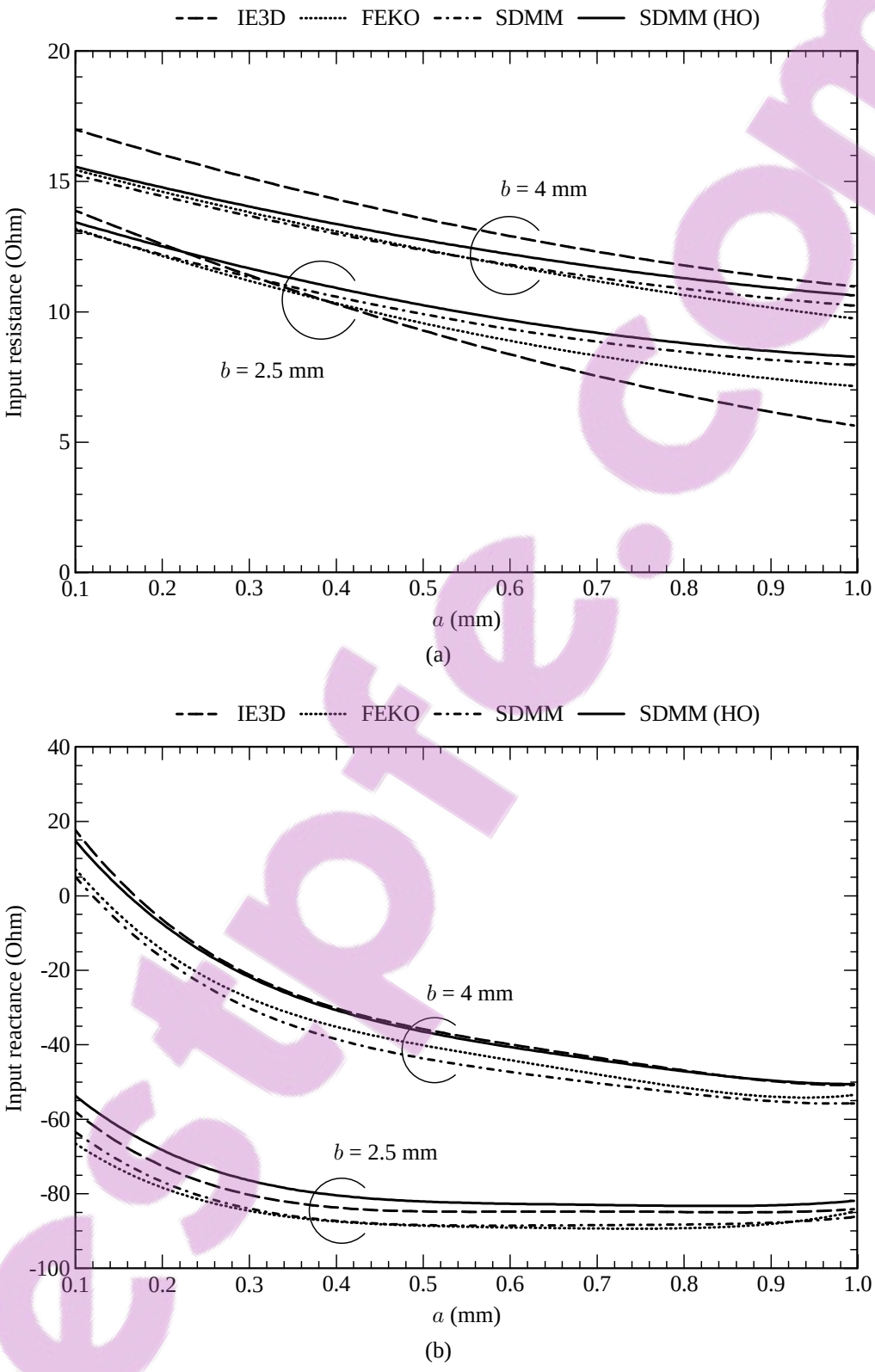

Figure 4.11 Input impedance (at 1.8 GHz) of the circular capacitor patch. (a) Input resistance. (b) Input reactance.

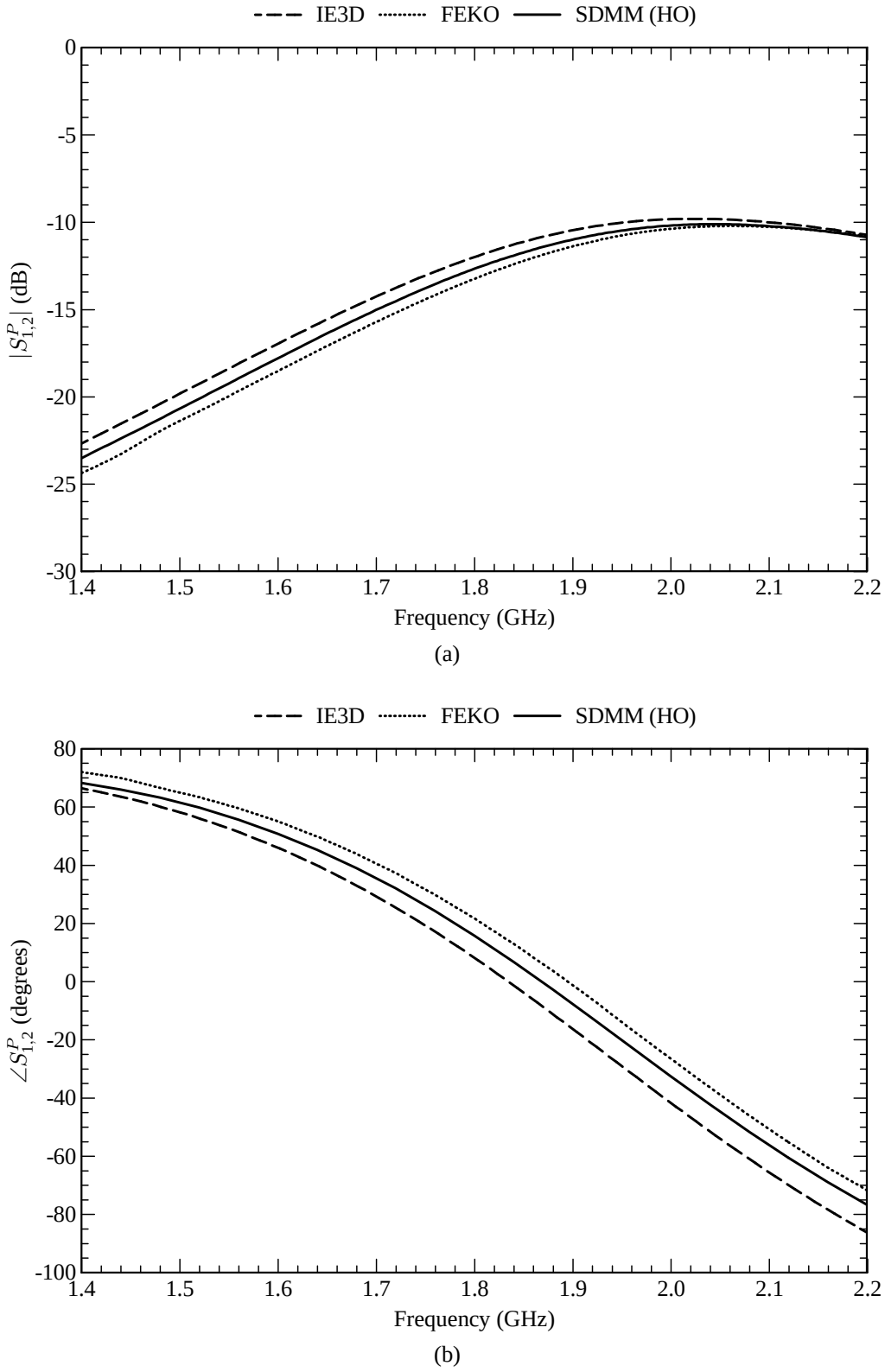

Figure 4.12 Coupling between the two circular capacitor patches. (a) Magnitude. (b) Phase.

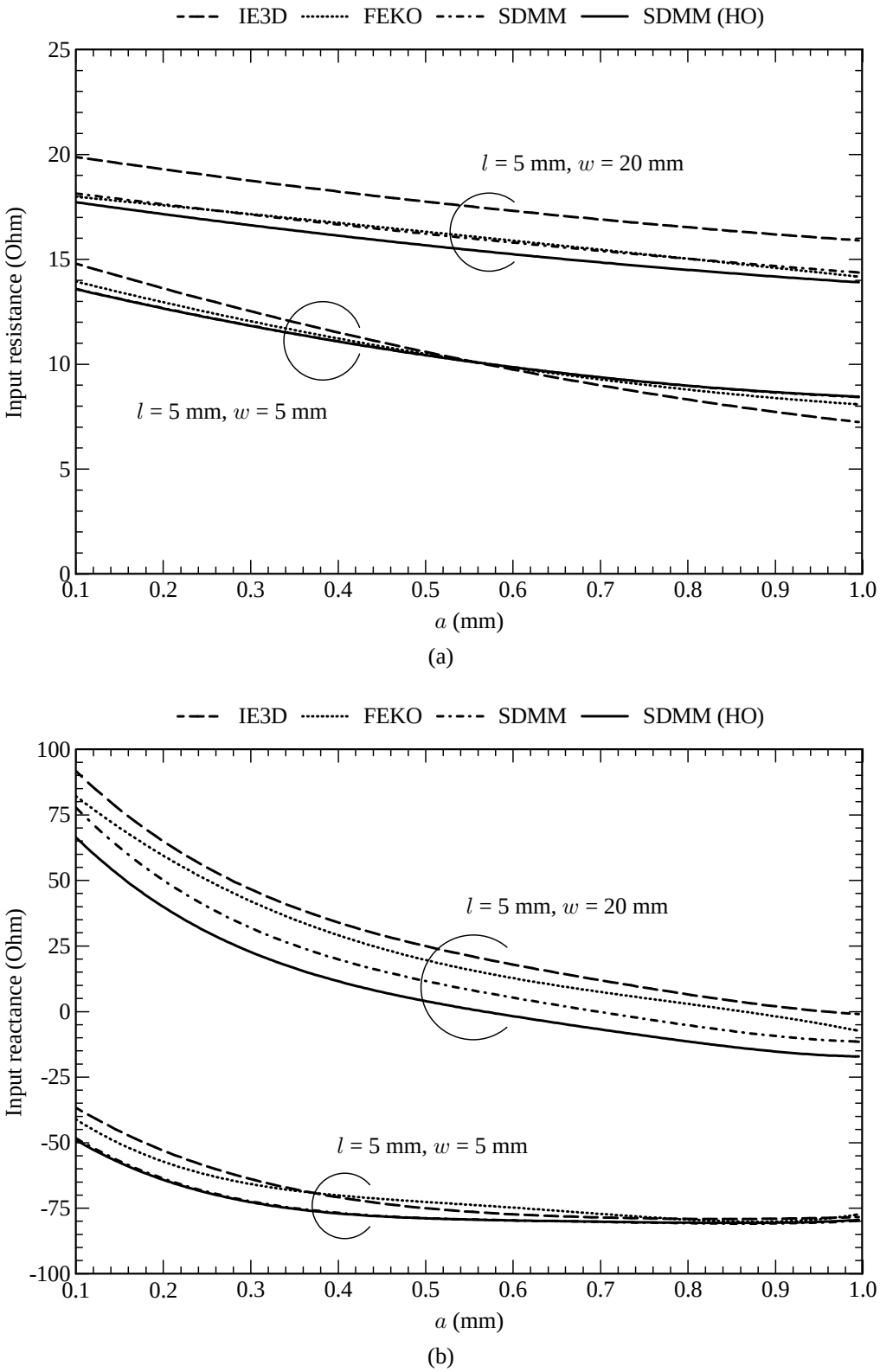

Figure 4.13 Input impedance (at 1.8 GHz) of the rectangular capacitor patch. (a) Input resistance. (b) Input reactance.

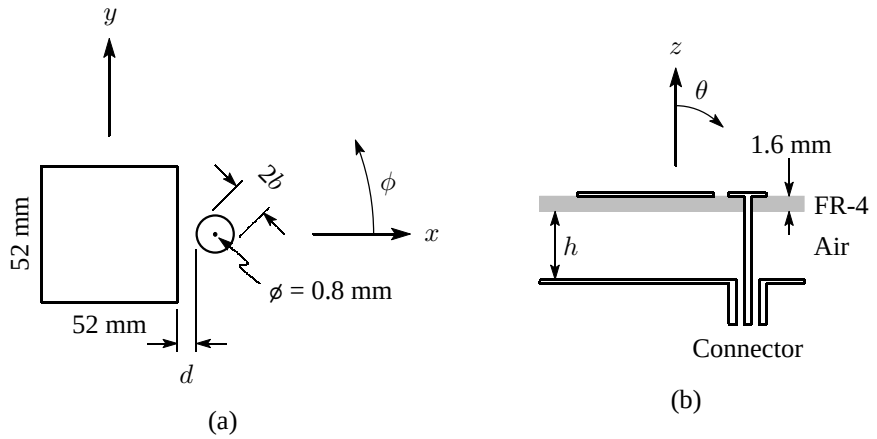

Figure 4.14 Geometry of the antenna element with a circular capacitor patch. (a) Top view of the antenna element. (b) Side view of the multilayered substrate with $\varepsilon_r = 4.25$ and $\tan\delta_\varepsilon = 0.02$ for the FR-4 layer and with $\varepsilon_r = 1$ and $\tan\delta_\varepsilon = 0$ for the air layer.

4.2.4 Antenna Elements with Capacitive Feed Probes

The new antenna element is excited by making use of capacitive coupling through either a circular probe-fed capacitor patch or a rectangular probe-fed capacitor patch. In terms of validating the SDMM implementation, both configurations will now be considered.

First consider the antenna element with a circular capacitor patch, as shown in Figure 4.14. In order to obtain a better understanding in terms of the choice and number of basis functions that are required to model the antenna element, Figures 4.15 and 4.16 provide some convergence tests. The results in Figure 4.15 show how the input impedance of the antenna varies as a function of the number of sinusoidal entire-domain modes on the resonant patch when keeping the number of segments on the probe fixed. Each curve in Figures 4.15(a) and (b) starts with the (1,0) x-directed mode on the left-hand side of the x axis, after which other x-directed modes are added accumulatively as one moves towards the right-hand side of the x axis (i.e. for a specific x-directed mode, all the modes towards its left are also included). Furthermore, in the two graphs, each curve corresponds with a specific number of y-directed modes. The first curve assumes that there is no y-directed mode, after which y-directed modes are added accumulatively for the rest of the curves. From these results it can definitely be seen that the results converge as the number of x- and y-directed modes is increased. The results in Figure 4.16 show how the input impedance of the antenna varies as a function of the number of segments on the probe (each full PWS basis function spans two adjacent segments) when keeping the number of sinusoidal entire-domain basis functions on the resonant patch fixed. Here too, it can be seen that the results converge as the number of segments is increased.

Based on the convergence tests, the electric current density on the structure was finally modelled with eleven entire-domain sinusoidal basis functions on the resonant patch, the single circular

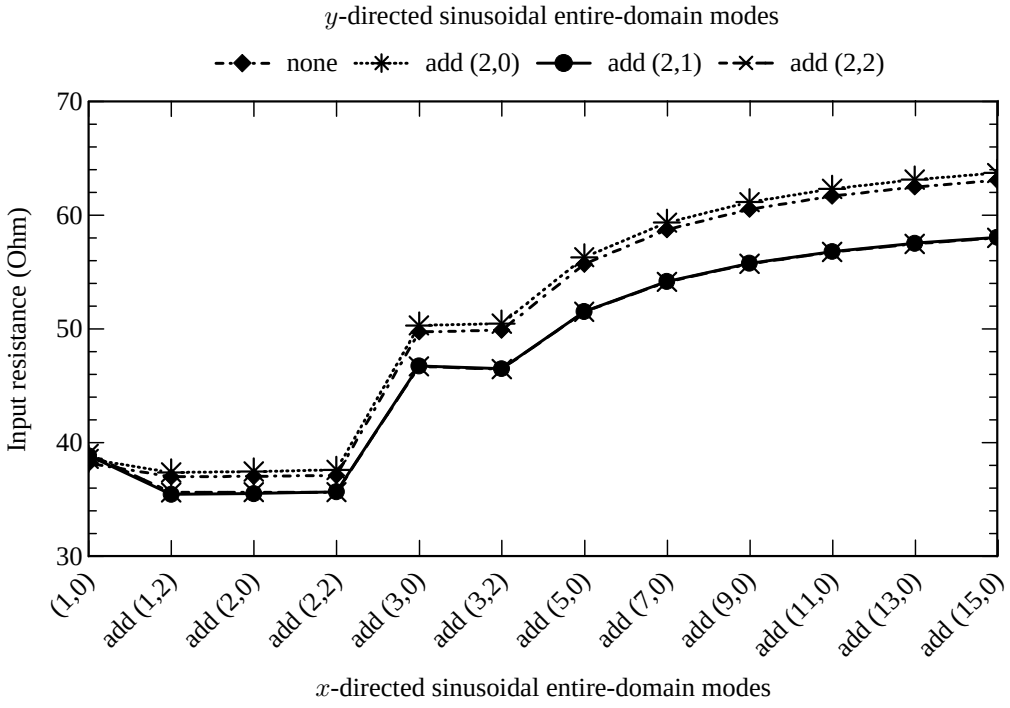

(a)

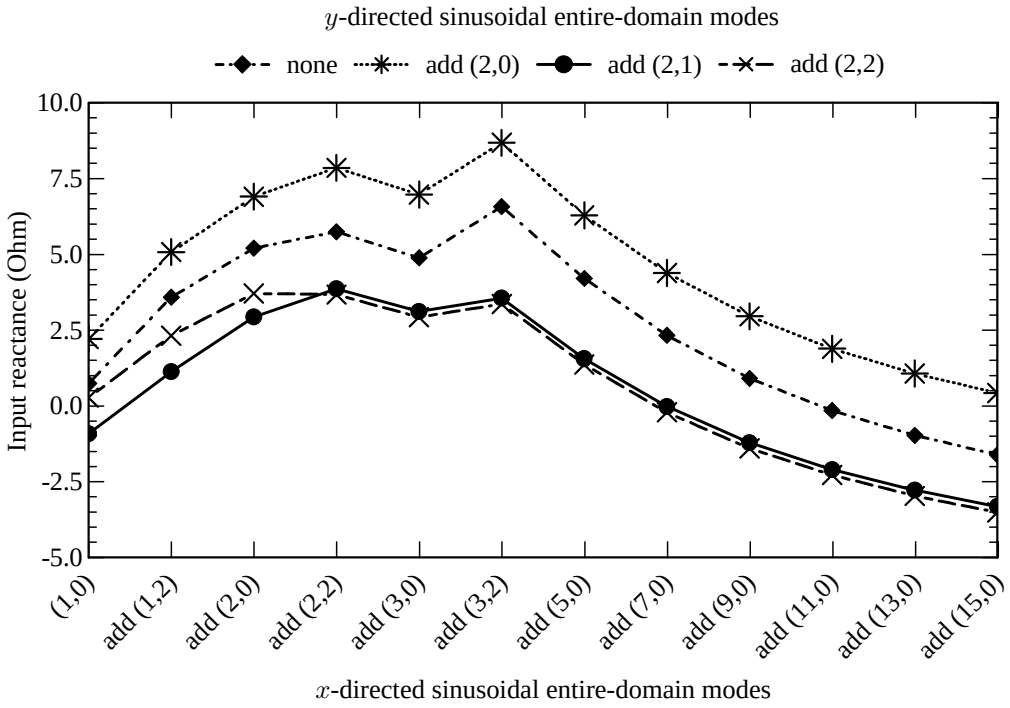

(b)

Figure 4.15 Input impedance (at 1.8 GHz and with four segments on the probe) of the antenna element with a circular capacitor patch, but as a function of the entire-domain sinusoidal basis functions on the resonant patch. Parameters: b = 4.5 mm and d = 4 mm. (a) Input resistance. (b) Input reactance.

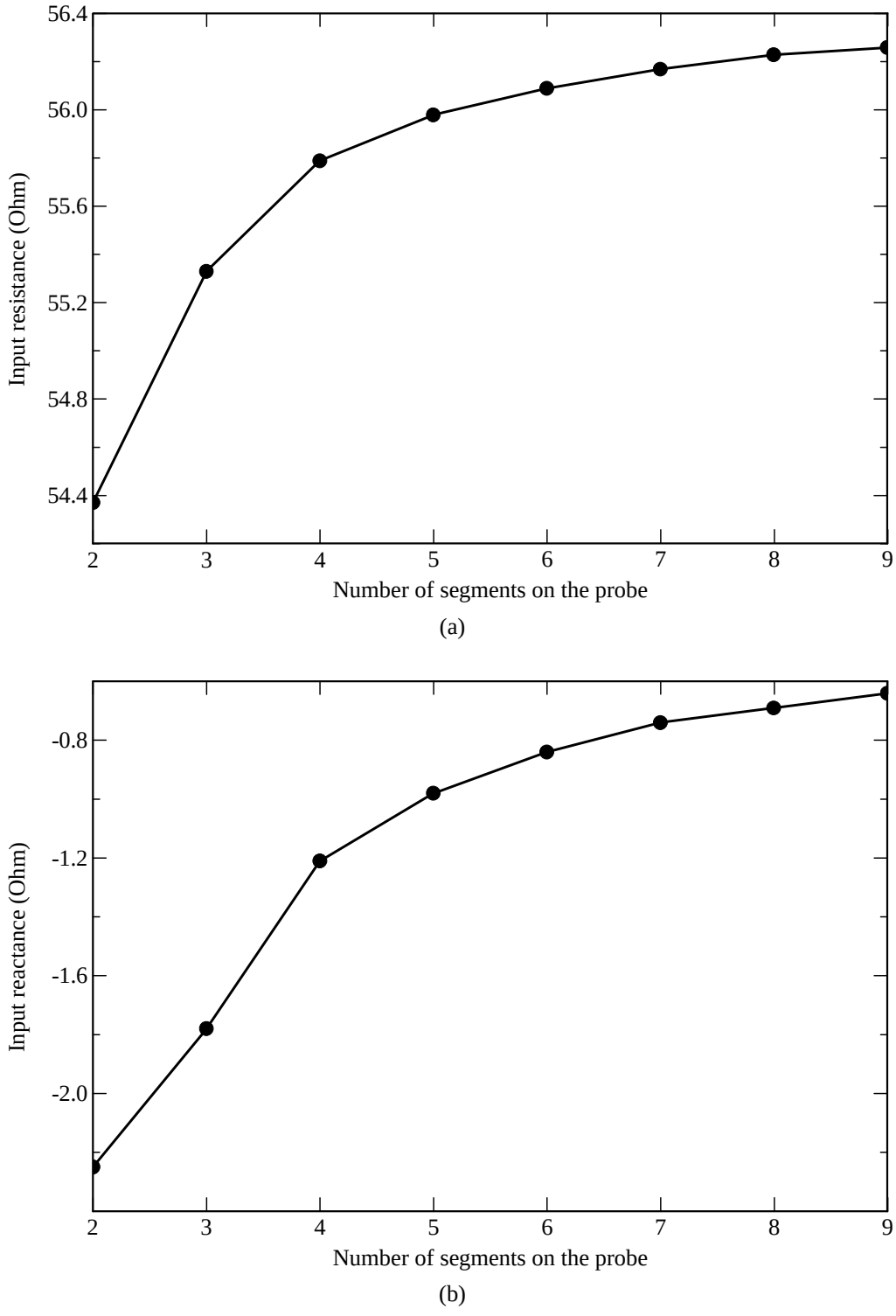

Figure 4.16 Input impedance (at 1.8 GHz) of the antenna element with a circular capacitor patch, but as a function of the number of segments on the probe. For the entire-domain sinusoidal basis functions on the resonant patch, the (1,0), (1,2), (2,0), (2,2), (3,0), (3,2), (5,0), (7,0) and (9,0) modes were used for the x-directed current, while the (2,0) and (2,1) modes were used for the y-directed current. Parameters: b = 4.5 mm and d = 4 mm. (a) Input resistance. (b) Input reactance.

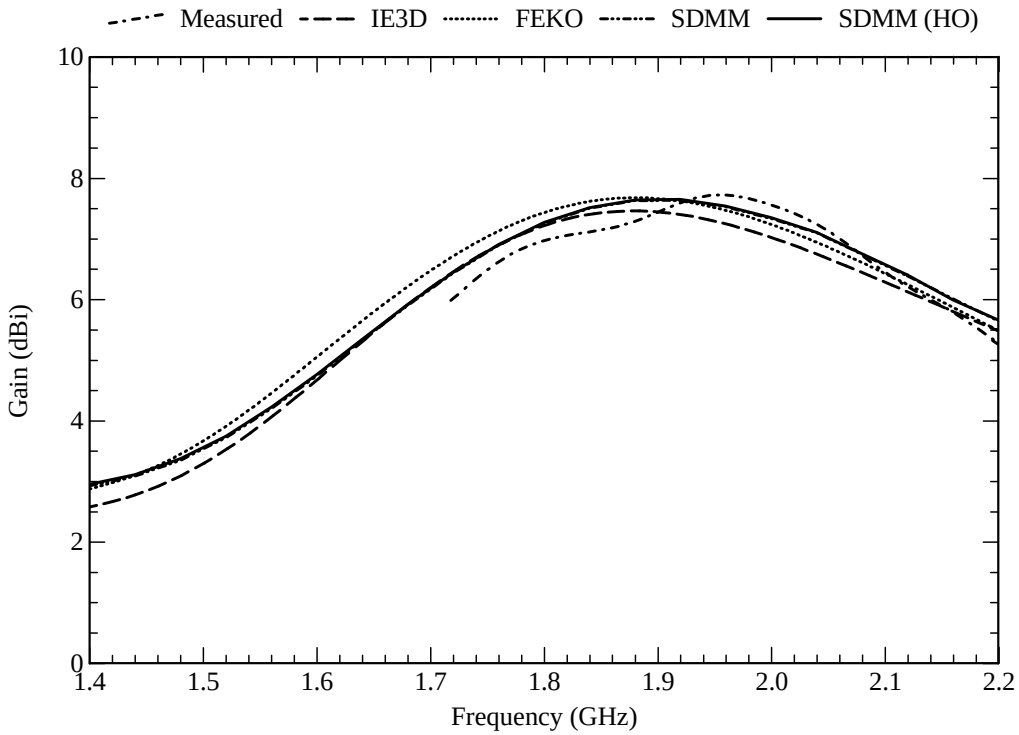

Figure 4.17 Gain of the patch antenna with a circular capacitor patch. Parameters: b = 4.5 mm and d = 4 mm.

attachment mode on the capacitor patch, and four PWS basis functions on the probe (excluding the one associated with the attachment mode). For the entire-domain sinusoidal basis functions, the (1,0), (1,2), (2,0), (2,2), (3,0), (3,2), (5,0), (7,0) and (9,0) modes were used for the x-directed current, while the (2,0) and (2,1) modes were used for the y-directed current. The electric current density on the resonant patch is primarily directed along the x direction. Figure 4.17 shows the simulated and measured gain of the antenna element, from which it can be seen that the agreement between the three codes and the measurements, is very good. Here, SDMM refers to the implementation using the normal circular attachment mode, while SDMM (HO) refers to the implementation using the higher-order circular attachment mode. As can be seen, there is practically no difference in the results obtained with the two circular attachment modes. Figure 4.18 shows the simulated and measured input impedance of the antenna element, from which it can also be seen that the agreement between the three codes and the measurements, is fairly good. The simulation with the higher-order circular attachment mode appears to provide results that agree better with those of the two commercial codes and the measurements than that of the normal circular attachment mode, especially for the reactive part of the input impedance. Figure 4.19 shows the simulated radiation patterns in the *E*-plane and the *H*-plane of the antenna element. From these it can be seen that, once again, the agreement between the three codes is fairly good, while there is practically no difference in the results obtained with the two circular attachment modes. The cross-polarised pattern in the *E*-plane of the antenna element is very low and therefore has not

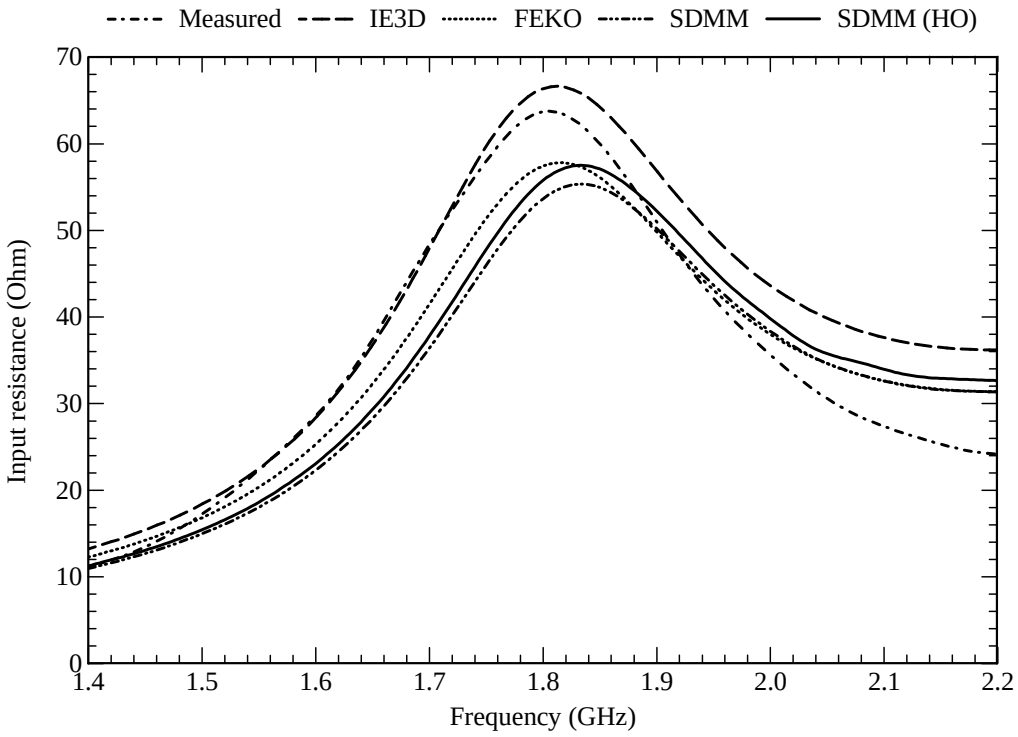

(a)

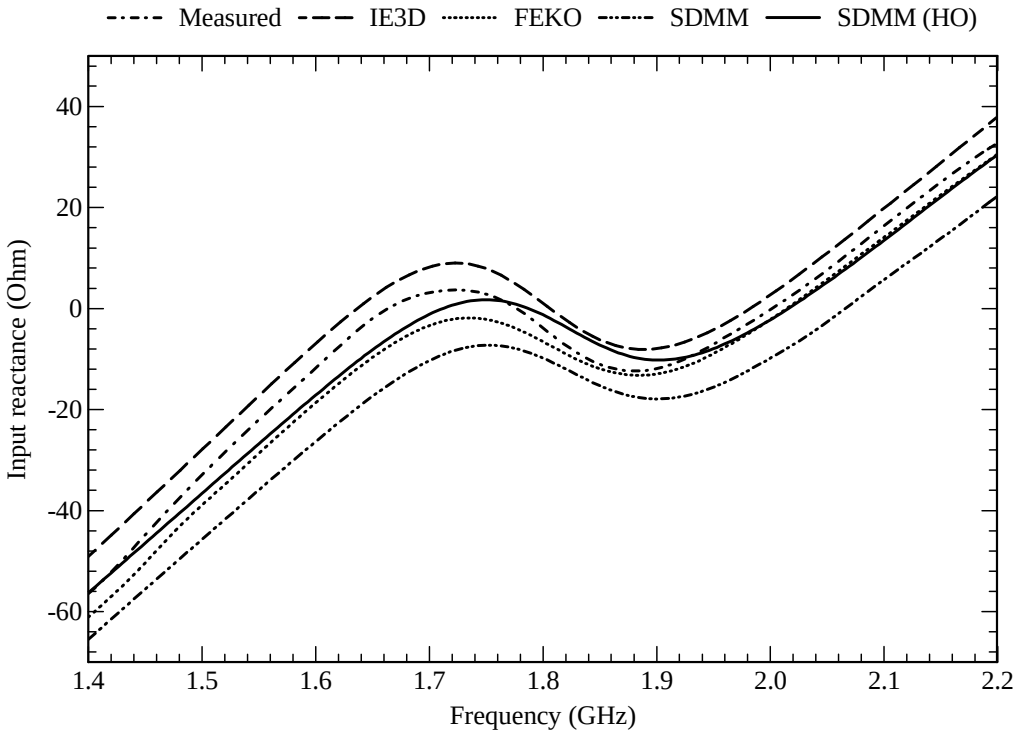

(b)

Figure 4.18 Input impedance of the antenna element with a circular capacitor patch. Parameters: b = 4.5 mm and d = 4 mm. (a) Input resistance. (b) Input reactance.

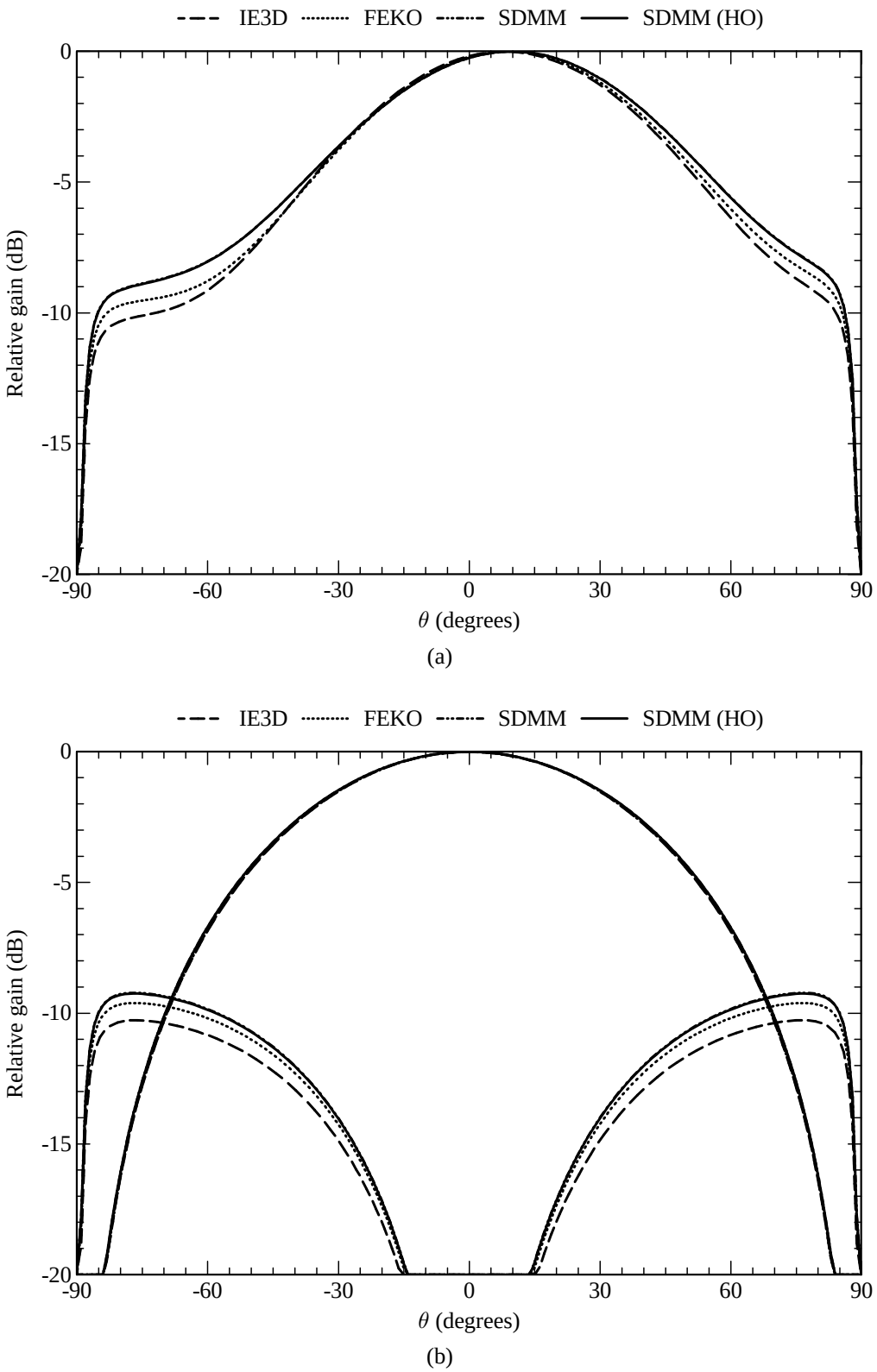

Figure 4.19 Radiation patterns (at 1.8 GHz) of the antenna element with a circular capacitor patch. Parameters: b = 4.5 mm and d = 4 mm. (a) Radiation pattern in the E-plane ($\phi = 0^\circ$). (b) Radiation pattern in the H-plane ($\phi = 90^\circ$).

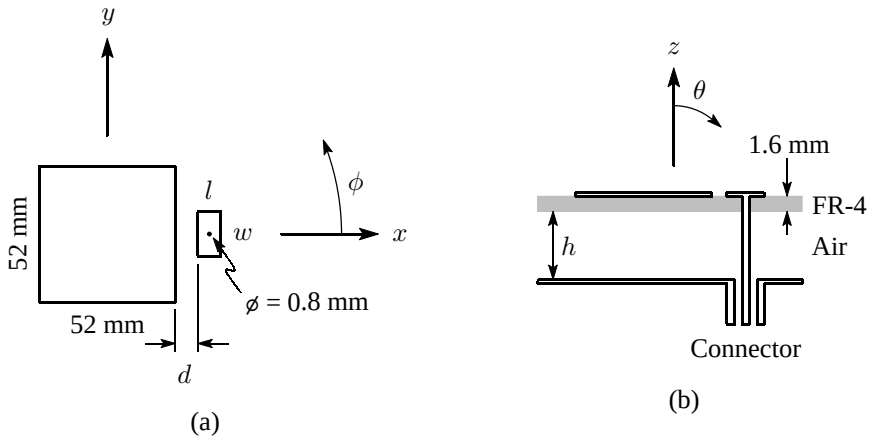

Figure 4.20 Geometry of the antenna element with a rectangular capacitor patch. (a) Top view of the antenna element. (b) Side view of the multilayered substrate with $\varepsilon_r = 4.25$ and $\tan\delta_\varepsilon = 0.02$ for the FR-4 layer and with $\varepsilon_r = 1$ and $\tan\delta_\varepsilon = 0$ for the air layer.

been shown. On the other hand, it can be seen that the cross-polarised pattern in the *H*-plane is somewhat higher, especially towards the horizon (i.e. as θ approaches $\pm 90^\circ$). This behaviour is due to the symmetry in one plane of the structure, but the asymmetry in the orthogonal plane.

Now, consider the patch antenna element with a rectangular capacitor patch, as shown in Figure 4.20. The electric current density on the structure was modelled with eleven entire-domain sinusoidal basis functions on the resonant patch, the circular attachment mode, and twenty-two subdomain rooftop basis functions on the capacitor patch. Four PWS basis functions were used on the probe (excluding the one associated with the attachment mode). For the entire-domain sinusoidal basis functions, the (1,0), (1,2), (2,0), (2,2), (3,0), (3,2), (5,0), (7,0) and (9,0) modes were used for the x-directed current, while the (2,0) and (2,1) modes were used for the y-directed current. A radius of 2.5 mm was used for the attachment mode. Figure 4.21 shows the simulated and measured gain of the antenna element, from which it can be seen that the agreement between the three codes and the measurements, is very good. Here too, there is practically no difference in the results obtained with the two circular attachment modes. Figure 4.22 shows the simulated and measured input impedance of the antenna element, from which it can also be seen that the agreement between the three codes and the measurements, is fairly good. The input reactance as simulated by the SDMM implementation, seems to be slightly lower when compared to the rest. Also, as compared to the antenna element with the circular capacitor patch, there is not so much difference between the results obtained with the two circular attachment modes. Figure 4.23 shows the simulated radiation patterns in the *E*-plane and the *H*-plane of the antenna element. From these it can be seen that, once again, the agreement between the three codes is fairly good and that there is also practically no difference in the results obtained with the two circular attachment modes. The cross-polarised pattern in the *H*-plane shows some spread between the results of the three codes. However, the SDMM results lie in between those of the other two codes. Also,

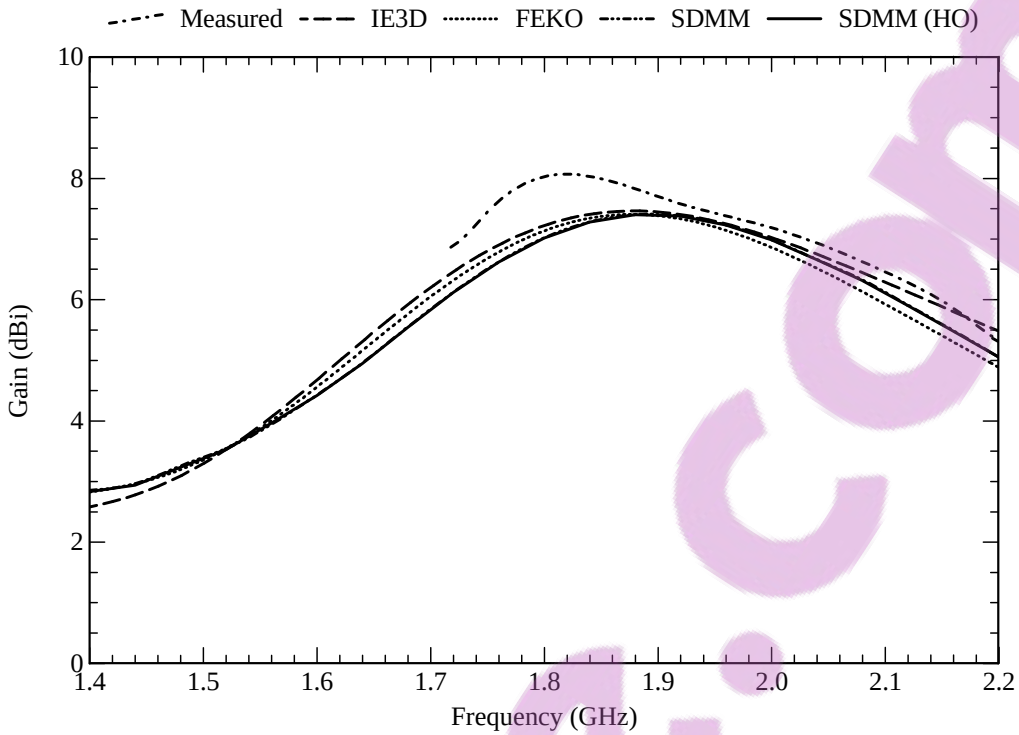

Figure 4.21 Gain of the antenna element with a rectangular capacitor patch. Parameters: l = 5 mm, w = 10 mm and d = 8 mm.

the cross-polarised pattern of this antenna element appears to be slightly higher than the one for the element with the circular capacitor patch.

Following from all of the results that have been presented in this section, it can be concluded that the SDMM implementation compares very well with measurements and also with the two commercial codes. In the next section, it will now be used to characterise antenna elements with capacitive feed probes. The higher-order circular attachment mode will be used henceforth, as it appears to provide results that agree well with those of the two commercial codes and the measurements when considering all the configurations that were used for the validation.

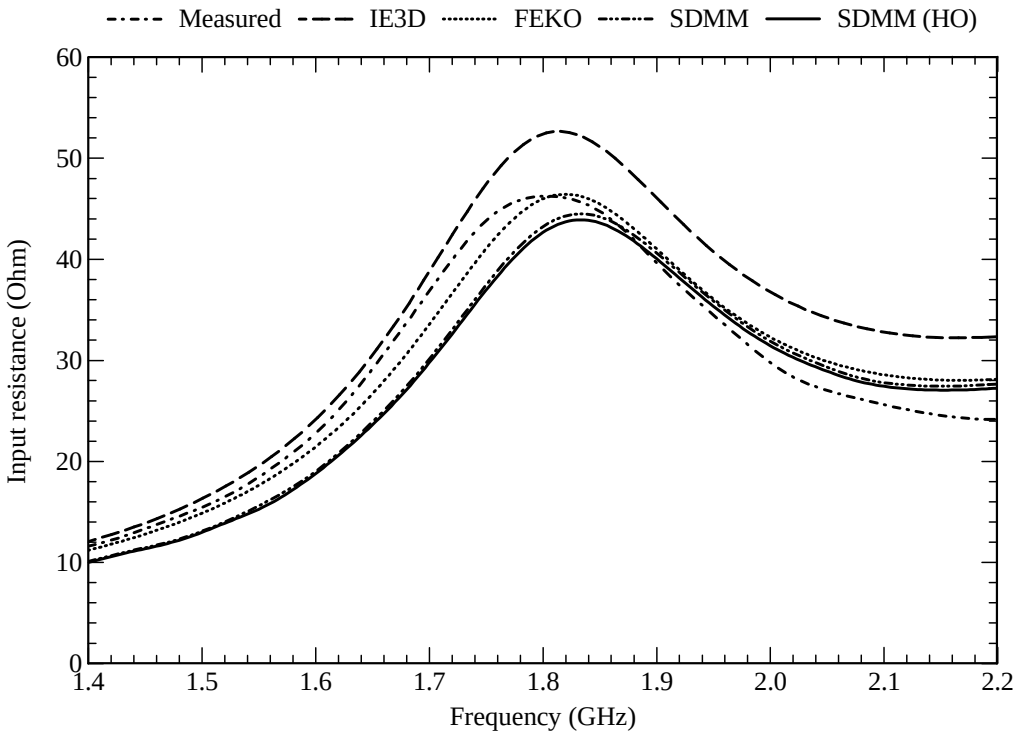

(a)

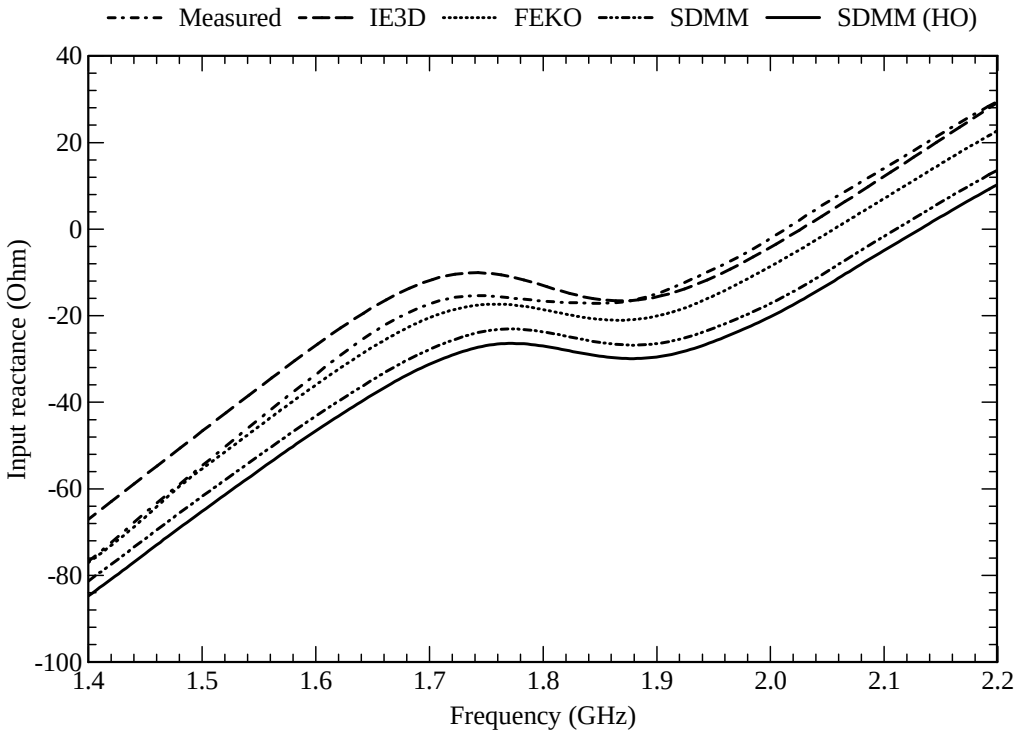

(b)

Figure 4.22 Input impedance of the antenna element with a rectangular capacitor patch. Parameters: l = 5 mm, w = 10 mm and d = 8 mm. (a) Input resistance. (b) Input reactance.

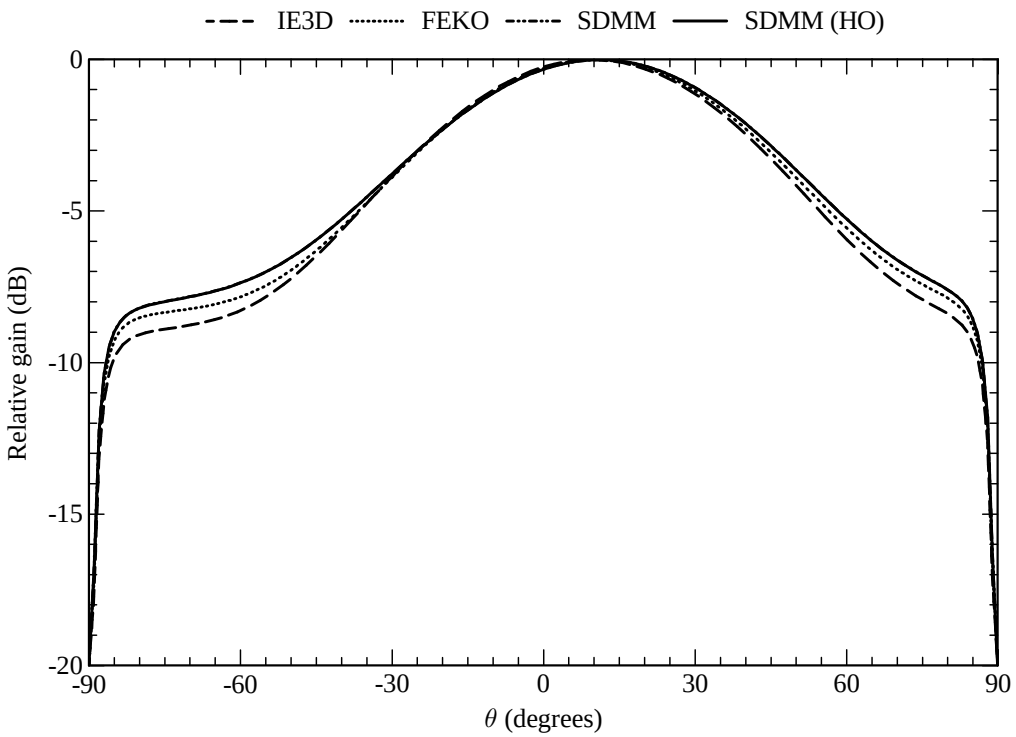

(a)

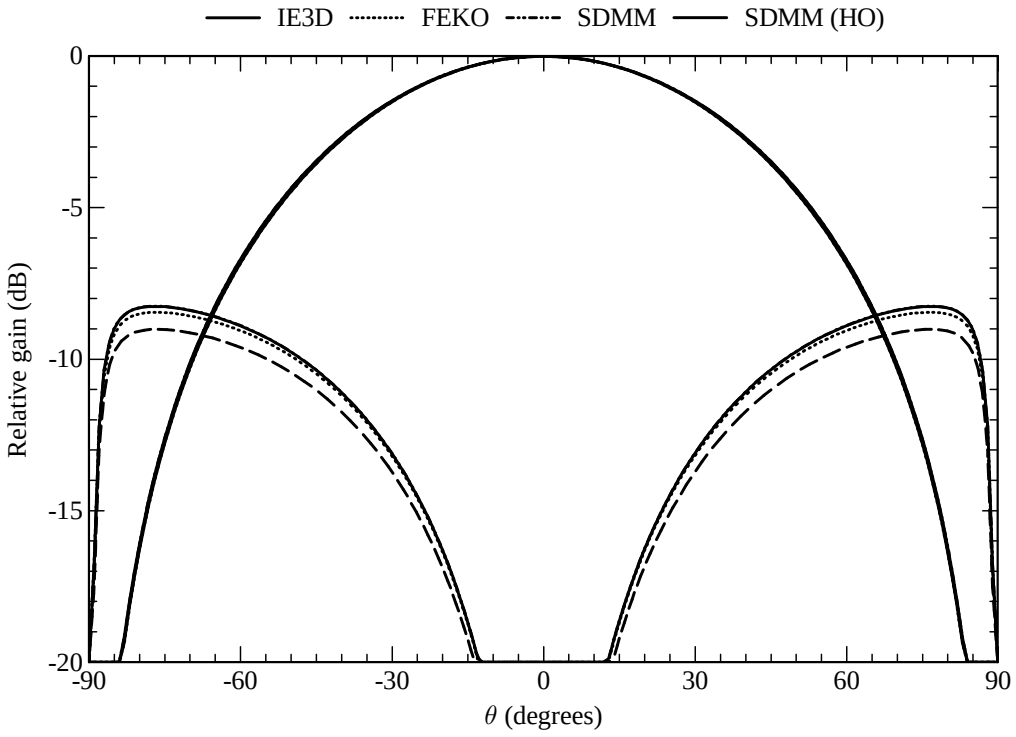

(b)

Figure 4.23 Radiation patterns (at 1.8 GHz) of the antenna element with a rectangular capacitor patch. Parameters: l = 5 mm, w = 10 mm and d = 8 mm. (a) Radiation pattern in the E-plane ($\phi = 0^\circ$). (b) Radiation pattern in the H-plane ($\phi = 90^\circ$).

4.3 CHARACTERISATION OF ANTENNA ELEMENTS WITH CAPACITIVE FEED PROBES

For both the antenna element with the circular capacitor patch, as shown in Figure 4.14, and the one with the rectangular capacitor patch, as shown in Figure 4.20, there are some key geometrical parameters that can be used to control the antenna's input impedance and bandwidth. In both cases, the size of the capacitor patch, as well as the gap-width between the resonant patch and the capacitor patch, mainly determines the input impedance of the antenna element. The bandwidth of the antenna element is mainly determined by the thickness of the substrate. The effect of these parameters will now be addressed in more detail.

4.3.1 Input Impedance of the Antenna Element

Consider the antenna element with the circular capacitor patch, as shown in Figure 4.14. The radius of the capacitor patch is denoted by b, while the gap width between the resonant patch and the capacitor patch is denoted by d. Figure 4.24(a) shows the effect of the gap width on the antenna input impedance, while Figure 4.24(b) shows the effect of the radius of the capacitor patch on the antenna's input impedance. The same basis functions as in Section 4.2.4 were used for the analysis. From the results it can be seen that the gap width affects both the input resistance and the input reactance, but that its effect on the input resistance is more significant than on the input reactance. Both the input resistance and input reactance decrease as the gap is widened. Furthermore, it can be seen that the radius of the capacitor patch mainly affects the input reactance, while it has hardly any effect on the input resistance. The input reactance becomes more inductive as the radius (and therefore the size) of the capacitor patch is increased.

Now, consider the antenna element with the rectangular capacitor patch, as shown in Figure 4.20. The length of the capacitor patch is denoted by l and its width by w, while the gap width between the resonant patch and the capacitor patch is denoted by d. Figure 4.25(a) shows the effect of the gap width on the antenna's input impedance, Figure 4.25(b) shows the effect of the length of the capacitor patch on the antenna's input impedance, while Figure 4.25(c) shows the effect of the width of the capacitor patch on the antenna's input impedance. Once again, the same basis functions as in Section 4.2.4 were used for the analysis. From the results it can be seen that the gap width once again affects both the input resistance and the input reactance, but that its effect on the input resistance is more significant than on the input reactance. Both the input resistance and input reactance decrease as the gap is widened. Both the length and the width of the capacitor patch mainly affects the input reactance, while they only have a very small effect on the input resistance. The input reactance becomes more inductive as the dimensions (and therefore the size) of the capacitor patch are increased.

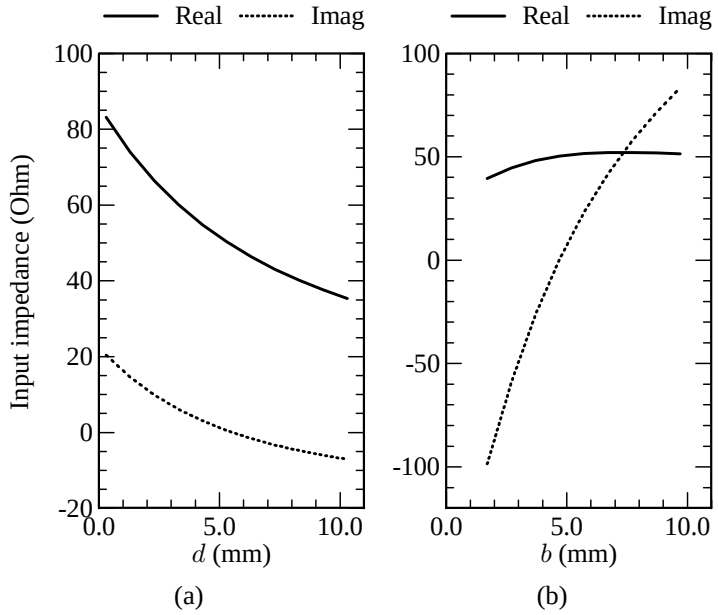

Figure 4.24 Effect (at 1.8 GHz) of some geometrical parameters on the input impedance of the antenna element with the circular capacitor patch. (a) Gap width between rectangular resonant patch and capacitor patch (keep b = 4.5 mm). (b) Radius of the capacitor patch (keep d = 4 mm).

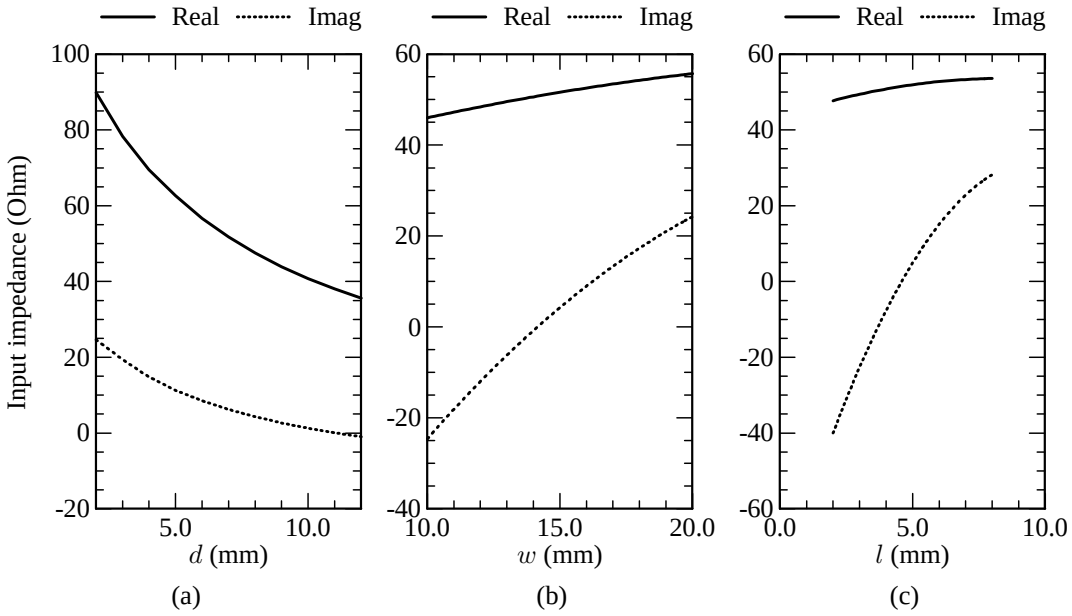

Figure 4.25 Effect (at 1.8 GHz) of some geometrical parameters on the input impedance of the antenna element with the rectangular capacitor patch. (a) Gap width between rectangular resonant patch and capacitor patch (keep l = 5 mm and w = 10 mm). (b) Length of the capacitor patch (keep d = 8 mm and l = 5 mm). (c) Width of the capacitor patch (keep d = 8 mm and w = 10 mm).

4.3.2 Impedance Bandwidth of the Antenna Element

Figures 4.26 and 4.27 show the impedance bandwidth, at various substrate thicknesses, for the antenna elements with the circular and rectangular capacitor patches respectively. Here, the same basis functions as in Section 4.2.4 were also used for the analysis. The bandwidths that correspond to voltage standing-wave ratios (VSWRs) of 1.5:1 and 2:1, are shown. For both sets of results, the thickness of the air layer, denoted by h in Figures 4.14 and 4.20, was varied from 12.5 mm to 25 mm. At every thickness of the air layer, an attempt was made to maximise the impedance bandwidth of the antenna element (i.e. to have as much as possible of the input impedance loci inside the relevant constant VSWR circles on the Smith chart).

It can be seen that the impedance bandwidth increases with increasing substrate thickness, up to a certain point where it more or less seems to taper off and decrease again. A possible explanation for this behaviour is that the coupling mechanism between the various parts of the antenna element is quite complex and also that an attempt was made to match the antenna to 50 Ω at each substrate thickness that was evaluated. For an impedance match on the thinner substrates, the capacitor patch has to be relatively large and closely spaced to the resonant patch. As the substrate thickness is increased, the capacitor patch has to become smaller and also spaced farther apart from the resonant patch. Therefore, the fact that the overall size of the structure and the spacing between the different parts change with substrate thickness, most probably explains the unusual trend (i.e. the relation between impedance bandwidth and substrate thickness does not remain linear). In this context, it is worthwhile to also refer to some results in [193], concerning probe-fed microstrip patch antennas on electrically thick substrates. In [193], the authors indeed show that the impedance bandwidth of probe-fed microstrip patch antennas increases with substrate thickness up to a certain point, after which it decreases again.

As has already been pointed out, the capacitor patch has to be bigger in size and closer to the resonant patch for the thinner air layers, while for thicker air layers, it has to be smaller in size and farther away from the resonant patch. These relationships clearly place a limit on the range of substrate thicknesses that can be used, and therefore also the achievable bandwidths that can be obtained. For example, if the substrate is too thin, the capacitor patch cannot be placed close enough to the resonant patch and would probably have to be positioned below the resonant patch. It can be seen that for these particular antenna elements and specific operating frequency, the optimum bandwidth is achieved for air layers that are between 15 mm and 20 mm thick. Figure 4.28 shows the behaviour of the impedance loci on a Smith chart for the antenna element with the circular capacitor patch. It can be seen that, for a thinner substrate thickness, the loci exhibits a rather wide loop, but that for thicker substrates, the loop becomes tighter.

From the results that have been presented in this section, it is apparent that there are a number of parameters that can be used to control the behaviour of these antenna elements. Such a knowledge, of which parameters are responsible for which behaviour, is very important, especially in an array

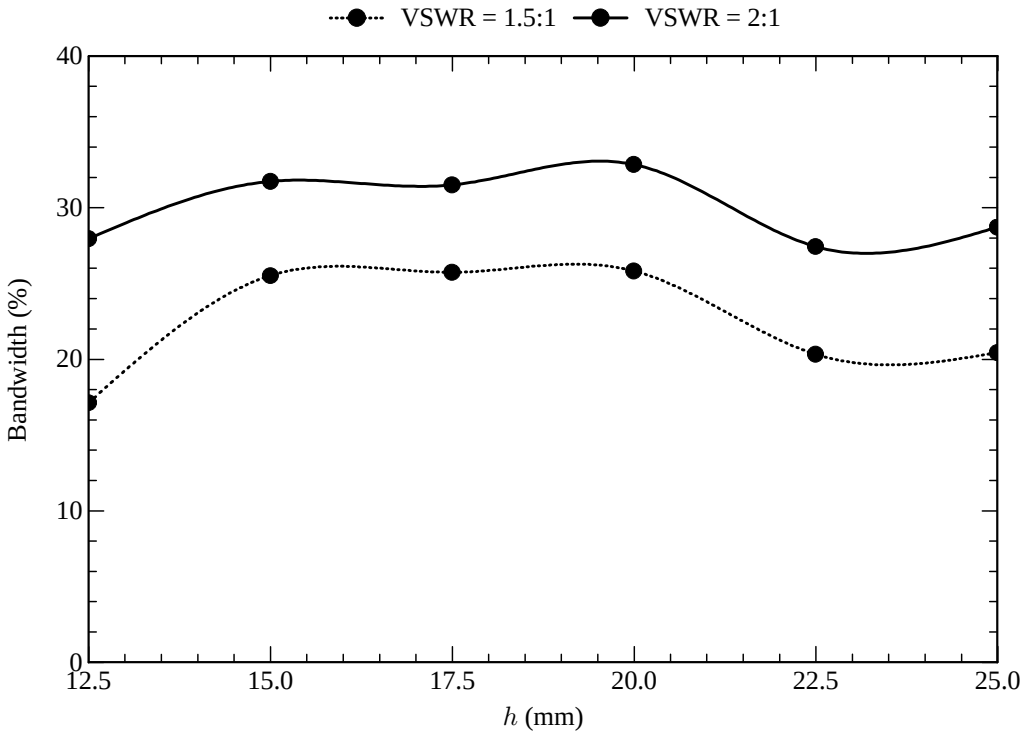

Figure 4.26 Bandwidth (more or less around 1.8 GHz) versus substrate thickness for the antenna element with the circular capacitor patch.

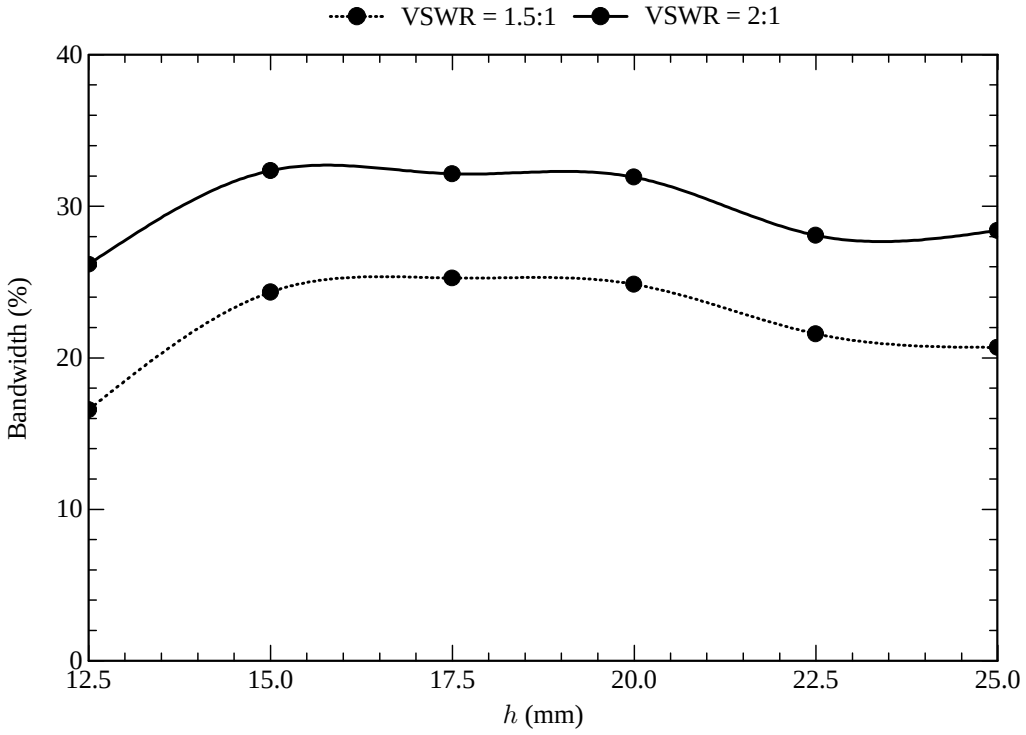

Figure 4.27 Bandwidth (more or less around 1.8 GHz) versus substrate thickness for the antenna element with the rectangular capacitor patch.

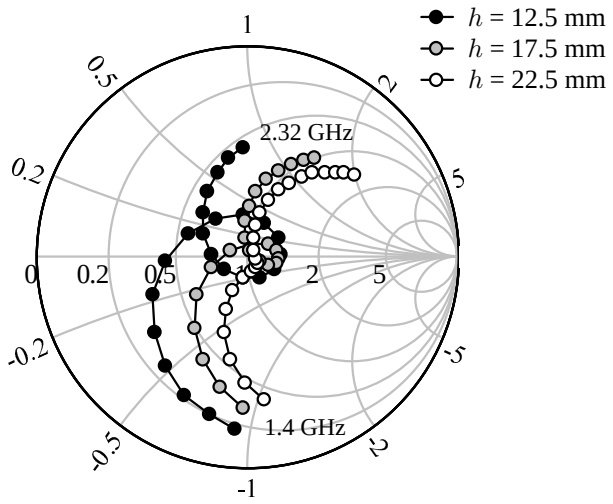

Figure 4.28 Impedance loci (normalised to 50 Ω) of the antenna element with the circular capacitor patch.

environment where there are even more parameters that have an influence on the behaviour of each element. In the next section, it will now be shown how these antenna elements can be used in typical antenna applications.

4.4 APPLICATIONS

Microstrip patch antennas are very often used in array configurations where there might be specific requirements in terms of antenna gain, beamwidth and polarisation. In this section, a number of applications are addressed where patch antennas with capacitive feed probes can be very useful. In Section 4.4.1, it is first shown how the cross-polarisation levels can be reduced for a single antenna element. This is then followed by a discussion on dual-polarised elements in Section 4.4.2. The building block for some of the arrays that are investigated, consists of two elements that are positioned in a back-to-back configuration. The characteristics of such a configuration are addressed in Section 4.4.3. In Sections 4.4.4 and 4.4.5, vertically- and horizontally-polarised arrays are presented, while Sections 4.4.6, 4.4.7 and 4.4.8 are devoted to various $\pm 45^\circ$ slant-polarised arrays. Finally, in Section 4.5, it is shown how the capacitive feed can be used with resonant patches that are not rectangular in shape.

4.4.1 Antenna Element with Reduced Cross-Polarisation Levels

As is evident from the results in Section 4.2.4, an antenna element with a single probe-fed capacitor patch might have cross-polarisation levels in the *H*-plane that are unacceptably high for some applications. It is possible to reduce these levels by making the structure more symmetric. This can be done by adding another probe-fed capacitor patch on the opposite side of the resonant patch, as illustrated in Figure 4.29. However, it is important that the second capacitor patch gets excited exactly out of phase (i.e. a 180° phase difference) with the first capacitor patch. The only

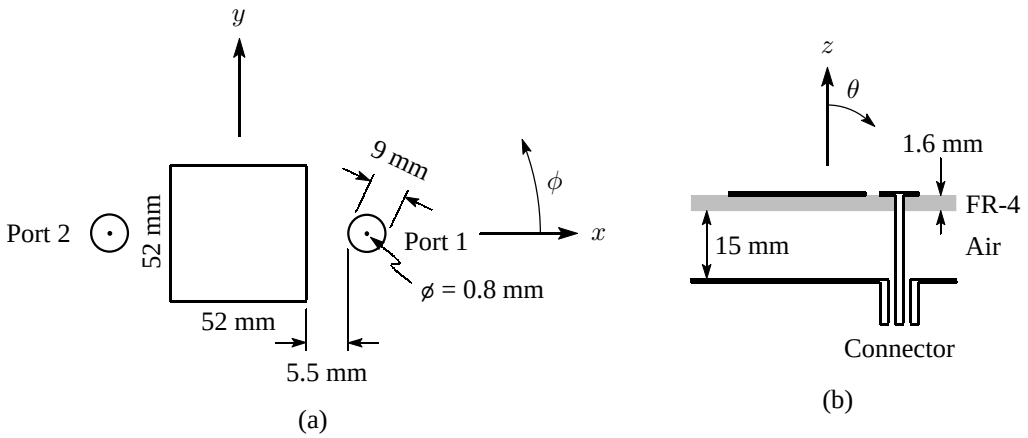

Figure 4.29 Geometry of the antenna element with two capacitor patches for reduced cross-polarisation levels. (a) Top view of the antenna element. (b) Side view of the multilayered substrate with $\varepsilon_r = 4.25$ and $\tan\delta_\varepsilon = 0.02$ for the FR-4 layer and with $\varepsilon_r = 1$ and $\tan\delta_\varepsilon = 0$ for the air layer.

drawback of such an element is that it requires some sort of feed network below the ground plane in order to split the signal and to provide the phase shift. However, this is usually not a problem in an antenna array, as it requires a feed network anyway.

Due to the fact that the antenna element is driven by two ports, the input impedance at a specific port is a function of the self-impedance at that port as well as the mutual impedance between the two ports. It is possible to express the input impedance at any of the ports by making use of the Z-parameters associated with the two ports. The Z-parameters relate the port voltages to the port currents through

$$\begin{Bmatrix} V_1 \\ V_2 \end{Bmatrix} = \begin{bmatrix} Z^P_{1,1} & Z^P_{1,2} \\ Z^P_{2,1} & Z^P_{2,2} \end{bmatrix} \cdot \begin{Bmatrix} I_1 \\ I_2 \end{Bmatrix}, \tag{4.2}$$

where V_1 and V_2 are the voltages at ports 1 and 2 respectively, and I_1 and I_2 are the currents at these ports. The voltage at port 1 can therefore be expressed as

$$V_1 = Z^P_{1,1} I_1 + Z^P_{1,2} I_2. \tag{4.3}$$

From (4.3), it then follows that the input impedance at port 1, Z^{in}_1, can be expressed as

$$\begin{aligned} Z^{\text{in}}_1 &= \frac{V_1}{I_1} \\ &= Z^P_{1,1} + Z^P_{1,2}\left(\frac{I_2}{I_1}\right). \end{aligned} \tag{4.4}$$

Now, due to the 180° phase difference between I_1 and I_2, $I_2 = -I_1$. The input impedance at port 1 then reduces to

$$Z^{\text{in}}_1 = Z^P_{1,1} - Z^P_{1,2}. \tag{4.5}$$

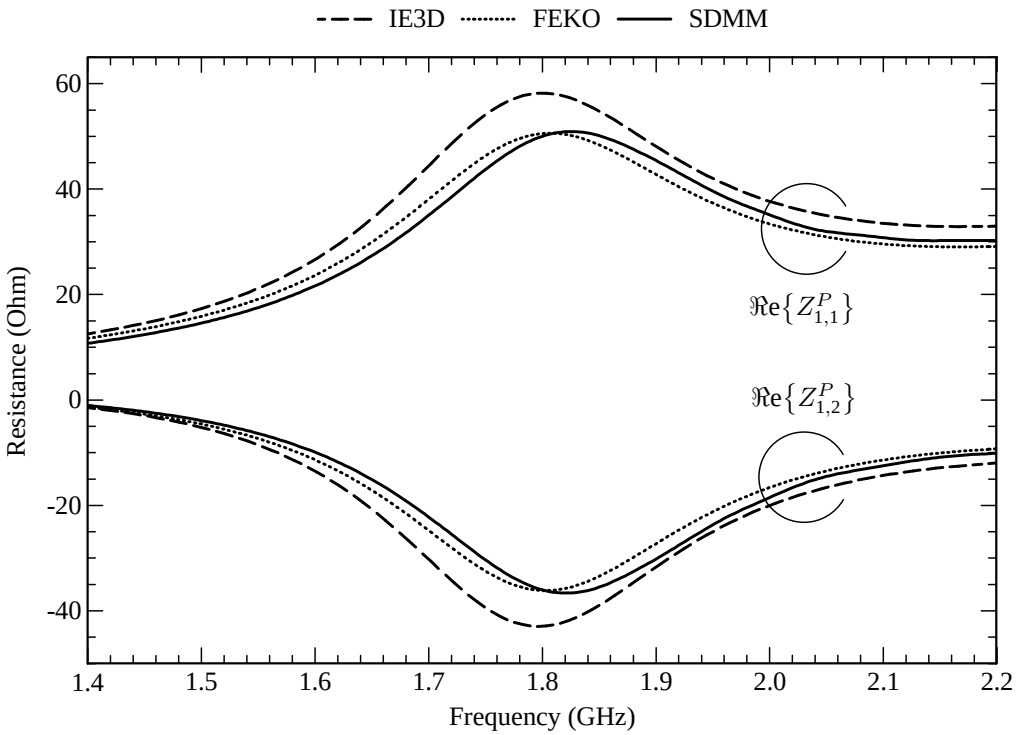

(a)

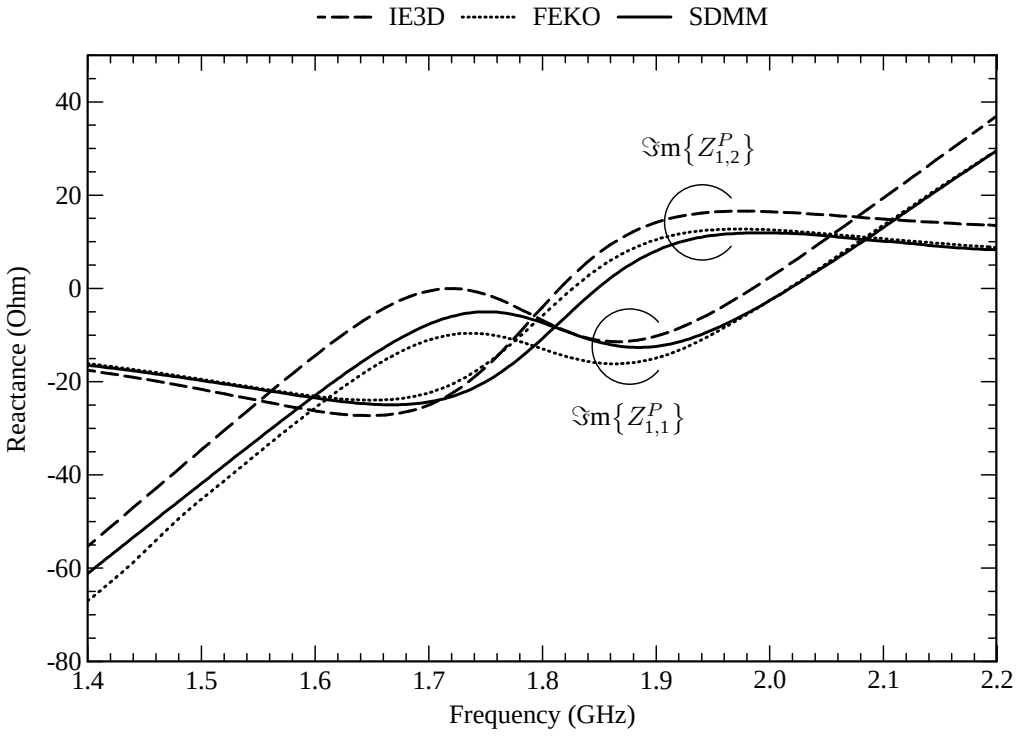

(b)

Figure 4.30 *Z*-parameters of the two ports of the antenna element with two capacitor patches for reduced cross-polarisation levels. (a) Resistive part of the *Z*-parameters. (b) Reactive part of the *Z*-parameters.

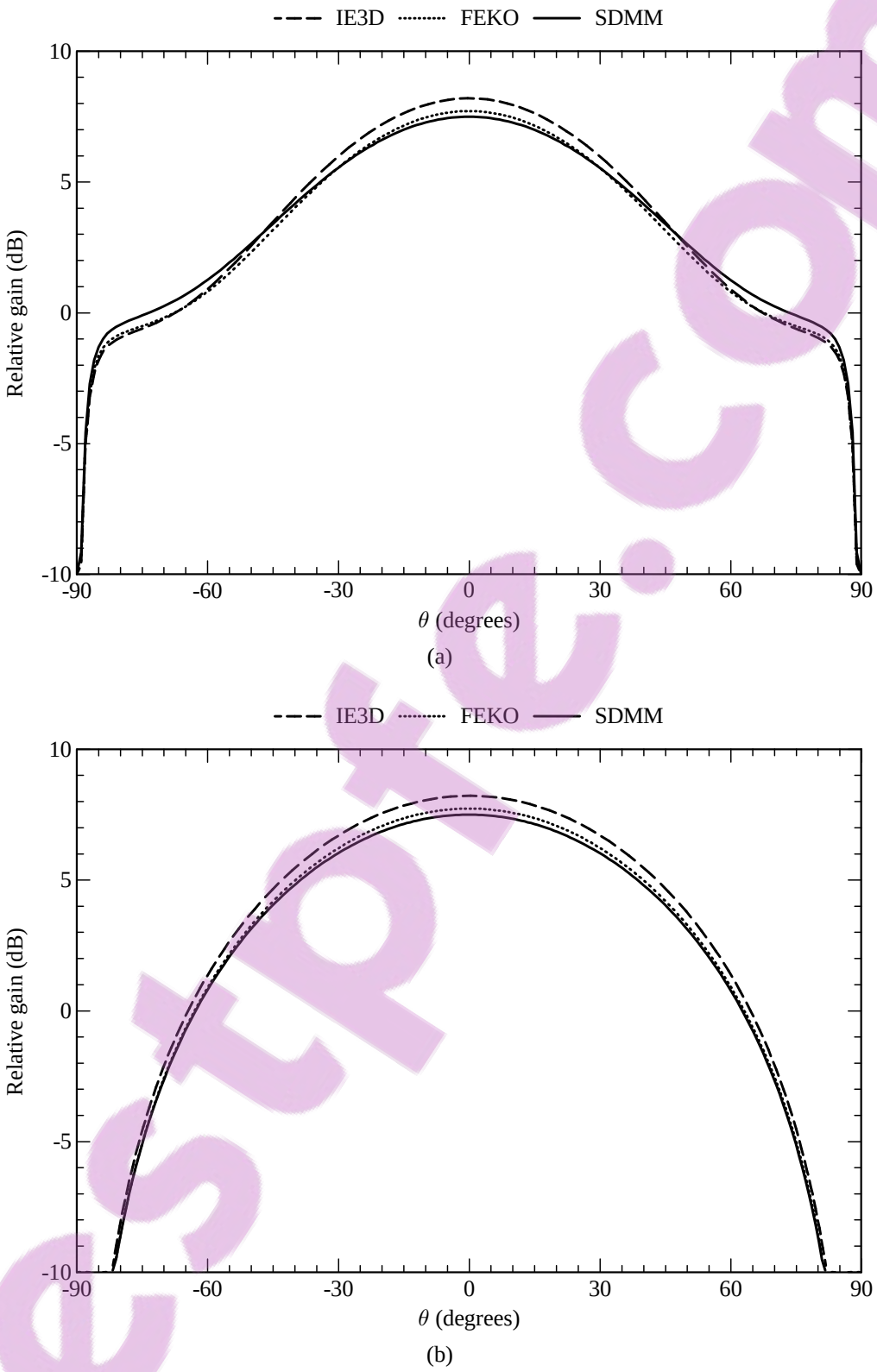

Figure 4.31 Radiation patterns (at 1.8 GHz) of the antenna element with two capacitor patches for reduced cross-polarisation levels. (a) Radiation pattern in the E-plane ($\phi = 0^\circ$). (b) Radiation pattern in the H-plane ($\phi = 90^\circ$).

If one now wants to set the input impedance at port 1 equal to Z_0, it implies that

$$\Re\mathrm{e}\{Z^P_{1,1}\} - \Re\mathrm{e}\{Z^P_{1,2}\} = Z_0 \tag{4.6}$$

and that

$$\Im\mathrm{m}\{Z^P_{1,1}\} = \Im\mathrm{m}\{Z^P_{1,2}\}. \tag{4.7}$$

Of course, the expression for the input impedance at port 2 follows in a similar way. For a Z_0 input impedance at port 2,

$$\Re\mathrm{e}\{Z^P_{2,2}\} - \Re\mathrm{e}\{Z^P_{2,1}\} = Z_0 \tag{4.8}$$

and

$$\Im\mathrm{m}\{Z^P_{2,2}\} = \Im\mathrm{m}\{Z^P_{2,1}\} \tag{4.9}$$

have to be satisfied. The antenna element can be designed through an iterative process. As in Section 4.3, the size of the capacitor patches, as well as the separation distance between each capacitor patch and the resonant patch, can be used to control $Z^P_{1,1}$ and $Z^P_{2,2}$. For specific values of $Z^P_{1,2}$ and $Z^P_{2,1}$, which should be equal by the way, $Z^P_{1,1}$ and $Z^P_{2,2}$ can then be changed until (4.6) to (4.9) are satisfied.

Figure 4.30 shows the simulated *Z*-parameters of the antenna element in Figure 4.29. This element was designed for an input impedance of 100 Ω at each port. As stated before, the element will usually be implemented with a power splitter below the ground plane, which can then transform the overall input impedance down to 50 Ω. From the results it can be seen that the agreement between all three codes is quite good. Figure 4.31 shows the simulated radiation patterns in the *E*-plane and the *H*-plane of the antenna element. The cross-polar levels in the *H*-plane have now effectively been reduced to levels that fall well below the range of the graph. Once again, the three codes show good agreement. The same basis functions as in Section 4.2.4 were used for the SDMM analysis.

4.4.2 Dual-Polarised Antenna Element

In many applications, it is necessary to have antenna elements with two orthogonal polarisations. This can be achieved with the antenna element depicted in Figure 4.32. Here, one port is used to generate the one polarisation, while the other port is used to generate the orthogonal polarisation. The electric current density on the resonant patch will primarily be directed along the x direction for port 1, while that for port 2, will primarily be directed along the y direction.

The dimensions of the dual-polarised element of Figure 4.32 are similar to those of the single-polarised element of Section 4.2.4. The electric current density on the structure was modelled with eighteen entire-domain sinusoidal basis functions on the resonant patch, the single higher-order circular attachment mode on each capacitor patch, and four PWS basis functions on each probe (excluding the one associated with the attachment mode). For the entire-domain sinusoidal

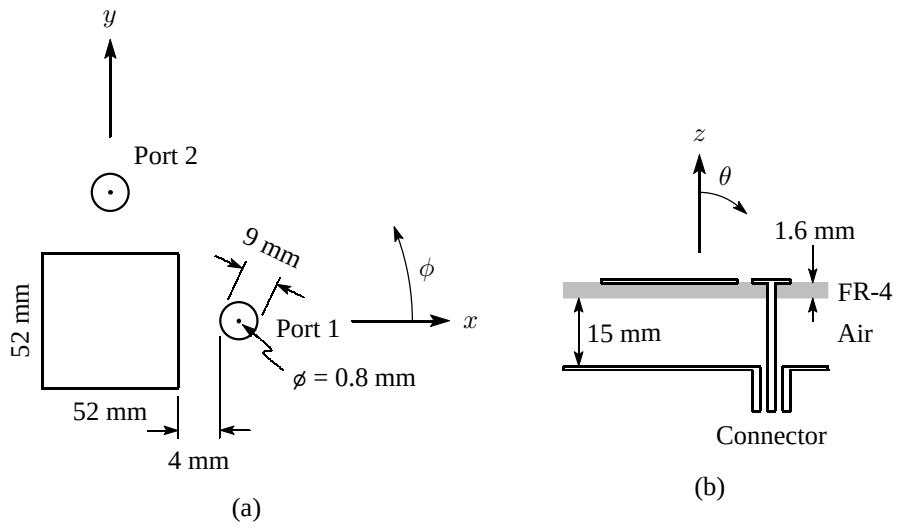

Figure 4.32 Geometry of the dual-polarised antenna element. (a) Top view of the antenna element. (b) Side view of the multilayered substrate with $\varepsilon_r = 4.25$ and $\tan\delta_\varepsilon = 0.02$ for the FR-4 layer and with $\varepsilon_r = 1$ and $\tan\delta_\varepsilon = 0$ for the air layer.

basis functions, the (1,0), (1,2), (2,0), (2,1), (3,0), (3,2), (5,0), (7,0) and (9,0) modes were used for the x-directed current, while the same set of modes were also used for the y-directed current.

Figure 4.33(a) shows the simulated and measured reflection coefficient at port 1 of the antenna element, while Figure 4.33(b) shows the simulated and measured coupling between the two ports of the antenna element. From these it can be seen that the element remains well matched over a wide bandwidth, although a second port was introduced (note that the dimensions of the capacitor patches, as well as the distance between each capacitor patch and the resonant patch, were kept equal to those of Section 4.2.4 for the single-polarised antenna element). It can also be seen that the coupling between the two ports vary between approximately -15 dB and -20 dB over the operating frequency band. In both cases, the agreement between the measurements and the simulations, is quite good. In this case, the results of FEKO, as well as those of the SDMM, seems to compare slightly better to the measurements than the results of IE3D do.

For some applications, the coupling between the two ports of the dual-polarised antenna element might be too high. This can be improved by using symmetric feeds, similar to those in Section 4.4.1. It might, however, require a more complex feed network. In some of the following sections, it will also be shown how various array configurations can be used to realise dual-polarised antennas with less coupling between the two ports.

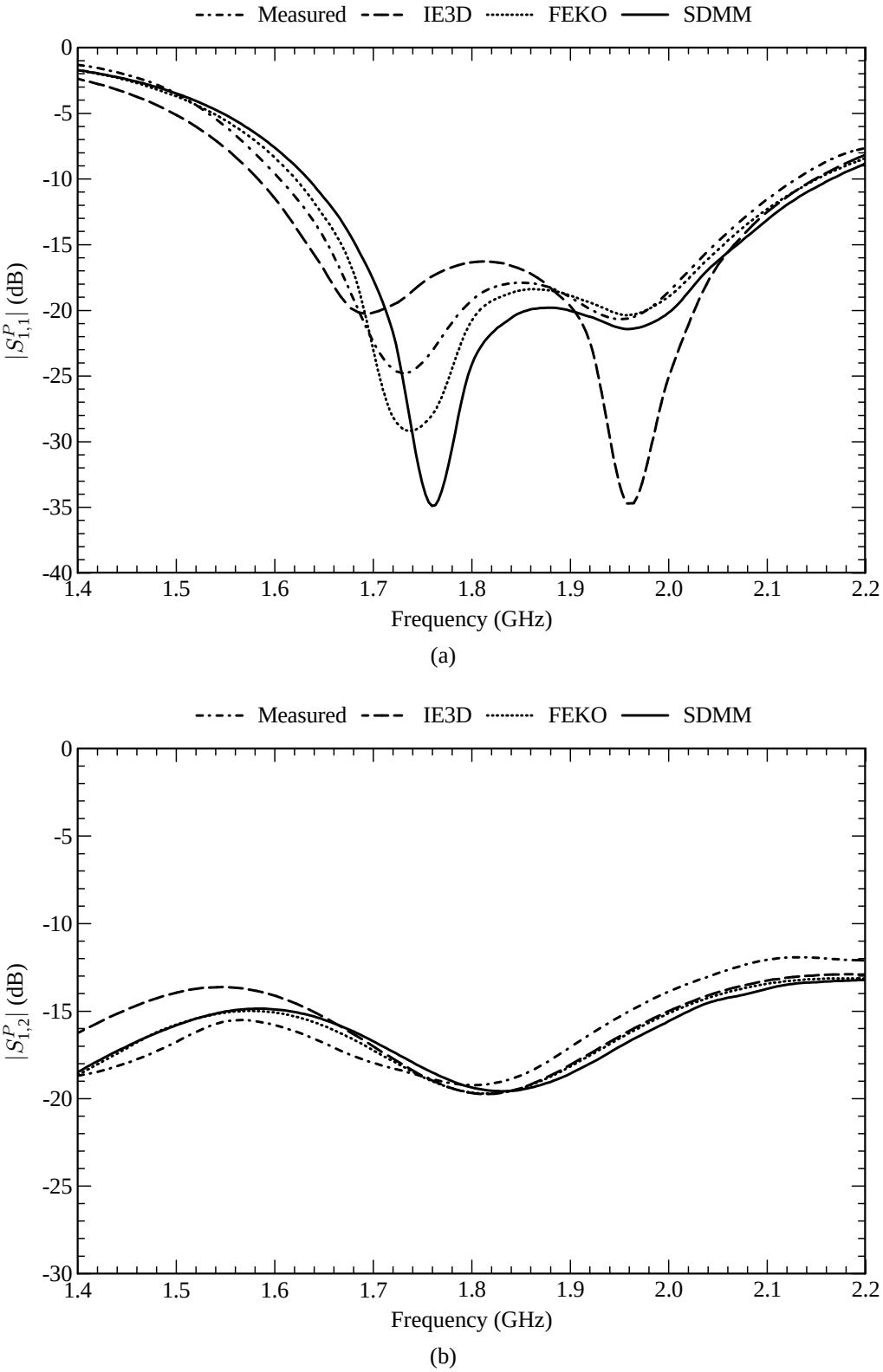

Figure 4.33 *S*-parameters of the dual-polarised antenna element. (a) Reflection coefficient at port 1. (b) Coupling between the two ports.

4.4.3 Two-Element Linearly-Polarised Array

An alternative way to reduce the cross-polarisation levels of a probe-fed patch antenna, is to use two elements that are positioned in a back-to-back configuration, as shown in Figure 4.34. Here, as is the case in Section 4.4.1, the two ports have to be excited exactly out of phase (i.e. a 180° phase difference). The resulting effect is that the co-polarised currents on the two resonant patches are aligned, but that the fields radiated by the cross-polarised currents, cancel out.

The two-element array has to be excited by a feed network, similar to the one in Section 4.4.1, and therefore the input impedance at each port is a function of the self-impedance at that port as well as the mutual impedance between the two ports. In order to design such a two-element array, it is important to know how the separation distance between the two elements affects both the self-impedance at each port and the mutual impedances between the two ports. Figure 4.35(a) shows how the self-impedance at port 1, $Z^P_{1,1}$, varies with the separation distance, s, between the two patches, while Figure 4.35(b) shows how the mutual impedance, $Z^P_{1,2}$, varies with the separation distance. Both these have been simulated with the SDMM. It can be seen that separation distance has a more profound effect on the mutual impedance between the two ports, than on the self-impedance at each port. Once again, the antenna element can be designed through an iterative process. As in Section 4.3, the size of the capacitor patches, as well as the separation distance between them and the resonant patches, can be used to control $Z^P_{1,1}$ and $Z^P_{2,2}$. For specific values of $Z^P_{1,2}$ and $Z^P_{2,1}$, which should be equal, $Z^P_{1,1}$ and $Z^P_{2,2}$ can then be changed until (4.6) to (4.9) are satisfied.

Figure 4.36 shows the simulated Z-parameters of the two-element antenna array in Figure 4.34, which was designed for an input impedance of 50 Ω at each port (this corresponds to a separation distance, s, of 30 mm). From the results it can be seen that the agreement between the measurements and all three codes, is quite good. Figure 4.37 shows the simulated radiation patterns in the E-plane and the H-plane of the two-element antenna array. The cross-polar levels in both planes fall well below the range of the graph. Once again, the three codes show good agreement. It can be seen that the beamwidth in the E-plane is narrowed due to the alignment of the two elements. The electric current density on the structure was modelled with eleven entire-domain sinusoidal basis functions on each resonant patch, the single higher-order circular attachment mode on each capacitor patch, and four PWS basis functions on each probe (excluding the one associated with the attachment mode). For the entire-domain sinusoidal basis functions, the (1,0), (1,2), (2,0), (2,2), (3,0), (3,2), (5,0), (7,0) and (9,0) modes were used for the x-directed current, while the (2,0) and (2,1) modes were used for the y-directed current.

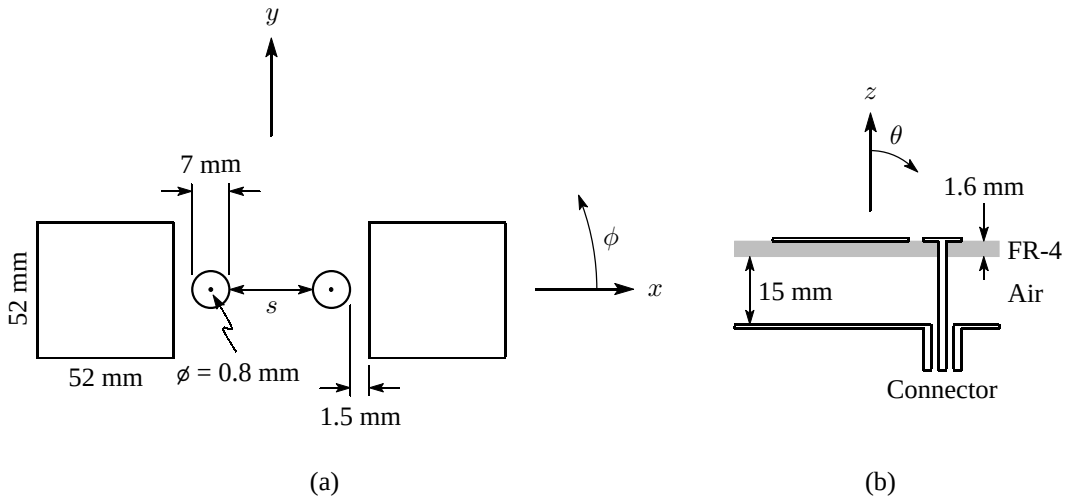

Figure 4.34 Geometry of the two-element linearly-polarised array. (a) Top view of the array. (b) Side view of the multilayered substrate with $\varepsilon_r = 4.25$ and $\tan\delta_\varepsilon = 0.02$ for the FR-4 layers and with $\varepsilon_r = 1$ and $\tan\delta_\varepsilon = 0$ for the air layer.

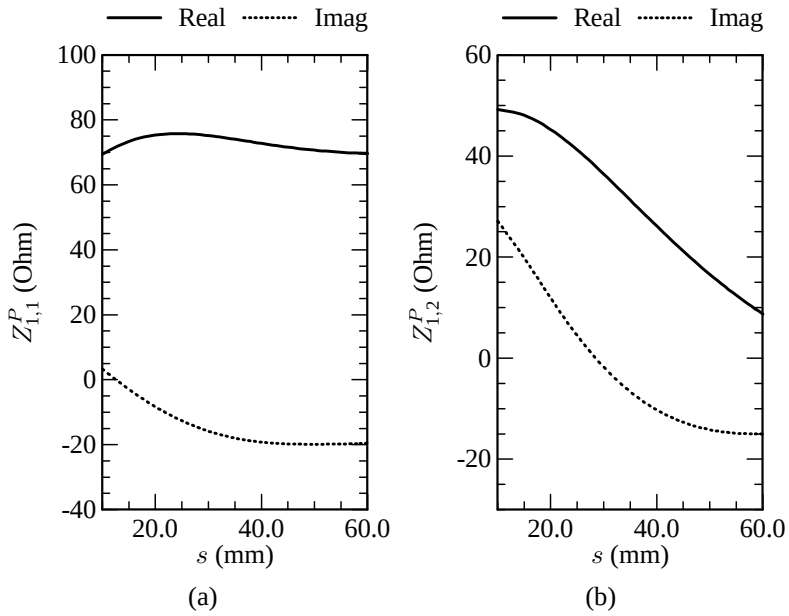

Figure 4.35 Effect (at 1.8 GHz) of the separation distance on the *Z*-parameters of the two-element linearly-polarised array. (a) Self-impedance at port 1. (b) Mutual impedance between the two ports.

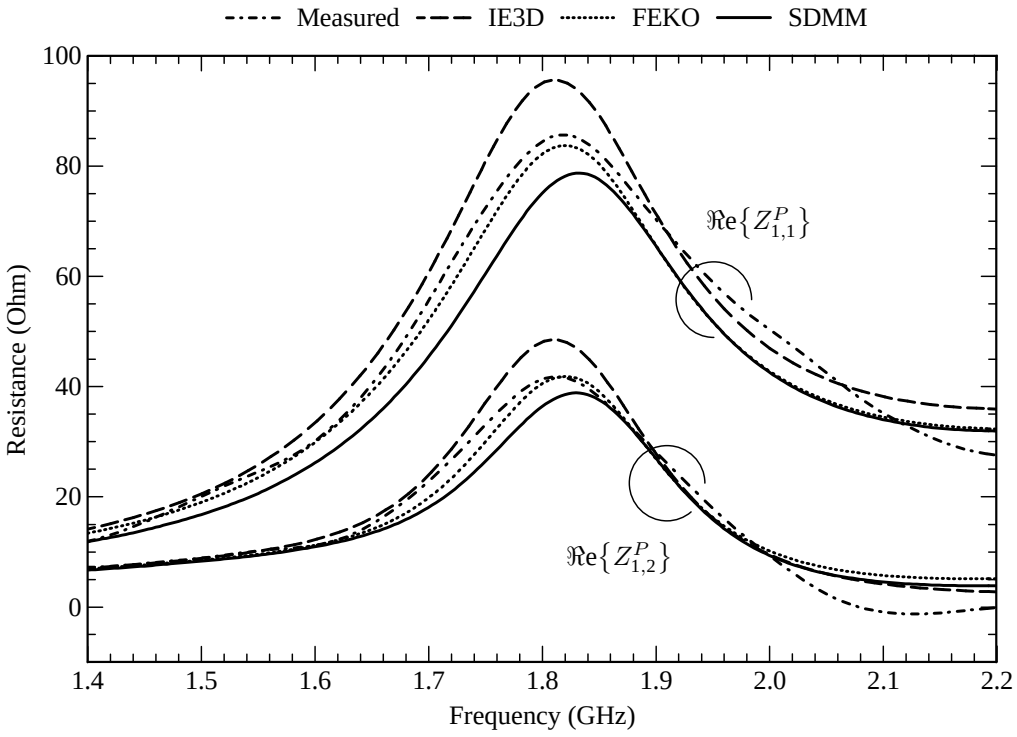

(a)

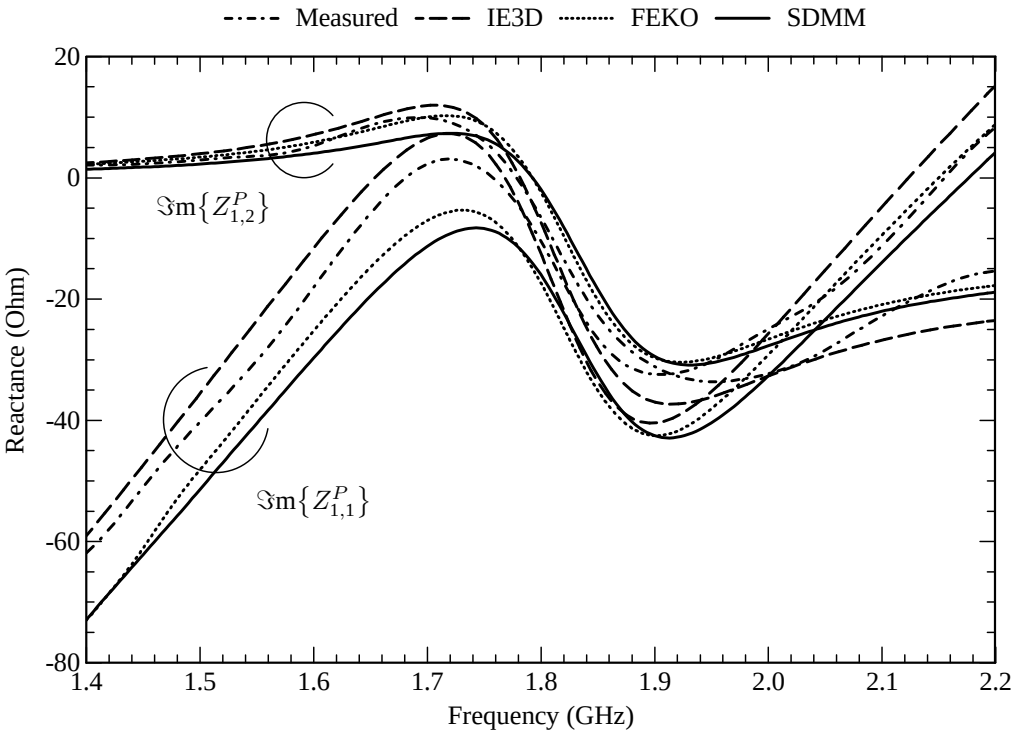

(b)

Figure 4.36 Z-parameters of the two-element linearly-polarised array (s = 30 mm). (a) Resistive part of the Z-parameters. (b) Reactive part of the Z-parameters.

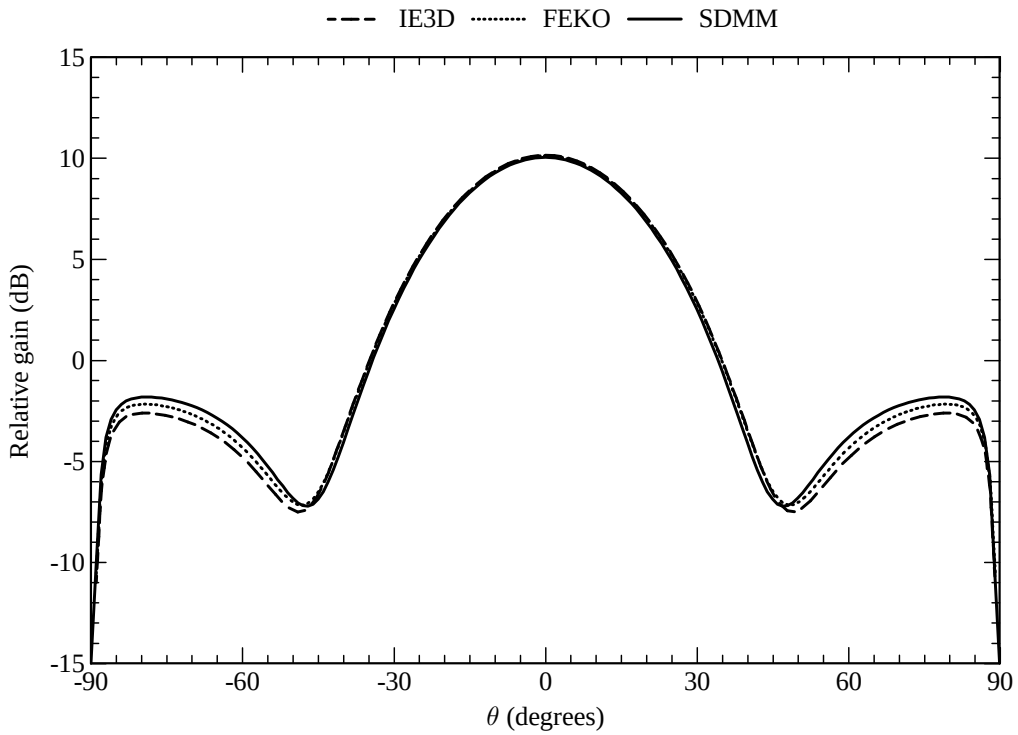

(a)

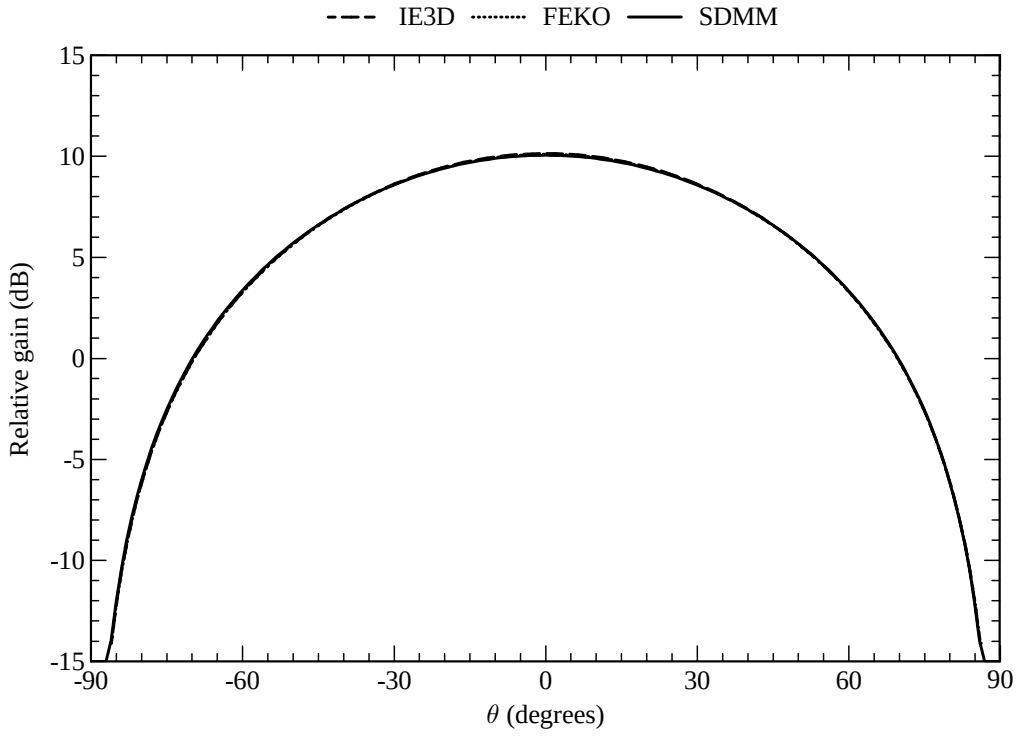

(b)

Figure 4.37 Radiation patterns (at 1.8 GHz) of the two-element linearly-polarised array (s = 30 mm). (a) Radiation pattern in the E-plane ($\phi = 0^\circ$). (b) Radiation pattern in the H-plane ($\phi = 90^\circ$).

4.4.4 Four-Element Vertically-Polarised Array

Many applications require the use of linear vertically-polarised antenna arrays. An example of such an array is shown in Figure 4.38. This particular one consists of a pair of two-element sub-arrays. Note that the resonant patches are all equally separated. As can be seen from Figure 4.38, two of the probes are excited exactly out of phase with respect to the other two probes. This is done to reduce cross-polarisation levels. The array was designed so that the input impedance at each port is equal to 50 Ω.

The electric current density on the structure was modelled with eleven entire-domain sinusoidal basis functions on each resonant patch, the single higher-order circular attachment mode on each capacitor patch and four PWS basis functions on each probe (excluding the one associated with the attachment mode). For the entire-domain sinusoidal basis functions, the (1,0), (1,2), (2,0), (2,2), (3,0), (3,2), (5,0), (7,0) and (9,0) modes were used for the y-directed current, while the (2,0) and (2,1) modes were used for the x-directed current. The feed network was modelled with Sonnet's circuit analysis module. Table 4.1 shows how the computer-memory requirements, for the storage of the interaction matrix, varies among the three codes.[1] It can be seen that the memory requirements of the SDMM are substantially lower then that of the other two codes. Also, for the SDMM, the amount of duplicate entries in the interaction matrix equates to 67.88%.[2]

Table 4.1
Computer memory required for the storage of the interaction matrix associated with the four-element vertically-polarised antenna array.

Method	Unknowns	Memory (MB)
IE3D	2560	100.0
FEKO	2576	101.3
SDMM	64	0.063

Figure 4.39 shows the simulated reflection coefficient at the input port of the feed network. It can be seen that there is close agreement between the results of the FEKO and SDMM codes, but that the reflection coefficient, as simulated by IE3D, is somewhat lower. However, as shown in Table 4.2, the 10 dB return-loss bandwidths for all three codes seem to be comparable. Figure 4.40 shows the simulated radiation patterns in the *E*-plane and the *H*-plane of the antenna array. The

[1] For comparison, it is assumed that all the codes store the entire interaction matrix (i.e. N^2 values) in the computer's memory. This assumption is always valid for the SDMM code, while it is also valid for FEKO when the default settings are used, and for IE3D when the full matrix solver is used.

[2] The amount of duplicate entries within the interaction matrix makes no difference in the amount of matrix entries that are actually stored within the computer's memory (the entire matrix is always stored). It only gives an indication of the amount of matrix elements that are not calculated directly, but that are merely copied from other entries (i.e. the speedup in filling the matrix).

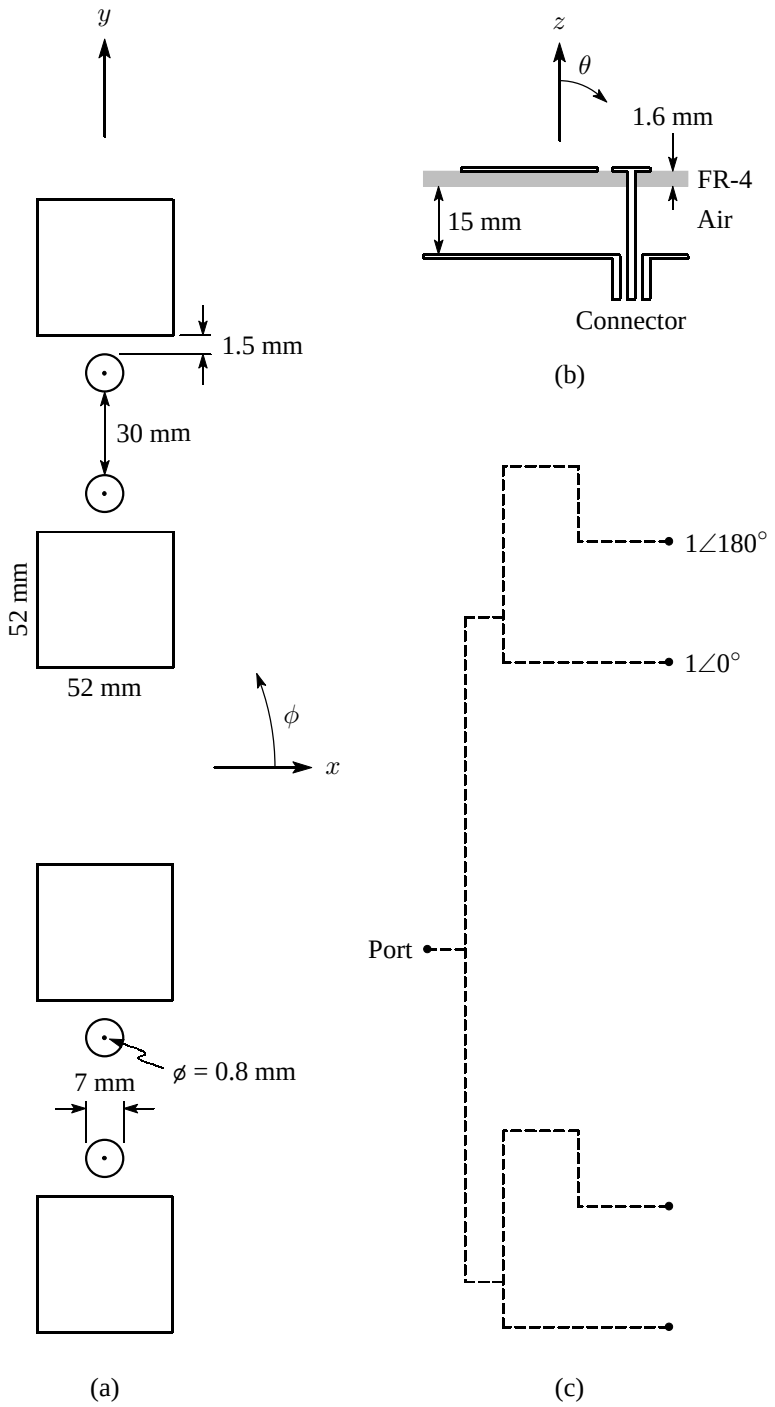

Figure 4.38 Geometry of the four-element vertically-polarised array. (a) Top view of the array. (b) Side view of the multilayered substrate with $\varepsilon_r = 4.25$ and $\tan\delta_\varepsilon = 0.02$ for the FR-4 layers and with $\varepsilon_r = 1$ and $\tan\delta_\varepsilon = 0$ for the air layer. (c) Schematic of the feed network.

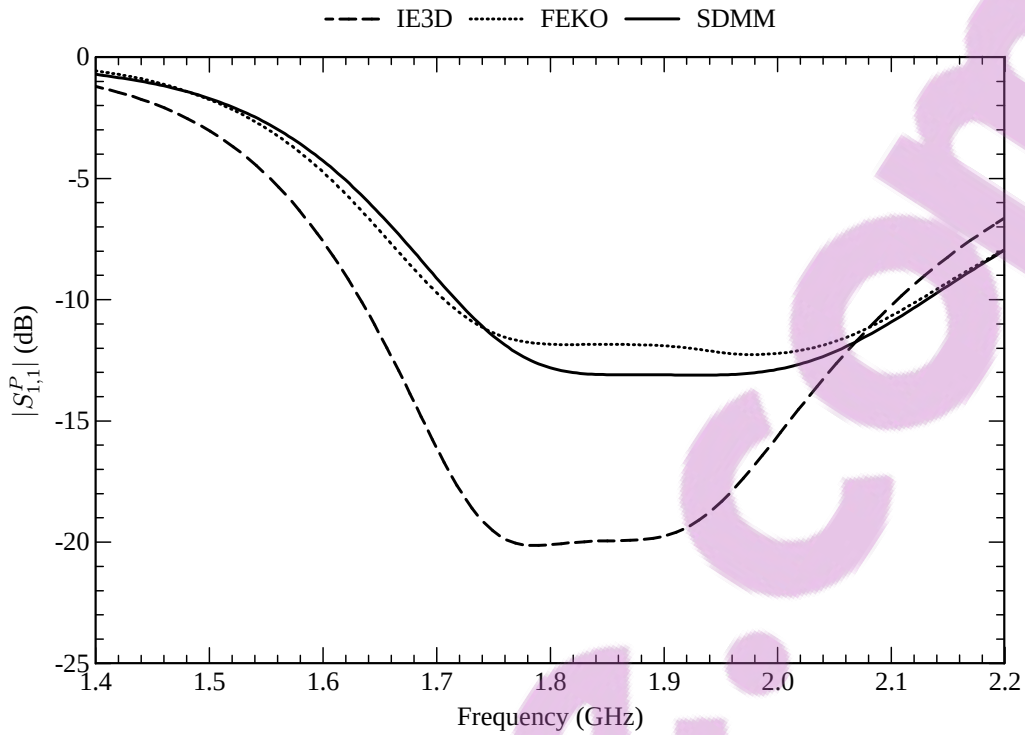

Figure 4.39 Reflection coefficient at the input port of the feed network for the four-element vertically-polarised array.

cross-polar levels in both planes fall well below the range of the graph. In terms of the radiation patterns, the three codes show very good agreement. It can be seen that the beamwidth in the *E*-plane is narrowed due to the vertical alignment of the antenna elements.

Table 4.2
10 dB Return-loss bandwidth at the input port of the four-element vertically-polarised antenna array.

Method	Bandwidth (%)
IE3D	25.7
FEKO	21.9
SDMM	21.3

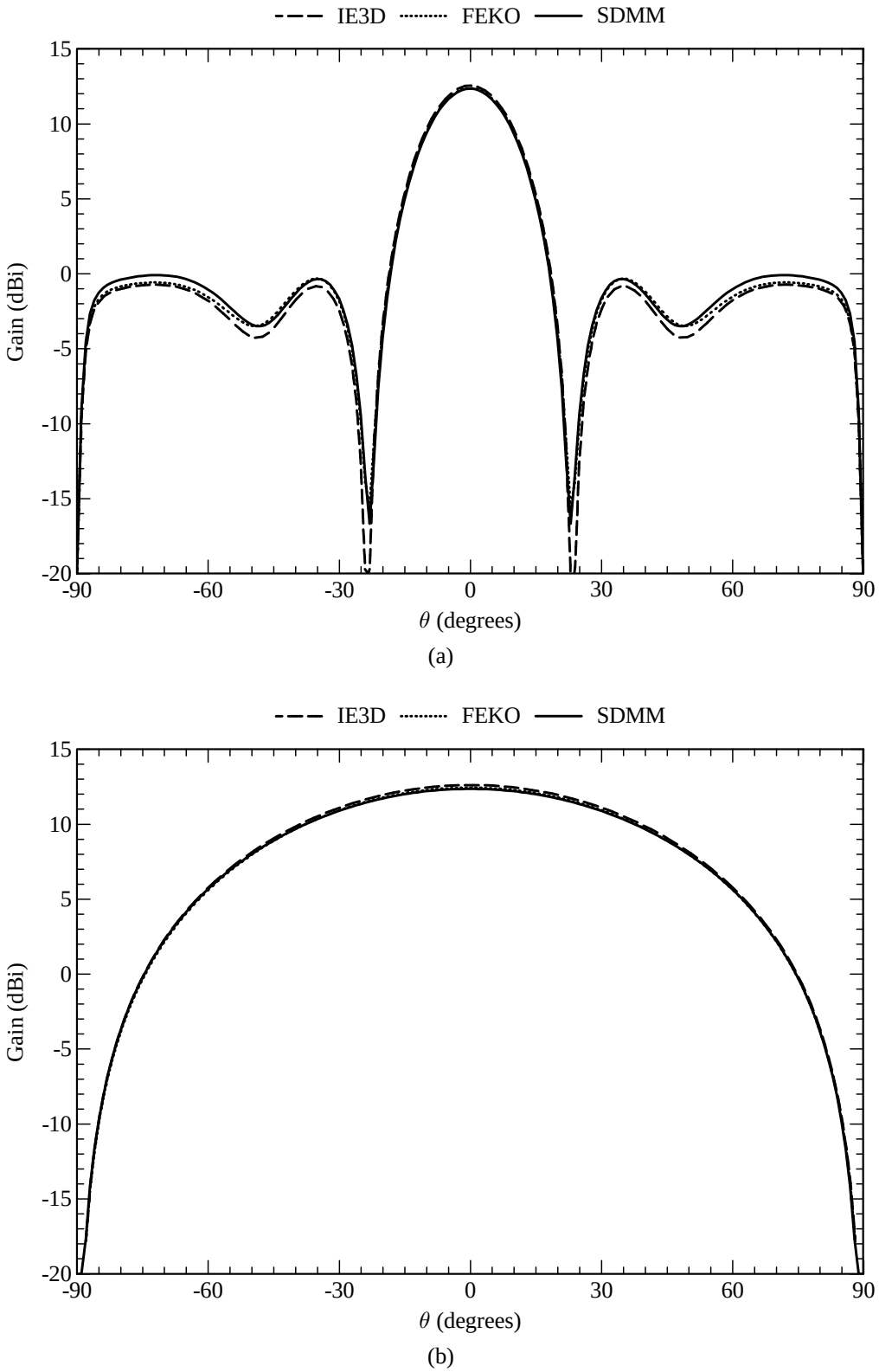

Figure 4.40 Radiation patterns (at 1.8 GHz) of the four-element vertically-polarised array. (a) Radiation pattern in the E-plane ($\phi = 90°$). (b) Radiation pattern in the H-plane ($\phi = 0°$).

4.4.5 Four-Element Horizontally-Polarised Array

For some applications, a linear horizontally-polarised antenna array is more advantageous than vertically polarised ones. An example of such an array is shown in Figure 4.41. This particular one consists of four elements, each with two capacitor patches to reduce cross-polarisation levels. As can be seen from Figure 4.41, four of the probes are excited exactly out of phase with respect to the other four probes. The array was designed so that the input impedance at each port is equal to 50 Ω.

The electric current density on the structure was modelled with eleven entire-domain sinusoidal basis functions on each resonant patch, the single higher-order circular attachment mode on each capacitor patch, and four PWS basis functions on each probe (excluding the one associated with the attachment mode). For the entire-domain sinusoidal basis functions, the (1,0), (1,2), (2,0), (2,2), (3,0), (3,2), (5,0), (7,0) and (9,0) modes were used for the x-directed current, while the (2,0) and (2,1) modes were used for the y-directed current. The feed network was modelled with Sonnet's circuit analysis module. Table 4.3 shows how the computer-memory requirements, for the storage of the interaction matrix, varies among the three codes. It can be seen that the memory requirements of the SDMM are once again substantially lower then that of the other two codes. Also, for the SDMM, the amount of duplicate entries in the interaction matrix equates to 83.11%.

Table 4.3
Computer memory required for the storage of the interaction matrix associated with the four-element horizontally-polarised antenna array.

Method	Unknowns	Memory (MB)
IE3D	4216	271.2
FEKO	2944	132.3
SDMM	84	0.108

Figure 4.42 shows the simulated reflection coefficient at the input port of the feed network. It can be seen that there is good agreement between the results of all three codes. The simulated 10 dB return-loss bandwidths are shown in Table 4.4, from which it can be seen that the agreement is also quite good. Figure 4.43 shows the simulated radiation patterns in the *E*-plane and the *H*-plane of the antenna array. The cross-polar levels in both planes fall well below the range of the graph. In terms of the radiation patterns, the three codes show very good agreement. The antenna gain, as simulated by IE3D, however, appears to be a fraction higher than that of the other two codes. It can also be seen that the beamwidth in the *H*-plane is narrowed due to the vertical alignment of the antenna elements.

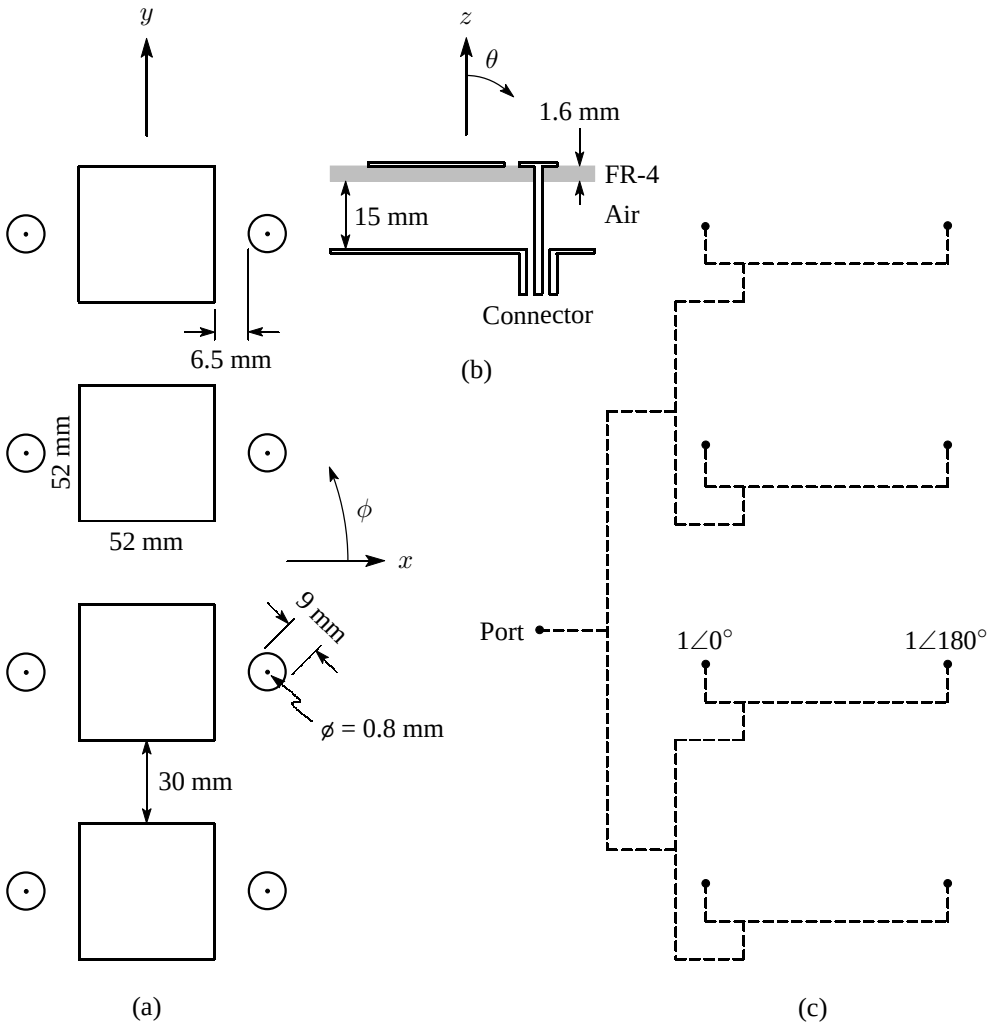

Figure 4.41 Geometry of the four-element horizontally-polarised array. (a) Top view of the array. (b) Side view of the multilayered substrate with $\varepsilon_r = 4.25$ and $\tan\delta_\varepsilon = 0.02$ for the FR-4 layers and with $\varepsilon_r = 1$ and $\tan\delta_\varepsilon = 0$ for the air layer. (c) Schematic of the feed network.

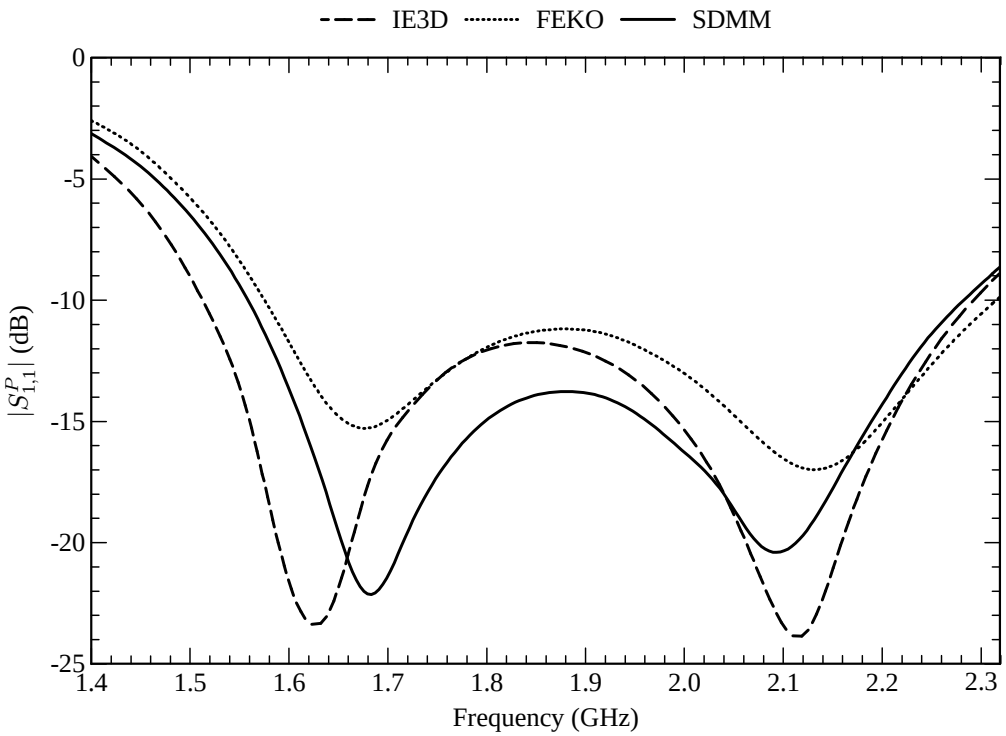

Figure 4.42 Reflection coefficient at the input port of the feed network for the four-element horizontally-polarised array.

Table 4.4
10 dB Return-loss bandwidth at the input port of the four-element horizontally-polarised antenna array.

Method	Bandwidth (%)
IE3D	41.1
FEKO	38.6
SDMM	38.5

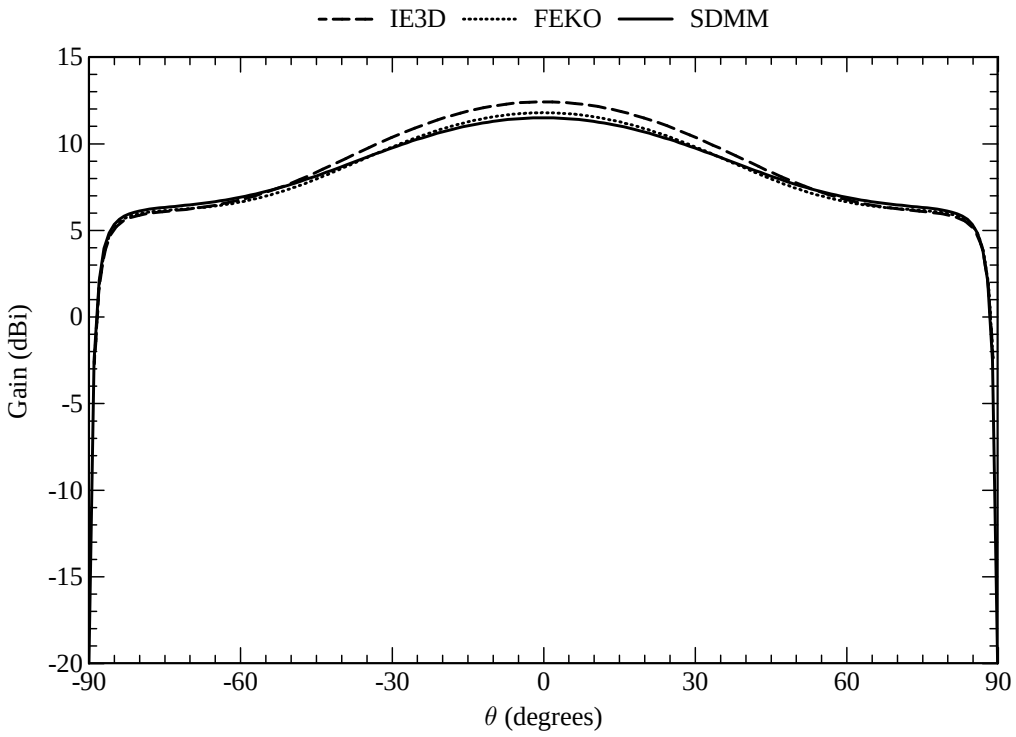

(a)

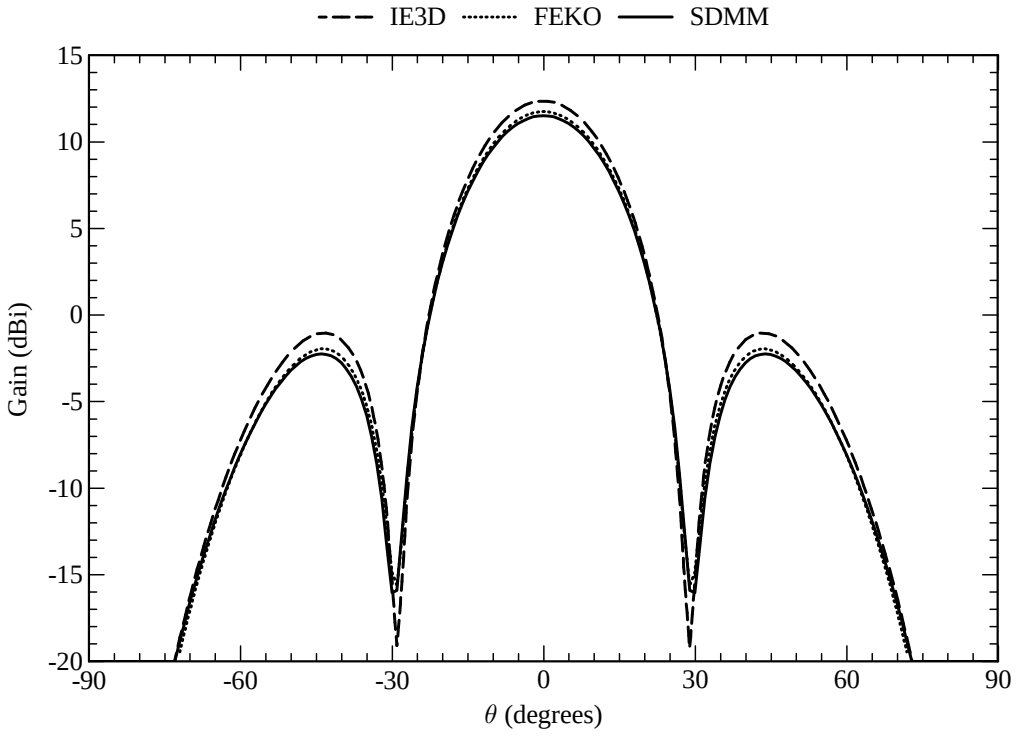

(b)

Figure 4.43 Radiation patterns (at 1.8 GHz) of the four-element horizontally-polarised array. (a) Radiation pattern in the E-plane ($\phi = 0^\circ$). (b) Radiation pattern in the H-plane ($\phi = 90^\circ$).

4.4.6 Four-Element $\pm 45^\circ$ Slant-Polarised Array

Linear antenna arrays with $\pm 45^\circ$ slant polarisation are nowadays very popular for use on cellular base stations. Like other dual-polarised antennas, these antennas also have two ports, one for the $+45^\circ$ polarisation and one for the -45° polarisation. They are usually required to have a wide beamwidth in the azimuth plane and a narrow beamwidth in the elevation plane. To achieve these requirements, they are therefore usually also constructed as linear arrays. Figure 4.44 shows the geometry of such an array that can be realised by means of patch antenna elements with capacitive feed probes.

The array can be viewed as two subarrays, each consisting of two dual-polarised elements. In each subarray, the probes that are diagonally opposite to each other, provide the one polarisation, while the other two probes provide the orthogonal polarisation. The two probes that are diagonally opposite to each other, are excited exactly out of phase (i.e. a 180° phase difference) so that the co-polarised fields add constructively and the cross-polarised fields cancel out. The input impedance at a specific probe is a function of the self-impedance at that probe as well as the mutual impedance between that probe and all the other probes. This array was designed by taking into account only the mutual impedance between two diagonally opposite probes in each subarray. The size of the capacitor patches, as well as the separation distance between them and the resonant patches, was then altered until (4.6) to (4.9) were satisfied for the two diagonally opposite probes. The array was designed so that the input impedance at each port is equal to 50 Ω.

The electric current density on the structure was modelled with eighteen entire-domain sinusoidal basis functions on each resonant patch, the single higher-order circular attachment mode on each capacitor patch, and four PWS basis functions on each probe (excluding the one associated with the attachment mode). For the entire-domain sinusoidal basis functions, the (1,0), (1,2), (2,0), (2,1), (3,0), (3,2), (5,0), (7,0) and (9,0) modes were used for the $+45^\circ$-directed current, while the same set of modes were also used for the -45°-directed current. The feed network was modelled with Sonnet's circuit analysis module. Table 4.5 shows how the computer-memory requirements, for the storage of the interaction matrix, varies among the three codes. It can be seen that the memory requirements of the SDMM are once again substantially lower then that of the other two codes. Also, for the SDMM, the amount of duplicate entries in the interaction matrix equates to 83.41%.

Table 4.5
Computer memory required for the storage of the interaction matrix associated with the four-element $\pm 45^\circ$ slant-polarised antenna array.

Method	Unknowns	Memory (MB)
IE3D	4076	253.5
FEKO	2912	129.4
SDMM	112	0.191

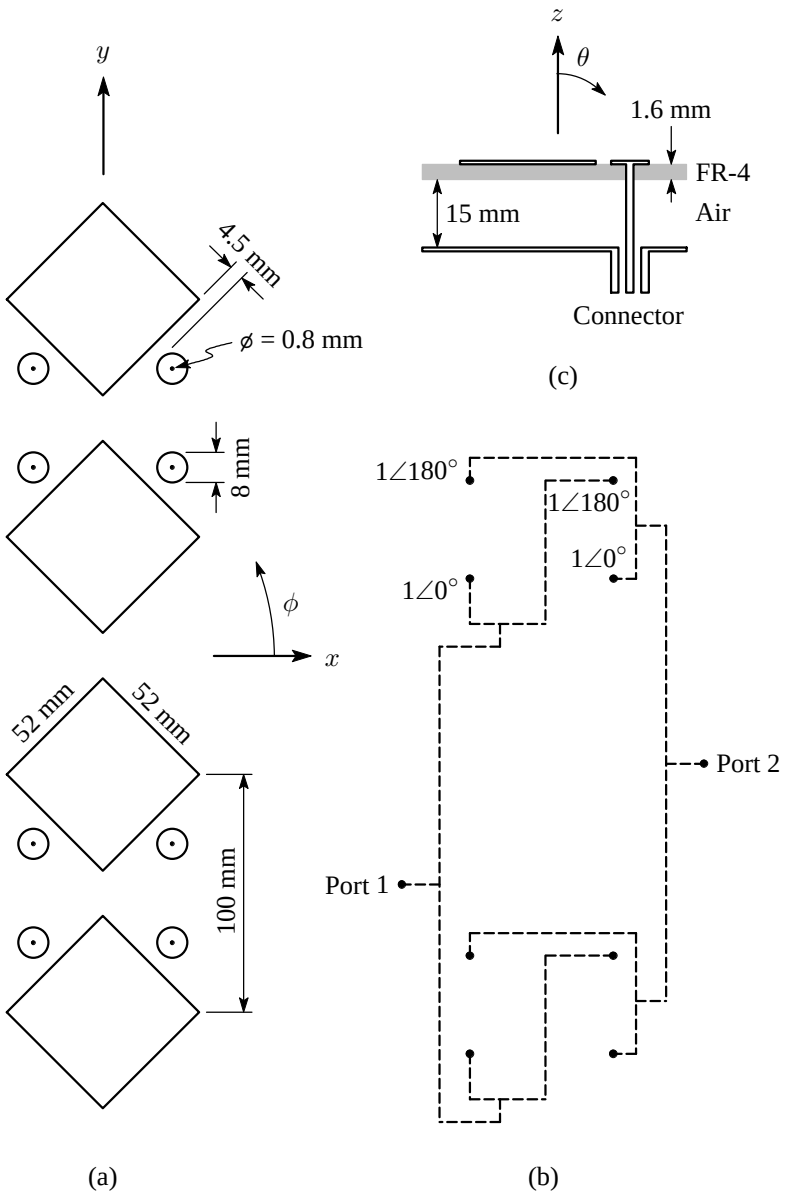

Figure 4.44 Geometry of the four-element $\pm 45^{\circ}$ slant-polarised array. (a) Top view of the array. (b) Side view of the multilayered substrate with $\varepsilon_r = 4.25$ and $\tan\delta_\varepsilon = 0.02$ for the FR-4 layers and with $\varepsilon_r = 1$ and $\tan\delta_\varepsilon = 0$ for the air layer. (c) Schematic of the feed network.

Figure 4.45(a) shows the simulated reflection coefficient at port 1 of the feed network, while Figure 4.45(b) shows the simulated coupling between the two ports of the feed network. The simulated 10 dB return-loss bandwidths for port 1 are shown in Table 4.6. For the reflection coefficient, the results of the SDMM lies between those of IE3D and FEKO, while all three codes compare fairly well in terms of the coupling results. The coupling, as simulated by IE3D, is slightly higher than as simulated by the other two codes. Overall though, the impedance bandwidth of the array seems to be satisfactory for most cellular applications (the array was designed to roughly operate within the GSM 1800 frequency band, but was not optimised as such), while the decoupling of the two ports is close to the 25 dB to 30 dB that is normally used for cellular applications [194, 195].

Table 4.6
10 dB Return-loss bandwidth at port 1 of the four-element $\pm 45^{\circ}$ slant-polarised antenna array.

Method	Bandwidth (%)
IE3D	29.8
FEKO	27.8
SDMM	27.0

The gain associated with the co-polarised radiation patterns, G_{copol}, as well as the gain associated with the cross-polarised radiation pattern, G_{xpol}, can be calculated as

$$G_{\text{copol}}(\theta,\phi) = \frac{4\pi \left| E^{\text{scat}}_{\text{copol}}(\theta,\phi) \right|^2}{2\eta_{(0)} P_{\text{in}}} \tag{4.10}$$

and

$$G_{\text{xpol}}(\theta,\phi) = \frac{4\pi \left| E^{\text{scat}}_{\text{xpol}}(\theta,\phi) \right|^2}{2\eta_{(0)} P_{\text{in}}}, \tag{4.11}$$

where the absolute values of the co-polarised and cross-polarised electric fields, $E^{\text{scat}}_{\text{copol}}$ and $E^{\text{scat}}_{\text{xpol}}$, are given by

$$\left| E^{\text{scat}}_{\text{copol}}(\theta,\phi) \right| = \left| \frac{E^{\text{scat}}_{\theta}(\theta,\phi) + E^{\text{scat}}_{\phi}(\theta,\phi)}{\sqrt{2}} \right| \tag{4.12}$$

and

$$\left| E^{\text{scat}}_{\text{xpol}}(\theta,\phi) \right| = \left| \frac{E^{\text{scat}}_{\theta}(\theta,\phi) - E^{\text{scat}}_{\phi}(\theta,\phi)}{\sqrt{2}} \right| \tag{4.13}$$

respectively. Figure 4.46 shows the simulated co-polarised and cross-polarised radiation patterns in the azimuth and elevation planes of the antenna array. From these it can be seen that the agreement between the three codes is very good, and that the array has a cross-polar discrimination factor of about 18 dB to 20 dB. This should suffice for most cellular applications [195, 196]. The elevation beamwidth can be decreased by adding more elements to the array. This will also increase the gain of the array.

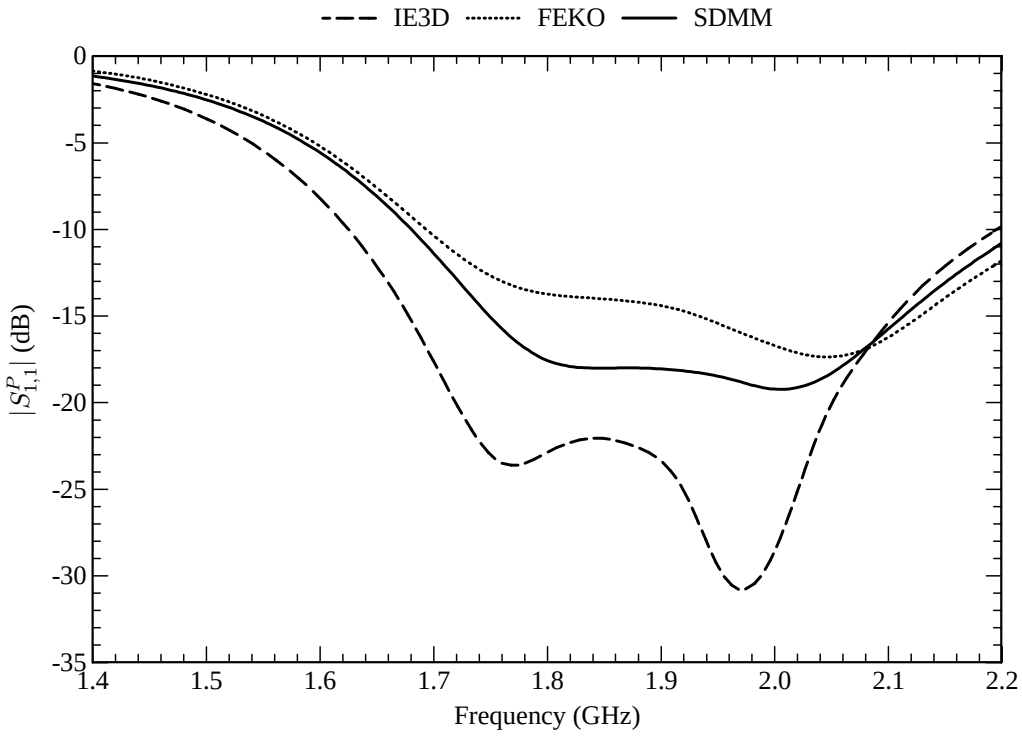

(a)

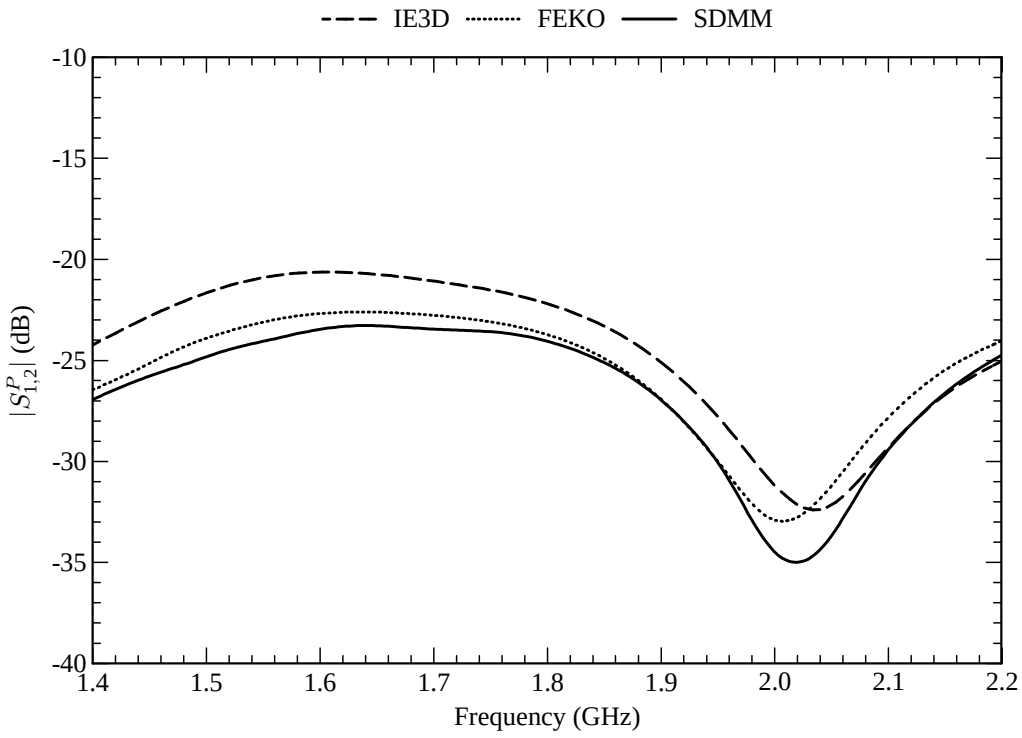

(b)

Figure 4.45 *S*-parameters of the four-element $\pm 45^\circ$ slant-polarised array. (a) Reflection coefficient at port 1 of the feed network. (b) Coupling between the two ports of the feed network.

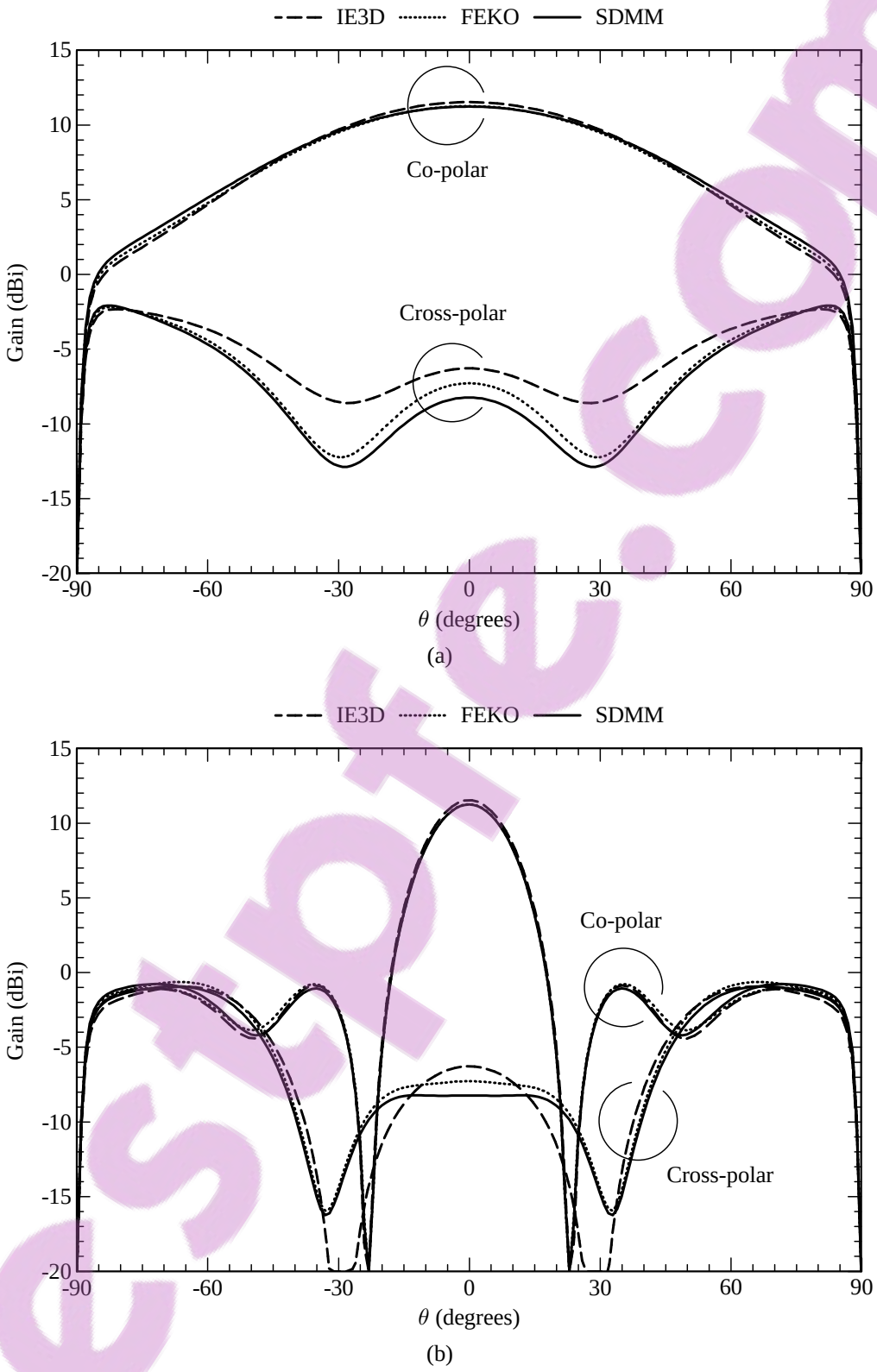

Figure 4.46 Radiation patterns (at 1.8 GHz) of the four-element $\pm 45^{\circ}$ slant-polarised array. (a) Radiation pattern in the azimuth plane ($\phi = 0^{\circ}$). (b) Radiation pattern in the elevation plane ($\phi = 0^{\circ}$).

4.4.7 Five-Element $\pm 45^\circ$ Slant-Polarised Array

An alternative form of the $\pm 45^\circ$ slant-polarised antenna array is shown in Figures 4.47. It consists of a zig-zag type of arrangement where adjacent antenna elements are positioned in a back-to-back configuration. Of the five resonant patches, the bottom four patches provide the one polarisation, while the top four patches provide the orthogonal polarisation. It can therefore be seen that the topmost and bottommost patches only provide one polarisation each, but that the three patches in the middle provide both polarisations. All of the probes connected to port 1, are associated with the one polarisation, while those connected to port 2, are associated with the orthogonal polarisation. The antenna array was designed by only taking into account the mutual coupling between two adjacent probes. By following the same approach as in Section 4.4.3, the input impedance at each port was designed to be equal to 50 Ω.

The electric current density on the structure was modelled with eighteen entire-domain sinusoidal basis functions on each resonant patch, the single higher-order circular attachment mode on each capacitor patch, and four PWS basis functions on each probe (excluding the one associated with the attachment mode). For the entire-domain sinusoidal basis functions, the (1,0), (1,2), (2,0), (2,1), (3,0), (3,2), (5,0), (7,0) and (9,0) modes were used for the $+45^\circ$-directed current, while the same set of modes were also used for the -45°-directed current. The feed network was modelled with IE3D, after which the *S*-parameters of the array and the feed network were cascaded by means of Sonnet's circuit analysis module. Table 4.7 shows how the computer-memory requirements, for the storage of the interaction matrix associated with the array, varies among the three full-wave codes. It can be seen that the memory requirements of the SDMM are once again substantially lower then that of the other two codes. Also, for the SDMM, the amount of duplicate entries in the interaction matrix equates to 82.42%. An physical model of this antenna, as shown in Figure 4.48, was also constructed in order to compare the simulations to measurements.

Table 4.7
Computer memory required for the storage of the interaction matrix associated with the five-element $\pm 45^\circ$ slant-polarised antenna array.

Method	Unknowns	Memory (MB)
IE3D	5682	492.6
FEKO	3472	183.9
SDMM	130	0.258

Figure 4.49 shows the simulated and measured gain (all cases including losses in the feed network) of the antenna, from which it can be seen that the agreement between the three codes is very good, but that the measured gain is only slightly lower than the simulated gain. This can be ascribed to the rather small ground plane that was used for the physical antenna model.

Figure 4.50(a) shows the measured and simulated reflection coefficient at port 1 of the feed network, while Figure 4.50(b) shows the measured and simulated coupling between the two ports of the feed network. The simulated 10 dB return-loss bandwidths for port 1 are shown in Table 4.8. In terms of the reflection coefficient, there is close agreement between the measured results and the IE3D results, as well as close agreement between the SDMM results and the FEKO results. There is a small difference between the measured/IE3D results and the SDMM/FEKO results. The overall bandwidth, however, appears to be more or less the same for all four sets of results. As far as the coupling between the two ports goes, the measured results and simulated results all agree fairly well. From these results it can be seen that the impedance bandwidth of the antenna is sufficiently wide for most cellular applications and that the decoupling between the two ports seem to be slightly better than that of the array in Section 4.4.6.

Table 4.8
10 dB Return-loss bandwidth at port 1 of the five-element $\pm 45^{\circ}$ slant-polarised antenna array.

Method	Bandwidth (%)
Measured	28.4
IE3D	32.4
FEKO	30.0
SDMM	28.7

Figure 4.51 shows the measured and simulated co-polarised and cross-polarised radiation patterns in the azimuth plane of the antenna array, while Figure 4.52 shows the measured and simulated co-polarised and cross-polarised radiation patterns in the elevation plane of the antenna array. From these it can be seen that the agreement between the three codes is quite good and that the simulations compare fairly well with the measurements, given the finite size of the ground plane that was used for the physical antenna model. In this case it can be seen that the beamwidth of the co-polarised pattern in the azimuth plane is slightly narrower than that of the array in Section 4.4.6. This is due to the somewhat larger horizontal dimensions of the array. The cross-polar discrimination of this array is better than 20 dB over most of the usable beamwidth in the two planes.

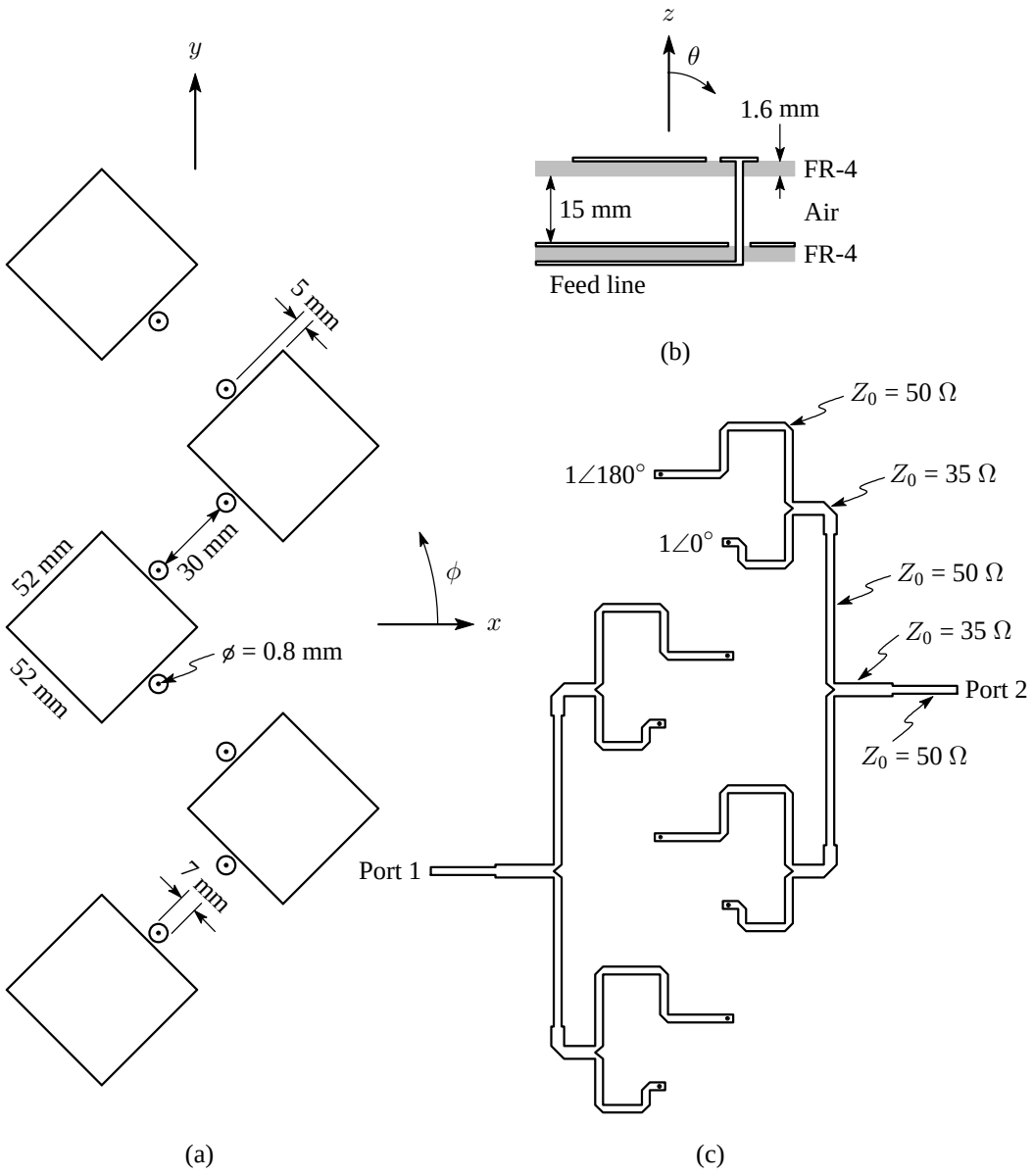

Figure 4.47 Geometry of the five-element ±45° slant-polarised array. (a) Top view of the array. (b) Side view of the multilayered substrate with $\varepsilon_r = 4.25$ and $\tan\delta_\varepsilon = 0.02$ for the FR-4 layers and with $\varepsilon_r = 1$ and $\tan\delta_\varepsilon = 0$ for the air layer. (c) Feed network for the array.

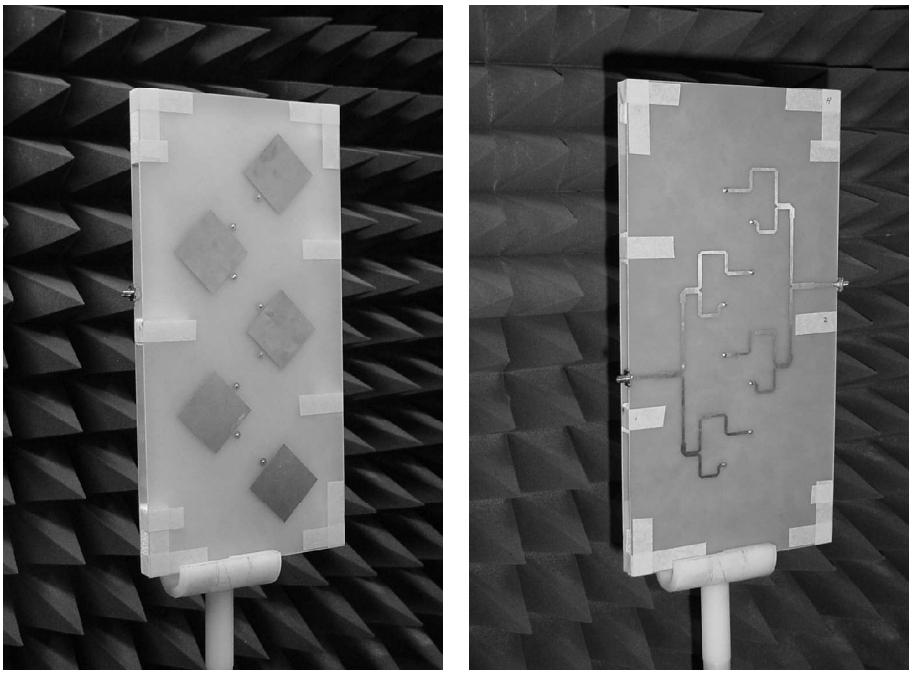

(a) (b)

Figure 4.48 Photographs of the five-element $\pm 45^{\circ}$ slant-polarised array. (a) Antenna elements. (b) Feed network.

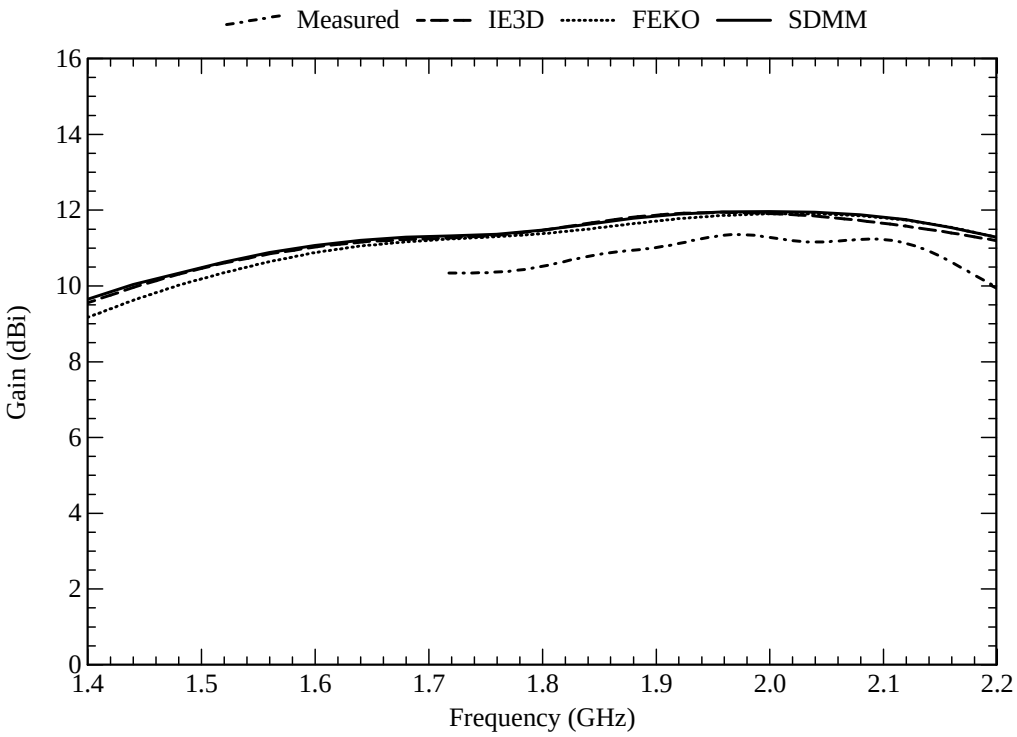

Figure 4.49 Gain of the five-element $\pm 45^{\circ}$ slant-polarised array.

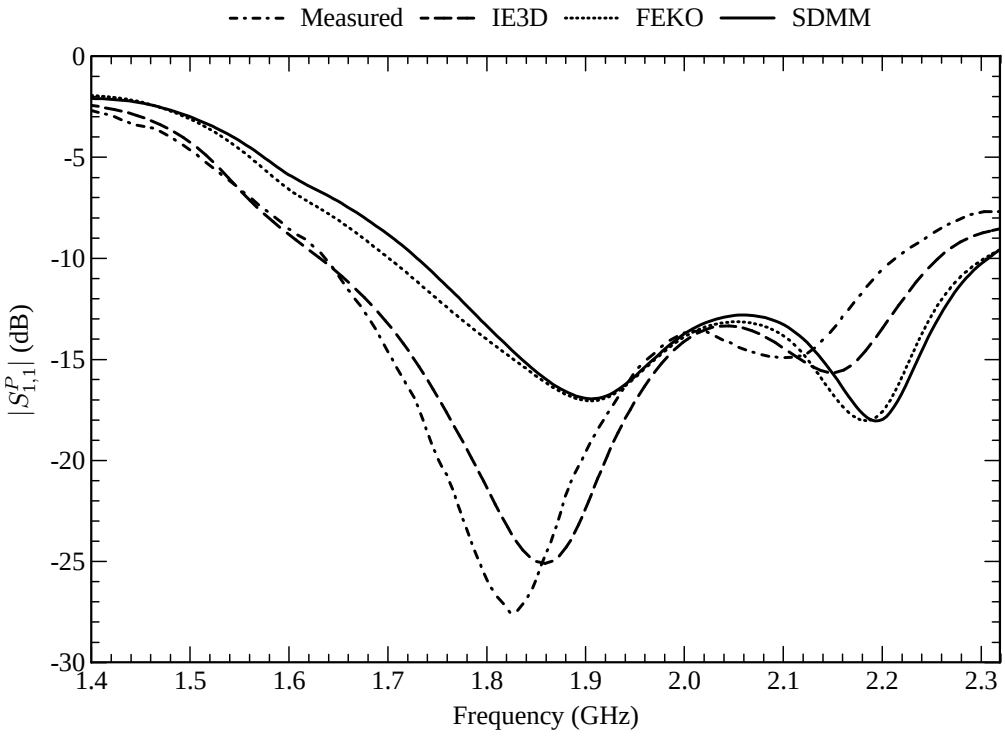

(a)

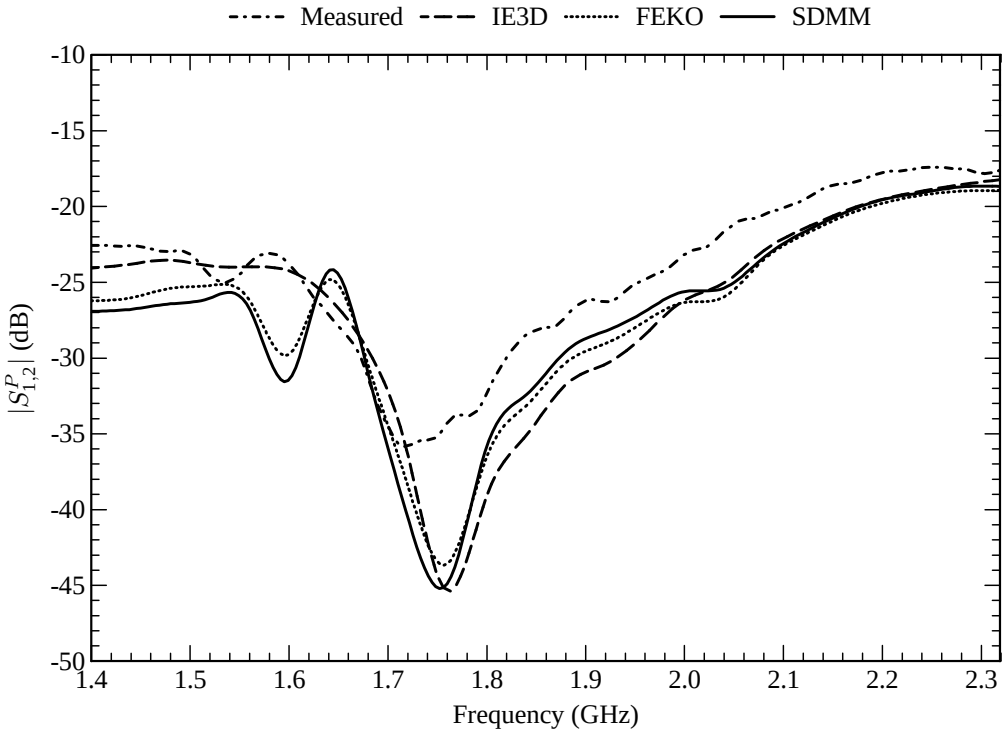

(b)

Figure 4.50 *S*-parameters of the five-element $\pm 45^\circ$ slant-polarised array. (a) Reflection coefficient at port 1 of the feed network. (b) Coupling between the two ports of the feed network.

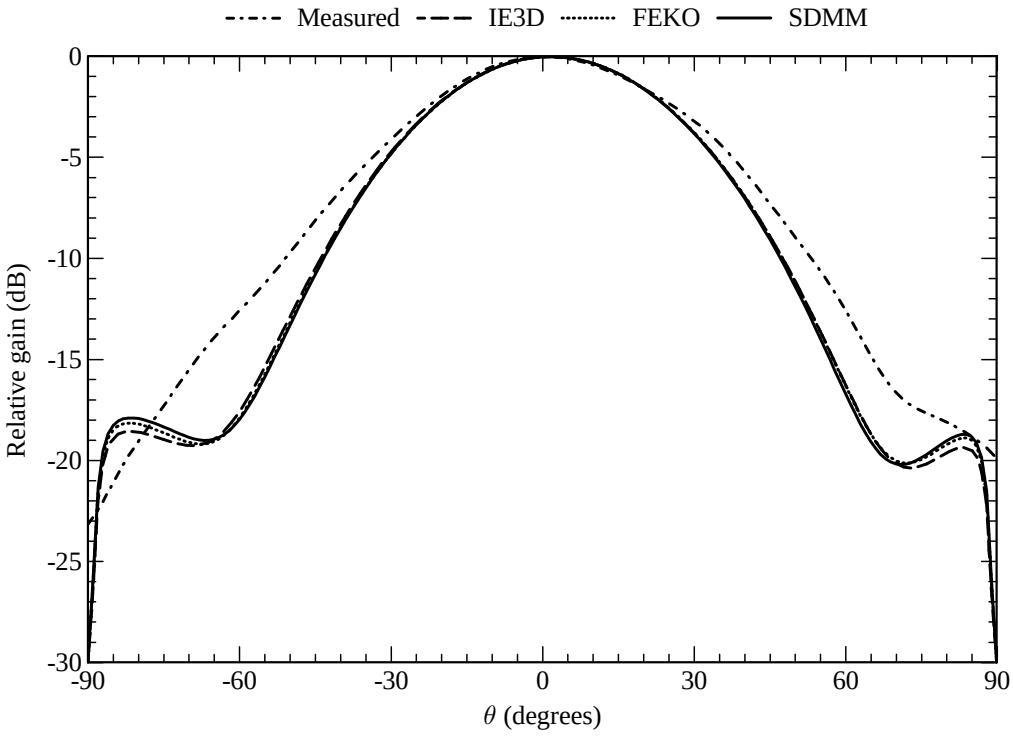

(a)

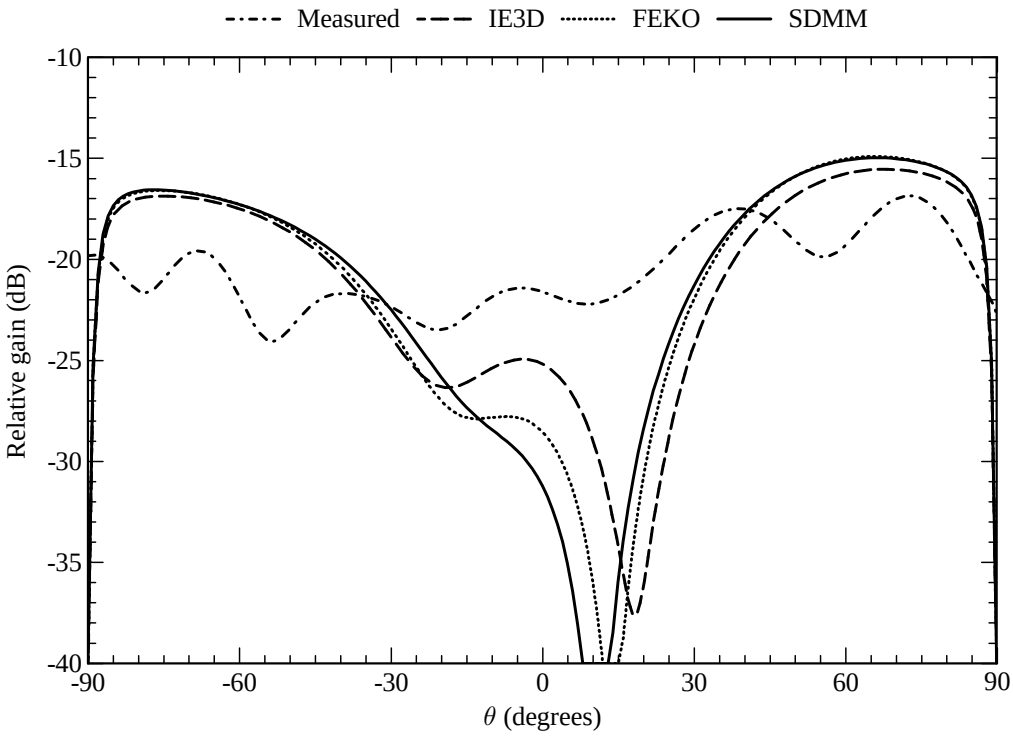

(b)

Figure 4.51 Radiation patterns (at 1.8 GHz) in the azimuth plane ($\phi = 0^\circ$) of the five-element $\pm 45^\circ$ slant-polarised array. (a) Co-polarised pattern. (b) Cross-polarised pattern.

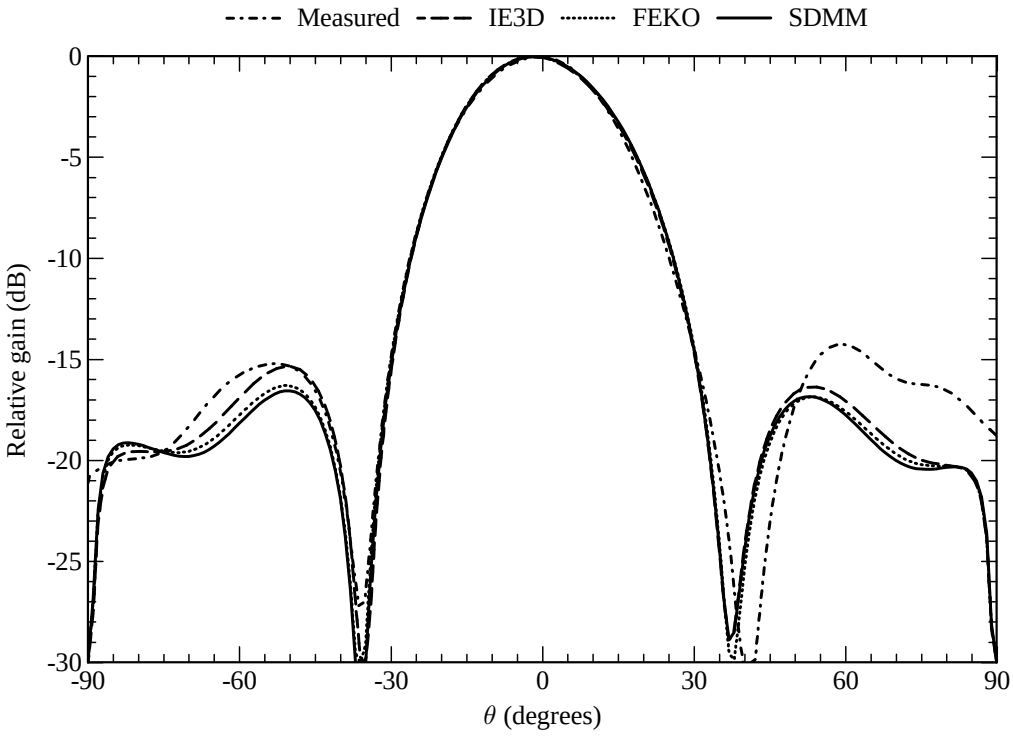

(a)

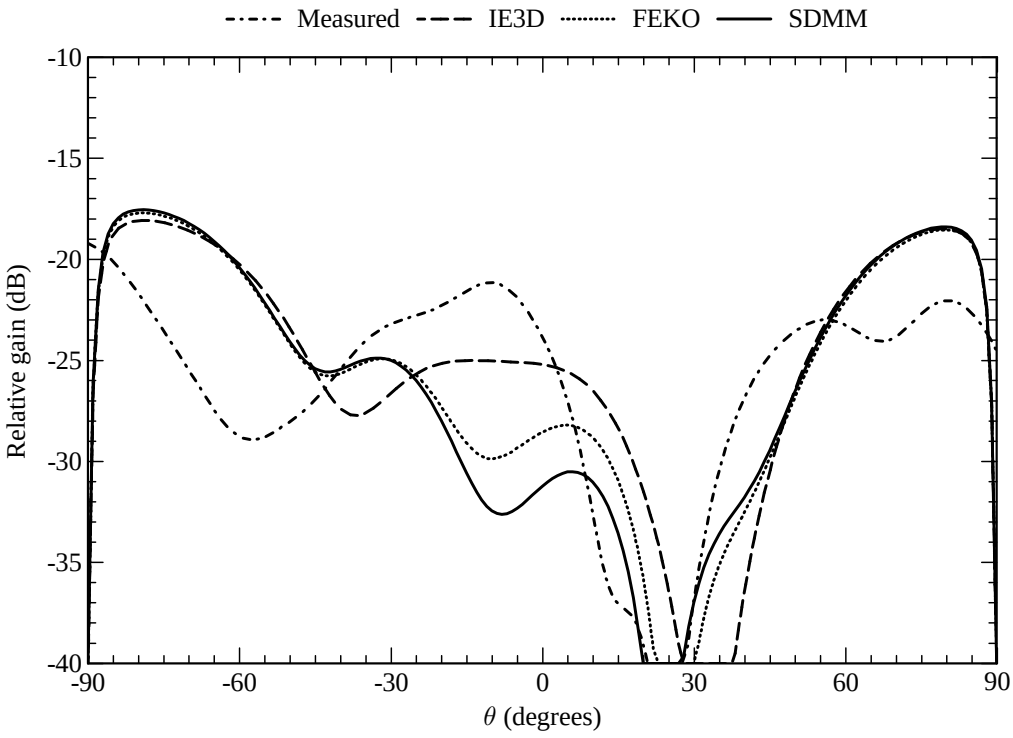

(b)

Figure 4.52 Radiation patterns (at 1.8 GHz) in the elevation plane ($\phi = 90^\circ$) of the five-element $\pm 45^\circ$ slant-polarised array. (a) Co-polarised pattern. (b) Cross-polarised pattern.

4.4.8 Nine-Element $\pm 45^\circ$ Slant-Polarised Array

Many cellular base station installations require antennas with higher gains and narrower elevation beamwidths than those that have been presented to far. This can be achieved by adding more elements to the antenna array, thereby extending the length of the array. In this section, an antenna array is presented that is more or less comparable in size to that of a typical high-gain cellular base station antenna.

Consider the antenna array in Figure 4.53. It is a somewhat larger version of the one in Section 4.4.7. The electric current density on the structure was modelled with eighteen entire-domain sinusoidal basis functions on each resonant patch, the single higher-order circular attachment mode on each capacitor patch, and four PWS basis functions on each probe (excluding the one associated with the attachment mode). For the entire-domain sinusoidal basis functions, the (1,0), (1,2), (2,0), (2,1), (3,0), (3,2), (5,0), (7,0) and (9,0) modes were used for the $+45^\circ$-directed current, while the same set of modes were also used for the -45°-directed current. The feed network was modelled with Sonnet's circuit analysis module. Table 4.9 shows how the computer-memory requirements, for the storage of the interaction matrix associated with the array, varies among the three full-wave codes. It can be seen that the memory requirements of the SDMM are basically insignificant, but that those for the other two codes are greater than the available memory on most personal computers. For the SDMM, the amount of duplicate entries in the interaction matrix equates to 90.07%.

Table 4.9
Computer memory required for the storage of the interaction matrix associated with the nine-element $\pm 45^\circ$ slant-polarised antenna array.

Method	Unknowns	Memory (MB)
IE3D	7747	915.8
FEKO	6176	582.0
SDMM	242	0.894

Figure 4.54(a) shows the simulated reflection coefficient at port 1 of the feed network, while Figure 4.54(b) shows the simulated coupling between the two ports of the feed network. The simulated 10 dB return-loss bandwidths for port 1 are shown in Table 4.10. In terms of the reflection coefficient, there is close agreement between the SDMM results and the FEKO results, but there is a slight frequency shift when compared to the IE3D results. The overall bandwidth, however, appears to be more or less the same for all three sets of results. As far as the coupling between the two ports goes, the simulated results all agree fairly well. From these results it can be seen that the impedance bandwidth of the antenna is sufficiently wide for most cellular applications and that the decoupling between the two ports is also quite good.

Table 4.10
10 dB Return-loss bandwidth at port 1 of the nine-element $\pm 45^{\circ}$ slant-polarised antenna array.

Method	Bandwidth (%)
IE3D	20.8
FEKO	20.5
SDMM	19.4

Figure 4.55 shows the simulated co-polarised and cross-polarised radiation patterns in the azimuth and elevation planes of the antenna array. From these it can be seen that the agreement between the three codes is quite good. It can also be seen that the extra elements have raised the gain of the antenna and that the beamwidth in the elevation plane has been narrowed. The cross-polar discrimination of this array is also better than 20 dB over most of the usable beamwidth in the two principal planes.

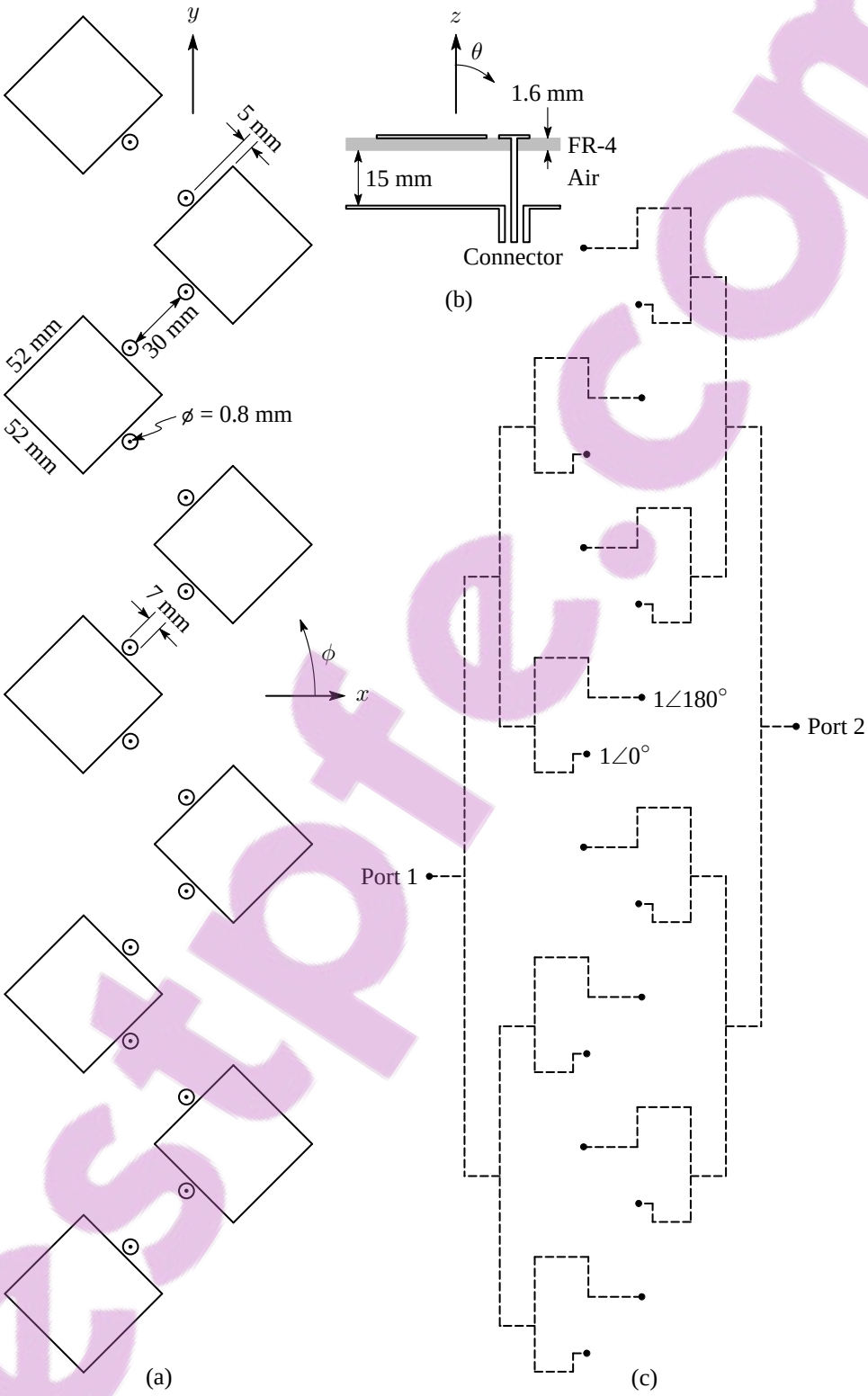

Figure 4.53 Geometry of the nine-element $\pm 45^{\circ}$ slant-polarised array. (a) Top view of the array. (b) Side view of the multilayered substrate with $\varepsilon_r = 4.25$ and $\tan\delta_\varepsilon = 0.02$ for the FR-4 layers and with $\varepsilon_r = 1$ and $\tan\delta_\varepsilon = 0$ for the air layer. (c) Schematic of the feed network.

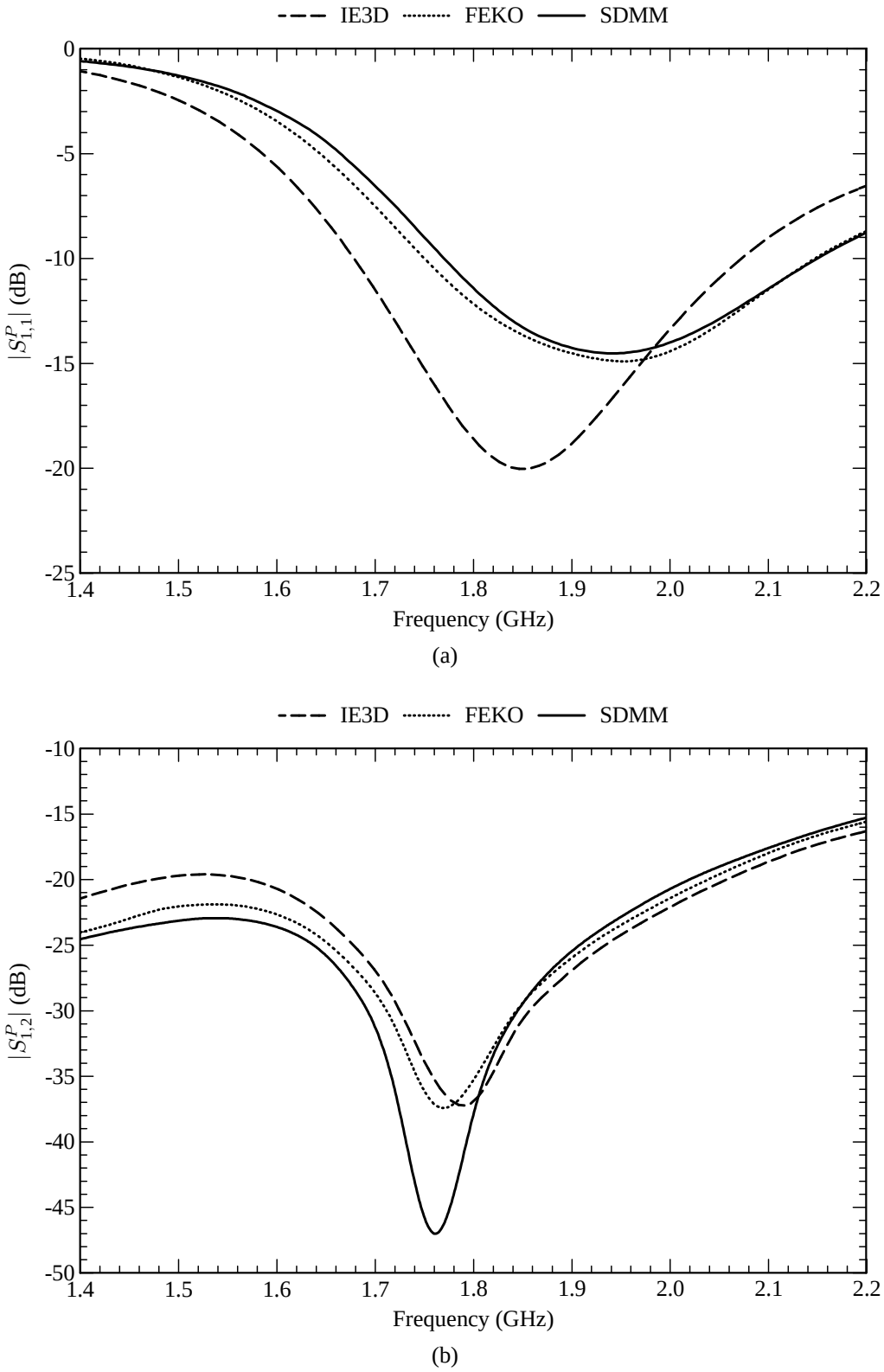

Figure 4.54 *S*-parameters of the nine-element $\pm 45^\circ$ slant-polarised array. (a) Reflection coefficient at port 1 of the feed network. (b) Coupling between the two ports of the feed network.

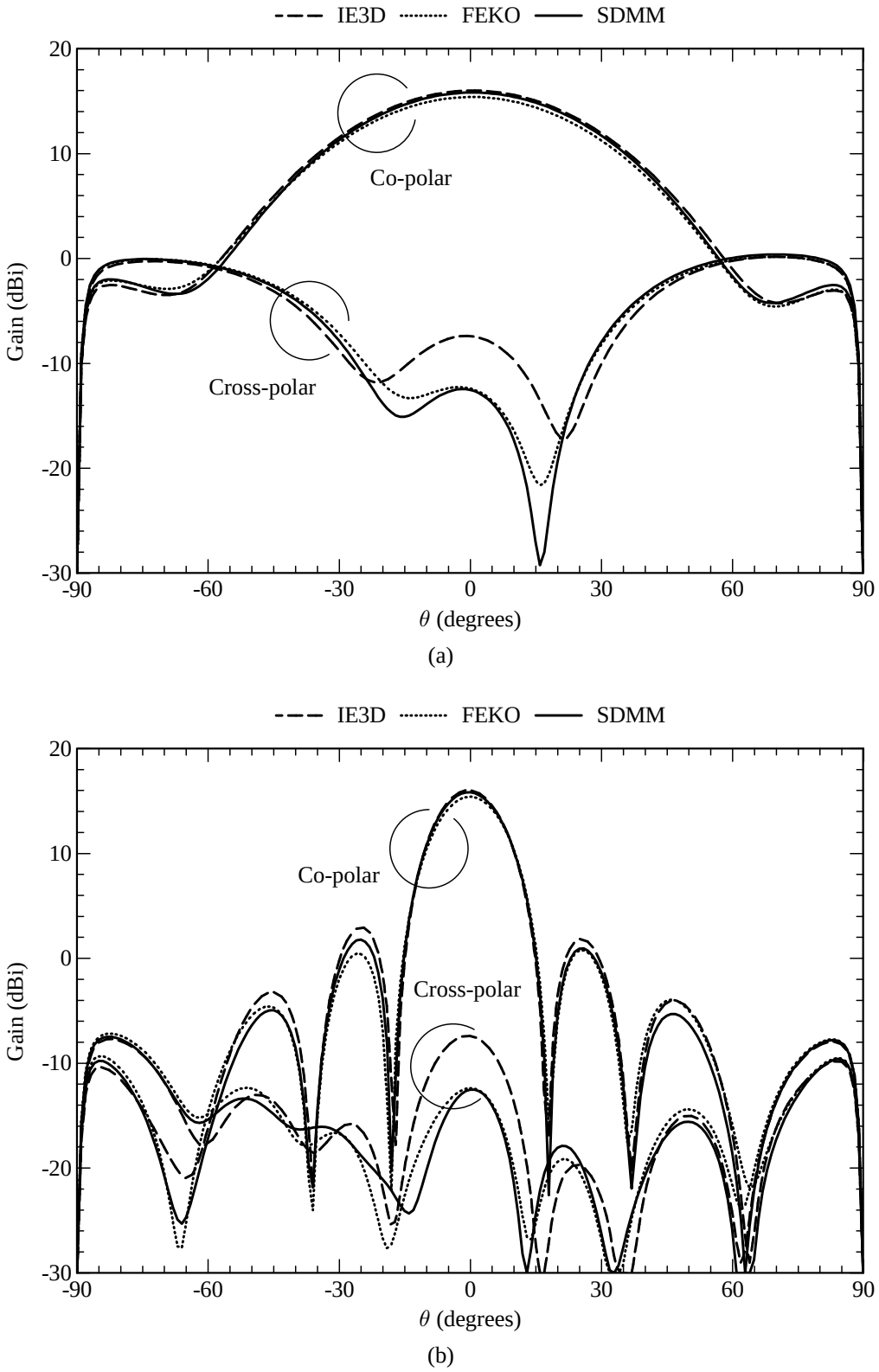

Figure 4.55 Radiation patterns (at 1.8 GHz) of the nine-element $\pm 45^{\circ}$ slant-polarised array. (a) Radiation pattern in the azimuth plane ($\phi = 0^{\circ}$). (b) Radiation pattern in the elevation plane ($\phi = 0^{\circ}$).

4.4.9 Thirty Six-Element $\pm 45^\circ$ Slant-Polarised Array

The concept of adaptive antenna systems, also called smart antennas, has lately been a topic of extensive research. It can be used to increase the capacity of cellular communications systems. Essentially, it is an antenna array of which a relatively narrow beam can be steered towards the mobile subscriber. As such, the antenna effectively suppresses interference that comes from other directions. A common way to realise an adaptive antenna, is to place a number of linear antenna arrays next to each other, and to connect the input/output ports of the individual arrays by means of a suitable beamforming network [194, 197]. Usually, it is required that these arrays should only be able to scan in the azimuth plane [198].

In this section, four of the nine-element $\pm 45^\circ$ slant-polarised arrays, as presented in Section 4.4.8, are positioned next to each other in order to form an array that is suitable for adaptive beamforming in the azimuth plane. The geometry of the array is shown in Figure 4.56. The dimensions of the antenna elements, as well as the spacings between them, are exactly the same as those in Figure 4.53. Each subarray also has a feed network with two ports, similar to the one in Figure 4.53.

The electric current density on the structure was modelled with eighteen entire-domain sinusoidal basis functions on each resonant patch, the single higher-order circular attachment mode on each capacitor patch, and four PWS basis functions on each probe (excluding the one associated with the attachment mode). For the entire-domain sinusoidal basis functions, the (1,0), (1,2), (2,0), (2,1), (3,0), (3,2), (5,0), (7,0) and (9,0) modes were used for the $+45^\circ$-directed current, while the same set of modes were also used for the -45°-directed current. The feed networks were modelled with Sonnet's circuit analysis module. Due to the size of the antenna array, it was only modelled with the SDMM, which makes extensive use of entire-domain basis functions. Table 4.11 illustrates how the computer-memory requirements of the SDMM would compare to that of IE3D and FEKO. It can be seen that, for a non-iterative solution, the memory requirements of the two commercial codes would be greater than the available memory on most personal computers. For the SDMM, the amount of duplicate entries in the interaction matrix equates to 97.55%.

Table 4.11
Computer memory required for the storage of the interaction matrix associated with the thirty six-element $\pm 45^\circ$ slant-polarised antenna array.

Method	Unknowns	Memory
IE3D	30988	14.3 GB (estimated)
FEKO	24704	9.1 GB (estimated)
SDMM	968	14.3 MB

Figure 4.57 shows the coupling between the different subarrays. This includes coupling between

co-polar ports (e.g. two $+45^\circ$ ports), as well as coupling between cross-polar ports (e.g. a $+45^\circ$ port and a -45° port). As shown in Figure 4.56, subarray 1 represents a subarray at the edge of the array, while subarray 2 represents a subarray in the middle of the array. Figure 4.57(a) shows the coupling between subarray 1 and all of the other subarrays, while Figure 4.57(b) shows the coupling between subarray 2 and all of the other subarrays. From these two figures, it can be seen that the coupling between all ports in the array is relatively low. In most cases the coupling is below 30 dB.

Figure 4.58 shows the simulated co-polarised and cross-polarised radiation patterns in the azimuth and elevation planes of the antenna array when all the co-polar ports are driven with equal amplitude and phase. It can be seen that the horizontal distribution of the subarrays effectively narrows the beamwidth in the azimuth plane. The cross-polar discrimination of this array is in the order of 25 dB over most of the usable beamwidth in the two principal planes.

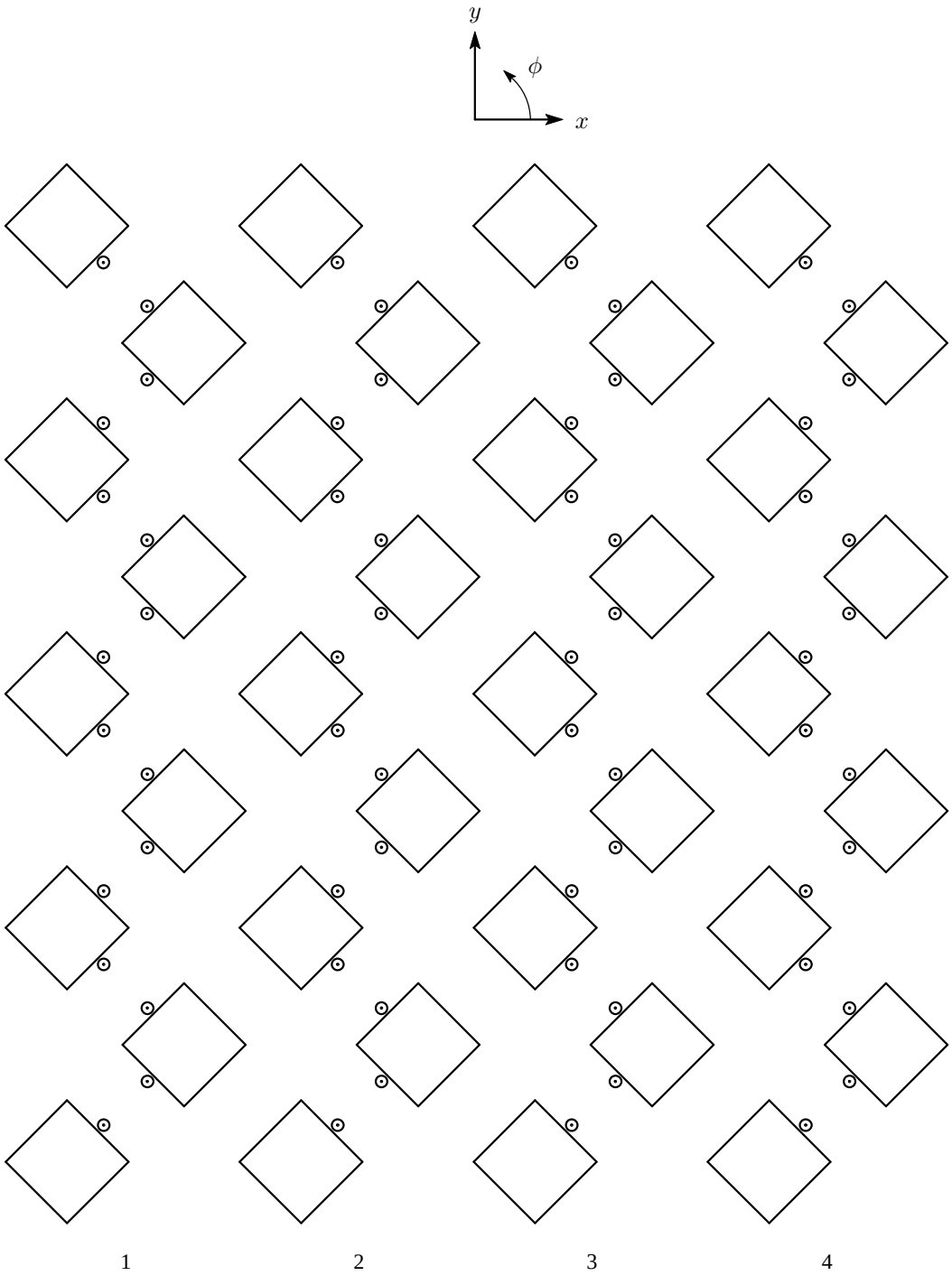

Figure 4.56 Geometry of the thirty six-element $\pm 45^{\circ}$ slant-polarised array. This array consists of four linear subarrays that are positioned next to each other.

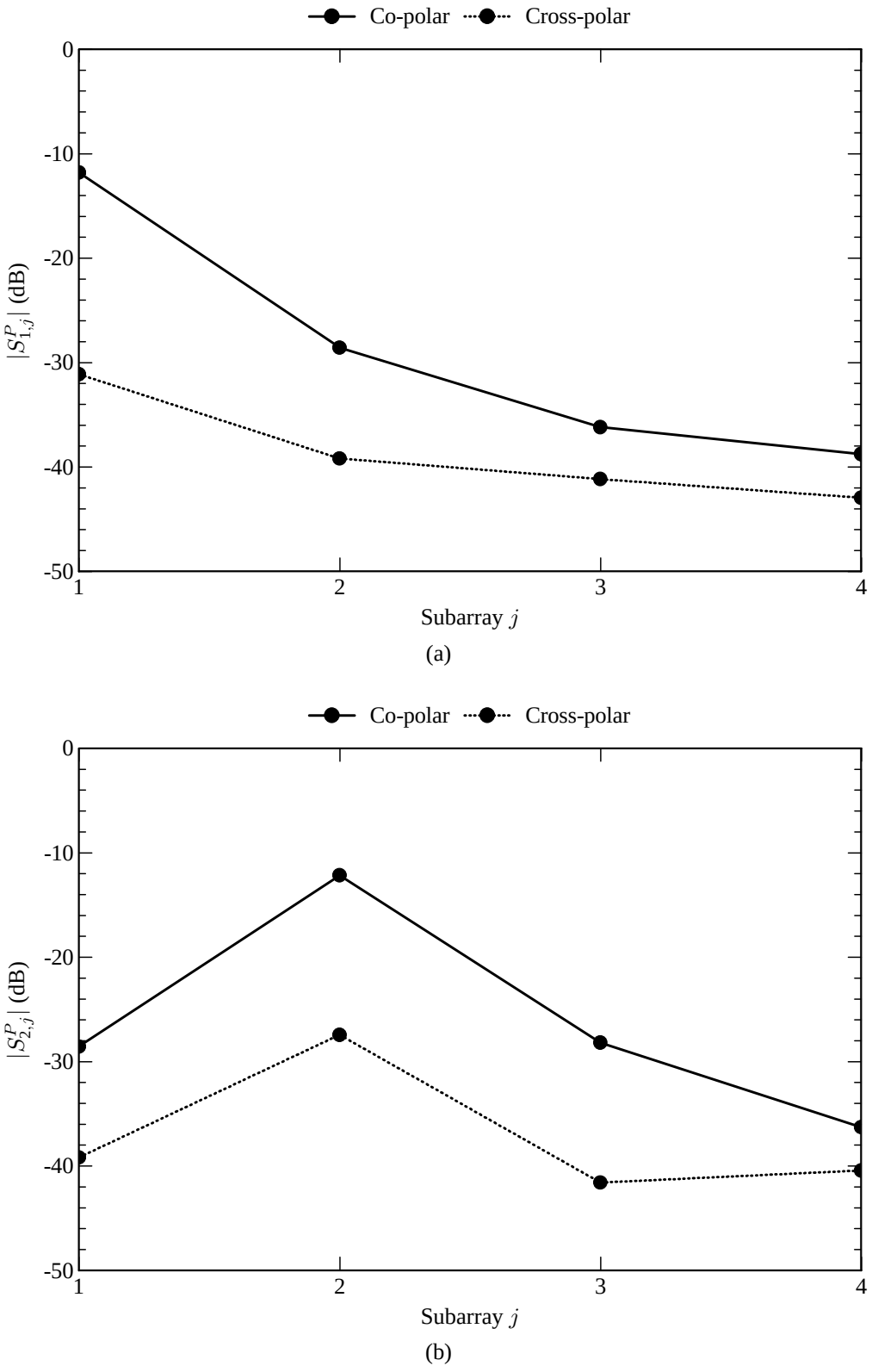

Figure 4.57 Co-polar and cross-polar coupling (at 1.8 GHz) between the linear subarrays of the thirty six-element $\pm 45^\circ$ slant-polarised array. (a) Coupling to subarray 1. (b) Coupling to subarray 2.

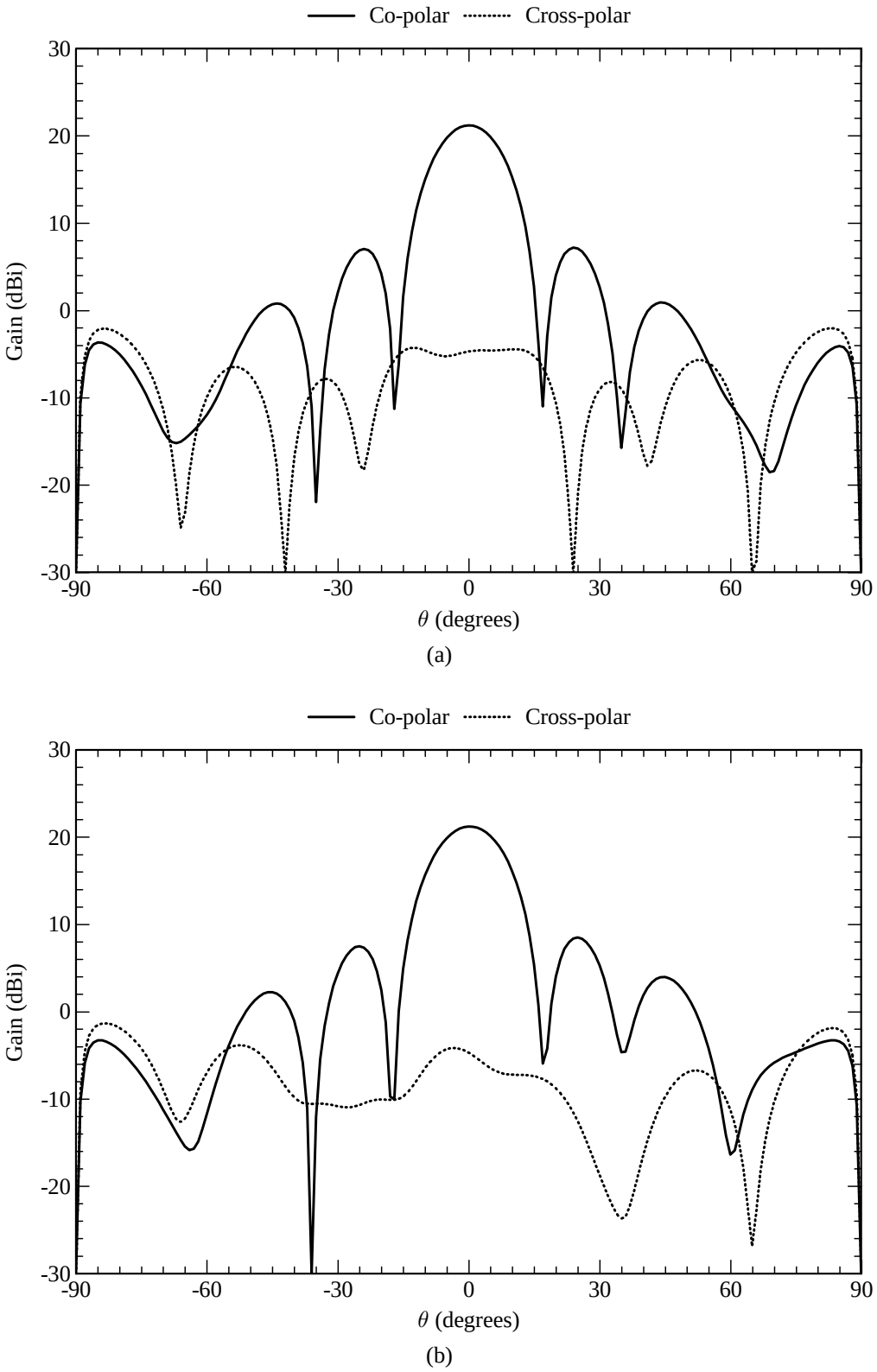

Figure 4.58 Radiation patterns (at 1.8 GHz) of the thirty six-element $\pm 45^{\circ}$ slant-polarised array when the co-polar ports are excited with equal amplitude and phase. (a) Radiation pattern in the azimuth plane ($\phi = 0^{\circ}$). (b) Radiation pattern in the elevation plane ($\phi = 0^{\circ}$).

4.4.10 Eighty-Element $\pm 45^\circ$ Slant-Polarised Array

Lindmark [194] has shown how up to twelve subarrays can be used to realise an adaptive antenna. In order to illustrate the computational benefits of the SDMM for such large problems, this section presents an antenna array that consists of ten linear subarrays, each one being $\pm 45^\circ$ slant polarised. The geometry of the array is shown in Figure 4.59. The dimensions of the antenna elements, as well as the spacings between them, are exactly the same as those in Figure 4.44. Each subarray also has a feed network with two ports, one for each polarisation.

The electric current density on the structure was modelled with eighteen entire-domain sinusoidal basis functions on each resonant patch, the single higher-order circular attachment mode on each capacitor patch, and four PWS basis functions on each probe (excluding the one associated with the attachment mode). For the entire-domain sinusoidal basis functions, the (1,0), (1,2), (2,0), (2,1), (3,0), (3,2), (5,0), (7,0) and (9,0) modes were used for the $+45^\circ$-directed current, while the same set of modes were also used for the -45°-directed current. The feed networks were modelled with Sonnet's circuit analysis module. Once again, due to the size of the antenna array, it was only modelled with the SDMM. Table 4.12 illustrates how the computer-memory requirements of the SDMM would compare to that of IE3D and FEKO. It can be seen that, for a non-iterative solution, the memory requirements of the two commercial codes would far outweigh the available memory on any personal computer. For the SDMM, the amount of duplicate entries in the interaction matrix equates to 98.89%.

Table 4.12
Computer memory required for the storage of the interaction matrix associated with the eighty-element $\pm 45^\circ$ slant-polarised antenna array.

Method	Unknowns	Memory
IE3D	81520	99.0 GB (estimated)
FEKO	58240	50.5 GB (estimated)
SDMM	2240	76.6 MB

Figure 4.60 shows the coupling between some of the subarrays. This includes coupling between co-polar ports (e.g. two $+45^\circ$ ports), as well as coupling between cross-polar ports (e.g. a $+45^\circ$ port and a -45° port). As shown in Figure 4.59, subarray 1 represents a subarray at the edge of the array, while subarray 5 represents a subarray in the middle of the array. Figure 4.60(a) shows the coupling between subarray 1 and all of the other subarrays, while Figure 4.60(b) shows the coupling between subarray 5 and all of the other subarrays. From these two figures, it can be seen that the coupling between the subarrays is substantially higher than the coupling for the configuration in Figure 4.56.

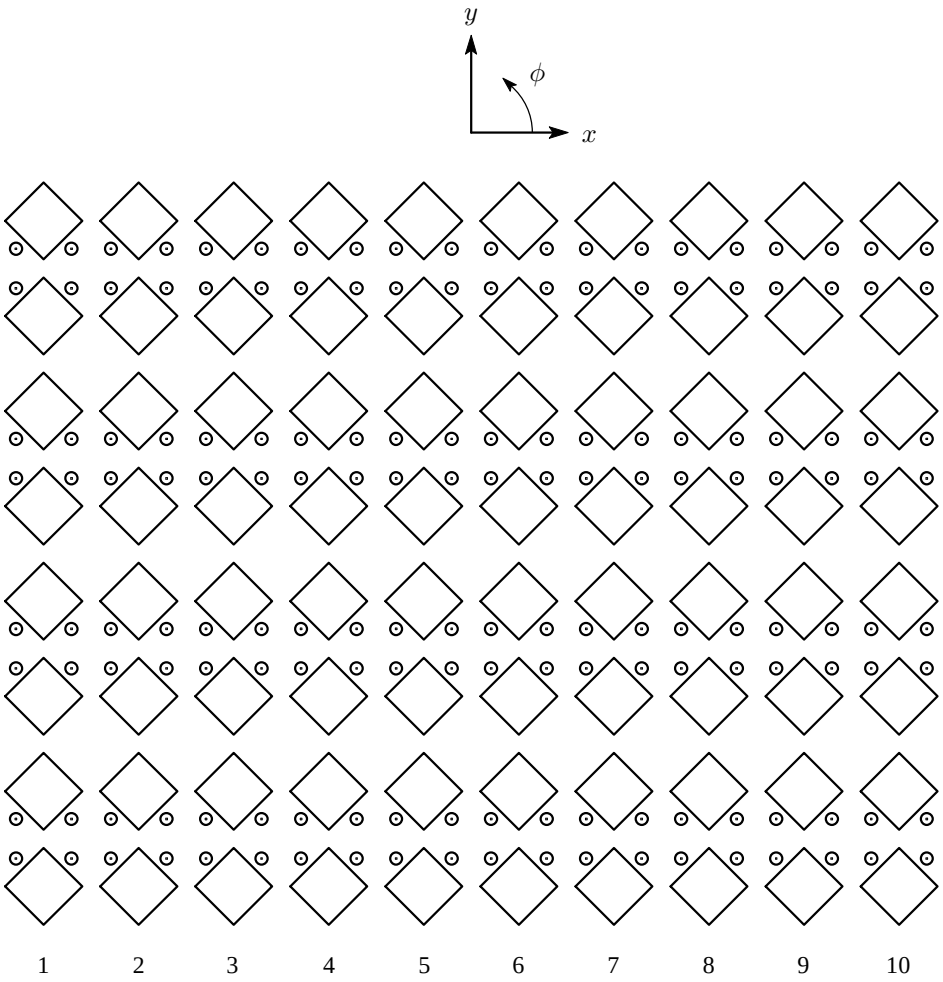

Figure 4.59 Geometry of the eighty-element $\pm 45^{\circ}$ slant-polarised array. This array consists of ten linear subarrays that are positioned next to each other.

Figure 4.61 shows the simulated co-polarised and cross-polarised radiation patterns in the azimuth and elevation planes of the antenna array when all the co-polar ports are driven with equal amplitude and phase. It can be seen that the ten subarrays narrows the beamwidth in the azimuth plane significantly. However, the cross-polar discrimination of this array is not good at all. It appears to be only about 10 dB.

The results in this section and the previous section show that the layout of the antenna elements is very important when good isolation between subarrays, as well as low cross-polarisation levels, is required. In terms of these requirements, the zig-zag configuration of Figure 4.56 is definitely superior.

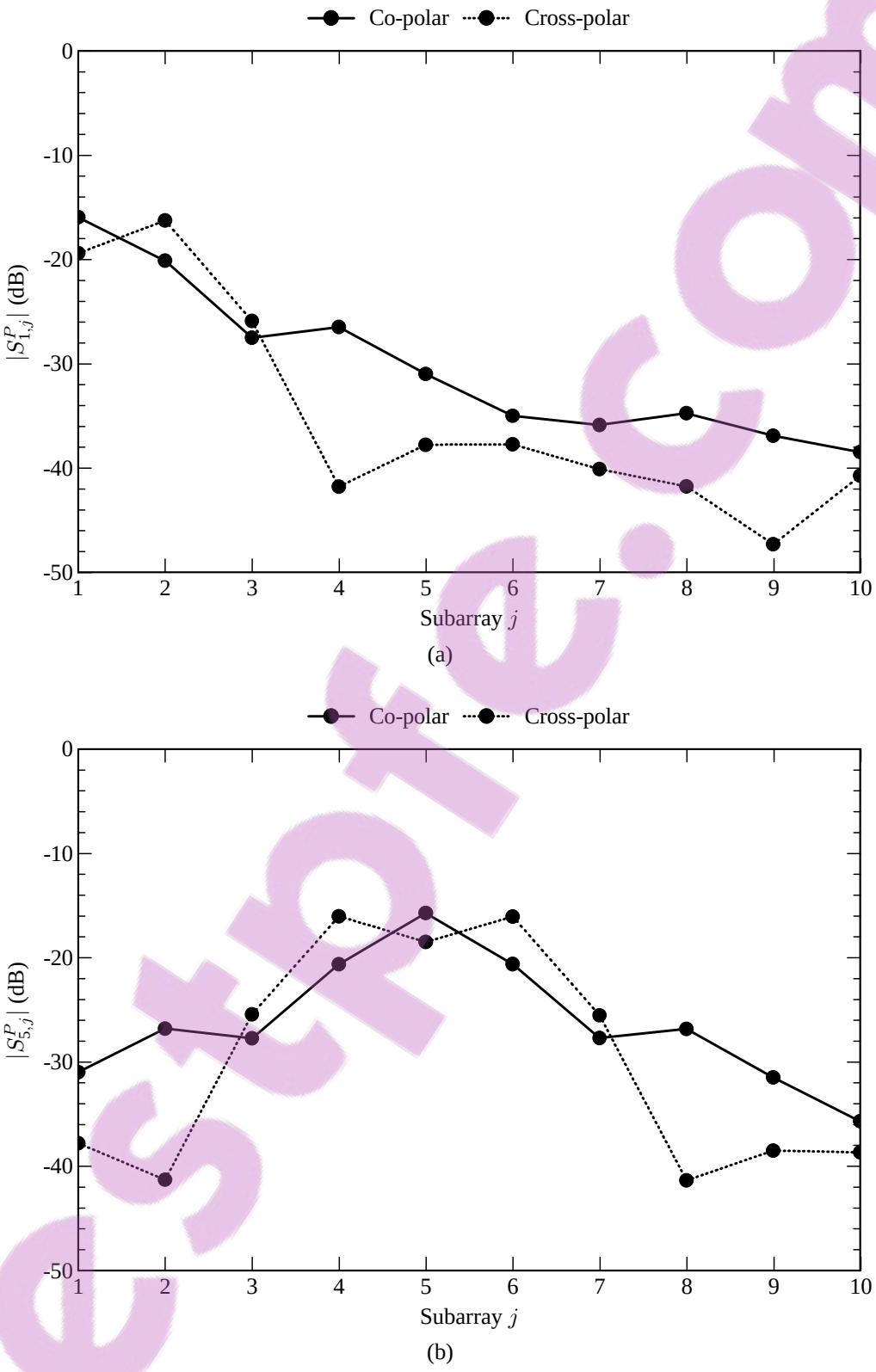

Figure 4.60 Co-polar and cross-polar coupling (at 1.8 GHz) between the linear subarrays of the eighty-element $\pm 45^\circ$ slant-polarised array. (a) Coupling to subarray 1. (b) Coupling to subarray 5.

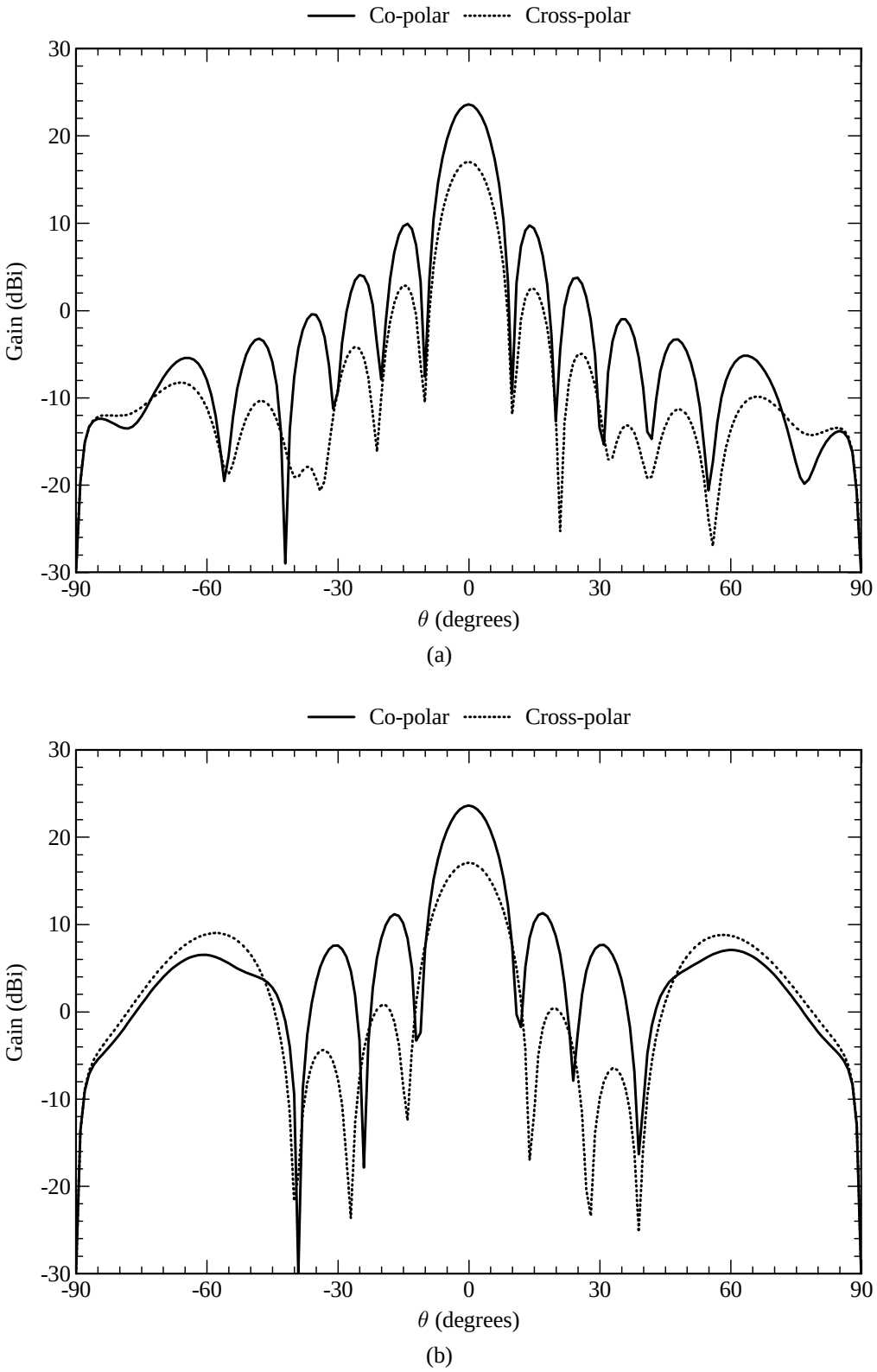

Figure 4.61 Radiation patterns (at 1.8 GHz) of the eighty-element $\pm 45^{\circ}$ slant-polarised array when the co-polar ports are excited with equal amplitude and phase. (a) Radiation pattern in the azimuth plane ($\phi = 0^{\circ}$). (b) Radiation pattern in the elevation plane ($\phi = 0^{\circ}$).

4.5 ALTERNATIVELY-SHAPED PATCHES

So far, only antenna elements with rectangular resonant patches have been investigated. However, it is possible to use alternative shapes for the resonant patches. Two shapes that have been found to be useful, are the circular patch and annular-ring patch. Figures 4.62 and 4.63 depict the geometry of two antenna elements that were designed to operate at a centre frequency of more or less 1.8 GHz. The annular ring was designed to operate in its TM_{11} mode. The capacitive feed probe is an ideal feeding mechanism for the annular ring as it is impossible to obtain an impedance match for the annular ring in its TM_{11} mode when using a direct feed to the ring. This happens to be the case even when using thin substrates.

The antenna elements in Figures 4.62 and 4.63 were analysed with IE3D, as the SDMM implementation in this thesis only applies to antenna elements with rectangular resonant patches. For verification purposes, a physical model of each antenna element was constructed on a 150 mm $\times$ 150 mm ground plane. Both these antenna elements have impedance loci that are very similar to that of the antenna element with the rectangular resonant patch. Table 4.13 shows the measured and simulated 10 dB return-loss bandwidths of the two antenna elements. The measured and simulated bandwidth values compare very well, while they are also comparable to that of the antenna element with a rectangular resonant patch.

Table 4.13
Measured and simulated 10 dB return-loss bandwidths of the antenna elements with alternatively-shaped patches.

	Circular	Annular ring
Measured	27.9%	26.1%
IE3D	26.8%	25.9%

Figure 4.64 shows the measured and simulated radiation patterns in the *E*-plane and the *H*-plane of the antenna element with a circular resonant patch, while Figure 4.65 shows the same for the the antenna element with a annular-ring resonant patch. The corresponding gain values are shown in Table 4.14. All the measured and simulated results compare favourably, while the radiation patterns and gain values of the two elements are also very similar.

Table 4.14
Measured and simulated gain values of the antenna elements with alternatively-shaped patches.

	Circular	Annular ring
Measured	8.6 dBi	8.5 dBi
IE3D	8.8 dBi	8.0 dBi

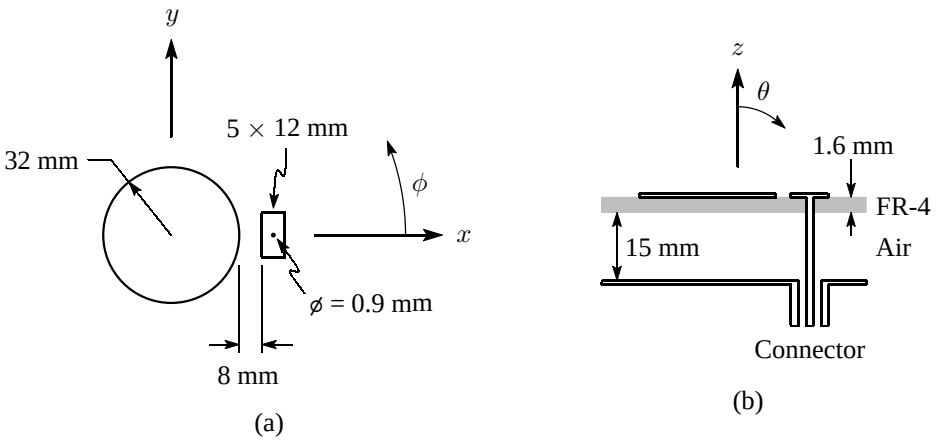

Figure 4.62 Geometry of the antenna element with a circular resonant patch. (a) Top view of the antenna element. (b) Side view of the multilayered substrate with $\varepsilon_r = 4.25$ and $\tan\delta_\varepsilon = 0.02$ for the FR-4 layer and with $\varepsilon_r = 1$ and $\tan\delta_\varepsilon = 0$ for the air layer.

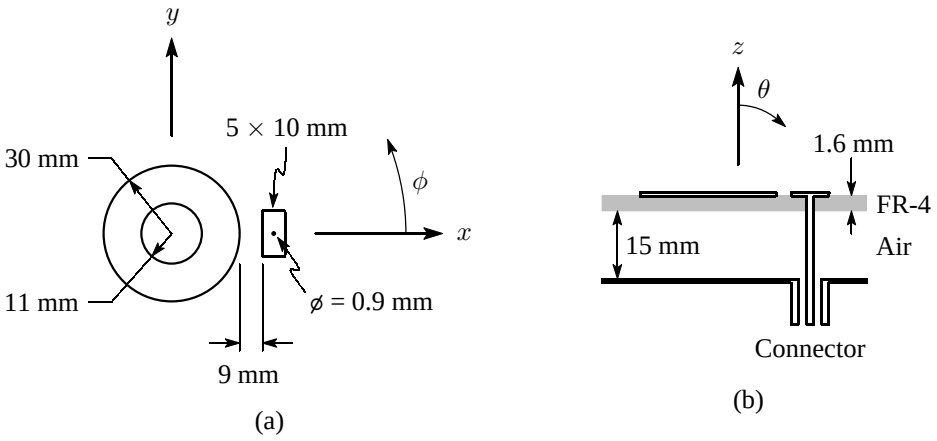

Figure 4.63 Geometry of the antenna element with an annular-ring resonant patch. (a) Top view of the antenna element. (b) Side view of the multilayered substrate with $\varepsilon_r = 4.25$ and $\tan\delta_\varepsilon = 0.02$ for the FR-4 layer and with $\varepsilon_r = 1$ and $\tan\delta_\varepsilon = 0$ for the air layer.

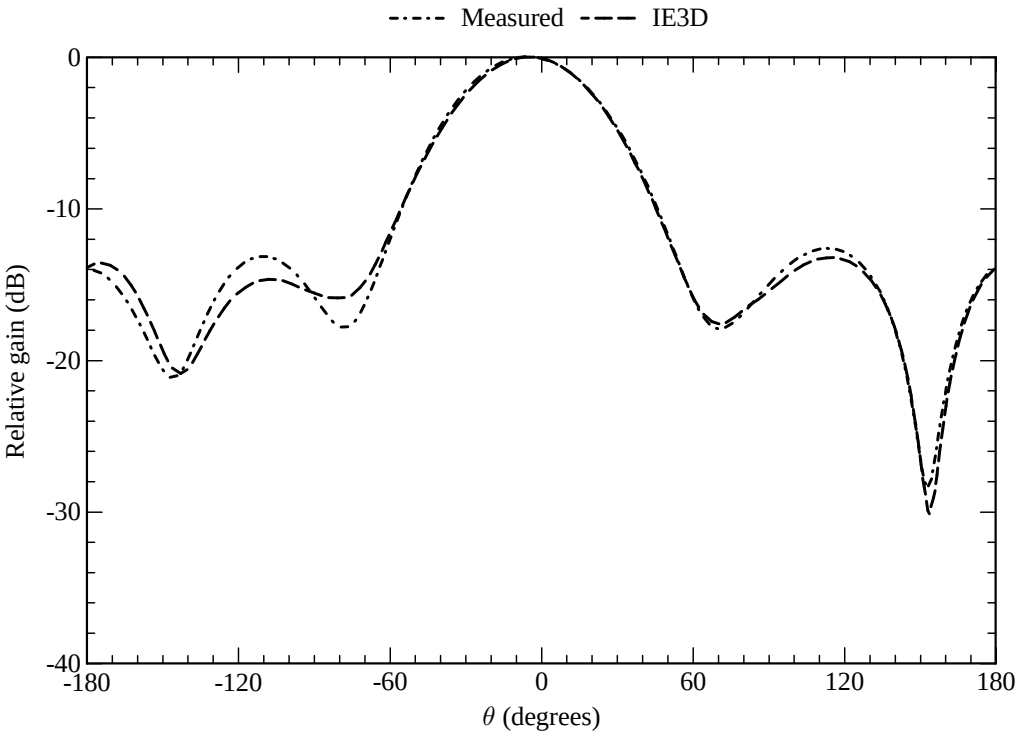

(a)

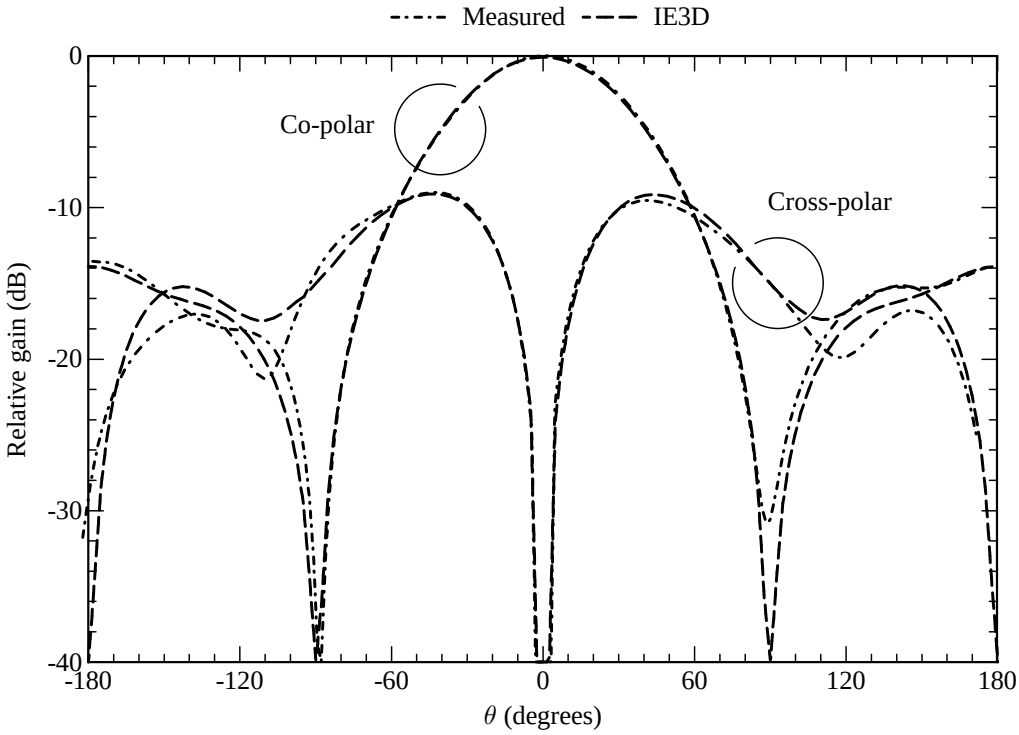

(b)

Figure 4.64 Radiation patterns (at 1.8 GHz) of the antenna element with a circular resonant patch. (a) Co-polar radiation pattern in the *E*-plane ($\phi = 0^\circ$). (b) Co-polar and cross-polar radiation patterns in the *H*-plane ($\phi = 90^\circ$).

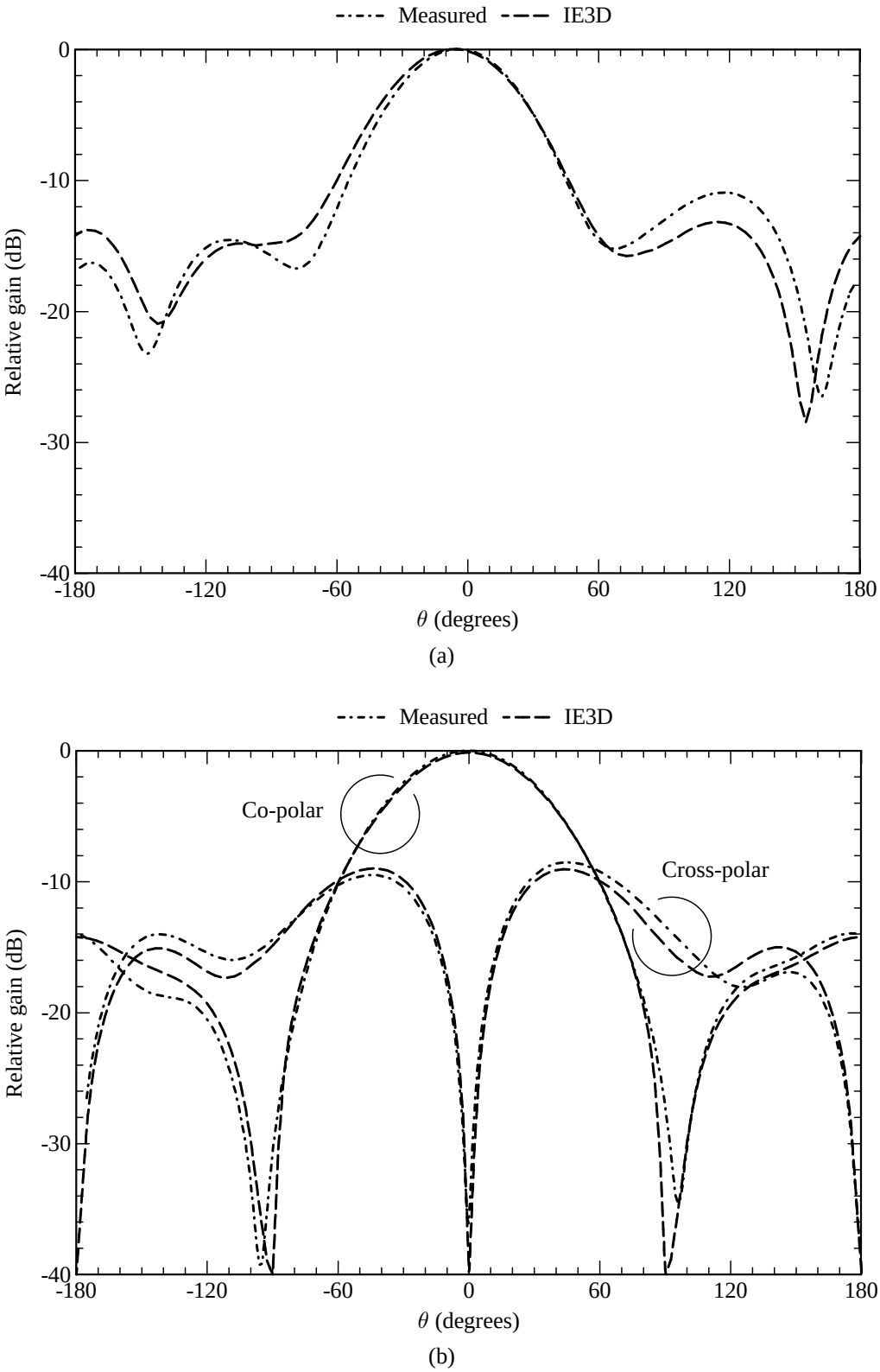

Figure 4.65 Radiation patterns (at 1.8 GHz) of the antenna element with an annular-ring resonant patch. (a) Co-polar radiation pattern in the *E*-plane ($\phi = 0^\circ$). (b) Co-polar and cross-polar radiation patterns in the *H*-plane ($\phi = 90^\circ$).

4.6 CONCLUDING REMARKS

This chapter presented a number of numerical and experimental results, in order to verify that the SDMM implementation is accurate, to characterise the new antenna elements and to show how they can be used for different applications.

The SDMM implementation was verified by first analysing isolated parts of the antenna elements, such as the probes and probe-fed capacitor patches. The results compares favourably to published data. The circular and rectangular attachment-mode approaches were weighed up against each other in terms of their abilities to model rectangular probe-fed patches of various sizes and on various substrate thicknesses. It turned out that the circular attachment mode is more versatile than the rectangular attachment mode. The rectangular attachment mode was unable to model the electric current density on very small probe-fed patches, such as those that are used for the capacitor patches. The higher-order circular attachment mode proved to be quite successful for the modelling of the electric current density on the circular capacitor patches. Most importantly, the SDMM implementation also proved to be accurate for the analysis of complete antenna elements, consisting of a resonant patch that is excited by a small probe-fed capacitor patch. Throughout, the SDMM results compared well with published results, measurements and the results of other commercial codes.

The new antenna elements were characterised in order to show how the various dimensions of the structure affects the input impedance and impedance bandwidth of the antenna element. This knowledge is very important in the design of such elements or antenna arrays consisting of such elements. It was shown that the size of the capacitor and the gap width between the capacitor patch and the resonant patch, are the two important parameters for controlling the input impedance of the antenna element. The size of the capacitor patch has a more profound effect on the input reactance, while the gap width largely affects the input resistance. The bandwidth of the antenna element increases together with the thickness of the air substrate, but only to a certain point, after which it would appear that the gap width between the capacitor patch and the resonant element becomes too large. Also, for a rather thin air substrate, the capacitor patch cannot be placed close enough to the resonant patch, therefore also placing a lower limit on the impedance bandwidth. On the high end, it was shown that impedance bandwidths of well over 30% can be achieved for a VSWR of 2:1.

It was also shown how the antenna element can be used in a number of different applications. The examples included linear vertically-polarised arrays, linear horizontally-polarised arrays, as well as a number of $\pm 45^{\circ}$ slant-polarised arrays. These are often required in applications such as cellular communications. Some of the arrays that were analysed, are electrically large and served as good examples to show how efficient the SDMM implementation is in terms of computer-memory requirements. For a fixed amount of computer memory, the SDMM implementation can be used

to analyse much larger arrays than what is possible with the commercial codes. Throughout all the applications that were presented, the simulation results of the SDMM also compared well with measurements and the results of the two commercial codes that were used.

One feature of the SDMM implementation that proved to be very successful, is the identification of duplicate entries within the interaction matrix. This is done so that these entries do not need to be evaluated more than once. Figure 4.66 shows a typical relation between the number of unknowns and the number of entries in the interaction matrix that has to be evaluated after all the duplicate entries have been identified. The relation in Figure 4.66 is based on the problems that were solved in this chapter and is of course very dependant on the antenna geometry and types of basis functions that are used. However, it can be seen that, in general, it would appear that there is a linear relation between the number of entries to be evaluated and the number of unknowns. Without this feature, the number of entries to be evaluated would be proportional to the square of the number of unknowns. As shown in Figure 4.67, it turned out that the time required to evaluate the relevant entries in the interaction matrix, also has a linear relation with the number of unknowns. Once again, this is based on the problems that were analysed in this chapter.

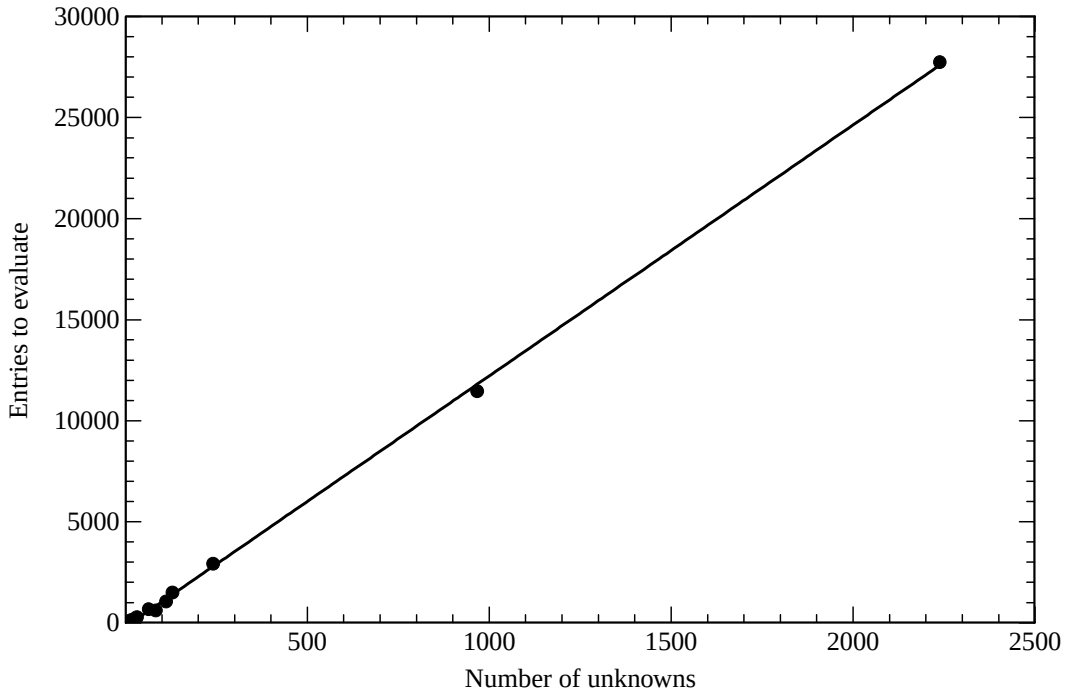

Figure 4.66 Number of entries in the interaction matrix of the SDMM that has to be evaluated after all duplicate entries have been identified.

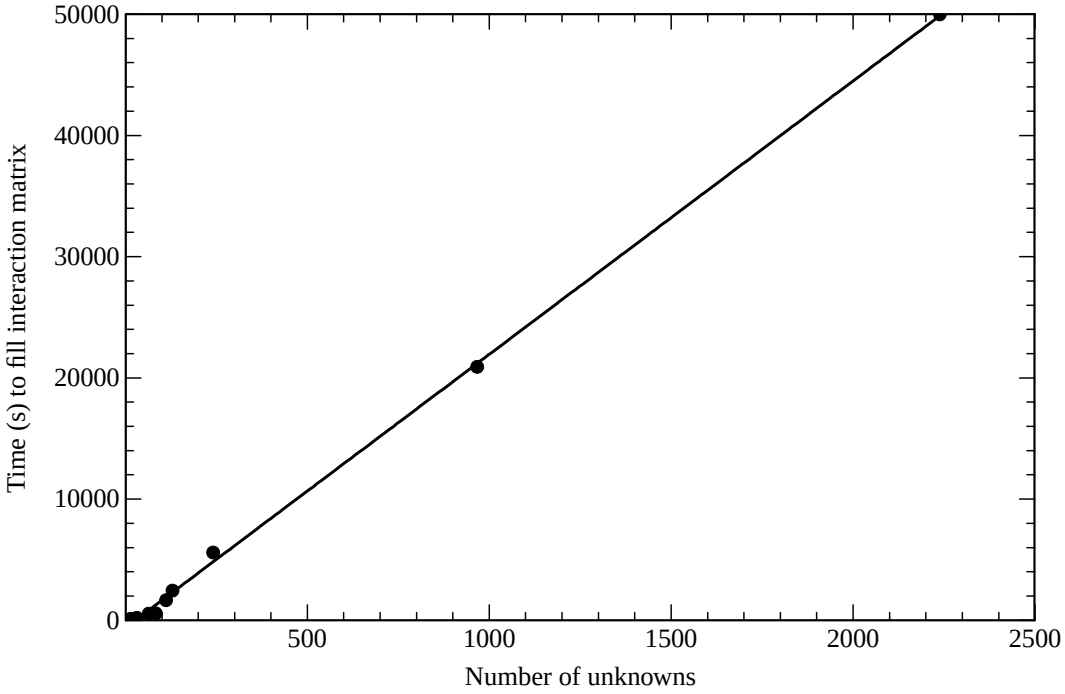

Figure 4.67 Time required to fill the interaction matrix of the SDMM on a 2.6 GHz Pentium 4 processor at one frequency point.

CHAPTER 5

Conclusions and Future Research

5.1 GENERAL CONCLUSIONS

The principal contributions of this study include the development of a new capacitive feeding mechanism for wideband probe-fed microstrip patch antennas as well as the implementation of a spectral-domain moment-method formulation for the efficient analysis of large, finite arrays of these elements. Such antenna configurations are very useful in the wireless communications industry, but extremely difficult to analyse with commercially available software.

The new feeding mechanism for wideband probe-fed microstrip patch antennas consists of a small probe-fed capacitor patch that is situated next to the resonant patch, both patches residing on the same substrate layer. The gap between the capacitor patch and the resonant patch effectively acts as a series capacitor, thereby overcoming the inductance usually associated with probe-fed microstrip patch antennas on thick substrates. It has been demonstrated, that by using such a feeding mechanism, impedance bandwidths in the order of 32% can be achieved for a voltage standing-wave ratio (VSWR) of 2:1, while 25% can be achieved for a VSWR of 1.5:1.[1] These are better than the 10% to 15% bandwidths that are required for wireless communications systems such as the Global System for Mobile (GSM) Communications and the Universal Mobile Telecommunications System (UMTS). A major advantage of the new feeding mechanism is that only a single substrate is required to support the antenna. This implies cost savings when compared to other approaches, as well as simplified manufacturing techniques and light weight.

[1] These impedance bandwidths were achieved with a specific substrate and at a specific operating frequency. It might be possible to increase these bandwidths with other substrate materials and at other operating frequencies.

The design of the new antenna element is very straightforward. The substrate thickness is determined by the required impedance bandwidth. Thereafter, the size of the resonant element can be found by using conventional methods. The characterisation of the new antenna elements has shown that there are basically only two parameters that have to be altered in order to match the input impedance of the antenna to that of the feed network. These are the size of the capacitor patch and the size of the gap between the capacitor patch and the resonant patch. The size of the capacitor patch mainly determines the reactive part of the input impedance, while the size of the gap mainly determines the resistive part of the input impedance. Results for both rectangular and circular capacitor patches have been shown. It has also been demonstrated, both through numerical modelling and measurements, how the new feeding mechanism can be applied to rectangular, circular and annular-ring elements.

As is the case with other probe-fed microstrip patch antennas on thick substrates, the new antenna element also has a slightly squinted radiation pattern in the *E*-plane and slightly higher cross-polarisation levels in the *H*-plane. However, these can be rectified by using symmetric probes or by using proper orientation of the elements in an array configuration. Numerical modelling and experimental measurements have shown how the antenna element can be used in various antenna array configurations. These include vertically polarised, horizontally polarised and slant-polarised arrays. It has also been shown that acceptable cross-polarisation levels and port-decoupling can be achieved for dual-polarised arrays.

For the numerical modelling of the new antenna element, as well as arrays that are based on it, a SDMM formulation, which can handle any number of substrate layers on an infinite ground plane, has been implemented. The formulation is based on a unique combination of entire-domain and subdomain basis functions, leading to considerable savings in computer-memory requirements when compared to commercial codes (both in the spectral and spatial domains) that normally only use subdomain basis functions. With this formulation, the electric current density on the resonant patches is modelled with a set of entire-domain modes, that on the rectangular capacitor patches with rectangular rooftop basis functions and that on the probes with piecewise-sinusoidal basis functions. A circular attachment mode is used to model the electric current density at the probe-to-patch junctions. In addition, all of the electric current density on the circular capacitor patches can be modelled with only the attachment mode. This makes antenna elements with circular capacitor patches much more efficient to analyse. Examples have been shown where the savings in terms of computer memory is more than 2500 times when compared to some commercial moment-method (MM) codes. This savings can even become larger when larger antenna arrays are analysed. In terms of accuracy, the numerical formulation compares well with other commercial codes.

Commercial SDMM codes are normally based on an underlying rectangular grid, implying that the modelled structure often has to be modified in order to fit into the grid. This new model allows for arbitrary-sized basis functions that can also have an arbitrary orientation with respect to each

other. There is therefore no need to modify the geometry of the actual structure.

A very important type of basis function, which is required when a probe is connected to a microstrip patch, is the so-called attachment mode. In the literature, various attachment modes have been proposed for the SDMM, but it was not clear as to what the limitations of each one are. Some of these modes have been studied in various situations, resulting in a better understanding of where they are applicable. The circular attachment mode has also been extended for a more accurate description of the electric current density on small circular probe-fed capacitor patches.

One of the difficulties associated with the SDMM, is the highly oscillating nature of the interaction integrands for basis and testing functions that are widely separated. A recent publication dealt with this issue by proposing a new integration path in the complex plane over which the integrand decays exponentially. However, this method becomes less efficient as the basis and testing functions move closer to each other, even more so for thick substrates. This method has been extended and can now also be used in situations where the basis and testing functions are relatively close to each other on a relatively thick substrate. The conditions under which this method is valid, have also been extended.

When using the MM, the interactions between all basis and testing functions have to be calculated. However, depending on the implementation, there are often identical interactions that have to be calculated repeatedly. On a rectangular grid, these duplicate entries can easily be identified and eliminated, but becomes much more difficult with a mixture of lower-order and higher-order basis functions that are arbitrarily orientated. Special algorithms have been developed to deal with such a mixture of basis and testing functions, and proves to speed up the solution significantly.

One drawback of the SDMM, is that numerical integration is still required to evaluate each of the entries of the interaction matrix. It makes this implementation of the SDMM slower than commercial codes, where the entries are evaluated in the spatial domain and where lookup tables and other methods can be used to speed up the evaluation of the Green's function. However, due to the fact that this formulation uses far fewer basis functions, the difference in computational time is only observed for the analysis of single antenna elements and small arrays. For larger antenna arrays, the computational times are comparable, while for very large arrays, this implementation of the SDMM will be quicker. Another drawback of the SDMM, when compared to commercial codes, is that it is limited to specific geometries (it has after all been developed for a specific application). Some experience is also required in terms of the entire-domain basis functions that should be used on the resonant patches.

5.2 FUTURE RESEARCH

As is the case with all research, there are always more aspects that can be investigated than what is practically possible. Here also, there are some aspects of both the new antenna and the numerical

formulation that can be extended.

Although the new antenna elements have been characterised to some extent, it would be useful to have more comprehensive guidelines to design such antenna elements. This should include geometrical parameters as well as the optimum choice of material properties, especially dielectric constants and substrate thicknesses. The SDMM, which has been implemented, can be used to analyse various configurations, while the results can be used to build up a database. The design guidelines can then be extracted from such a database. Optimisation techniques, such as genetic algorithms [199–201], can also be useful.

It has been shown by other authors that superstrates can have some advantageous effects on the performance of microstrip patch antennas, such as widening of the impedance bandwidth [202–205]. Also, in practice, most antennas are covered by a radome for protection. It would therefore be interesting to study the effects of superstrates when used in conjunction with the new antenna element and associated antenna arrays. This can of course be handled most easily with the current numerical formulation as it already caters for an arbitrary number of substrate/superstrate layers.

The size of the new antenna element can further be reduced by reducing the length of the rectangular resonant patch to one quarter of a wavelength and shorting the side opposite to the capacitor patch. Such an element could be useful in applications where really small antennas with wide bandwidth are required. However, from a modelling point of view, it would not be possible to use the current formulation. The analysis would require vertical current strips and it would most likely not be possible to use entire-domain basis functions on the quarter-wave patch.

Some applications, especially space applications, require the use of circular polarisation. There are various ways to obtain circular polarisation with conventional probe-fed microstrip patch antennas. It can be done with one probe, two probes, or by using sequentially rotated patches. It should be possible to apply the same ideas to the new antenna element.

It should be a fairly straightforward process to extend the numerical formulation so that circular and annular-ring resonant patches can also be included. It is possible to model the electric current density on such shapes with entire-domain basis functions of which the Fourier transforms are already available in the literature [28, 51, 128, 206, 207]. The analysis of antennas with these patch shapes might even prove to be more efficient as it might be possible to use the separation of variables while evaluating the integrals associated with the interaction-matrix entries. The integration limits and integration intervals for interaction-matrix entries that contain these functions, would have to be determined as well.

While the numerical integration, associated with the interaction between a basis function and a testing function, has already been optimised, there is a specific case where all the integration

strategies that have been implemented, are still inefficient. This is for lateral overlap between a small basis/testing function, such as a subdomain function, and a large testing/basis function, such as an entire-domain function. This can, for example, occur when the gap between the two functions is very small and the functions are not aligned, or when the two functions are on separate layers and overlap laterally.[2] In such cases, the centres of the two functions can still be laterally separated to such an extent, that the integrand associate with the interaction between the two functions, become very oscillatory. Due to the fact that the functions overlap, the integration strategy for laterally separated functions cannot be used, while the integration strategy for overlapping functions become very inefficient. The development of an integration strategy that can handle such situations, would be very useful.

The modelling of wideband antennas often require the analysis to be performed over a large number of frequency points. It is possible to reduce the computational time by analysing the antenna at only a few selected frequency points and to then use interpolation in some intelligent way to find the response at other frequency points. One such a technique uses rational functions to interpolate the response [208, 209], while another uses interpolation of the interaction-matrix entries [210]. Such techniques should also prove to be useful for the numerical formulation that has been implemented here.

[2] Although overlapping large and small basis/testing functions on separate layers are not required for the modelling of the new antenna element, the numerical formulation could also be used to handle other configurations that require such overlapping basis/tesing functions. An example is stacked patches.

References

[1] D. M. Pozar and D. H. Schaubert, Eds., *Microstrip Antennas: The Analysis and Design of Microstrip Antennas and Arrays*. New York: IEEE Press, 1995.

[2] R. B. Waterhouse, "Microstrip patch antennas," in *Handbook of Antennas in Wireless Communications*, L. C. Godara, Ed. Boca Raton: CRC Press, 2002.

[3] D. H. Schaubert, "A review of some microstrip antenna characteristics," in *Microstrip Antennas: The Analysis and Design of Microstrip Antennas and Arrays*, D. M. Pozar and D. H. Schaubert, Eds. New York: IEEE Press, 1995, pp. 59–67.

[4] C. A. Balanis, *Antenna Theory: Analysis and Design*, 2nd ed. New York: John Wiley & Sons, 1997.

[5] W. Chen and K.-F. Lee, "Input impedance of coaxially fed rectangular microstrip antenna on electrically thick substrate," *Microwave and Optical Technology Letters*, vol. 6, no. 6, pp. 387–390, May 1993.

[6] W. Chen, "Spectral domain moment method analysis of coaxially-fed rectangular microstrip antennas," Ph.D. thesis, University of Toledo, Toledo, Ohio, 1996.

[7] K. F. Lee and W. Chen, Eds., *Advances in Microstrip and Printed Antennas*. New York: John Wiley & Sons, 1997.

[8] G. Mayhew-Ridgers, J. W. Odendaal, and J. Joubert, "New feeding mechanism for annular-ring microstrip antenna," *Electronics Letters*, vol. 36, no. 7, pp. 605–606, Mar. 2000.

[9] ——, "Single-layer capacitive feed for wideband probe-fed microstrip antenna elements," *IEEE Transactions on Antennas and Propagation*, vol. 51, no. 6, pp. 1405–1407, June 2003.

[10] ——, "Entire-domain versus subdomain attachment modes for the spectral-domain moment-method analysis of probe-fed microstrip patch antennas," *IEEE Transactions on Antennas and Propagation*, vol. 52, no. 6, pp. 1616–1620, June 2004.

[11] ——, "Array performance of a new annular-ring microstrip antenna element," in *Proceedings of the USNC/URSI National Radio Science Meeting*, Salt Lake City, Utah, July 2000, p. 313.

[12] ——, "New feeding mechanism for probe-fed microstrip antennas on thick substrates," in *Proceedings of the SATCAM 2000 Conference*, Somerset West, South Africa, Sept. 2000.

[13] ——, "Attachment modes for spectral-domain moment-method analysis of probe-fed microstrip patch antennas," in *Proceedings of the IEEE Africon 2002 Conference*, vol. 2, George, South Africa, Oct. 2002, pp. 525–526.

[14] ——, "Spectral-domain moment-method analysis of wideband patch antenna arrays with capacitive probe feeds," in *Proceedings of the 2004 URSI International Symposium on Electromagnetic Theory*, vol. 2, Pisa, Italy, May 2004, pp. 670–672.

[15] J. T. Aberle, D. B. Davidson, U. Jakobus, F. J. C. Meyer, and I. P. Theron, "Computational electromagnetics for wireless and RF applications," Short course taught at the University of Stellenbosch, Sept. 1999.

[16] W. C. Chew, J. M. Jin, E. Michielssen, and J. M. Song, "Recent advances in fast algorithms for computational electromagnetics," Short course taught at the AP-S International Symposium and USNC/URSI National Radio Science Meeting, Salt Lake City, July 2000.

[17] D. Sanchez-Hernandez, "A survey of broadband microstrip patch antennas," *Microwave Journal*, pp. 60–84, Sept. 1996.

[18] D. M. Pozar, "Review of bandwidth enhancement techniques for microstrip antennas," in *Microstrip Antennas: The Analysis and Design of Microstrip Antennas and Arrays*, D. M. Pozar and D. H. Schaubert, Eds. New York: IEEE Press, 1995, pp. 157–166.

[19] H. F. Pues and A. R. Van de Capelle, "Impedance-matching technique for increasing the bandwidth of microstrip antennas," *IEEE Transactions on Antennas and Propagation*, vol. AP-37, no. 11, pp. 1345–1354, Nov. 1989.

[20] H. An, B. K. J. C. Nauwelaers, and A. R. Van de Capelle, "Broadband microstrip antenna design with the simplified real frequency technique," *IEEE Transactions on Antennas and Propagation*, vol. 42, no. 2, pp. 129–136, Feb. 1994.

[21] D. de Haaij, J. W. Odendaal, and J. Joubert, "Increasing the bandwidth of a microstrip patch antenna with a single parallel resonant circuit," in *Proceedings of the IEEE Africon 2002 Conference*, vol. 2, George, South Africa, Oct. 2002, pp. 527–528.

[22] C. Wood, "Improved bandwidth of microstrip antennas using parasitic elements," *IEE Proceedings*, vol. 127, pt. H, no. 4, pp. 231–234, Aug. 1980.

[23] G. Kumar and K. C. Gupta, "Broad-band microstrip antennas using additional resonators gap-coupled to the radiating edges," *IEEE Transactions on Antennas and Propagation*, vol. AP-32, no. 12, pp. 1375–1379, Dec. 1984.

[24] ——, "Nonradiating edges and four edges gap-coupled multiple resonator broad-band microstrip antennas," *IEEE Transactions on Antennas and Propagation*, vol. AP-33, no. 2, pp. 173–178, Feb. 1985.

[25] ——, "Directly coupled multiple resonator wide-band microstrip antennas," *IEEE Transactions on Antennas and Propagation*, vol. AP-33, no. 6, pp. 588–593, June 1985.

[26] R. B. Waterhouse, "Design of probe-fed stacked patches," *IEEE Transactions on Antennas and Propagation*, vol. 47, no. 12, pp. 1780–1784, Dec. 1999.

[27] C. S. Lee, V. Nalbandian, and F. Schwering, "Planar dual-band microstrip antenna," *IEEE Transactions on Antennas and Propagation*, vol. 43, no. 8, pp. 892–894, Aug. 1995.

[28] A. N. Tulintseff, S. M. Ali, and J. A. Kong, "Input impedance of a probe-fed stacked circular microstrip antenna," *IEEE Transactions on Antennas and Propagation*, vol. 39, no. 3, pp. 381–390, Mar. 1991.

[29] A. Mitchell, M. Lech, D. M. Kokotoff, and R. B. Waterhouse, "Search for high-performance probe-fed stacked patches using optimisation," *IEEE Transactions on Antennas and Propagation*, vol. 51, no. 2, pp. 249–255, Feb. 2003.

[30] D. M. Kokotoff, J. T. Aberle, and R. B. Waterhouse, "Rigorous analysis of probe-fed printed annular ring antennas," *IEEE Transactions on Antennas and Propagation*, vol. 47, no. 2, pp. 384–388, Feb. 1999.

[31] J. P. Damiano, J. Bennegueouche, and A. Papiernik, "Study of multilayer microstrip antennas with radiating elements of various geometry," *IEE Proceedings*, vol. 137, pt. H, no. 3, pp. 163–170, June 1990.

[32] Z. Fan and K.-F. Lee, "Analysis of electromagnetically coupled patch antennas," *Microwave and Optical Technology Letters*, vol. 6, no. 7, pp. 436–441, June 1993.

[33] H. R. Hassani and D. Mirshekar-Syahkal, "Analysis of stacked rectangular patch antennas with nonaligned patches or unequal patch sizes," *IEEE Transactions on Antennas and Propagation*, vol. 42, no. 9, pp. 1333–1336, Sept. 1994.

[34] Z. N. Chen and M. Y. W. Chia, "Broad-band suspended pobe-fed plate antenna with low cross-polarization levels," *IEEE Transactions on Antennas and Propagation*, vol. 51, no. 2, pp. 345–346, Feb. 2003.

[35] ——, "Design of broadband probe-fed plate antenna with stub," *IEE Proceedings on Microwaves, Antennas and Propagation*, vol. 148, no. 4, pp. 221–226, Aug. 2001.

[36] C. L. Mak, K. M. Luk, K. F. Lee, and Y. L. Chow, "Experimental study of a microstrip patch antenna with a L-shaped probe," *IEEE Transactions on Antennas and Propagation*, vol. 48, no. 5, pp. 777–783, May 2000.

[37] Y.-X. Guo, C. L. Mak, K. M. Luk, and K. F. Lee, "Analysis and design of L-probe proximity-fed patch antennas," *IEEE Transactions on Antennas and Propagation*, vol. 49, no. 2, pp. 145–149, Feb. 2001.

[38] Y.-X. Guo, K.-M. Luk, and K.-F. Lee, "L-probe proximity-fed annular ring microstrip antennas," *IEEE Transactions on Antennas and Propagation*, vol. 49, no. 1, pp. 19–21, Jan. 2001.

[39] C. L. Mak, K. M. Luk, and K. F. Lee, "Wideband triangular patch antenna," *IEE Proceedings on Microwaves, Antennas and Propagation*, vol. 146, no. 2, pp. 167–168, Apr. 1999.

[40] C.-L. Mak, K.-F. Lee, and K.-M. Luk, "T-probe proximity fed broadband patch antenna," in *Proceedings of the AP2000 Millennium Conference on Antennas and Propagation*, Davos, Switzerland, Apr. 2000.

[41] F. S. Fong, H. F. Pues, and M. J. Withers, "Wideband multilayer coaxial-fed microstrip antenna element," *Electronics Letters*, vol. 21, no. 11, pp. 497–499, May 1985.

[42] G. A. E. Vandenbosch and A. R. Van de Capelle, "Study of the capacitively fed microstrip antenna element," *IEEE Transactions on Antennas and Propagation*, vol. 42, no. 12, pp. 1648–1652, Dec. 1994.

[43] G. A. E. Vandenbosch, "Network model for capacitively fed microstrip element," *Electronics Letters*, vol. 35, no. 19, pp. 1597–1600, Sept. 1999.

[44] P. S. Hall, "Probe compensation in thick microstrip patches," *Electronics Letters*, vol. 23, no. 11, pp. 606–607, May 1987.

[45] J. Anguera, C. Puente, J. Romeu, C. Borja, and G. Font, "An optimum method to design probe-fed single-layer single-patch wideband microstrip antenna," in *Proceedings of the AP2000 Millennium Conference on Antennas and Propagation*, Davos, Switzerland, Apr. 2000.

[46] Z.-F. Liu, P.-S. Kooi, L.-W. Li, M.-S. Leong, and T.-S. Yeo, "A method for designing broadband microstrip antennas in multilayered planar structures," *IEEE Transactions on Antennas and Propagation*, vol. 47, no. 9, pp. 1416–1420, Sept. 1999.

[47] M. A. González de Aza, J. Zapata, and J. A. Encinar, "Broad-band cavity-backed and capacitively probe-fed microstrip patch arrays," *IEEE Transactions on Antennas and Propagation*, vol. 48, no. 5, pp. 784–789, May 2000.

[48] Z. N. Chen and M. Y. W. Chia, "Broadband suspended plate antenna with probe-fed strip," *IEE Proceedings on Microwaves, Antennas and Propagation*, vol. 148, no. 1, pp. 37–40, Feb. 2001.

[49] K.-F. Tong, K.-M. Luk, K.-F. Lee, and R. Q. Lee, "A broad-band U-slot rectangular patch antenna on a microwave substrate," *IEEE Transactions on Antennas and Propagation*, vol. 48, no. 6, pp. 954–960, June 2000.

[50] S. Weigand, G. H. Huff, K. H. Pan, and J. T. Bernhard, "Analysis and design of broad-band single-layer rectangular U-slot microstrip patch antennas," *IEEE Transactions on Antennas and Propagation*, vol. 51, no. 3, pp. 457–468, Mar. 2003.

[51] Z. Nie, W. C. Chew, and Y. T. Lo, "Analysis of the annular-ring-loaded circular-disk microstrip antenna," *IEEE Transactions on Antennas and Propagation*, vol. 38, no. 6, pp. 806–813, June 1990.

[52] D. M. Kokotoff, R. B. Waterhouse, and J. T. Aberle, "An annular-ring coupled to a shorted patch," *IEEE Transactions on Antennas and Propagation*, vol. 45, no. 5, pp. 913–914, May 1997.

[53] R. E. Munson, "Conformal microstrip antennas and microstrip phased arrays," *IEEE Transactions on Antennas and Propagation*, vol. AP-22, pp. 74–78, Jan. 1974.

[54] A. G. Derneryd, "Linear polarised microstrip antennas," *IEEE Transactions on Antennas and Propagation*, vol. AP-24, pp. 846–851, Nov. 1976.

[55] ——, "A theoretical investigation of the rectangular microstrip antenna element," *IEEE Transactions on Antennas and Propagation*, vol. AP-26, no. 4, pp. 532–533, July 1978.

[56] K. R. Carver and J. W. Mink, "Microstrip antenna technology," *IEEE Transactions on Antennas and Propagation*, vol. AP-29, no. 1, pp. 2–24, Jan. 1981.

[57] H. Pues and A. Van de Capelle, "Accurate transmission-line model for the rectangular microstrip antenna," *IEE Proceedings*, vol. 131, pt. H, no. 6, pp. 334–340, Dec. 1984.

[58] E. H. Van Lil and A. R. Van de Capelle, "Transmission-line model for mutual coupling between microstrip antennas," *IEEE Transactions on Antennas and Propagation*, vol. AP-32, no. 8, pp. 816–821, Aug. 1984.

[59] Y. T. Lo, D. Solomon, and W. F. Richards, "Theory and experiment on microstrip antennas," *IEEE Transactions on Antennas and Propagation*, vol. AP-27, no. 2, pp. 137–145, Mar. 1979.

[60] W. F. Richards, Y. T. Lo, and D. D. Harrison, "An improved theory for microstrip antennas and applications," *IEEE Transactions on Antennas and Propagation*, vol. AP-29, no. 1, pp. 38–46, Jan. 1981.

[61] F. Zavosh, "Novel printed antenna configurations for enhanced performance," Ph.D. thesis, Arizona State University, Tempe, Arizona, 1995.

[62] E. Penard and J.-P. Daniel, "Mutual coupling between microstrip antennas," *Electronics Letters*, vol. 18, no. 4, pp. 605–607, July 1982.

[63] T. Huynh, K.-F. Lee, S. R. Chebolu, and R. Q. Lee, "Mutual coupling between rectangular microstrip patch antennas," *Microwave and Optical Technology Letters*, vol. 5, no. 11, pp. 572–576, Oct. 1992.

[64] J. Gómez-Tagle and C. G. Christodoulou, "Extended cavity model analysis of stacked microstrip ring antennas," *IEEE Transactions on Antennas and Propagation*, vol. 45, no. 11, pp. 1626–1635, Nov. 1997.

[65] F. Abboud, J. P. Damiano, and A. Papiernik, "A new model for calculating the input impedance of coax-fed circular microstrip antennas with and without air gaps," *IEEE Transactions on Antennas and Propagation*, vol. 38, no. 11, pp. 1882–1885, Nov. 1990.

[66] J.-M. Ribero, J.-P. Damiano, and R. Staraj, "Accurate analysis and synthesis of annular-ring microstrip antennas," *IEE Proceedings on Microwaves, Antennas and Propagation*, vol. 144, no. 5, pp. 341–346, Oct. 1997.

[67] D. R. Jackson, S. A. Long, J. T. Williams, and V. B. Davis, "Computer-aided design of rectangular microstrip antennas," in *Advances in Microstrip and Printed Antennas*, K. F. Lee and W. Chen, Eds. New York: John Wiley & Sons, 1997.

[68] V. Palanisamy and R. Garg, "Analysis of arbitrarily shaped microstrip patch antennas using segmentation technique and cavity model," *IEEE Transactions on Antennas and Propagation*, vol. AP-34, no. 10, pp. 1208–1213, Oct. 1986.

[69] A. Hoorfar and V. Jamnejad, "Electomagnetic modeling and analysis of wireless communication antennas," *IEEE Microwave Magazine*, vol. 4, no. 1, p. 51, 2003.

[70] R. F. Harrington, "Matrix methods for field problems," *Proceedings of the IEEE*, vol. 55, pp. 136–149, Feb. 1967.

[71] ——, *Field Computation by Moment Methods*. New York: Macmillan, 1968.

[72] R. Harrington, "Origin and development of the method of moments for field computation," *IEEE Antennas and Propagation Society Magazine*, pp. 31–36, June 1990.

[73] C. A. Balanis, *Advanced Engineering Electromagnetics*. New York: John Wiley & Sons, 1989.

[74] W. L. Stutzman and G. A. Thiele, *Antenna Theory and Design*, 2nd ed. New York: John Wiley & Sons, 1998.

[75] T. K. Sarkar, A. R. Djordjevic, and B. M. Kolundzija, "Method of moments applied to antennas," in *Handbook of Antennas in Wireless Communications*, L. C. Godara, Ed. Boca Raton: CRC Press, 2002.

[76] T. H. Hubing, "Survey of numerical electromagnetic modeling techniques," University of Missouri-Rolla, Missouri-Rolla, Missouri, Tech. Rep. TR91-1-001.3, Sept. 1991.

[77] J. Jin, *The Finite Element Method in Electromagnetics*. New York: John Wiley & Sons, 1993.

[78] P. P. Silvester and R. L. Ferrari, *Finite Elements for Electrical Engineers*, 3rd ed. Cambridge: Cambridge University Press, 1996.

[79] J. L. Volakis, A. Chatterjee, and L. C. Kempel, *Finite Element Method for Electromagnetics: Antennas, Microwave Circuits and Scattering Applications*. Oxford and New York: Oxford University Press and IEEE Press, 1998.

[80] A. F. Peterson, S. L. Ray, and R. Mittra, *Computational Methods for Electromagnetics*. Oxford and New York: Oxford University Press and IEEE Press, 1998.

[81] M. A. González de Aza, J. A. Encinar, and J. Zapata, "Radiation pattern computation of cavity-backed and probe-fed stacked microstrip patch arrays," *IEEE Transactions on Antennas and Propagation*, vol. 48, no. 4, pp. 502–509, Apr. 2000.

[82] K. S. Yee, "Numerical solution of initial boundary value problems involving Maxwell's equations in isotropic media," *IEEE Transactions on Antennas and Propagation*, vol. 14, no. 5, pp. 302–307, May 1966.

[83] A. Taflove, *Computational Electromagnetics: the Finite Difference Time Domain Method*. Boston: Artech House, 1995.

[84] ——, *Advances in Computational Electromagnetics: the Finite Difference Time Domain Method*. Boston: Artech House, 1998.

[85] A. Z. Elsherbeni and C. G. Christodoulou, "The finite difference time domain technique for microstrip antenna applications," in *Handbook of Antennas in Wireless Communications*, L. C. Godara, Ed. Boca Raton: CRC Press, 2002.

[86] C. Wu, K.-L. Wu, Z.-Q. Bi, and J. Litva, "Accurate characterization of planar printed antennas using finite-difference time-domain method," *IEEE Transactions on Antennas and Propagation*, vol. 40, no. 5, pp. 526–534, May 1992.

[87] J. R. Mosig and F. E. Gardiol, "General integral equation formulation for microstrip antennas and scatterers," *IEE Proceedings*, vol. 132, pt. H, no. 7, pp. 424–432, Dec. 1985.

[88] J. R. Mosig, "Arbitrarily shaped microstrip structures and their analysis with a mixed potential integral equation," *IEEE Transactions on Microwave Theory and Techniques*, vol. 36, no. 2, pp. 314–323, Feb. 1988.

[89] M. J. Notter and C. G. Parini, "Modelling of arbitrary shaped M/S patch antennas in multiple substrate media," *Electronics Letters*, vol. 26, no. 1, pp. 50–52, Jan. 1990.

[90] D. Zheng and K. A. Michalski, "Analysis of arbitrarily shaped coax-fed microstrip antennas—A hybrid mixed-potential integral equation approach," *Microwave and Optical Technology Letters*, vol. 3, no. 6, pp. 200–203, June 1990.

[91] ——, "Analysis of arbitrarily shaped coax-fed microstrip antennas with thick substrates," *Electronics Letters*, vol. 26, no. 12, pp. 794–795, June 1990.

[92] M.-J. Tsai, F. De Flaviis, O. Fordham, and N. G. Alexópoulos, "Modeling planar arbitrary shaped microstrip elements in multilayered media," *IEEE Transactions on Microwave Theory and Techniques*, vol. 45, no. 3, pp. 330–337, Mar. 1997.

[93] C.-F. Wang, F. Ling, and J.-M. Jin, "A fast full-wave analysis of scattering and radiation from large finite arrays of microstrip antennas," *IEEE Transactions on Antennas and Propagation*, vol. 46, no. 10, pp. 1467–1474, Oct. 1998.

[94] F. Ling, D. Jiao, and J.-M. Jin, "Efficient electromagnetic modeling of microstrip structures in multilayer media," *IEEE Transactions on Antennas and Propagation*, vol. 47, no. 9, pp. 1810–1818, Sept. 1999.

[95] J. J. van Tonder, "Electromagnetic radiation by planar antennas buried in layered media," Ph.D. thesis, University of Stellenbosch, Stellenbosch, South Africa, 1995.

[96] K. A. Michalski and J. R. Mosig, "Multilayered media Green's functions in integral equation formulations," *IEEE Transactions on Antennas and Propagation*, vol. 45, no. 3, pp. 508–519, Mar. 1997.

[97] K. A. Michalski and D. Zheng, "Electromagnetic scattering and radiation by surfaces of arbitrary shape in layered media, Part I: Theory," *IEEE Transactions on Antennas and Propagation*, vol. 38, no. 3, pp. 335–344, Mar. 1990.

[98] K. A. Michalski, "Extrapolation methods for Sommerfeld integral tails," *IEEE Transactions on Antennas and Propagation*, vol. 46, no. 10, pp. 1405–1418, Oct. 1998.

[99] D. G. Fang, J. J. Yang, and G. Y. Delisle, "Discrete image theory for horizontal electric dipoles in a multilayered medium," *IEE Proceedings*, vol. 135, pt. H, no. 5, pp. 297–303, Oct. 1988.

[100] Y. L. Chow, J. J. Yang, D. G. Fang, and G. E. Howard, "A closed-form spatial Green's function for the thick microstrip substrate," *IEEE Transactions on Antennas and Propagation*, vol. 39, no. 3, pp. 588–592, Mar. 1991.

[101] G. Dural and M. I. Aksun, "Closed-form Green's functions for general sources and stratified media," *IEEE Transactions on Microwave Theory and Techniques*, vol. 43, no. 7, pp. 1545–1552, July 1995.

[102] M. I. Aksun, "A robust approach for the derivation of closed-form Green's functions," *IEEE Transactions on Antennas and Propagation*, vol. 44, no. 5, pp. 651–658, May 1996.

[103] N. Hojjat, S. Safavi-Naeini, and Y. L. Chow, "Numerical computation of complex image Green's functions for multilayer dielectric media: Near-field zone and the interface region," *IEE Proceedings on Microwaves, Antennas and Propagation*, vol. 145, no. 6, pp. 449–454, Dec. 1998.

[104] S. M. Rao, D. Wilton, and A. W. Glisson, "Electromagnetic scattering by surfaces of arbitrary shape," *IEEE Transactions on Antennas and Propagation*, vol. AP-30, no. 3, pp. 409–418, May 1982.

[105] K. A. Michalski and D. Zheng, "Electromagnetic scattering and radiation by surfaces of arbitrary shape in layered media, Part II: Implementation and results for contiguous half-spaces," *IEEE Transactions on Antennas and Propagation*, vol. 38, no. 3, pp. 345–352, Mar. 1990.

[106] E. H. Newman and D. M. Pozar, "Electromagnetic modeling of composite wire and surface geometries," *IEEE Transactions on Antennas and Propagation*, vol. AP-26, no. 6, pp. 784–788, Nov. 1978.

[107] I. Tekin and E. H. Newman, "Method of moments solution for a wire attached to an arbitrary faceted surface," *IEEE Transactions on Antennas and Propagation*, vol. 46, no. 4, pp. 559–562, Apr. 1998.

[108] J. M. Taboada, J. L. Rodríguez, F. Obelleiro, and M. R. Pino, "Method of moments solution for wires attached to perfect electric conducting surfaces using floating attachment modes," in *Proceedings of the IEEE Antennas and Propagation Society International Symposium*, 2001, pp. 754–757.

[109] W. C. Chew, J.-M. Jin, C.-C. Lu, E. Michielssen, and J. M. Song, "Fast solution methods in electromagnetics," *IEEE Transactions on Antennas and Propagation*, vol. 45, no. 3, pp. 533–543, Mar. 1997.

[110] M. F. Cátedra and E. Gago, "Spectral domain analysis of conducting patches of arbitrary geometry in multilayer media using the CG-FFT method," *IEEE Transactions on Antennas and Propagation*, vol. 38, no. 10, pp. 1530–1536, Oct. 1990.

[111] J. Basterrechea and M. Cátedra, "Computation of microstrip S-parameters using a CG-FFT scheme," *IEEE Transactions on Microwave Theory and Techniques*, vol. 42, no. 2, pp. 234–240, Feb. 1994.

[112] S. A. Bokhari, J.-F. Zürcher, J. R. Mosig, and F. E. Gardiol, "Near fields of microstrip antennas," *IEEE Transactions on Antennas and Propagation*, vol. 43, no. 2, pp. 188–197, Feb. 1995.

[113] Y. Zhuang, C. Wu, and J. Litva, "A combined full-wave CG-FFT method for rigorous analysis of large microstrip antenna arrays," *IEEE Transactions on Antennas and Propagation*, vol. 44, no. 1, pp. 102–109, Jan. 1996.

[114] J. M. Song, C. C. Lu, W. C. Chew, and S. W. Lee, "Fast Illinois solver code (FISC)," *IEEE Antennas and Propagation Magazine*, vol. 40, no. 3, pp. 27–34, June 1998.

[115] F. X. Canning and K. Rogovin, "Fast direct solution of standard moment-method matrices," *IEEE Antennas and Propagation Magazine*, vol. 40, no. 3, pp. 15–26, June 1998.

[116] R. H. Jansen, "The spectral-domain approach for microwave integrated circuits," *IEEE Transactions on Microwave Theory and Techniques*, vol. MTT-33, no. 10, pp. 1043–1056, Oct. 1985.

[117] L. Vegni, R. Cicchetti, and P. Capece, "Spectral dyadic Green's function formulation for planar integrated structures," *IEEE Transactions on Antennas and Propagation*, vol. 36, no. 8, pp. 1057–1065, Aug. 1988.

[118] T. Itoh and W. Menzel, "A full-wave analysis method for open microstrip structures," *IEEE Transactions on Antennas and Propagation*, vol. AP-29, no. 1, pp. 63–68, Jan. 1981.

[119] M. I. Aksun and R. Mittra, "Choices of expansion and testing functions for the method of moments applied to a class of electromagnetic problems," *IEEE Transactions on Microwave Theory and Techniques*, vol. 41, no. 3, pp. 503–509, Mar. 1993.

[120] L. Barlatey, J. R. Mosig, and F. E. Gardiol, "Hybrid integral equation approach for patch antennas in multilayered substrates," *IEE Proceedings*, vol. 137, pt. H, no. 2, pp. 99–107, Apr. 1990.

[121] M. D. Deshpande and M. C. Bailey, "Input impedance of microstrip antennas," *IEEE Transactions on Antennas and Propagation*, vol. AP-30, no. 4, pp. 645–650, July 1982.

[122] D. M. Pozar and S. M. Voda, "A rigorous analysis of a microstripline fed patch antenna," *IEEE Transactions on Antennas and Propagation*, vol. AP-35, no. 12, pp. 1343–1350, Dec. 1987.

[123] E. H. Newman and D. Forrai, "Scattering from a microstrip patch," *IEEE Transactions on Antennas and Propagation*, vol. AP-35, no. 3, pp. 245–251, Mar. 1987.

[124] J. P. Damiano and A. Papiernik, "Survey of analytical and numerical models for probe-fed microstrip antennas," *IEE Proceedings on Microwaves, Antennas and Propagation*, vol. 141, no. 1, pp. 15–22, Feb. 1994.

[125] A. B. Smolders, M. E. J. Jeuken, and A. G. Tijhuis, "Improved computational efficiency in the analysis of finite arrays of thick microstrip antennas," *Journal of Electromagnetic Waves and Applications*, vol. 15, no. 4, pp. 517–555, 2001.

[126] M. C. Bailey, "Analysis of elliptical and circular microstrip antennas using moment method," *IEEE Transactions on Antennas and Propagation*, vol. AP-33, no. 9, pp. 954–959, Sept. 1985.

[127] S. Pinhas, S. Shtrikman, and D. Treves, "Moment-method solution of the center-fed microstrip disk antenna invoking feed and edge current singularities," *IEEE Transactions on Antennas and Propagation*, vol. 37, no. 12, pp. 1516–1522, Dec. 1989.

[128] J. T. Aberle, "Analysis of probe-fed circular microstrip antennas," Ph.D. thesis, University of Massachusetts, Amherst, Massachusetts, 1989.

[129] J. T. Aberle and D. M. Pozar, "Analysis of infinite arrays of probe-fed rectangular microstrip patches using a rigorous feed model," *IEE Proceedings*, vol. 136, pt. H, no. 2, pp. 110–119, Apr. 1989.

[130] ——, "Rigorous and versatile solutions for probe-fed microstrip patch antennas and arrays," in *Proceedings of the IEEE Antennas and Propagation Society International Symposium*, 1990, pp. 350–353.

[131] ——, "Analysis of infinite arrays of one- and two-probe-fed circular patches," *IEEE Transactions on Antennas and Propagation*, vol. 38, no. 4, pp. 421–432, Apr. 1990.

[132] ——, "Accurate and versatile solutions for probe-fed microstrip patch antennas and arrays," *Electromagnetics*, vol. 11, pp. 1–19, 1991.

[133] J. T. Aberle, D. M. Pozar, and C. R. Birtcher, "Evaluation of input impedance and radar cross section of probe-fed microstrip patch elements using an accurate feed model," *IEEE Transactions on Antennas and Propagation*, vol. 39, no. 12, pp. 1691–1696, Dec. 1991.

[134] D. Chatterjee and R. G. Plumb, "A hybrid formulation for the probe-to-patch attachment-mode current for rectangular microstrip antennas," *IEEE Transactions on Antennas and Propagation*, vol. 44, no. 5, pp. 677–686, May 1996.

[135] D. M. Kokotoff, R. B. Waterhouse, and J. T. Aberle, "On the use of attachment modes in the analysis of printed antennas," in *Proceedings of the Progress in Electromagnetics Research Symposium*, 1998.

[136] W.-J. Tsay and J. T. Aberle, "Analysis of a microstrip line terminated with a shorting pin," *IEEE Transactions on Antennas and Propagation*, vol. 40, no. 4, pp. 645–651, Apr. 1992.

[137] M. C. Bailey and M. D. Deshpande, "Integral equation formulation of microstrip antennas," *IEEE Transactions on Antennas and Propagation*, vol. AP-30, no. 4, pp. 651–656, July 1982.

[138] D. G. Shively, M. D. Deshpande, and C. R. Cockrell, "Scattering from arbitrarily shaped microstrip patch antennas," NASA Langley Research Center, Hampton, Virginia, NASA Technical Paper 3291, Dec. 1992.

[139] D. G. Shively and M. C. Bailey, "Analysis of microstrip patch antennas with nonzero surface resistance," NASA Langley Research Center, Hampton, Virginia, NASA Technical Paper 3362, Aug. 1993.

[140] T. Vaupel and V. Hansen, "Improved spectral domain analysis based on complete analytical solutions of the asymptotic sytem matrix," in *Proceedings of the International Symposium on Electromagnetic Theory*, vol. 2, Thessaloniki, Greece, May 1998, pp. 557–559.

[141] T. Vaupel, "Elektrodynamische analyse von (M)MIC-und submm-wellenstrukturen basierend auf einem oberflächen/volumenintegralgleichungsverfahren," Ph.D. thesis, Bergischen Universität-Gesamthochschule Wuppertal, Wuppertal, Germany, 1999.

[142] T. Vaupel and V. Hansen, "Electrodynamic analysis of combined microstrip and coplanar/slotline structures with 3-D components based on a surface/volume integral-equation approach," *IEEE Transactions on Antennas and Propagation*, vol. 47, no. 9, pp. 1788–1800, Sept. 1999.

[143] T. Becks and I. Wolff, "Analysis of 3-D metallization structures by a full-wave spectral domain technique," *IEEE Transactions on Microwave Theory and Techniques*, vol. 40, no. 12, pp. 2219–2227, Dec. 1992.

[144] R. Shavit, "Dielectric cover effect on rectangular microstrip antenna array," *IEEE Transactions on Antennas and Propagation*, vol. 42, no. 8, pp. 1180–1184, Aug. 1994.

[145] J. T. Aberle and D. M. Pozar, "A full-wave solution for the mutual coupling between circular microstrip patch antennas," *Microwave and Optical Technology Letters*, vol. 2, no. 4, pp. 130–132, Apr. 1989.

[146] J. R. Mosig and F. E. Gardiol, "Analytical and numerical techniques in the Green's function treatment of microstrip antennas and scatterers," *IEE Proceedings*, vol. 130, pt. H, no. 2, pp. 175–182, Mar. 1983.

[147] J. P. Damiano, "Computation of input impedance in microstrip antennas. Graphic representation and numerical integration of oscillating functions," *IEE Proceedings*, vol. 134, pt. H, no. 5, pp. 456–466, Oct. 1987.

[148] G. Splitt, "Rectangular electromagnetically coupled microstrip antennas in multilayered structures," in *Proceedings of the 18th European Microwave Conference*, Stockholm, Sweden, Sept. 1988.

[149] ——, "Improved numerical strategies for rigorous analysis of microstrip antennas," in *Proceedings of the 23th European Microwave Conference*, Madrid, Spain, Sept. 1993.

[150] ——, "A rapid method for arbitrary microstrip structures using the FFT-algorithm," in *Proceedings of the 20th European Microwave Conference*, Budapest, Ungarn, Sept. 1990, pp. 1481–1486.

[151] J. T. Aberle, *User Manual and Report: MSCOTR, Version 0.9*, Arizona State University, Tempe, Arizona, 1997.

[152] S.-O. Park and C. A. Balanis, "Analytical technique to evaluate the asymptotic part of the impedance matrix of Sommerfeld-type integrals," *IEEE Transactions on Antennas and Propagation*, vol. 45, no. 5, pp. 798–805, May 1997.

[153] ——, "Dispersion characteristics of open microstrip lines using closed-form asymptotic extraction," *IEEE Transactions on Microwave Theory and Techniques*, vol. 45, no. 3, pp. 458–460, Mar. 1997.

[154] ——, "Closed-form asymptotic extraction method for coupled microstrip lines," *IEEE Microwave and Guided Wave Letters*, vol. 7, no. 3, pp. 84–86, Mar. 1997.

[155] S.-O. Park, C. A. Balanis, and C. R. Birtcher, "Analytical evaluation of the asymptotic impedance matrix of a grounded dielectric slab with roof-top functions," *IEEE Transactions on Antennas and Propagation*, vol. 46, no. 2, pp. 251–259, Feb. 1998.

[156] S.-O. Park and C. A. Balanis, "Analytical evaluation of the asymptotic impedance matrix of asymmetric gap discontinuities," *IEEE Transactions on Microwave Theory and Techniques*, vol. 46, no. 8, pp. 1132–1140, Aug. 1998.

[157] V. S. Reddy and R. Garg, "Efficient analytical evaluation of the asymptotic part of Sommerfeld type reaction integrals in microstrip/slot structures," *IEE Proceedings on Microwaves, Antennas and Propagation*, vol. 147, no. 1, pp. 1–7, Feb. 2000.

[158] C.-B. Chae, S.-O. Park, K.-W. Suh, and H.-W. Jung, "Analytical asymptotic extraction techniques for right angles bend discontinuities," in *Proceedings of the Progress in Electromagnetics Research Symposium*, Cambridge, Massachusetts, July 2000.

[159] H. T. Hui, E. K. N. Yung, X. Q. Sheng, and C. H. Chan, "A hybrid evaluation method for the full-wave analysis of microstrip structures," *IEEE Transactions on Antennas and Propagation*, vol. 51, no. 7, pp. 1656–1658, July 2003.

[160] K. A. Michalski and C. M. Butler, "Evaluation of Sommerfeld integrals arising in the ground stake antenna problem," *IEE Proceedings*, vol. 134, pt. H, no. 1, pp. 93–97, Feb. 1987.

[161] H.-Y. Yang, A. Nakatani, and J. A. Castañeda, "Efficient evaluation of spectral integrals in the moment method solution of microstrip antennas and circuits," *IEEE Transactions on Antennas and Propagation*, vol. 38, no. 7, pp. 1127–1130, July 1990.

[162] U. V. Gothelf and A. Østergaard, "Full-wave analysis of a two slot microstrip filter using a new algorithm for computation of the spectral integrals," *IEEE Transactions on Microwave Theory and Techniques*, vol. 41, no. 1, pp. 101–108, Jan. 1993.

[163] H. H. Balik and C. J. Railton, "Efficient numerical integration of the matrix for the analysis of open planar circuits and antennas," in *Proceedings of the International Symposium on Electromagnetic Theory*, vol. 2, Thessaloniki, Greece, May 1998, pp. 630–632.

[164] G. Vecchi, M. Sereno-Garino, and M. Orefice, "Fast spectral evaluation of reaction integrals for separated domains," in *Proceedings of the IEEE Antennas and Propagation Society International Symposium*, 1996, pp. 1750–1753.

[165] M. Sereno-Garino, "On the spectral evaluation of mutual coupling between planar antennas," in *Proceedings of the IEEE Antennas and Propagation Society International Symposium*, 1998, pp. 1522–1525.

[166] M. Sereno-Garino, G. Vecchi, and M. Orefice, "Efficient spectral evaluation of mutual coupling between planar antennas," in *Proceedings of the International Symposium on Electromagnetic Theory*, vol. 2, Thessaloniki, Greece, May 1998, pp. 633–635.

[167] M. Sereno-Garino, "Spectral and multiresolution techniques for the numerical analysis of planar printed antennas and arrays," Ph.D. thesis, Politecnico di Torino, Torino, Italy, 1999.

[168] ——, "Efficient spectral evaluation of mutual coupling between planar antennas," *Radio Science*, vol. 35, no. 2, pp. 511–523, Mar. 2000.

[169] C. J. Railton and S. A. Meade, "Fast rigorous analysis of shielded planar filters," *IEEE Transactions on Microwave Theory and Techniques*, vol. 40, no. 5, pp. 978–985, May 1992.

[170] J. C. Rautio, "Planar electromagnteic analysis," *IEEE Microwave Magazine*, vol. 4, no. 1, pp. 35–41, Mar. 2003.

[171] D. M. Pozar, "Analysis of finite phased arrays of printed dipoles," *IEEE Transactions on Antennas and Propagation*, vol. AP-33, no. 10, pp. 1045–1053, Oct. 1985.

[172] ——, "Finite phased arrays of rectangular microstrip patches," *IEEE Transactions on Antennas and Propagation*, vol. AP-34, no. 5, pp. 658–665, May 1986.

[173] M. D. Deshpande and M. C. Bailey, "Analysis of finite phased arrays of circular microstrip patches," *IEEE Transactions on Antennas and Propagation*, vol. 37, no. 11, pp. 1355–1360, Nov. 1989.

[174] D. M. Pozar and D. H. Schaubert, "Analysis of an infinite array of rectangular microstrip patches with idealized probe feeds," *IEEE Transactions on Antennas and Propagation*, vol. AP-32, no. 10, pp. 1101–1107, Oct. 1984.

[175] J. T. Aberle, D. M. Pozar, and J. Manges, "Phased arrays of probe-fed stacked microstrip patches," *IEEE Transactions on Antennas and Propagation*, vol. 42, no. 7, pp. 920–927, July 1994.

[176] K. F. Lee, W. Chen, and R. Q. Lee, "Probe-fed microstrip antennas," in *Advances in Microstrip and Printed Antennas*, K. F. Lee and W. Chen, Eds. New York: John Wiley & Sons, 1997.

[177] L. T. Hildebrand, "The analysis of microstrip wire-grid antenna arrays," M.Eng. thesis, University of Pretoria, Pretoria, South Africa, 1992.

[178] W. C. Chew, *Waves and Fields in Inhomogeneous Media*. New York: Van Nostrand Reinhold, 1990.

[179] Z. Fan and K.-F. Lee, "Spectral domain analysis of rectangular microstrip antennas with an air gap," *Microwave and Optical Technology Letters*, vol. 5, no. 7, pp. 315–318, June 1992.

[180] E. O. Brigham, *The Fast Fourier Transform and its Applications*. London: Prentice-Hall, 1988.

[181] C. F. du Toit, "The numerical computation of Bessel functions of the first and second kind for integer orders and complex arguments," *IEEE Transactions on Antennas and Propagation*, vol. 38, no. 9, pp. 1341–1349, Sept. 1990.

[182] M. Abramowitz and I. A. Stegun, Eds., *Handbook of Mathematical Functions*. Washington DC: National Bureau of Standards, 1964.

[183] D. M. Pozar, "Input impedance and mutual coupling of rectangular microstrip antennas," *IEEE Transactions on Antennas and Propagation*, vol. AP-30, no. 6, pp. 1191–1196, Nov. 1982.

[184] W. H. Press, S. A. Teukolsky, W. T. Vetterling, and B. P. Flannery, *Numerical Recipes in C: The Art of Scientific Computing*, 2nd ed. Cambridge: Cambridge University Press, 1997.

[185] K. C. Gupta, R. Garg, and R. Chadha, *Computer-Aided Design of Microwave Circuits*. Boston: Artech House, 1981.

[186] *IE3D User's Manual, Release 8*, Zealand Software, Inc., Fremont, California, Jan. 2001.

[187] *FEKO User's Manual, Suite 4.0*, EM Software & Systems-S.A. (Pty) Ltd., Stellenbosch, South Africa, Dec. 2002.

[188] *Sonnet User's Guide, Release 9*, Sonnet Software, Inc., North Syracuse, New York, May 2003.

[189] C.-L. Chi and N. G. Alexópoulos, "Radiation by a probe through a substrate," *IEEE Transactions on Antennas and Propagation*, vol. AP-34, no. 9, pp. 1080–1091, Sept. 1986.

[190] W. Gesang, E. Rothwell, K. M. Chen, K. Burket, W. P. Hansen, and J. L. Lin, "Receiving and scattering characteristics of an imaged monopole beneath a lossy sheet," *IEEE Transactions on Antennas and Propagation*, vol. 41, no. 3, pp. 287–294, Mar. 1993.

[191] N. G. Alexópoulos, D. R. Jackson, and P. B. Katéhi, "Criteria for nearly omnidirectional radiation patterns for printed antennas," *IEEE Transactions on Antennas and Propagation*, vol. AP-33, no. 2, pp. 195–205, Feb. 1985.

[192] D. H. Schaubert, D. M. Pozar, and A. Adrian, "Effect of microstrip antenna substrate thickness and permittivity: Comparison of theories with experiment," *IEEE Transactions on Antennas and Propagation*, vol. 37, no. 6, pp. 677–682, June 1989.

[193] E. Chang, S. A. Long, and W. F. Richards, "Experimental investigation of electrically thick rectangular microstrip antennas," *IEEE Transactions on Antennas and Propagation*, vol. AP-34, no. 6, pp. 767–772, June 1986.

[194] B. Lindmark, S. Lundgren, J. R. Sanford, and C. Beckman, "Dual-polarised array for signal-processing applications in wireless communications," *IEEE Transactions on Antennas and Propagation*, vol. 46, no. 6, pp. 758–763, June 1998.

[195] A. Singer. (1998, July) A comparison of space diversity and polarization diversity receive systems for cellular and PCS systems. Celwave. [Online]. Available: http://www.celwave.com/poldiv1.html/

[196] Basics of dual-polarized antennas. The International Engineering Consortium. [Online]. Available: http://www.iec.org

[197] B. Johannisson, "Adaptive base station antennas for mobile communications systems," in *Proceedings of the 1998 IEEE AP-S Conference on Antennas and Propagation for Wireless Communications*, Waltham, Massachusetts, Nov. 1998.

[198] F. Demmerle and W. Wiesbeck, "A biconical multibeam antenna for space-division multiple access," *IEEE Transactions on Antennas and Propagation*, vol. 46, no. 6, pp. 782–787, June 1998.

[199] R. L. Haupt, "An introduction to genetic algorithms for electromagnetics," *IEEE Antennas and Propagation Magazine*, vol. 37, no. 2, pp. 7–15, Apr. 1995.

[200] J. M. Johnson and Y. Rahmat-Samii, "Genetic algorithms in engineering electromagnetics," *IEEE Antennas and Propagation Magazine*, vol. 39, no. 4, pp. 7–25, Aug. 1997.

[201] D. S. Wiele and E. Michielssen, "Genetic algorithm optimization applied to electromagnetics: A review," *IEEE Transactions on Antennas and Propagation*, vol. 45, no. 3, pp. 343–353, Mar. 1997.

[202] Z. Fan and K.-F. Lee, "Input impedance of annular-ring microstrip antennas with a dielectric cover," *IEEE Transactions on Antennas and Propagation*, vol. 40, no. 8, pp. 992–995, Aug. 1992.

[203] ——, "Input impedance of circular-disk microstrip antennas with a dielectric cover," *Microwave and Optical Technology Letters*, vol. 5, no. 13, pp. 701–704, Dec. 1992.

[204] Ç. S. Gürel and E. Yazgan, "Bandwidth widening in an annular ring microstrip antenna with superstrate," in *Proceedings of the IEEE Antennas and Propagation Society International Symposium*, 1995, pp. 692–695.

[205] X.-H. Shen and G. A. E. Vandenbosch, "Enhancing the impedance bandwidth of microstrip antennas with a superstrate (cover)," in *Proceedings of the AP2000 Millennium Conference on Antennas and Propagation*, Davos, Switzerland, Apr. 2000.

[206] S. M. Ali, W. C. Chew, and J. A. Kong, "Vector Hankel transform analysis of annular-ring microstrip antenna," *IEEE Transactions on Antennas and Propagation*, vol. AP-30, no. 4, pp. 637–644, July 1982.

[207] M. Davidovitz and Y. T. Lo, "Rigorous analysis of a circular patch antenna excited by a microstrip transmission line," *IEEE Transactions on Antennas and Propagation*, vol. 37, no. 8, pp. 949–958, Aug. 1989.

[208] G. J. Burke, E. K. Miller, S. Chakrabarti, and K. Demarest, "Using model-based parameter estimation to increase the efficiency of computing electromagnetic transfer functions," *IEEE Transactions on Microwave Theory and Techniques*, vol. 25, pp. 2807–2809, July 1989.

[209] K. Kottapalli, T. K. Sarkar, Y. Hua, E. K. Miller, and G. J. Burke, "Accurate computation of wide-band response of electromagnetic systems utilizing narrow-band information," *IEEE Transactions on Microwave Theory and Techniques*, vol. 39, pp. 682–687, Apr. 1991.

[210] K. L. Virga and Y. Rahmat-Samii, "Efficient wide-band evaluation of mobile communications antennas using $[Z]$ or $[Y]$ matrix interpolation with the method of moments," *IEEE Transactions on Antennas and Propagation*, vol. 47, no. 1, pp. 65–76, Jan. 1999.

[211] I. S. Gradshteyn and I. M. Ryzhik, *Table of Integrals, Series and Products*, 6th ed., A. Jeffrey and D. Zwillinger, Eds. San Diego: Academic Press, 2000.

[212] (2001) Online compendium of formulas involving the special functions of mathematics: BesselJ. Wolfram Research, Inc. [Online]. Available: http://functions.wolfram.com/Elementary/BesselJ/

APPENDIX A

Derivations Related to the Green's Function

In this appendix, it is shown how the spectral-domain Green's-function components of (3.56) to (3.63), for planarly multilayered substrates, can be derived from the spatial-domain form given by Chew [178]. The derivation is available in the literature [6], but is included here for completeness sake. Although this particular derivation is presented, the spectral-domain Green's-function components can of course also be derived in other ways. Furthermore, due to the presence of vertical electric current densities, some of the Green's-function components have to be integrated over the z and/or z' variables. In the text of Chapter 3, these are referred to as expanded Green's-function components. The expressions for these expanded Green's-function components will also be presented in this appendix as they are not, to the author's knowledge, available elsewhere.

A.1 SPECTRAL-DOMAIN GREEN'S-FUNCTION COMPONENTS

As shown by Chew [178], the spatial-domain dyadic Green's function for the planarly multilayered medium in Figure 3.4, can be expressed as

$$\bar{\mathbf{G}}(\mathbf{r}|\mathbf{r}') = \frac{-j}{8\pi^2}\int_{-\infty}^{\infty}\int_{-\infty}^{\infty}\frac{1}{k_{z(\ell')}k_\rho^2}\left[\bar{\mathbf{M}}(k_x,k_y,\mathbf{r}|\mathbf{r}')+\bar{\mathbf{N}}(k_x,k_y,\mathbf{r}|\mathbf{r}')\right]dk_xdk_y - \frac{1}{k_{(\ell')}^2}\,\delta(\mathbf{r}-\mathbf{r}')\,\hat{z}\hat{z}, \quad \text{(A.1)}$$

where

$$\bar{\mathbf{M}}(k_x,k_y,\mathbf{r}|\mathbf{r}') = \left(\nabla\times\hat{z}\right)\left(\nabla'\times\hat{z}\right)e^{-jk_x(x-x')-jk_y(y-y')}F^{\mathrm{TE}}_{(\ell)\pm}(z,z') \quad \text{(A.2)}$$

and

$$\bar{\mathbf{N}}(k_x, k_y, \mathbf{r}|\mathbf{r}') = \left[\frac{\nabla \times \nabla \times \hat{z}}{j\omega\varepsilon_{(\ell)}}\right]\left[\frac{\nabla' \times \nabla' \times \hat{z}}{-j\omega\mu_{(\ell')}}\right] e^{-jk_x(x-x')-jk_y(y-y')} F^{\mathrm{TM}}_{(\ell)\pm}(z, z'), \tag{A.3}$$

with

$$\nabla = -jk_x\,\hat{x} - jk_y\,\hat{y} + \frac{\partial}{\partial z}\,\hat{z} \tag{A.4}$$

and

$$\nabla' = jk_x\,\hat{x} + jk_y\,\hat{y} + \frac{\partial}{\partial z'}\,\hat{z}. \tag{A.5}$$

By applying the two-dimensional Fourier transform of (3.18), to (A.1), the spectral-domain dyadic Green's function for a planarly multilayered medium can be expressed as [6]

$$\tilde{\bar{\mathbf{G}}}(k_x, k_y, z|z') = \frac{-\omega\mu_{(\ell')}}{2k_{z(\ell')}k_\rho^2}\left[\tilde{\bar{\mathbf{M}}}(-k_x, -k_y, z|z') + \tilde{\bar{\mathbf{N}}}(-k_x, -k_y, z|z')\right] - \frac{1}{j\omega\varepsilon_{(\ell')}}\,\delta(z-z')\,\hat{z}\hat{z}, \tag{A.6}$$

where

$$\tilde{\bar{\mathbf{M}}}(k_x, k_y, z|z') = \left(\nabla \times \hat{z}\right)\left(\nabla' \times \hat{z}\right) F^{\mathrm{TE}}_{(\ell)\pm}(z, z') \tag{A.7}$$

and

$$\tilde{\bar{\mathbf{N}}}(k_x, k_y, z|z') = \left(\frac{\nabla \times \nabla \times \hat{z}}{j\omega\varepsilon_{(\ell)}}\right)\left(\frac{\nabla' \times \nabla' \times \hat{z}}{-j\omega\mu_{(\ell')}}\right) F^{\mathrm{TM}}_{(\ell)\pm}(z, z'). \tag{A.8}$$

The curl operations in the expression for $\tilde{\bar{\mathbf{M}}}$ can be carried out as

$$\nabla \times \hat{z} = -jk_x\,\hat{x} + jk_y\,\hat{y} \tag{A.9}$$

and

$$\nabla' \times \hat{z} = jk_x\,\hat{x} - jk_y\,\hat{y}, \tag{A.10}$$

resulting in

$$\left(\nabla \times \hat{z}\right)\left(\nabla' \times \hat{z}\right) = k_y^2\,\hat{x}\hat{x} + k_x^2\,\hat{y}\hat{y} - k_xk_y\,\hat{x}\hat{y} - k_xk_y\,\hat{y}\hat{x}. \tag{A.11}$$

Similarly, the curl operations in the expression for $\tilde{\bar{\mathbf{N}}}$ can be carried out as

$$\nabla \times \nabla \times \hat{z} = -jk_x\frac{\partial}{\partial z}\,\hat{x} - jk_y\frac{\partial}{\partial z}\,\hat{y} + k_\rho^2\hat{z} \tag{A.12}$$

and

$$\nabla' \times \nabla' \times \hat{z} = jk_x\frac{\partial}{\partial z'}\,\hat{x} + jk_y\frac{\partial}{\partial z'}\,\hat{y} + k_\rho^2\hat{z}, \tag{A.13}$$

resulting in

$$\begin{aligned}\left(\nabla \times \nabla \times \hat{z}\right)\left(\nabla' \times \nabla \times \hat{z}\right) = \frac{\partial^2}{\partial z\partial z'}\left(k_x^2\,\hat{x}\hat{x} + k_y^2\,\hat{y}\hat{y} + k_xk_y\,\hat{x}\hat{y} + k_xk_y\,\hat{y}\hat{x}\right)\\ - jk_\rho^2\frac{\partial}{\partial z}\left(k_x\,\hat{x}\hat{z} + jk_y\,\hat{y}\hat{z}\right) - jk_\rho^2\frac{\partial}{\partial z}\left(k_x\,\hat{x}\hat{z} + jk_y\,\hat{y}\hat{z}\right) + k_\rho^4\,\hat{z}\hat{z}.\end{aligned} \tag{A.14}$$

Finally, by replacing the curl operators in (A.7) and (A.8) with their relevant expressions, it follows from (A.6) that the components of the spectral-domain dyadic Green's function can be expressed as

$$\tilde{\bar{\mathbf{G}}} = \hat{x}\,\tilde{G}_{xx}\,\hat{x} + \hat{x}\,\tilde{G}_{xy}\,\hat{y} + \hat{x}\,\tilde{G}_{xz}\,\hat{z} + \hat{y}\,\tilde{G}_{yx}\,\hat{x} + \hat{y}\,\tilde{G}_{yy}\,\hat{y} + \hat{y}\,\tilde{G}_{yz}\,\hat{z} + \hat{z}\,\tilde{G}_{zx}\,\hat{x} + \hat{z}\,\tilde{G}_{zy}\,\hat{y} + \hat{z}\,\tilde{G}_{zz}\,\hat{z}, \tag{A.15}$$

with

$$\tilde{G}_{xx}(k_x, k_y, z|z') = \frac{-\omega\mu_{(\ell')}}{2k_{z(\ell')}k_\rho^2}\left[k_y^2 F^{\text{TE}}_{(\ell)\pm}(z,z') + \frac{k_x^2}{\omega^2\mu_{(\ell')}\varepsilon_{(\ell)}}\frac{\partial^2}{\partial z'\partial z}F^{\text{TM}}_{(\ell)\pm}(z,z')\right], \tag{A.16}$$

$$\tilde{G}_{yy}(k_x, k_y, z|z') = \frac{-\omega\mu_{(\ell')}}{2k_{z(\ell')}k_\rho^2}\left[k_x^2 F^{\text{TE}}_{(\ell)\pm}(z,z') + \frac{k_y^2}{\omega^2\mu_{(\ell')}\varepsilon_{(\ell)}}\frac{\partial^2}{\partial z'\partial z}F^{\text{TM}}_{(\ell)\pm}(z,z')\right], \tag{A.17}$$

$$\begin{aligned}\tilde{G}_{xy}(k_x, k_y, z|z') &= \tilde{G}_{yx}(k_x, k_y, z|z') \\ &= \frac{-\omega\mu_{(\ell')}}{2k_{z(\ell')}k_\rho^2}\,k_x k_y\left[-F^{\text{TE}}_{(\ell)\pm}(z,z') + \frac{1}{\omega^2\mu_{(\ell')}\varepsilon_{(\ell)}}\frac{\partial^2}{\partial z'\partial z}F^{\text{TM}}_{(\ell)\pm}(z,z')\right],\end{aligned} \tag{A.18}$$

$$\tilde{G}_{xz}(k_x, k_y, z|z') = \frac{jk_x}{2k_{z(\ell')}\omega\varepsilon_{(\ell)}}\frac{\partial}{\partial z}F^{\text{TM}}_{(\ell)\pm}(z,z'), \tag{A.19}$$

$$\tilde{G}_{yz}(k_x, k_y, z|z') = \frac{jk_y}{2k_{z(\ell')}\omega\varepsilon_{(\ell)}}\frac{\partial}{\partial z}F^{\text{TM}}_{(\ell)\pm}(z,z'), \tag{A.20}$$

$$\tilde{G}_{zx}(k_x, k_y, z|z') = \frac{-jk_x}{2k_{z(\ell')}\omega\varepsilon_{(\ell)}}\frac{\partial}{\partial z'}F^{\text{TM}}_{(\ell)\pm}(z,z'), \tag{A.21}$$

$$\tilde{G}_{zy}(k_x, k_y, z|z') = \frac{-jk_y}{2k_{z(\ell')}\omega\varepsilon_{(\ell)}}\frac{\partial}{\partial z'}F^{\text{TM}}_{(\ell)\pm}(z,z') \tag{A.22}$$

and

$$\tilde{G}_{zz}(k_x, k_y, z|z') = \frac{-k_\rho^2}{2k_{z(\ell')}\omega\varepsilon_{(\ell)}}F^{\text{TM}}_{(\ell)\pm}(z,z') - \frac{1}{j\omega\varepsilon_{(\ell')}}\delta(z-z'). \tag{A.23}$$

These are the expressions given in (3.56) to (3.63).

A.2 EXPANDED GREEN'S-FUNCTION COMPONENTS

The expanded Green's-function components include all those expressions where the product of the Green's function and the vertical current-density variation on the probes has to be integrated over z and/or z'. A single function, $f_n(z)$, can be used to represent the piecewise sinusoidal (PWS) parts of the basis and/or testing functions on the probes, as well as the probe part of the attachment modes. This function $f_n(z)$ can be expressed as

$$f_n(z) = \begin{cases} f^{PZ}_{nz}(z) = a\,e^{jk_F z} + b\,e^{-jk_F z}, & \text{for the probe basis/tesing functions} \\ f^{AZ}_{na}(z) = a\,e^{jk_F z} + b\,e^{-jk_F z}, & \text{for the probe part of the attachment modes,} \end{cases} \tag{A.24}$$

where

$$a = \begin{cases} \dfrac{-e^{-jk_F z_1}}{j2\sin[k_F(z_2-z_1)]}, & nz \geq 1,\ z_{nz}^{PZ} \leq z \leq z_{nz}^{PZ} + \Delta z_{nz}^{PZ+} \\ \dfrac{e^{-jk_F z_1}}{j2\sin[k_F(z_2-z_1)]}, & nz \geq 2,\ z_{nz}^{PZ} - \Delta z_{nz}^{PZ-} \leq z \leq z_{nz}^{PZ} \\ \dfrac{e^{-jk_F z_1}}{j2\sin[k_F(z_2-z_1)]}, & z_{na}^{AZ} - \Delta z_{na}^{AZ-} \leq z \leq z_{na}^{AZ} \end{cases} \tag{A.25}$$

and

$$b = \begin{cases} \dfrac{e^{jk_F z_2}}{j2\sin[k_F(z_2-z_1)]}, & nz \geq 1,\ z_{nz}^{PZ} \leq z \leq z_{nz}^{PZ} + \Delta z_{nz}^{PZ+} \\ \dfrac{-e^{jk_F z_2}}{j2\sin[k_F(z_2-z_1)]}, & nz \geq 2,\ z_{nz}^{PZ} - \Delta z_{nz}^{PZ-} \leq z \leq z_{nz}^{PZ} \\ \dfrac{-e^{jk_F z_2}}{j2\sin[k_F(z_2-z_1)]}, & z_{na}^{AZ} - \Delta z_{na}^{AZ-} \leq z \leq z_{na}^{AZ}, \end{cases} \tag{A.26}$$

with

$$z_1 = \begin{cases} z_{nz}^{PZ}, & nz \geq 1,\ z_{nz}^{PZ} \leq z \leq z_{nz}^{PZ} + \Delta z_{nz}^{PZ+} \\ z_{nz}^{PZ} - \Delta z_{nz}^{PZ-}, & nz \geq 2,\ z_{nz}^{PZ} - \Delta z_{nz}^{PZ-} \leq z \leq z_{nz}^{PZ} \\ z_{na}^{AZ} - \Delta z_{na}^{AZ-}, & z_{na}^{AZ} - \Delta z_{na}^{AZ-} \leq z \leq z_{na}^{AZ} \end{cases} \tag{A.27}$$

and

$$z_2 = \begin{cases} z_{nz}^{PZ} + \Delta z_{nz}^{PZ+}, & nz \geq 1,\ z_{nz}^{PZ} \leq z \leq z_{nz}^{PZ} + \Delta z_{nz}^{PZ+} \\ z_{nz}^{PZ}, & nz \geq 2,\ z_{nz}^{PZ} - \Delta z_{nz}^{PZ-} \leq z \leq z_{nz}^{PZ} \\ z_{na}^{AZ}, & z_{na}^{AZ} - \Delta z_{na}^{AZ-} \leq z \leq z_{na}^{AZ}. \end{cases} \tag{A.28}$$

The other parameters have already been defined in Sections 3.5.1, 3.6.1 and 3.6.2.

For planarly-orientated testing functions and vertically-orientated basis functions (or for calculating the far fields from vertically-orientated basis functions), the integrals

$$\tilde{G}_{xz}^{I}(k_x, k_y, z) = \int_{z'} \tilde{G}_{xz}(k_x, k_y, z|z') f_n(z')\, dz' \tag{A.29}$$

and

$$\tilde{G}_{yz}^{I}(k_x, k_y, z) = \int_{z'} \tilde{G}_{yz}(k_x, k_y, z|z') f_n(z')\, dz' \tag{A.30}$$

need to be evaluated. They can be expanded as

$$\tilde{G}_{xz}^{I}(k_x, k_y, z) = \begin{cases} \tilde{G}_{xz}^{I+}(k_x, k_y, z) & z \geq z_2' \\ \tilde{G}_{xz}^{I-}(k_x, k_y, z) & z \leq z_1' \end{cases} \tag{A.31}$$

and

$$\tilde{G}_{yz}^{I}(k_x, k_y, z) = \begin{cases} \tilde{G}_{yz}^{I+}(k_x, k_y, z) & z \geq z_2' \\ \tilde{G}_{yz}^{I-}(k_x, k_y, z) & z \leq z_1'. \end{cases} \tag{A.32}$$

By using the expressions in (A.24) to (A.28), the expression for $\tilde{G}_{xz}^{I+}$ can be derived as

$$
\begin{aligned}
&\tilde{G}_{xz}^{I+}(k_x,k_y,z) \\
&= \int_{z_1'}^{z_2'} \tilde{G}_{xz}(k_x,k_y,z|z')f_n(z')\,dz', \quad z \geq z_2' \\
&= \frac{-jk_x}{2k_{z(\ell')}\omega\varepsilon_{(\ell)}} \int_{z_1'}^{z_2'} \frac{\partial}{\partial z} F_{(\ell)+}^{\text{TM}}(z,z')\Big(a'\,e^{jk_F z'} + b'\,e^{-jk_F z'}\Big)dz' \\
&= \frac{k_x k_{z(\ell)} A_{(\ell)+}^{\text{TM}}}{2k_{z(\ell')}\omega\varepsilon_{(\ell)}}\Big(-e^{-jk_{z(\ell)}z} + \check{R}_{(\ell),(\ell-1)}^{\text{TM}}\,e^{-j2k_{z(\ell)}d_{(\ell-1)}}\,e^{jk_{z(\ell)}z}\Big) \\
&\quad \cdot \Bigg(\frac{a'}{j[k_{z(\ell')}+k_F]}\Big\{e^{j[k_{z(\ell')}+k_F]z_2'} - e^{j[k_{z(\ell')}+k_F]z_1'}\Big\} \\
&\quad + \frac{b'}{j[k_{z(\ell')}-k_F]}\Big\{e^{j[k_{z(\ell')}-k_F]z_2'} - e^{j[k_{z(\ell')}-k_F]z_1'}\Big\} \\
&\quad + \frac{a'\check{R}_{(\ell'),(\ell'+1)}^{\text{TM}}\,e^{j2k_{z(\ell')}d_{(\ell')}}}{j[-k_{z(\ell')}+k_F]}\Big\{e^{j[-k_{z(\ell')}+k_F]z_2'} - e^{j[-k_{z(\ell')}+k_F]z_1'}\Big\} \\
&\quad + \frac{b'\check{R}_{(\ell'),(\ell'+1)}^{\text{TM}}\,e^{j2k_{z(\ell')}d_{(\ell')}}}{j[-k_{z(\ell')}-k_F]}\Big\{e^{j[-k_{z(\ell')}-k_F]z_2'} - e^{j[-k_{z(\ell')}-k_F]z_1'}\Big\}\Bigg).
\end{aligned}
\tag{A.33}
$$

It then also follows that $\tilde{G}_{yz}^{I+} = \tilde{G}_{xz}^{I+}\big|_{k_x=k_y}$. Furthermore, the expression for $\tilde{G}_{xz}^{I-}$ can be derived as

$$
\begin{aligned}
&\tilde{G}_{xz}^{I-}(k_x,k_y,z) \\
&= \int_{z_1'}^{z_2'} \tilde{G}_{xz}(k_x,k_y,z|z')f_n(z')\,dz', \quad z \leq z_1' \\
&= \frac{-jk_x}{2k_{z(\ell')}\omega\varepsilon_{(\ell)}} \int_{z_1'}^{z_2'} \frac{\partial}{\partial z} F_{(\ell)-}^{\text{TM}}(z,z')\Big(a'\,e^{jk_F z'} + b'\,e^{-jk_F z'}\Big)dz' \\
&= \frac{k_x k_{z(\ell)} A_{(\ell)-}^{\text{TM}}}{2k_{z(\ell')}\omega\varepsilon_{(\ell)}}\Big(e^{jk_{z(\ell)}z} - \check{R}_{(\ell'),(\ell'+1)}^{\text{TM}}\,e^{j2k_{z(\ell')}d_{(\ell')}}\,e^{-jk_{z(\ell)}z}\Big) \\
&\quad \cdot \Bigg(\frac{a'}{j[-k_{z(\ell')}+k_F]}\Big\{e^{j[-k_{z(\ell')}+k_F]z_2'} - e^{j[-k_{z(\ell')}+k_F]z_1'}\Big\} \\
&\quad + \frac{b'}{j[-k_{z(\ell')}-k_F]}\Big\{e^{j[-k_{z(\ell')}-k_F]z_2'} - e^{j[-k_{z(\ell')}-k_F]z_1'}\Big\} \\
&\quad + \frac{a'\check{R}_{(\ell),(\ell-1)}^{\text{TM}}\,e^{-j2k_{z(\ell-1)}d_{(\ell)}}}{j[k_{z(\ell')}+k_F]}\Big\{e^{j[k_{z(\ell')}+k_F]z_2'} - e^{j[k_{z(\ell')}+k_F]z_1'}\Big\} \\
&\quad + \frac{b'\check{R}_{(\ell),(\ell-1)}^{\text{TM}}\,e^{-j2k_{z(\ell-1)}d_{(\ell)}}}{j[k_{z(\ell')}-k_F]}\Big\{e^{j[k_{z(\ell')}-k_F]z_2'} - e^{j[k_{z(\ell')}-k_F]z_1'}\Big\}\Bigg).
\end{aligned}
\tag{A.34}
$$

Once again, it then also follows that $\tilde{G}_{yz}^{I-} = \tilde{G}_{xz}^{I-}\big|_{k_x=k_y}$.

For vertically-orientated testing functions and planarly-orientated expansion functions, the inte-

grals

$$\tilde{G}^I_{zx}(k_x, k_y, z') = \int_z f_m(z)\tilde{G}_{zx}(k_x, k_y, z|z')\,dz \tag{A.35}$$

and

$$\tilde{G}^I_{zy}(k_x, k_y, z') = \int_z f_m(z)\tilde{G}_{zy}(k_x, k_y, z|z')\,dz \tag{A.36}$$

need to be evaluated. They can be expanded as

$$\tilde{G}^I_{zx}(k_x, k_y, z) = \begin{cases} \tilde{G}^{I+}_{zx}(k_x, k_y, z) & z \geq z'_2 \\ \tilde{G}^{I-}_{zx}(k_x, k_y, z) & z \leq z'_1 \end{cases} \tag{A.37}$$

and

$$\tilde{G}^I_{zy}(k_x, k_y, z) = \begin{cases} \tilde{G}^{I+}_{zy}(k_x, k_y, z) & z \geq z'_2 \\ \tilde{G}^{I-}_{zy}(k_x, k_y, z) & z \leq z'_1. \end{cases} \tag{A.38}$$

By using the expressions in (A.24) to (A.28), the expression for $\tilde{G}^{I+}_{zx}$ can be derived as

$$\begin{aligned}
&\tilde{G}^{I+}_{zx}(k_x, k_y, z') \\
&= \int_{z_1}^{z_2} f_m(z)\tilde{G}_{zx}(k_x, k_y, z|z')\,dz, \quad z' \leq z_1 \\
&= \frac{jk_x}{2k_{z(\ell')}\omega\varepsilon_{(\ell)}} \int_{z_1}^{z_2} \left(a\,e^{jk_F z} + b\,e^{-jk_F z}\right) \frac{\partial}{\partial z'} F^{\text{TM}}_{(\ell)+}(z, z')\,dz \\
&= \frac{-k_x A^{\text{TM}}_{(\ell)+}}{2\omega\varepsilon_{(\ell)}} \left(e^{jk_{z(\ell')}z'} - \check{R}^{\text{TM}}_{(\ell'),(\ell'+1)}\, e^{j2k_{z(\ell')}d_{(\ell')}}\, e^{-jk_{z(\ell')}z'}\right) \\
&\quad \cdot \left(\frac{a}{j[-k_{z(\ell)} + k_F]} \left\{e^{j[-k_{z(\ell)}+k_F]z_2} - e^{j[-k_{z(\ell)}+k_F]z_1}\right\}\right. \\
&\quad + \frac{b}{j[-k_{z(\ell)} - k_F]} \left\{e^{j[-k_{z(\ell)}-k_F]z_2} - e^{j[-k_{z(\ell)}-k_F]z_1}\right\} \\
&\quad + \frac{a\check{R}^{\text{TM}}_{(\ell),(\ell-1)}\, e^{-j2k_{z(\ell-1)}d_{(\ell)}}}{j[k_{z(\ell)} + k_F]} \left\{e^{j[k_{z(\ell)}+k_F]z_2} - e^{j[k_{z(\ell)}+k_F]z_1}\right\} \\
&\quad \left. + \frac{b\check{R}^{\text{TM}}_{(\ell),(\ell-1)}\, e^{-j2k_{z(\ell-1)}d_{(\ell)}}}{j[k_{z(\ell)} - k_F]} \left\{e^{j[k_{z(\ell)}-k_F]z_2} - e^{j[k_{z(\ell)}-k_F]z_1}\right\}\right).
\end{aligned} \tag{A.39}$$

It then also follows that $\tilde{G}^{I+}_{zy} = \tilde{G}^{I+}_{zx}\big|_{k_x=k_y}$. Furthermore, the expression for $\tilde{G}^{I-}_{zx}$ can be derived as

$$\begin{aligned}
&\tilde{G}^{I-}_{zx}(k_x, k_y, z') \\
&= \int_{z_1}^{z_2} f_m(z)\tilde{G}_{zx}(k_x, k_y, z|z')\,dz, \quad z' \geq z_2 \\
&= \frac{jk_x}{2k_{z(\ell')}\omega\varepsilon_{(\ell)}} \int_{z_1}^{z_2} \left(a\,e^{jk_F z} + b\,e^{-jk_F z}\right) \frac{\partial}{\partial z'} F^{\text{TM}}_{(\ell)-}(z, z')\,dz
\end{aligned}$$

$$
\begin{aligned}
&= \frac{-k_x A^{\mathrm{TM}}_{(\ell)-}}{2\omega\varepsilon_{(\ell)}}\left(-e^{-jk_{z(\ell')}z'} + \check{R}^{\mathrm{TM}}_{(\ell),(\ell-1)}\, e^{-j2k_{z(\ell)}d_{(\ell-1)}}\, e^{jk_{z(\ell')}z'}\right)\\
&\cdot\left(\frac{a}{j[k_{z(\ell)}+k_F]}\left\{e^{j[k_{z(\ell)}+k_F]z_2} - e^{j[k_{z(\ell)}+k_F]z_1}\right\}\right.\\
&+ \frac{b}{j[k_{z(\ell)}-k_F]}\left\{e^{j[k_{z(\ell)}-k_F]z_2} - e^{j[k_{z(\ell)}-k_F]z_1}\right\}\\
&+ \frac{a\check{R}^{\mathrm{TM}}_{(\ell'),(\ell'+1)}\, e^{j2k_{z(\ell')}d_{(\ell')}}}{j[-k_{z(\ell)}+k_F]}\left\{e^{j[-k_{z(\ell)}+k_F]z_2} - e^{j[-k_{z(\ell)}+k_F]z_1}\right\}\\
&\left.+ \frac{b\check{R}^{\mathrm{TM}}_{(\ell'),(\ell'+1)}\, e^{j2k_{z(\ell')}d_{(\ell')}}}{j[-k_{z(\ell)}-k_F]}\left\{e^{j[-k_{z(\ell)}-k_F]z_2} - e^{j[-k_{z(\ell)}-k_F]z_1}\right\}\right). \qquad \text{(A.40)}
\end{aligned}
$$

Once again, it then also follows that $\tilde{G}^{I-}_{zy} = \tilde{G}^{I-}_{zx}\big|_{k_x=k_y}$.

For vertically-orientated testing functions and vertically-orientated expansion functions that do not overlap vertically, the integral

$$\tilde{G}^{I}_{zz}(k_x,k_y,z) = \int_{z'} \tilde{G}_{zz}(k_x,k_y,z|z')f_n(z')\,dz' \qquad \text{(A.41)}$$

needs to be evaluated. It can be expanded as

$$\tilde{G}^{I}_{zz}(k_x,k_y,z) = \begin{cases} \tilde{G}^{I+}_{zz}(k_x,k_y,z) & z \geq z'_2 \\ \tilde{G}^{I-}_{zz}(k_x,k_y,z) & z \leq z'_1. \end{cases} \qquad \text{(A.42)}$$

By using the expressions in (A.24) to (A.28), the expression for $\tilde{G}^{I+}_{zz}$ can be derived as

$$
\begin{aligned}
&\tilde{G}^{I+}_{zz}(k_x,k_y,z)\\
&= \int_{z'_1}^{z'_2} \tilde{G}_{zz}(k_x,k_y,z|z')f_n(z')\,dz', \quad z \geq z'_2\\
&= \frac{-k_\rho^2}{2k_{z(\ell')}\omega\varepsilon_{(\ell)}}\int_{z'_1}^{z'_2} F^{\mathrm{TM}}_{(\ell)+}(z,z')\left(a'\,e^{jk_Fz'} + b'\,e^{-jk_Fz'}\right)dz'\\
&\quad - \frac{1}{j\omega\varepsilon_{(\ell')}}\int_{z'_1}^{z'_2}\delta(z-z')\left(a'\,e^{jk_Fz'} + b'\,e^{-jk_Fz'}\right)dz'\\
&= \frac{-k_\rho^2 A^{\mathrm{TM}}_{(\ell)+}}{2k_{z(\ell')}\omega\varepsilon_{(\ell)}}\left(e^{-jk_{z(\ell)}z} + \check{R}^{\mathrm{TM}}_{(\ell),(\ell-1)}\, e^{-j2k_{z(\ell)}d_{(\ell-1)}}\, e^{jk_{z(\ell)}z}\right)\\
&\cdot\left(\frac{a'}{j[k_{z(\ell')}+k_F]}\left\{e^{j[k_{z(\ell')}+k_F]z'_2} - e^{j[k_{z(\ell')}+k_F]z'_1}\right\}\right.\\
&+ \frac{b'}{j[k_{z(\ell')}-k_F]}\left\{e^{j[k_{z(\ell')}-k_F]z'_2} - e^{j[k_{z(\ell')}-k_F]z'_1}\right\}\\
&\left.+ \frac{a'\check{R}^{\mathrm{TM}}_{(\ell'),(\ell'+1)}\, e^{j2k_{z(\ell')}d_{(\ell')}}}{j[-k_{z(\ell')}+k_F]}\left\{e^{j[-k_{z(\ell')}+k_F]z'_2} - e^{j[-k_{z(\ell')}+k_F]z'_1}\right\}\right.
\end{aligned}
$$

$$+\frac{b'\check{R}^{\mathrm{TM}}_{(\ell'),(\ell'+1)}\,e^{j2k_{z(\ell')}d_{(\ell')}}}{j[-k_{z(\ell')}-k_F]}\left\{e^{j[-k_{z(\ell')}-k_F]z_2'}-e^{j[-k_{z(\ell')}-k_F]z_1'}\right\}\Bigg). \tag{A.43}$$

Also, the expression for $\tilde{G}^{I-}_{zz}$ can be derived as

$$\begin{aligned}
&\tilde{G}^{I-}_{zz}(k_x,k_y,z)\\
&=\int_{z_1'}^{z_2'}\tilde{G}_{xz}(k_x,k_y,z|z')f_n(z')\,dz',\quad z\le z_1'\\
&=\frac{-k_\rho^2}{2k_{z(\ell')}\omega\varepsilon_{(\ell)}}\int_{z_1'}^{z_2'}F^{\mathrm{TM}}_{(\ell)-}(z,z')\left(a'\,e^{jk_Fz'}+b'\,e^{-jk_Fz'}\right)dz'\\
&\quad-\frac{1}{j\omega\varepsilon_{(\ell')}}\int_{z_1'}^{z_2'}\delta(z-z')\left(a'\,e^{jk_Fz'}+b'\,e^{-jk_Fz'}\right)dz'\\
&=\frac{-k_\rho^2A^{\mathrm{TM}}_{(\ell)-}}{2k_{z(\ell')}\omega\varepsilon_{(\ell)}}\left(e^{jk_{z(\ell)}z}+\check{R}^{\mathrm{TM}}_{(\ell'),(\ell'+1)}\,e^{j2k_{z(\ell')}d_{(\ell')}}\,e^{-jk_{z(\ell)}z}\right)\\
&\quad\cdot\Bigg(\frac{a'}{j[-k_{z(\ell')}+k_F]}\left\{e^{j[-k_{z(\ell')}+k_F]z_2'}-e^{j[-k_{z(\ell')}+k_F]z_1'}\right\}\\
&\quad+\frac{b'}{j[-k_{z(\ell')}-k_F]}\left\{e^{j[-k_{z(\ell')}-k_F]z_2'}-e^{j[-k_{z(\ell')}-k_F]z_1'}\right\}\\
&\quad+\frac{a'\check{R}^{\mathrm{TM}}_{(\ell),(\ell-1)}\,e^{-j2k_{z(\ell-1)}d_{(\ell)}}}{j[k_{z(\ell')}+k_F]}\left\{e^{j[k_{z(\ell')}+k_F]z_2'}-e^{j[k_{z(\ell')}+k_F]z_1'}\right\}\\
&\quad+\frac{b'\check{R}^{\mathrm{TM}}_{(\ell),(\ell-1)}\,e^{-j2k_{z(\ell-1)}d_{(\ell)}}}{j[k_{z(\ell')}-k_F]}\left\{e^{j[k_{z(\ell')}-k_F]z_2'}-e^{j[k_{z(\ell')}-k_F]z_1'}\right\}\Bigg).
\end{aligned}\tag{A.44}$$

For vertically-orientated testing functions and vertically-orientated expansion functions that do overlap vertically, the integral

$$\tilde{G}^{II}_{zz}(k_x,k_y)=\int_z\int_{z'}f_m(z)\tilde{G}_{zz}(k_x,k_y,z|z')f_n(z')\,dz'dz \tag{A.45}$$

needs to be evaluated. It can be expanded as

$$\tilde{G}^{II}_{zz}(k_x,k_y,z)=\begin{cases}\tilde{G}^{IZ+}_{zz}(k_x,k_y,z)+\tilde{G}^{IZ-}_{zz}(k_x,k_y,z), & z_1=z_1',\ z_2=z_2'\\ \tilde{G}^{II+}_{zz}(k_x,k_y,z), & z_1\ge z_2'\\ \tilde{G}^{II-}_{zz}(k_x,k_y,z), & z_2\le z_1'.\end{cases} \tag{A.46}$$

By using the expressions in (A.24) to (A.28), the expression for $\tilde{G}^{IZ+}_{zz}$ can be derived as

$$\begin{aligned}
&\tilde{G}^{IZ+}_{zz}(k_x,k_y)\\
&=\int_{z_1}^{z_2}\int_{z_1'}^{z}f_m(z)\tilde{G}_{zz}(k_x,k_y,z|z')f_n(z')\,dz'dz,\quad z_1=z_1',\ z_2=z_2',\ z\ge z'
\end{aligned}$$

$$
\begin{aligned}
&= \frac{-k_\rho^2}{2k_{z(\ell')}\omega\varepsilon_{(\ell)}} \int_{z_1}^{z_2}\int_{z_1'}^{z} \left(a\,e^{jk_F z} + b\,e^{-jk_F z}\right) F^{\mathrm{TM}}_{(\ell)+}(z,z') \left(a'\,e^{jk_F z'} + b'\,e^{-jk_F z'}\right) dz'dz \\
&\quad - \frac{1}{j\omega\varepsilon_{(\ell')}} \int_{z_1}^{z_2}\int_{z_1'}^{z} \left(a\,e^{jk_F z} + b\,e^{-jk_F z}\right) \delta(z-z') \left(a'\,e^{jk_F z'} + b'\,e^{-jk_F z'}\right) dz'dz \\
&= \frac{-k_\rho^2 A^{\mathrm{TM}}_{(\ell)+}}{2k_{z(\ell')}\omega\varepsilon_{(\ell)}} \Bigg[\Bigg(\frac{-a'}{j[k_{z(\ell')}+k_F]}\, e^{j[k_{z(\ell')}+k_F]z_1'} - \frac{b'}{j[k_{z(\ell')}-k_F]}\, e^{j[k_{z(\ell')}-k_F]z_1'} \\
&\quad - \frac{a'\check{R}^{\mathrm{TM}}_{(\ell'),(\ell'+1)}\, e^{j2k_{z(\ell')}d_{(\ell')}}}{j[-k_{z(\ell')}+k_F]}\, e^{j[-k_{z(\ell')}+k_F]z_1'} - \frac{b'\check{R}^{\mathrm{TM}}_{(\ell'),(\ell'+1)}\, e^{j2k_{z(\ell')}d_{(\ell')}}}{j[-k_{z(\ell')}-k_F]}\, e^{j[-k_{z(\ell')}-k_F]z_1'} \Bigg) \\
&\quad \cdot \Bigg(\frac{a}{j[-k_{z(\ell)}+k_F]} \left\{ e^{j[-k_{z(\ell)}+k_F]z_2} - e^{j[-k_{z(\ell)}+k_F]z_1} \right\} \\
&\quad + \frac{b}{j[-k_{z(\ell)}-k_F]} \left\{ e^{j[-k_{z(\ell)}-k_F]z_2} - e^{j[-k_{z(\ell)}-k_F]z_1} \right\} \\
&\quad + \frac{a\check{R}^{\mathrm{TM}}_{(\ell),(\ell-1)}\, e^{-j2k_{z(\ell)}d_{(\ell-1)}}}{j[k_{z(\ell)}+k_F]} \left\{ e^{j[k_{z(\ell)}+k_F]z_2} - e^{j[k_{z(\ell)}+k_F]z_1} \right\} \\
&\quad + \frac{b\check{R}^{\mathrm{TM}}_{(\ell),(\ell-1)}\, e^{-j2k_{z(\ell)}d_{(\ell-1)}}}{j[k_{z(\ell)}-k_F]} \left\{ e^{j[k_{z(\ell)}-k_F]z_2} - e^{j[k_{z(\ell)}-k_F]z_1} \right\} \Bigg) \\
&\quad - \frac{aa'}{[k_{z(\ell')}+k_F][k_{z(\ell')}-k_{z(\ell)}+2k_F]} \left\{ e^{j[k_{z(\ell')}-k_{z(\ell)}+2k_F]z_2} - e^{j[k_{z(\ell')}-k_{z(\ell)}+2k_F]z_1} \right\} \\
&\quad - \frac{ab'}{k_{z(\ell')}-k_F}\, j(z_2-z_1) \\
&\quad + \frac{aa'\check{R}^{\mathrm{TM}}_{(\ell'),(\ell'+1)}\, e^{j2k_{z(\ell')}d_{(\ell')}}}{[k_{z(\ell')}-k_F][-k_{z(\ell')}-k_{z(\ell)}+2k_F]} \left\{ e^{j[-k_{z(\ell')}-k_{z(\ell)}+2k_F]z_2} - e^{j[-k_{z(\ell')}-k_{z(\ell)}+2k_F]z_1} \right\} \\
&\quad + \frac{ab'\check{R}^{\mathrm{TM}}_{(\ell'),(\ell'+1)}\, e^{j2k_{z(\ell')}d_{(\ell')}}}{[k_{z(\ell')}+k_F][-k_{z(\ell')}-k_{z(\ell)}]} \left\{ e^{j[-k_{z(\ell')}-k_{z(\ell)}]z_2} - e^{j[-k_{z(\ell')}-k_{z(\ell)}]z_1} \right\} \\
&\quad - \frac{ba'}{k_{z(\ell')}+k_F}\, j(z_2-z_1) \\
&\quad - \frac{bb'}{[k_{z(\ell')}-k_F][k_{z(\ell')}-k_{z(\ell)}-2k_F]} \left\{ e^{j[k_{z(\ell')}-k_{z(\ell)}-2k_F]z_2} - e^{j[k_{z(\ell')}-k_{z(\ell)}-2k_F]z_1} \right\} \\
&\quad + \frac{ba'\check{R}^{\mathrm{TM}}_{(\ell'),(\ell'+1)}\, e^{j2k_{z(\ell')}d_{(\ell')}}}{[k_{z(\ell')}-k_F][-k_{z(\ell')}-k_{z(\ell)}]} \left\{ e^{j[-k_{z(\ell')}-k_{z(\ell)}]z_2} - e^{j[-k_{z(\ell')}-k_{z(\ell)}]z_1} \right\} \\
&\quad + \frac{bb'\check{R}^{\mathrm{TM}}_{(\ell'),(\ell'+1)}\, e^{j2k_{z(\ell')}d_{(\ell')}}}{[k_{z(\ell')}+k_F][-k_{z(\ell')}-k_{z(\ell)}-2k_F]} \left\{ e^{j[-k_{z(\ell')}-k_{z(\ell)}-2k_F]z_2} - e^{j[-k_{z(\ell')}-k_{z(\ell)}-2k_F]z_1} \right\} \\
&\quad - \frac{aa'\check{R}^{\mathrm{TM}}_{(\ell),(\ell-1)}\, e^{-j2k_{z(\ell)}d_{(\ell-1)}}}{[k_{z(\ell')}+k_F][k_{z(\ell')}+k_{z(\ell)}+2k_F]} \left\{ e^{j[k_{z(\ell')}+k_{z(\ell)}+2k_F]z_2} - e^{j[k_{z(\ell')}+k_{z(\ell)}+2k_F]z_1} \right\} \\
&\quad - \frac{ab'\check{R}^{\mathrm{TM}}_{(\ell),(\ell-1)}\, e^{-j2k_{z(\ell)}d_{(\ell-1)}}}{[k_{z(\ell')}-k_F][k_{z(\ell')}+k_{z(\ell)}]} \left\{ e^{j[k_{z(\ell')}+k_{z(\ell)}]z_2} - e^{j[k_{z(\ell')}+k_{z(\ell)}]z_1} \right\} \\
&\quad + \frac{aa'\check{R}^{\mathrm{TM}}_{(\ell),(\ell-1)}\check{R}^{\mathrm{TM}}_{(\ell'),(\ell'+1)}\, e^{-j2k_{z(\ell)}d_{(\ell-1)}}\, e^{j2k_{z(\ell')}d_{(\ell')}}}{[k_{z(\ell')}-k_F][-k_{z(\ell')}+k_{z(\ell)}+2k_F]} \left\{ e^{j[-k_{z(\ell')}+k_{z(\ell)}+2k_F]z_2} \right.
\end{aligned}
$$

$$
\begin{aligned}
&- e^{j[-k_{z(\ell')}+k_{z(\ell)}+2k_F]z_1}\Big\} \\
&+ \frac{ab'\check{R}^{\mathrm{TM}}_{(\ell),(\ell-1)}\check{R}^{\mathrm{TM}}_{(\ell'),(\ell'+1)}\, e^{-j2k_{z(\ell)}d_{(\ell-1)}}\, e^{j2k_{z(\ell')}d_{(\ell')}}}{k_{z(\ell')}+k_F}\, j(z_2-z_1) \\
&- \frac{ba'\check{R}^{\mathrm{TM}}_{(\ell),(\ell-1)}\, e^{-j2k_{z(\ell)}d_{(\ell-1)}}}{[k_{z(\ell')}+k_F][k_{z(\ell')}+k_{z(\ell)}]}\Big\{e^{j[k_{z(\ell')}+k_{z(\ell)}]z_2} - e^{j[k_{z(\ell')}+k_{z(\ell)}]z_1}\Big\} \\
&- \frac{bb'\check{R}^{\mathrm{TM}}_{(\ell),(\ell-1)}\, e^{-j2k_{z(\ell)}d_{(\ell-1)}}}{[k_{z(\ell')}-k_F][k_{z(\ell')}+k_{z(\ell)}-2k_F]}\Big\{e^{j[k_{z(\ell')}+k_{z(\ell)}-2k_F]z_2} - e^{j[k_{z(\ell')}+k_{z(\ell)}-2k_F]z_1}\Big\} \\
&+ \frac{ba'\check{R}^{\mathrm{TM}}_{(\ell),(\ell-1)}\check{R}^{\mathrm{TM}}_{(\ell'),(\ell'+1)}\, e^{-j2k_{z(\ell)}d_{(\ell-1)}}\, e^{j2k_{z(\ell')}d_{(\ell')}}}{k_{z(\ell')}-k_F}\, j(z_2-z_1) \\
&+ \frac{bb'\check{R}^{\mathrm{TM}}_{(\ell),(\ell-1)}\check{R}^{\mathrm{TM}}_{(\ell'),(\ell'+1)}\, e^{-j2k_{z(\ell)}d_{(\ell-1)}}\, e^{j2k_{z(\ell')}d_{(\ell')}}}{[k_{z(\ell')}+k_F][-k_{z(\ell')}+k_{z(\ell)}-2k_F]}\Big\{e^{j[-k_{z(\ell')}+k_{z(\ell)}-2k_F]z_2} \\
&- e^{j[-k_{z(\ell')}+k_{z(\ell)}-2k_F]z_1}\Big\}\Bigg]. \qquad \text{(A.47)}
\end{aligned}
$$

Also, the expression for $\tilde{G}^{IZ-}_{zz}$ can be derived as

$$
\begin{aligned}
&\tilde{G}^{IZ-}_{zz}(k_x,k_y) \\
&= \int_{z_1}^{z_2}\int_{z}^{z_2'} f_m(z)\tilde{G}_{zz}(k_x,k_y,z|z')f_n(z')\,dz'dz, \quad z_1=z_1',\ z_2=z_2',\ z\le z' \\
&= \frac{-k_\rho^2}{2k_{z(\ell')}\omega\varepsilon_{(\ell)}}\int_{z_1}^{z_2}\int_{z}^{z_2'}\Big(a\,e^{jk_Fz}+b\,e^{-jk_Fz}\Big)F^{\mathrm{TM}}_{(\ell)-}(z,z')\Big(a'\,e^{jk_Fz'}+b'\,e^{-jk_Fz'}\Big)\,dz'dz \\
&\quad - \frac{1}{j\omega\varepsilon_{(\ell')}}\int_{z_1}^{z_2}\int_{z}^{z_2'}\Big(a\,e^{jk_Fz}+b\,e^{-jk_Fz}\Big)\delta(z-z')\Big(a'\,e^{jk_Fz'}+b'\,e^{-jk_Fz'}\Big)\,dz'dz \\
&= \frac{-k_\rho^2 A^{\mathrm{TM}}_{(\ell)-}}{2k_{z(\ell')}\omega\varepsilon_{(\ell)}}\Bigg[\Bigg(\frac{a'}{j[-k_{z(\ell')}+k_F]}\,e^{j[-k_{z(\ell')}+k_F]z_1'}+\frac{b'}{j[-k_{z(\ell')}-k_F]}\,e^{j[-k_{z(\ell')}-k_F]z_1'} \\
&\quad + \frac{a'\check{R}^{\mathrm{TM}}_{(\ell),(\ell-1)}\, e^{-j2k_{z(\ell)}d_{(\ell-1)}}}{j[k_{z(\ell')}+k_F]}\,e^{j[k_{z(\ell')}+k_F]z_1'}+\frac{b'\check{R}^{\mathrm{TM}}_{(\ell),(\ell-1)}\, e^{-j2k_{z(\ell)}d_{(\ell-1)}}}{j[k_{z(\ell')}-k_F]}\,e^{j[k_{z(\ell')}-k_F]z_1'}\Bigg) \\
&\quad \cdot\Bigg(\frac{a}{j[k_{z(\ell)}+k_F]}\Big\{e^{j[k_{z(\ell)}+k_F]z_2}-e^{j[k_{z(\ell)}+k_F]z_1}\Big\} \\
&\quad + \frac{b}{j[k_{z(\ell)}-k_F]}\Big\{e^{j[k_{z(\ell)}-k_F]z_2}-e^{j[k_{z(\ell)}-k_F]z_1}\Big\} \\
&\quad + \frac{a\check{R}^{\mathrm{TM}}_{(\ell'),(\ell'+1)}\, e^{j2k_{z(\ell')}d_{(\ell')}}}{j[-k_{z(\ell)}+k_F]}\Big\{e^{j[-k_{z(\ell)}+k_F]z_2}-e^{j[-k_{z(\ell)}+k_F]z_1}\Big\} \\
&\quad + \frac{b\check{R}^{\mathrm{TM}}_{(\ell'),(\ell'+1)}\, e^{j2k_{z(\ell')}d_{(\ell')}}}{j[-k_{z(\ell)}-k_F]}\Big\{e^{j[-k_{z(\ell)}-k_F]z_2}-e^{j[-k_{z(\ell)}-k_F]z_1}\Big\}\Bigg) \\
&\quad + \frac{aa'}{[-k_{z(\ell')}+k_F][-k_{z(\ell')}+k_{z(\ell)}+2k_F]}\Big\{e^{j[-k_{z(\ell')}+k_{z(\ell)}+2k_F]z_2}-e^{j[-k_{z(\ell')}+k_{z(\ell)}+2k_F]z_1}\Big\} \\
&\quad + \frac{ab'}{-k_{z(\ell')}-k_F}\,j(z_2-z_1)
\end{aligned}
$$

$$
\begin{aligned}
&- \frac{aa'\check{R}^{\mathrm{TM}}_{(\ell),(\ell-1)}\, e^{-j2k_{z(\ell)}d_{(\ell-1)}}}{[-k_{z(\ell')}-k_F][k_{z(\ell')}+k_{z(\ell)}+2k_F]}\left\{e^{j[k_{z(\ell')}+k_{z(\ell)}+2k_F]z_2} - e^{j[k_{z(\ell')}+k_{z(\ell)}+2k_F]z_1}\right\}\\
&- \frac{ab'\check{R}^{\mathrm{TM}}_{(\ell),(\ell-1)}\, e^{-j2k_{z(\ell)}d_{(\ell-1)}}}{[-k_{z(\ell')}+k_F][k_{z(\ell')}+k_{z(\ell)}]}\left\{e^{j[k_{z(\ell')}+k_{z(\ell)}]z_2} - e^{j[k_{z(\ell')}+k_{z(\ell)}]z_1}\right\}\\
&+ \frac{ba'}{-k_{z(\ell')}+k_F}\, j(z_2-z_1)\\
&+ \frac{bb'}{[-k_{z(\ell')}-k_F][-k_{z(\ell')}+k_{z(\ell)}-2k_F]}\left\{e^{j[-k_{z(\ell')}+k_{z(\ell)}-2k_F]z_2} - e^{j[-k_{z(\ell')}+k_{z(\ell)}-2k_F]z_1}\right\}\\
&- \frac{ba'\check{R}^{\mathrm{TM}}_{(\ell),(\ell-1)}\, e^{-j2k_{z(\ell)}d_{(\ell-1)}}}{[-k_{z(\ell')}-k_F][k_{z(\ell')}+k_{z(\ell)}]}\left\{e^{j[k_{z(\ell')}+k_{z(\ell)}]z_2} - e^{j[k_{z(\ell')}+k_{z(\ell)}]z_1}\right\}\\
&- \frac{bb'\check{R}^{\mathrm{TM}}_{(\ell),(\ell-1)}\, e^{-j2k_{z(\ell)}d_{(\ell-1)}}}{[-k_{z(\ell')}+k_F][k_{z(\ell')}+k_{z(\ell)}-2k_F]}\left\{e^{j[+k_{z(\ell')}+k_{z(\ell)}-2k_F]z_2} - e^{j[+k_{z(\ell')}+k_{z(\ell)}-2k_F]z_1}\right\}\\
&+ \frac{aa'\check{R}^{\mathrm{TM}}_{(\ell'),(\ell'+1)}\, e^{j2k_{z(\ell')}d_{(\ell')}}}{[-k_{z(\ell')}+k_F][-k_{z(\ell')}-k_{z(\ell)}+2k_F]}\left\{e^{j[-k_{z(\ell')}-k_{z(\ell)}+2k_F]z_2} - e^{j[-k_{z(\ell')}-k_{z(\ell)}+2k_F]z_1}\right\}\\
&+ \frac{ab'\check{R}^{\mathrm{TM}}_{(\ell'),(\ell'+1)}\, e^{j2k_{z(\ell')}d_{(\ell')}}}{[-k_{z(\ell')}-k_F][-k_{z(\ell')}-k_{z(\ell)}]}\left\{e^{j[-k_{z(\ell')}-k_{z(\ell)}]z_2} - e^{j[-k_{z(\ell')}-k_{z(\ell)}]z_1}\right\}\\
&- \frac{aa'\check{R}^{\mathrm{TM}}_{(\ell),(\ell-1)}\check{R}^{\mathrm{TM}}_{(\ell'),(\ell'+1)}\, e^{-j2k_{z(\ell)}d_{(\ell-1)}}\, e^{j2k_{z(\ell')}d_{(\ell')}}}{[-k_{z(\ell')}-k_F][k_{z(\ell')}-k_{z(\ell)}+2k_F]}\left\{e^{j[k_{z(\ell')}-k_{z(\ell)}+2k_F]z_2}\right.\\
&\quad\left. - e^{j[k_{z(\ell')}-k_{z(\ell)}+2k_F]z_1}\right\}\\
&- \frac{ab'\check{R}^{\mathrm{TM}}_{(\ell),(\ell-1)}\check{R}^{\mathrm{TM}}_{(\ell'),(\ell'+1)}\, e^{-j2k_{z(\ell)}d_{(\ell-1)}}\, e^{j2k_{z(\ell')}d_{(\ell')}}}{-k_{z(\ell')}+k_F}\, j(z_2-z_1)\\
&+ \frac{ba'\check{R}^{\mathrm{TM}}_{(\ell'),(\ell'+1)}\, e^{j2k_{z(\ell')}d_{(\ell')}}}{[-k_{z(\ell')}+k_F][-k_{z(\ell')}-k_{z(\ell)}]}\left\{e^{j[-k_{z(\ell')}-k_{z(\ell)}]z_2} - e^{j[-k_{z(\ell')}-k_{z(\ell)}]z_1}\right\}\\
&+ \frac{bb'\check{R}^{\mathrm{TM}}_{(\ell'),(\ell'+1)}\, e^{j2k_{z(\ell')}d_{(\ell')}}}{[-k_{z(\ell')}-k_F][-k_{z(\ell')}-k_{z(\ell)}-2k_F]}\left\{e^{j[-k_{z(\ell')}-k_{z(\ell)}-2k_F]z_2} - e^{j[-k_{z(\ell')}-k_{z(\ell)}-2k_F]z_1}\right\}\\
&- \frac{ba'\check{R}^{\mathrm{TM}}_{(\ell),(\ell-1)}\check{R}^{\mathrm{TM}}_{(\ell'),(\ell'+1)}\, e^{-j2k_{z(\ell)}d_{(\ell-1)}}\, e^{j2k_{z(\ell')}d_{(\ell')}}}{-k_{z(\ell')}-k_F}\, j(z_2-z_1)\\
&- \frac{bb'\check{R}^{\mathrm{TM}}_{(\ell),(\ell-1)}\check{R}^{\mathrm{TM}}_{(\ell'),(\ell'+1)}\, e^{-j2k_{z(\ell)}d_{(\ell-1)}}\, e^{j2k_{z(\ell')}d_{(\ell')}}}{[-k_{z(\ell')}+k_F][k_{z(\ell')}-k_{z(\ell)}-2k_F]}\left\{e^{j[k_{z(\ell')}-k_{z(\ell)}-2k_F]z_2}\right.\\
&\quad\left. - e^{j[k_{z(\ell')}-k_{z(\ell)}-2k_F]z_1}\right\}\Bigg]\\
&- \frac{1}{j\omega\varepsilon_{(\ell')}}\left[\frac{aa'}{j2k_F}\left(e^{j2k_Fz_2} - e^{j2k_Fz_1}\right) - \frac{bb'}{j2k_F}\left(e^{-j2k_Fz_2} - e^{-j2k_Fz_1}\right)\right.\\
&\quad\left. + (ab'+ba')(z_2-z_1)\right]. \qquad \text{(A.48)}
\end{aligned}
$$

The expression for $\tilde{G}_{zz}^{II+}$ can be derived as

$$
\begin{aligned}
&\tilde{G}_{zz}^{II+}(k_x,k_y)\\
&=\int_{z_1}^{z_2}\int_{z_1'}^{z_2'} f_m(z)\tilde{G}_{zz}(k_x,k_y,z|z')f_n(z')\,dz'dz, \quad z_1\geq z_2'\\
&=\frac{-k_\rho^2}{2k_{z(\ell')}\omega\varepsilon_{(\ell)}}\int_{z_1}^{z_2}\int_{z_1'}^{z_2'}\left(a\,e^{jk_Fz}+b\,e^{-jk_Fz}\right)F_{(\ell)+}^{\mathrm{TM}}(z,z')\left(a'\,e^{jk_Fz'}+b'\,e^{-jk_Fz'}\right)dz'dz\\
&\quad-\frac{1}{j\omega\varepsilon_{(\ell')}}\int_{z_1}^{z_2}\int_{z}^{z_2'}\left(a\,e^{jk_Fz}+b\,e^{-jk_Fz}\right)\delta(z-z')\left(a'\,e^{jk_Fz'}+b'\,e^{-jk_Fz'}\right)dz'dz\\
&=\frac{-k_\rho^2A_{(\ell)+}^{\mathrm{TM}}}{2k_{z(\ell')}\omega\varepsilon_{(\ell)}}\left(\frac{a}{j[-k_{z(\ell)}+k_F]}\left\{e^{j[-k_{z(\ell)}+k_F]z_2}-e^{j[-k_{z(\ell)}+k_F]z_1}\right\}\right.\\
&\quad+\frac{b}{j[-k_{z(\ell)}-k_F]}\left\{e^{j[-k_{z(\ell)}-k_F]z_2}-e^{j[-k_{z(\ell)}-k_F]z_1}\right\}\\
&\quad+\frac{a\check{R}_{(\ell),(\ell-1)}^{\mathrm{TM}}\,e^{-j2k_{z(\ell)}d_{(\ell-1)}}}{j[k_{z(\ell)}+k_F]}\left\{e^{j[k_{z(\ell)}+k_F]z_2}-e^{j[k_{z(\ell)}+k_F]z_1}\right\}\\
&\quad\left.+\frac{b\check{R}_{(\ell),(\ell-1)}^{\mathrm{TM}}\,e^{-j2k_{z(\ell)}d_{(\ell-1)}}}{j[k_{z(\ell)}-k_F]}\left\{e^{j[k_{z(\ell)}-k_F]z_2}-e^{j[k_{z(\ell)}-k_F]z_1}\right\}\right)\\
&\quad\cdot\left(\frac{a'}{j[k_{z(\ell')}+k_F]}\left\{e^{j[k_{z(\ell')}+k_F]z_2'}-e^{j[k_{z(\ell')}+k_F]z_1'}\right\}\right.\\
&\quad+\frac{b'}{j[k_{z(\ell')}-k_F]}\left\{e^{j[k_{z(\ell')}-k_F]z_2'}-e^{j[k_{z(\ell')}-k_F]z_1'}\right\}\\
&\quad+\frac{a'\check{R}_{(\ell'),(\ell'+1)}^{\mathrm{TM}}\,e^{j2k_{z(\ell')}d_{(\ell')}}}{j[-k_{z(\ell')}+k_F]}\left\{e^{j[-k_{z(\ell')}+k_F]z_2'}-e^{j[-k_{z(\ell')}+k_F]z_1'}\right\}\\
&\quad\left.+\frac{b'\check{R}_{(\ell'),(\ell'+1)}^{\mathrm{TM}}\,e^{j2k_{z(\ell')}d_{(\ell')}}}{j[-k_{z(\ell')}-k_F]}\left\{e^{j[-k_{z(\ell')}-k_F]z_2'}-e^{j[-k_{z(\ell')}-k_F]z_1'}\right\}\right),
\end{aligned}
\tag{A.49}
$$

while the expression for $\tilde{G}_{zz}^{II-}$ can be derived as

$$
\begin{aligned}
&\tilde{G}_{zz}^{II-}(k_x,k_y)\\
&=\int_{z_1}^{z_2}\int_{z_1'}^{z_2'} f_m(z)\tilde{G}_{zz}(k_x,k_y,z|z')f_n(z')\,dz'dz, \quad z_2\leq z_1'\\
&=\frac{-k_\rho^2}{2k_{z(\ell')}\omega\varepsilon_{(\ell)}}\int_{z_1}^{z_2}\int_{z_1'}^{z_2'}\left(a\,e^{jk_Fz}+b\,e^{-jk_Fz}\right)F_{(\ell)-}^{\mathrm{TM}}(z,z')\left(a'\,e^{jk_Fz'}+b'\,e^{-jk_Fz'}\right)dz'dz\\
&\quad-\frac{1}{j\omega\varepsilon_{(\ell')}}\int_{z_1}^{z_2}\int_{z}^{z_2'}\left(a\,e^{jk_Fz}+b\,e^{-jk_Fz}\right)\delta(z-z')\left(a'\,e^{jk_Fz'}+b'\,e^{-jk_Fz'}\right)dz'dz\\
&=\frac{-k_\rho^2A_{(\ell)-}^{\mathrm{TM}}}{2k_{z(\ell')}\omega\varepsilon_{(\ell)}}\left(\frac{a}{j[k_{z(\ell)}+k_F]}\left\{e^{j[k_{z(\ell)}+k_F]z_2}-e^{j[k_{z(\ell)}+k_F]z_1}\right\}\right.\\
&\quad\left.+\frac{b}{j[k_{z(\ell)}-k_F]}\left\{e^{j[k_{z(\ell)}-k_F]z_2}-e^{j[k_{z(\ell)}-k_F]z_1}\right\}\right.
\end{aligned}
$$

$$
\begin{aligned}
&+ \frac{a\check{R}^{\mathrm{TM}}_{(\ell'),(\ell'+1)}\, e^{j2k_{z(\ell')}d_{(\ell')}}}{j[-k_{z(\ell)}+k_F]}\left\{e^{j[-k_{z(\ell)}+k_F]z_2} - e^{j[-k_{z(\ell)}+k_F]z_1}\right\} \\
&+ \frac{b\check{R}^{\mathrm{TM}}_{(\ell'),(\ell'+1)}\, e^{j2k_{z(\ell')}d_{(\ell')}}}{j[-k_{z(\ell)}-k_F]}\left\{e^{j[-k_{z(\ell)}-k_F]z_2} - e^{j[-k_{z(\ell)}-k_F]z_1}\right\}\Bigg) \\
&\cdot \Bigg(\frac{a'}{j[-k_{z(\ell')}+k_F]}\left\{e^{j[-k_{z(\ell')}+k_F]z'_2} - e^{j[-k_{z(\ell')}+k_F]z'_1}\right\} \\
&+ \frac{b'}{j[-k_{z(\ell')}-k_F]}\left\{e^{j[-k_{z(\ell')}-k_F]z'_2} - e^{j[-k_{z(\ell')}-k_F]z'_1}\right\} \\
&+ \frac{a'\check{R}^{\mathrm{TM}}_{(\ell),(\ell-1)}\, e^{-j2k_{z(\ell)}d_{(\ell-1)}}}{j[k_{z(\ell')}+k_F]}\left\{e^{j[k_{z(\ell')}+k_F]z'_2} - e^{j[k_{z(\ell')}+k_F]z'_1}\right\} \\
&+ \frac{b'\check{R}^{\mathrm{TM}}_{(\ell),(\ell-1)}\, e^{-j2k_{z(\ell)}d_{(\ell-1)}}}{j[k_{z(\ell')}-k_F]}\left\{e^{j[k_{z(\ell')}-k_F]z'_2} - e^{j[k_{z(\ell')}-k_F]z'_1}\right\}\Bigg).
\end{aligned}
\tag{A.50}
$$

APPENDIX B

Derivations Related to the Basis Functions

In this appendix, it is shown how the spatial-domain expression of the rectangular attachment mode can be derived. Although the derivation is available in the literature [6, 7], it is included here in a more compact form for completeness sake. It is also shown how the spectral-domain expressions for all of the basis functions can be derived. Please note that, in this appendix, a local (x, y, z) coordinate system is used for all the basis functions, instead of the (u, v, z) coordinate system as in Chapter 3. This is for easy comparison to most literature, where the standard (x, y, z) coordinate system is normally used.

B.1 SPATIAL REPRESENTATION OF THE RECTANGULAR ATTACHMENT MODE

Refer to Figure 3.10 for an illustration of the geometrical parameters associated with the rectangular attachment mode. The only differences here, are that the u and v axes are replaced by x and y axes respectively, and that the na subscript is dropped. In order to derive the expression for the rectangular attachment mode, the area between the patch and the ground plane can be viewed as a magnetic-wall cavity [6, 7, 129, 132]. Now, the electric field at (x, y) inside such a magnetic-wall cavity, excited by a uniform filament of current at the position $(\dot{x}^{AZ}, \dot{y}^{AZ})$, is found to be [6, 7]

$$\begin{aligned}\mathbf{E}^{AP}(x, y, \dot{x}^{AZ}, \dot{y}^{AZ}) &= E_z^{AP}(x, y, \dot{x}^{AZ}, \dot{y}^{AZ}) \\ &= \left\{ \frac{j\omega\mu_{(\text{eff})}}{LW} \sum_{\kappa=0}^{\infty} \sum_{i=0}^{\infty} \frac{\epsilon_\kappa \epsilon_i}{\varepsilon_{r(\text{eff})} k_0^2 - (\kappa\pi/L)^2 - (i\pi/W)^2} \right. \\ &\quad \cdot \cos\left[\frac{\kappa\pi}{L}\left(x + \frac{L}{2}\right)\right] \cos\left[\frac{\kappa\pi}{L}\left(\dot{x}^{AZ} + \frac{L}{2}\right)\right] \\ &\quad \left. \cdot \cos\left[\frac{i\pi}{W}\left(y + \frac{W}{2}\right)\right] \cos\left[\frac{i\pi}{W}\left(\dot{y}^{AZ} + \frac{W}{2}\right)\right] \right\} \hat{z},\end{aligned}$$

$$|x| \leq \frac{L}{2},\ |y| \leq \frac{W}{2},\ z \leq z^{AP}. \qquad \text{(B.1)}$$

It is assumed that the electric field is constant along the z direction. In (B.1), the Neumann numbers are given by

$$\epsilon_{\kappa,i} = \begin{cases} 1, & \kappa, i = 0 \\ 2, & \kappa, i > 0. \end{cases} \qquad \text{(B.2)}$$

Furthermore, $\varepsilon_{(\text{eff})}$ is the effective permittivity and $\mu_{(\text{eff})}$ the effective permeability of the layers below the patch.

The magnetic field inside the cavity can be derived from the electric field and is given by

$$\begin{aligned} \mathbf{H}^{AP}(x, y, \dot{x}^{AZ}, \dot{y}^{AZ}) &= \frac{-1}{j\omega\mu_{(\text{eff})}} \nabla \times \mathbf{E}^{AP}(x, y, \dot{x}^{AZ}, \dot{y}^{AZ}) \\ &= \frac{1}{j\omega\mu_{(\text{eff})}} \left(-\frac{\partial}{\partial y}\hat{x} + \frac{\partial}{\partial x}\hat{y} \right) E_z^{AP}(x, y, \dot{x}^{AZ}, \dot{y}^{AZ}), \\ & \qquad |x| \leq \frac{L}{2},\ |y| \leq \frac{W}{2},\ z \leq z^{AP}. \end{aligned} \qquad \text{(B.3)}$$

This in turn leads to the current density on the patch, which can be expressed as [6, 7]

$$\begin{aligned} \mathbf{J}^{AP}(x, y, \dot{x}^{AZ}, \dot{y}^{AZ}) &= -\hat{z} \times \mathbf{H}^{AP}(x, y, \dot{x}^{AZ}, \dot{y}^{AZ})|_{z=z^{AP}} \\ &= \frac{-1}{LW} \sum_{\kappa=0}^{\infty} \sum_{i=0}^{\infty} \frac{\epsilon_\kappa \epsilon_i}{\varepsilon_{r(\text{eff})} k_0^2 - (\kappa\pi/L)^2 - (i\pi/W)^2} \\ &\quad \left(\left\{ \frac{\kappa\pi}{L} \sin\left[\frac{\kappa\pi}{L}\left(x + \frac{L}{2} \right) \right] \cos\left[\frac{\kappa\pi}{L}\left(\dot{x}^{AZ} + \frac{L}{2} \right) \right] \right. \right. \\ &\qquad \left. \cdot \cos\left[\frac{i\pi}{W}\left(y + \frac{W}{2} \right) \right] \cos\left[\frac{i\pi}{W}\left(\dot{y}^{AZ} + \frac{W}{2} \right) \right] \right\} \hat{x} \\ &\quad + \left\{ \frac{i\pi}{W} \cos\left[\frac{\kappa\pi}{L}\left(x + \frac{L}{2} \right) \right] \cos\left[\frac{\kappa\pi}{L}\left(\dot{x}^{AZ} + \frac{L}{2} \right) \right] \right. \\ &\qquad \left. \left. \cdot \sin\left[\frac{i\pi}{W}\left(y + \frac{W}{2} \right) \right] \cos\left[\frac{i\pi}{W}\left(\dot{y}^{AZ} + \frac{W}{2} \right) \right] \right\} \hat{y} \right), \\ & \qquad |x| \leq \frac{L}{2},\ |y| \leq \frac{W}{2},\ z = z^{AP}. \end{aligned} \qquad \text{(B.4)}$$

By using the fact that [6, 7]

$$\sum_{\kappa=0}^{\infty} \frac{\epsilon_\kappa \cos(\kappa x)}{\kappa^2 - \alpha^2} (-1)^\kappa = \frac{-\pi \cos(\alpha x)}{\alpha \sin(\alpha\pi)}, \quad -\pi \leq x \leq \pi \qquad \text{(B.5)}$$

and

$$\sum_{\kappa=0}^{\infty} \frac{\epsilon_\kappa \kappa \sin(\kappa x)}{\kappa^2 - \alpha^2} (-1)^\kappa = \frac{-\pi \sin(\alpha x)}{\sin(\alpha\pi)}, \quad -\pi \leq x \leq \pi, \tag{B.6}$$

the expression in (B.4) can be simplified to yield [6, 7, 129, 132]

$$\mathbf{J}^{AP}(x, y, \dot{x}^{AZ}, \dot{y}^{AZ}) = \frac{-1}{2W} \sum_{i=0}^{\infty} \epsilon_i \cos\left[\frac{i\pi}{W}\left(\dot{y}^{AZ} + \frac{W}{2}\right)\right] \cdot \left\{ g_s(\beta, L, \dot{x}^{AZ}, x) f_c(i, W, y)\, \hat{x} + \left(\frac{i\pi}{W}\right) g_c(\beta, L, \dot{x}^{AZ}, x) f_s(i, W, y)\, \hat{y} \right\}, \quad |x| \leq \frac{L}{2},\ |y| \leq \frac{W}{2},\ z = z^{AP}, \tag{B.7}$$

where

$$g_s(\beta, L, \dot{x}^{AZ}, x) = \frac{\sin[\beta(x + \dot{x}^{AZ})] - \operatorname{sgn}(x - \dot{x}^{AZ}) \sin[\beta(L - |x - \dot{x}^{AZ}|)]}{\sin(\beta L)}, \tag{B.8}$$

$$g_c(\beta, L, \dot{x}^{AZ}, x) = \frac{\cos[\beta(x + \dot{x}^{AZ})] + \cos[\beta(L - |x - \dot{x}^{AZ}|)]}{\beta \sin(\beta L)}, \tag{B.9}$$

$$f_s(i, W, y) = \sin\left[\frac{i\pi}{W}\left(y + \frac{W}{2}\right)\right] \tag{B.10}$$

and

$$f_c(i, W, y) = \cos\left[\frac{i\pi}{W}\left(y + \frac{W}{2}\right)\right], \tag{B.11}$$

with

$$\operatorname{sgn}(x) = \begin{cases} 1, & x > 0 \\ 0, & x = 0 \\ -1, & x < 0 \end{cases} \tag{B.12}$$

and

$$\beta = \sqrt{\varepsilon_{r(\text{eff})} k_0^2 - \left(\frac{i\pi}{W}\right)^2}. \tag{B.13}$$

In (B.13), $k_0 = 2\pi/\lambda_0$, where λ_0 is the free-space wavelength. Also, as has been mentioned, $\varepsilon_{r(\text{eff})}$ is the effective relative permittivity of the layers below the patch. For two layers, it can be calculated as [65, 66, 179]

$$\varepsilon_{r(\text{eff})} = \frac{\varepsilon_{r(1)} \varepsilon_{r(2)} \left[h_{(1)} + h_{(2)}\right]}{\varepsilon_{r(1)} h_{(2)} + \varepsilon_{r(2)} h_{(1)}} \left[1 - \tan\delta_{\varepsilon(1)} \tan\delta_{\varepsilon(2)}\right]. \tag{B.14}$$

The patch part of the attachment mode is then defined to be

$$\mathbf{f}^{AP}(x, y) = \frac{1}{2\pi} \int_0^{2\pi} \mathbf{J}^{AP}(x, y, \dot{x}^{AZ}, \dot{y}^{AZ})\, d\phi, \tag{B.15}$$

where

$$\dot{x}^{AZ} = x^{AZ} + a\cos(\phi) \tag{B.16}$$

and

$$\dot{y}^{AZ} = y^{AZ} + a\sin(\phi) \tag{B.17}$$

describe a position on the surface of the probe, while (x^{AZ}, y^{AZ}) is the position of the centre of the probe relative to the centre of the patch, and a is the radius of the probe.

B.2 SPECTRAL REPRESENTATION OF THE BASIS FUNCTIONS

It will now be shown how the spectral form of each basis function can be derived. However, before doing so, it is appropriate to first define some general coordinates and unit vectors.

In some cases, it is more convenient to work with polar (ρ, ϕ) coordinates rather than rectangular (x, y) coordinates. The relationship between them is given by

$$\rho = \sqrt{x^2 + y^2} \tag{B.18}$$

$$\phi = \tan^{-1}\left(\frac{y}{x}\right) \tag{B.19}$$

and

$$x = \rho\cos(\phi) \tag{B.20}$$

$$y = \rho\sin(\phi). \tag{B.21}$$

The radial unit vector associated with the polar coordinate system, is given by

$$\hat{\rho} = \frac{x}{\sqrt{x^2 + y^2}}\,\hat{x} + \frac{y}{\sqrt{x^2 + y^2}}\,\hat{y}. \tag{B.22}$$

Similarly, the wavenumbers that correspond with the two coordinate systems are related through

$$k_\rho = \sqrt{k_x^2 + k_y^2} \tag{B.23}$$

$$\varphi = \tan^{-1}\left(\frac{k_y}{k_x}\right) \tag{B.24}$$

and

$$k_x = k_\rho\cos(\varphi) \tag{B.25}$$

$$k_y = k_\rho\sin(\varphi). \tag{B.26}$$

The unit vector for the wavenumber associated with the radial direction, is given by

$$\hat{k}_\rho = \frac{k_x}{\sqrt{k_x^2 + k_y^2}}\,\hat{x} + \frac{k_y}{\sqrt{k_x^2 + k_y^2}}\,\hat{y}. \tag{B.27}$$

B.2.1 Piecewise-Sinusoidal Basis Functions on the Probes

Refer to Figure 3.7 for an illustration of the geometrical parameters associated with the probes. The only differences here, are that the u and v axes are replaced by x and y axes respectively, and that the np subscript is dropped. As was shown in Section 3.5.1, the basis functions on the probes can be expressed as

$$\mathbf{f}^{PZ}(x,y,z) = \frac{1}{2\pi a}\, f^{PZ}(z)\,\hat{z}\,\Big|_{x^2+y^2=a^2} \tag{B.28}$$

in the spatial domain.

The two-dimensional Fourier transform of this function in most easily evaluated by changing to polar variables. Due to the fact that ρ is limited to the surface of the probe, one can set

$$x = a\cos(\phi) \tag{B.29}$$

and

$$y = a\sin(\phi). \tag{B.30}$$

Then, by taking the two-dimensional Fourier transform of $\mathbf{f}^{PZ}(x,y,z)$, as defined in (3.18), it follows that

$$\begin{aligned}
\tilde{\mathbf{f}}^{PZ}(k_x,k_y,z) &= \int_{-\infty}^{\infty}\int_{-\infty}^{\infty} \mathbf{f}^{PZ}(x,y,z)\, e^{-jk_x x}\, e^{-jk_y y}\, dxdy \\
&= \frac{1}{2\pi a}\, f^{PZ}(z)\left[\int_0^{2\pi} e^{-jk_\rho a\cos(\varphi)\cos(\phi) - jk_\rho a\sin(\varphi)\sin(\phi)}\, a\, d\phi\right]\hat{z} \\
&= \frac{1}{2\pi}\, f(z)^{PZ}\left[\int_0^{2\pi} e^{-jk_\rho a\cos(\varphi-\phi)}\, d\phi\right]\hat{z} \\
&= f(z)^{PZ} J_0(k_\rho a)\,\hat{z}.
\end{aligned} \tag{B.31}$$

Here, $J_0(\cdot)$ is the Bessel function of the first kind of order 0.

B.2.2 Rooftop Basis Functions on the Rectangular Capacitor Patches

Refer to Figure 3.8 for an illustration of the geometrical parameters associated with the subdomain rooftop basis functions on the rectangular capacitor patches. The only differences here, are that the u and v axes are replaced by x and y axes respectively, and that the ns subscript is dropped. As was shown in Section 3.5.2, in the spatial domain, the rooftop basis functions can be expressed as

$$\mathbf{f}^{SX}(x,y) = \left(1 - \frac{|x|}{\Delta l}\right)\mathrm{rect}\left(\frac{y}{\Delta w}\right)\hat{x}, \quad |x| \le \Delta l,\ z = z^S \tag{B.32}$$

for the x-directed functions and

$$\mathbf{f}^{SY}(x,y) = \left(1 - \frac{|y|}{\Delta w}\right)\mathrm{rect}\left(\frac{x}{\Delta l}\right)\hat{y}, \quad |y| \le \Delta w,\ z = z^S \tag{B.33}$$

for the y-directed functions. In compact notation, (B.32) and (B.33) can be expressed as

$$\mathbf{f}^{SX}(x,y) = \Lambda(\Delta l, x)\Pi(\Delta w, y)\,\hat{x}, \quad |x| \leq \Delta l,\ z = z^S \tag{B.34}$$

and

$$\mathbf{f}^{SY}(x,y) = \Lambda(\Delta w, y)\Pi(\Delta l, x)\,\hat{y}, \quad |y| \leq \Delta w,\ z = z^S, \tag{B.35}$$

where

$$\Lambda(\Delta l, x) = \begin{cases} 1 - \dfrac{|x|}{\Delta l}, & |x| \leq \Delta l \\ 0, & \text{otherwise} \end{cases} \tag{B.36}$$

is the triangular function and

$$\Pi(\Delta l, x) = \text{rect}\left(\frac{x}{\Delta l}\right) = \begin{cases} 1, & |x| \leq \dfrac{\Delta l}{2} \\ 0, & \text{otherwise} \end{cases} \tag{B.37}$$

is the rectangular function.

The two-dimensional Fourier transforms of $\mathbf{f}^{SX}(x,y)$ and $\mathbf{f}^{SY}(x,y)$ can be reduced to the product of two one-dimensional Fourier transforms due to the fact that the variables in (B.32) and (B.33) can be separated. The spectral forms of the rooftop basis functions are then given by

$$\tilde{\mathbf{f}}^{SX}(k_x,k_y) = \tilde{\Lambda}(\Delta l, k_x)\tilde{\Pi}(\Delta w, k_y)\,\hat{x}, \quad |x| \leq \Delta l,\ z = z^S \tag{B.38}$$

and

$$\tilde{\mathbf{f}}^{SY}(k_x,k_y) = \tilde{\Lambda}(\Delta w, k_y)\tilde{\Pi}(\Delta l, k_x)\,\hat{y}, \quad |y| \leq \Delta w,\ z = z^S, \tag{B.39}$$

where the Fourier transforms, $\tilde{\Lambda}(\Delta l, k_x)$ and $\tilde{\Pi}(\Delta l, k_x)$, of the triangular and rectangular functions are well known [180]. They are given by

$$\tilde{\Lambda}(\Delta l, k_x) = \frac{4}{k_x^2 \Delta l}\sin^2\left(\frac{k_x \Delta l}{2}\right) \tag{B.40}$$

and

$$\tilde{\Pi}(\Delta l, k_x) = \frac{2}{k_x}\sin\left(\frac{k_x \Delta l}{2}\right) \tag{B.41}$$

respectively. This finally leads to

$$\tilde{\mathbf{f}}^{SX}(k_x,k_y) = \frac{8}{\Delta l k_x^2 k_y}\sin^2\left(\frac{k_x \Delta l}{2}\right)\sin\left(\frac{k_y \Delta w}{2}\right)\hat{x}, \quad z = z^S \tag{B.42}$$

and

$$\tilde{\mathbf{f}}^{SY}(k_x,k_y) = \frac{8}{\Delta w k_y^2 k_x}\sin^2\left(\frac{k_y \Delta w}{2}\right)\sin\left(\frac{k_x \Delta l}{2}\right)\hat{y}, \quad z = z^S. \tag{B.43}$$

B.2.3 Sinusoidal Basis Functions on the Resonant Patches

Refer to Figure 3.9 for an illustration of the geometrical parameters associated with the entire-domain sinusoidal basis functions on the rectangular resonant patches. The only differences here, are that the u and v axes are replaced by x and y axes respectively, and that the ne subscript is dropped. As was shown in Section 3.5.3, in the spatial domain, the sinusoidal basis functions can be expressed as

$$\mathbf{f}^{EX}(x,y) = \sin\left[\frac{p^{EX}\pi}{L}\left(x+\frac{L}{2}\right)\right]\cos\left[\frac{q^{EX}\pi}{W}\left(y+\frac{W}{2}\right)\right]\hat{x}, \quad |x| \leq \frac{L}{2},\ |y| \leq \frac{W}{2},\ z = z^E \tag{B.44}$$

for the x-directed functions and as

$$\mathbf{f}^{EY}(x,y) = \sin\left[\frac{p^{EY}\pi}{W}\left(y+\frac{W}{2}\right)\right]\cos\left[\frac{q^{EY}\pi}{L}\left(x+\frac{L}{2}\right)\right]\hat{y}, \quad |x| \leq \frac{L}{2},\ |y| \leq \frac{W}{2},\ z = z^E \tag{B.45}$$

for the y-directed functions. In compact notation, (B.44) and (B.45) can be expressed as

$$\mathbf{f}^{EX}(x,y) = f_s(p^{EX},L,x)f_c(q^{EX},W,y)\,\hat{x}, \quad |x| \leq \frac{L}{2},\ |y| \leq \frac{W}{2},\ z = z^E \tag{B.46}$$

and

$$\mathbf{f}^{EY}(x,y) = f_s(p^{EY},W,y)f_c(q^{EY},L,x)\,\hat{y}, \quad |x| \leq \frac{L}{2},\ |y| \leq \frac{W}{2},\ z = z^E, \tag{B.47}$$

where $f_s(p,L,x)$ and $f_c(p,L,x)$ have already been defined in (B.10) and (B.11).

The two-dimensional Fourier transforms of $\mathbf{f}^{EX}(x,y)$ and $\mathbf{f}^{EY}(x,y)$ can be reduced to the product of two one-dimensional Fourier transforms, due to the fact that the variables in (B.46) and (B.47) can be separated. The spectral forms of the sinusoidal basis functions are then given by

$$\tilde{\mathbf{f}}^{EX}(k_x,k_y) = \tilde{f}_s(p^{EX},L,k_x)\tilde{f}_c(q^{EX},W,k_y)\,\hat{x}, \quad z = z^E \tag{B.48}$$

and

$$\tilde{\mathbf{f}}^{EY}(k_x,k_y) = \tilde{f}_s(p^{EY},W,k_y)\tilde{f}_c(q^{EY},L,k_x)\,\hat{y}, \quad z = z^E, \tag{B.49}$$

where the Fourier transforms, $\tilde{f}_s(p,L,k_x)$ and $\tilde{f}_c(p,L,k_x)$, of $f_s(p,L,x)$ and $f_c(p,L,x)$ can easily be derived. They are given by

$$\tilde{f}_s(p,L,k_x) = \frac{p\pi/L}{k_x^2-(p\pi/L)^2}\left[(-1)^p e^{-jk_xL/2} - e^{jk_xL/2}\right] \tag{B.50}$$

and

$$\tilde{f}_c(p, L, k_x) = \frac{jk_x}{k_x^2 - (p\pi/L)^2}\left[(-1)^p e^{-jk_xL/2} - e^{jk_xL/2}\right] \tag{B.51}$$

respectively. This finally leads to

$$\tilde{\mathbf{f}}^{EX}(k_x, k_y) = \frac{p^{EX}\pi/L}{k_x^2 - (p^{EX}\pi/L)^2}\left[(-1)^{p^{EX}} e^{-jk_xL/2} - e^{jk_xL/2}\right] \cdot \frac{jk_y}{k_y^2 - (q^{EX}\pi/W)^2}\left[(-1)^{q^{EX}} e^{-jk_yW/2} - e^{jk_yW/2}\right]\hat{x}, \quad z = z^E \tag{B.52}$$

and

$$\tilde{\mathbf{f}}^{EY}(k_x, k_y) = \frac{p^{EY}\pi/W}{k_y^2 - (p^{EY}\pi/W)^2}\left[(-1)^{p^{EY}} e^{-jk_yW/2} - e^{jk_yW/2}\right] \cdot \frac{jk_x}{k_x^2 - (q^{EY}\pi/L)^2}\left[(-1)^{q^{EY}} e^{-jk_xL/2} - e^{jk_xL/2}\right]\hat{y}, \quad z = z^E. \tag{B.53}$$

B.2.4 Rectangular Attachment Mode

It is possible to reduce the two-dimensional Fourier transform of $\mathbf{J}^{AP}(x, y, \dot{x}^{AZ}, \dot{y}^{AZ})$ to one-dimensional Fourier transforms, due to the fact that the variables in (B.7) can be separated. The spectral form of the patch part of the rectangular attachment mode is then given by [6, 7, 129, 132]

$$\tilde{\mathbf{J}}^{AP}(k_x, k_y, \dot{x}^{AZ}, \dot{y}^{AZ}) = \frac{-1}{2W}\sum_{i=0}^{\infty}\epsilon_i \cos\left[\frac{i\pi}{W}\left(\dot{y}^{AZ} + \frac{W}{2}\right)\right] \cdot \left\{\tilde{g}_s(\beta, L, \dot{x}^{AZ}, k_x)\tilde{f}_c(i, W, k_y)\,\hat{x} + \left(\frac{i\pi}{W}\right)\tilde{g}_c(\beta, L, \dot{x}^{AZ}, k_x)\tilde{f}_s(i, W, k_y)\,\hat{y}\right\}, \quad z = z^{AP}, \tag{B.54}$$

where

$$\begin{aligned}\tilde{g}_s(\beta, L, \dot{x}^{AZ}, k_x) &= \frac{-j2}{(k_x^2 - \beta^2)\sin(\beta L)}\left(\beta\left\{e^{j\beta\dot{x}^{AZ}}\sin\left[\frac{L(k_x - \beta)}{2}\right]\right.\right. \\ &\quad \left.\left. + e^{-j\beta\dot{x}^{AZ}}\sin\left[\frac{L(k_x + \beta)}{2}\right]\right\} - k_x\, e^{-jk_x\dot{x}^{AZ}}\sin(\beta L)\right) \\ &= \frac{-j2}{(k_x^2 - \beta^2)}\left[jk_x\, e^{-jk_x\dot{x}^{AZ}} + j\frac{\sin(k_xL/2)\beta\cos(\beta\dot{x}^{AZ})}{\sin(\beta L/2)}\right. \\ &\quad \left. - \frac{\cos(k_xL/2)\beta\sin(\beta\dot{x}^{AZ})}{\cos(\beta L/2)}\right]\end{aligned} \tag{B.55}$$

and

$$\tilde{g}_c(\beta, L, \dot{x}^{AZ}, k_x) = \frac{2}{(k_x^2 - \beta^2)\beta\sin(\beta L)}\left(k_x\left\{e^{j\beta\dot{x}^{AZ}}\sin\left[\frac{L(k_x - \beta)}{2}\right]\right.\right.$$

$$+ e^{-j\beta\dot{x}^{AZ}} \sin\left[\frac{L(k_x+\beta)}{2}\right]\Bigg\} - \beta\, e^{-jk_x\dot{x}^{AZ}} \sin(\beta L)\Bigg)$$
$$= \frac{2}{(k_x^2-\beta^2)}\Bigg[-e^{-jk_x\dot{x}^{AZ}} + \frac{\sin(k_xL/2)k_x\cos(\beta\dot{x}^{AZ})}{\beta\sin(\beta L/2)}$$
$$+ j\frac{\cos(k_xL/2)k_x\sin(\beta\dot{x}^{AZ})}{\beta\cos(\beta L/2)}\Bigg] \qquad \text{(B.56)}$$

are the Fourier transforms of $g_s(\beta, L, \dot{x}^{AZ}, x)$ and $g_c(\beta, L, \dot{x}^{AZ}, x)$ in (B.8) and (B.9) respectively. These expressions appear very intimidating, but can be derived from standard Fourier transforms. The expressions for the functions $\tilde{f}_s(i, W, k_y)$ and $\tilde{f}_c(i, W, k_y)$ have already been given in (B.50) and (B.51) respectively.

Substitution of all the relevant expressions into (B.54), leads to

$$\tilde{\mathbf{J}}^{AP}(k_x, k_y, \dot{x}^{AZ}, \dot{y}^{AZ})$$
$$= \frac{-1}{W}\sum_{i=0}^{\infty}\epsilon_i \cos\left[\frac{i\pi}{W}\left(\dot{y}^{AZ}+\frac{W}{2}\right)\right]\frac{(-1)^i e^{-jk_yW/2} - e^{jk_yW/2}}{(k_x^2-\beta^2)[k_y^2-(i\pi/W)^2]}$$
$$\cdot\Bigg\{jk_y\Bigg[jk_x\, e^{-jk_x\dot{x}^{AZ}} + j\frac{\sin(k_xL/2)\beta\cos(\beta\dot{x}^{AZ})}{\sin(\beta L/2)} - \frac{\cos(k_xL/2)\beta\sin(\beta\dot{x}^{AZ})}{\cos(\beta L/2)}\Bigg]\hat{x}$$
$$+\left(\frac{i\pi}{W}\right)^2\Bigg[-e^{-jk_x\dot{x}^{AZ}} + \frac{\sin(k_xL/2)k_x\cos(\beta\dot{x}^{AZ})}{\beta\sin(\beta L/2)} + j\frac{\cos(k_xL/2)k_x\sin(\beta\dot{x}^{AZ})}{\beta\cos(\beta L/2)}\Bigg]\hat{y}\Bigg\},$$
$$z = z^{AP}. \qquad \text{(B.57)}$$

The expression in (B.57) can now be separated into a regular component, which is a fast convergent series, and a singular component, which is a slowly convergent series. The spectral form of $\mathbf{J}^{AP}(x, y, \dot{x}^{AZ}, \dot{y}^{AZ})$ can therefore be expressed as [6, 7]

$$\tilde{\mathbf{J}}^{AP}(k_x, k_y, \dot{x}^{AZ}, \dot{y}^{AZ}) = \tilde{\mathbf{J}}^{AP,\text{reg}}(k_x, k_y, \dot{x}^{AZ}, \dot{y}^{AZ}) + \tilde{\mathbf{J}}^{AP,\text{sing}}(k_x, k_y, \dot{x}^{AZ}, \dot{y}^{AZ}), \qquad \text{(B.58)}$$

where

$$\tilde{\mathbf{J}}^{AP,\text{reg}}(k_x, k_y, \dot{x}^{AZ}, \dot{y}^{AZ})$$
$$= \frac{-1}{W}\sum_{i=0}^{\infty}\epsilon_i \cos\left[\frac{i\pi}{W}\left(\dot{y}^{AZ}+\frac{W}{2}\right)\right]\frac{(-1)^i e^{-jk_yW/2} - e^{jk_yW/2}}{(k_x^2-\beta^2)[k_y^2-(i\pi/W)^2]}$$
$$\cdot\left[k_y\,\hat{x} + k_x\frac{(i\pi/W)^2}{\beta^2}\,\hat{y}\right]\left[\frac{\beta\cos(\beta\dot{x}^{AZ})\sin(k_xL/2)}{\sin(\beta L/2)} - j\frac{\beta\sin(\beta\dot{x}^{AZ})\cos(k_xL/2)}{\cos(\beta L/2)}\right],$$
$$z = z^{AP} \qquad \text{(B.59)}$$

and

$$\begin{aligned}
&\tilde{\mathbf{J}}^{AP,\text{sing}}(k_x, k_y, \dot{x}^{AZ}, \dot{y}^{AZ}) \\
&= \frac{1}{W}\, e^{-jk_x\dot{x}^{AZ}} \sum_{i=0}^{\infty} \epsilon_i \cos\left[\frac{i\pi}{W}\left(\dot{y}^{AZ} + \frac{W}{2}\right)\right] \frac{(-1)^i e^{-jk_yW/2} - e^{jk_yW/2}}{(k_x^2 - \beta^2)[k_y^2 - (i\pi/W)^2]} \left[k_xk_y\,\hat{x} + \left(\frac{i\pi}{W}\right)^2 \hat{y}\right] \\
&= \frac{e^{-jk_x\dot{x}^{AZ}}}{k_y^2 - k_\alpha^2}\Big\{k_xk_y[A(k_\alpha) - A(k_y)]\,\hat{x} + [k_\alpha^2 A(k_\alpha) - k_y^2 A(k_y)]\,\hat{y}\Big\}, \quad z = z^{AP}.
\end{aligned} \tag{B.60}$$

In the final expression of (B.60), the substitutions

$$k_\alpha^2 = \varepsilon_{r(\text{eff})}k_0^2 - k_x^2, \tag{B.61}$$

$$k_y^2 - k_\alpha^2 = -\left[\varepsilon_{r(\text{eff})}k_0^2 - k_x^2 - k_y^2\right] = -k_{z(\text{eff})}^2 \tag{B.62}$$

and

$$A(\chi) = \frac{W}{\pi^2}\sum_{i=0}^{\infty} \epsilon_i \cos\left[\frac{i\pi}{W}\left(\dot{y}^{AZ} + \frac{W}{2}\right)\right] \frac{(-1)^i e^{-jk_yW/2} - e^{jk_yW/2}}{i^2 - (\chi W/\pi)^2} \tag{B.63}$$

have been made.

By using the fact that in general

$$\sum_{i=0}^{\infty} \frac{\epsilon_i \cos(ix)}{i^2 - \alpha^2} = \sum_{i=0}^{\infty} \frac{\epsilon_i \cos[i(\pi - x)]}{i^2 - \alpha^2}(-1)^i = \frac{-\pi \cos[\alpha(\pi - x)]}{\alpha \sin(\alpha\pi)}, \quad 0 \le x \le 2\pi, \tag{B.64}$$

$A(\chi)$ can be summed up in close form, leading to

$$\begin{aligned}
A(\chi) &= \frac{-1}{\chi}\left[\cos\left(\chi\dot{y}^{AZ} + \frac{\chi W}{2}\right)\frac{e^{-jk_yW/2}}{\sin(\chi W)} - \cos\left(\chi\dot{y}^{AZ} - \frac{\chi W}{2}\right)\frac{e^{jk_yW/2}}{\sin(\chi W)}\right] \\
&= \frac{j}{\chi}\left[\frac{\cos(\chi\dot{y}^{AZ})\sin(k_yW/2)}{\sin(\chi W/2)} - j\frac{\sin(\chi\dot{y}^{AZ})\cos(k_yW/2)}{\cos(\chi W/2)}\right].
\end{aligned} \tag{B.65}$$

If this expression for $A(\chi)$ is inserted into (B.60), $\tilde{\mathbf{J}}^{AP,\text{sing}}(k_x, k_y, \dot{x}^{AZ}, \dot{y}^{AZ})$ can be expressed as

$$\begin{aligned}
\tilde{\mathbf{J}}^{AP,\text{sing}}(k_x, k_y, \dot{x}^{AZ}, \dot{y}^{AZ}) = &\frac{j(k_x\,\hat{x} + k_y\,\hat{y})}{k_{z(\text{eff})}^2}\, e^{-j(k_x\dot{x}^{AZ} + k_y\dot{y}^{AZ})} \\
&- \frac{k_xk_y\,\hat{x} + k_\alpha^2\,\hat{y}}{k_{z(\text{eff})}^2}\, A(k_\alpha)\, e^{-jk_x\dot{x}^{AZ}}, \quad z = z^{AP}.
\end{aligned} \tag{B.66}$$

Following from (B.15), the spectral form of the rectangular attachment mode is given by

$$\tilde{\mathbf{f}}^{AP}(k_x, k_y) = \frac{1}{2\pi}\int_0^{2\pi} \tilde{\mathbf{J}}^{AP}(k_x, k_y, z, \dot{x}^{AZ}, \dot{y}^{AZ})\, d\phi. \tag{B.67}$$

Now, by realising that [6, 7]

$$\frac{1}{2\pi}\int_0^{2\pi} e^{-j(k_x\dot{x}^{AZ}+k_y\dot{y}^{AZ})}\,d\phi = J_0(k_\rho a)\,e^{-j(k_x x^{AZ}+k_y y^{AZ})}, \tag{B.68}$$

$$\frac{1}{2\pi}\int_0^{2\pi} e^{-jk_x\dot{x}^{AZ}}\cos(k_\alpha\dot{y}^{AZ})\,d\phi = J_0(\sqrt{\varepsilon_{r(\text{eff})}}k_0 a)\,e^{-jk_x x^{AZ}}\cos(k_\alpha y^{AZ}) \tag{B.69}$$

and

$$\frac{1}{2\pi}\int_0^{2\pi} e^{-jk_x\dot{x}^{AZ}}\sin(k_\alpha\dot{y}^{AZ})\,d\phi = J_0(\sqrt{\varepsilon_{r(\text{eff})}}k_0 a)\,e^{-jk_x x^{AZ}}\sin(k_\alpha y^{AZ}), \tag{B.70}$$

the spectral form of the rectangular attachment mode is finally given by

$$\begin{aligned}\tilde{\mathbf{f}}^{AP}(k_x,k_y) = {} & \frac{j(k_x\,\hat{x}+k_y\,\hat{y})}{k^2_{z(\text{eff})}}\,J_0(k_\rho a)\,e^{-j(k_x x^{AZ}+k_y y^{AZ})} \\ & - \frac{(k_x k_y\,\hat{x}+k_\alpha^2\,\hat{y})}{k^2_{z(\text{eff})}}\,A(k_\alpha)J_0(\sqrt{\varepsilon_{r(\text{eff})}}k_0 a)\,e^{-jk_x x^{AZ}} \\ & - \frac{1}{W}\sum_{i=0}^{\infty}\epsilon_i\cos\left[\frac{i\pi}{W}\left(y^{AZ}+\frac{W}{2}\right)\right]\frac{(-1)^i e^{-jk_y W/2}-e^{jk_y W/2}}{[k_y^2-(i\pi/W)^2][k_x^2-\beta^2]} \\ & \cdot\left[k_y\,\hat{x}+k_x\frac{(i\pi/W)^2}{\beta^2}\,\hat{y}\right]\left[\frac{\beta\cos(\beta x^{AZ})\sin(k_x L/2)}{\sin(\beta L/2)}\right. \\ & \left. - j\frac{\beta\sin(\beta x^{AZ})\cos(k_x L/2)}{\cos(\beta L/2)}\right]J_0(\sqrt{\varepsilon_{r(\text{eff})}}k_0 a), \quad z=z^{AP},\end{aligned} \tag{B.71}$$

with

$$A(k_\alpha) = \frac{j}{k_\alpha}\left[\frac{\cos(k_\alpha y^{AZ})\sin(k_y W/2)}{\sin(k_\alpha W/2)} - j\frac{\sin(k_\alpha y^{AZ})\cos(k_y W/2)}{\cos(k_\alpha W/2)}\right]. \tag{B.72}$$

B.2.5 Circular Attachment Mode

Refer to Figure 3.11 for an illustration of the geometrical parameters associated with the circular attachment mode. The only differences here, are that the u and v axes are replaced by x and y axes respectively, and that the na subscript is dropped. As was shown in Section 3.6.2, in the spatial domain, the patch part of the circular attachment mode can be expressed as

$$\mathbf{f}^{AP}(x,y) = \begin{cases} \dfrac{-\rho}{2\pi b^2}\,\hat{\rho}, & 0\le\rho<a,\ z=z^{AP} \\ \left(\dfrac{-\rho}{2\pi b^2}+\dfrac{1}{2\pi\rho}\right)\hat{\rho}, & a\le\rho\le b,\ z=z^{AP} \\ 0, & \rho>b,\ z=z^{AP}. \end{cases} \tag{B.73}$$

Now, for a general function $\mathbf{f}$, which is only a function of ρ, the two-dimensional Fourier transform

can be simplified as [127]

$$\begin{aligned}\tilde{\mathbf{f}}(k_x,k_y) &= \int_{-\infty}^{\infty}\int_{-\infty}^{\infty}\mathbf{f}(x,y)\,e^{-jk_x x}\,e^{-jk_y y}\,dxdy \\ &= \left[-j2\pi\int_0^{\infty}J_1(k_\rho\rho)f(\rho)\rho\,d\rho\right]\hat{k}_\rho, \quad \mathbf{f}(x,y)=f(\rho)\,\hat{\rho},\end{aligned} \tag{B.74}$$

where $J_1(\cdot)$ is the Bessel function of the first kind of order 1 (in general, $J_i(\cdot)$ is the Bessel function of the first kind of order i). This implies that the spectral form of the circular attachment mode can be written as

$$\tilde{\mathbf{f}}^{AP}(k_x,k_y) = -j2\pi\Bigg[\underbrace{\int_0^b J_1(k_\rho\rho)\frac{-\rho^2}{2\pi b^2}\,d\rho}_{\Upsilon_1(k_x,k_y)} + \underbrace{\int_a^b J_1(k_\rho\rho)\frac{1}{2\pi}\,d\rho}_{\Upsilon_2(k_x,k_y)}\Bigg]\hat{k}_\rho, \quad z=z^{AP}. \tag{B.75}$$

By using the integral properties of Bessel functions [73], it can be shown that

$$\int_0^{\alpha}\rho^2 J_1(k_\rho\rho)\,d\rho = \frac{\alpha^2}{k_\rho}J_2(k_\rho\alpha). \tag{B.76}$$

It is also known that [211]

$$\int_0^{\alpha}J_1(k_\rho\rho)\,d\rho = \frac{1}{k_\rho}\Big[1-J_0(k_\rho\alpha)\Big]. \tag{B.77}$$

With these relations, the integrals $\Upsilon_1(k_x,k_y)$ and $\Upsilon_2(k_x,k_y)$ can be evaluated as

$$\begin{aligned}\Upsilon_1(k_x,k_y) &= \int_0^b J_1(k_\rho\rho)\frac{-\rho^2}{2\pi b^2}\,d\rho \\ &= \frac{-1}{2\pi b^2}\int_0^b \rho^2 J_1(k_\rho\rho)\,d\rho \\ &= \frac{-1}{2\pi b^2}\left[\frac{\rho^2}{k_\rho}J_2(k_\rho\rho)\right]\Bigg|_0^b \\ &= \frac{-1}{2\pi k_\rho}J_2(k_\rho b)\end{aligned} \tag{B.78}$$

and

$$\begin{aligned}\Upsilon_2(k_x,k_y) &= \int_a^b J_1(k_\rho\rho)\frac{1}{2\pi}\,d\rho \\ &= \frac{1}{2\pi}\int_a^b J_1(k_\rho\rho)\,d\rho \\ &= \frac{1}{2\pi k_\rho}\Big[1-J_0(k_\rho\rho)\Big]\Big|_a^b \\ &= \frac{1}{2\pi k_\rho}\Big[J_0(k_\rho a)-J_0(k_\rho b)\Big]\end{aligned} \tag{B.79}$$

respectively.

By using the integrals in (B.78) and (B.79), the spectral form of the circular attachment mode can be expressed as

$$\tilde{\mathbf{f}}^{AP}(k_x,k_y)=\left[\frac{jJ_2(k_\rho b)}{k_\rho}-\frac{jJ_0(k_\rho a)}{k_\rho}+\frac{jJ_0(k_\rho b)}{k_\rho}\right]\left[\frac{k_x}{k_\rho}\,\hat{x}+\frac{k_y}{k_\rho}\,\hat{y}\right],\quad z=z^{AP}, \tag{B.80}$$

which can further be simplified by using the property of the Bessel function that [182, 212]

$$k_\rho\rho J_{i-1}(k_\rho\rho)+k_\rho\rho J_{i+1}(k_\rho\rho)=2iJ_i(k_\rho\rho). \tag{B.81}$$

Finally, the spectral form of the circular attachment mode can then be expressed as

$$\tilde{\mathbf{f}}^{AP}(k_x,k_y)=\left[\frac{j2J_1(k_\rho b)}{k_\rho^2 b}-\frac{jJ_0(k_\rho a)}{k_\rho}\right]\left[\frac{k_x}{k_\rho}\,\hat{x}+\frac{k_y}{k_\rho}\,\hat{y}\right],\quad z=z^{AP}. \tag{B.82}$$

B.2.6 Higher-Order Circular Attachment Mode

Refer to Figure 3.11 for an illustration of the geometrical parameters associated with the higher-order circular attachment mode. The only differences here, are that the u and v axes are replaced by x and y axes respectively, and that the na subscript is dropped. As was shown in Section 3.6.3, in the spatial domain, the patch part of the higher-order circular attachment mode can be expressed as

$$\mathbf{f}^{AP}(x,y)=\begin{cases}\dfrac{-\rho^3}{2\pi b^4}\,\hat{\rho}, & 0\le\rho<a,\ z=z^{AP}\\[2ex] \left(\dfrac{-\rho^3}{2\pi b^4}+\dfrac{1}{2\pi\rho}\right)\hat{\rho}, & a\le\rho\le b,\ z=z^{AP}\\[2ex] 0, & \rho>b,\ z=z^{AP}.\end{cases} \tag{B.83}$$

In a similar way to that shown in Section B.2.5, the spectral form of the higher-order circular attachment mode can be written as

$$\tilde{\mathbf{f}}^{AP}(k_x,k_y)=-j2\pi\Bigg[\underbrace{\int_0^b J_1(k_\rho\rho)\frac{-\rho^4}{2\pi b^4}\,d\rho}_{\Upsilon_3(k_x,k_y)}+\underbrace{\int_a^b J_1(k_\rho\rho)\frac{1}{2\pi}\,d\rho}_{\Upsilon_2(k_x,k_y)}\Bigg]\hat{k}_\rho,\quad z=z^{AP}. \tag{B.84}$$

By using the integral properties of Bessel functions [73], it can be shown that

$$\int_0^\alpha \rho^4 J_1(k_\rho\rho)\,d\rho=\frac{-\alpha^4}{k_\rho}J_4(k_\rho\alpha)+\frac{4\alpha^3}{k_\rho^2}J_3(k_\rho\alpha). \tag{B.85}$$

This can be used to evaluate the integral $\Upsilon_3(k_x, k_y)$ as

$$\begin{aligned}\Upsilon_3(k_x,k_y) &= \int_0^b J_1(k_\rho\rho)\frac{-\rho^4}{2\pi b^4}\,d\rho \\ &= \frac{-1}{2\pi b^4}\int_0^b \rho^4 J_1(k_\rho\rho)\,d\rho \\ &= \frac{-1}{2\pi b^4}\left[\frac{-\rho^4}{k_\rho}\,J_4(k_\rho\rho)+\frac{4\rho^3}{k_\rho^2}\,J_3(k_\rho\rho)\right]\Bigg|_0^b \\ &= \frac{1}{2\pi k_\rho}\,J_4(k_\rho b)-\frac{4}{2\pi k_\rho^2 b}\,J_3(k_\rho b). \end{aligned} \tag{B.86}$$

The integral $\Upsilon_2(k_x, k_y)$ has already been evaluated in Section B.2.5 and is given by (B.79).

By using the integrals in (B.79) and (B.86), the spectral form of the higher-order circular attachment mode can be expressed as

$$\tilde{\mathbf{f}}^{AP}(k_x,k_y) = \left[\frac{-jJ_4(k_\rho b)}{k_\rho}+\frac{j4J_3(k_\rho b)}{k_\rho^2 b}-\frac{jJ_0(k_\rho a)}{k_\rho}+\frac{jJ_0(k_\rho b)}{k_\rho}\right]\left[\frac{k_x}{k_\rho}\,\hat{x}+\frac{k_y}{k_\rho}\,\hat{y}\right], \quad z=z^{AP}. \tag{B.87}$$

Then, by making use of the property of the Bessel function in (B.81), the spectral-domain form of the higher-order circular attachment mode can further be simplified to

$$\tilde{\mathbf{f}}^{AP}(k_x,k_y) = \left[\frac{-j16J_1(k_\rho b)}{k_\rho^4 b^3}+\frac{j4J_1(k_\rho b)}{k_\rho^2 b}+\frac{j8J_0(k_\rho b)}{k_\rho^2 b^2}-\frac{jJ_0(k_\rho a)}{k_\rho}\right]\left[\frac{k_x}{k_\rho}\,\hat{x}+\frac{k_y}{k_\rho}\,\hat{y}\right], \quad z=z^{AP}. \tag{B.88}$$